Development of high throughput microfluidic platforms for the measurement of the protein solution thermodynamic properties

van Nhat Pham

Université Fédérale

Toulouse Midi-Pyrénées

THÈSE

En vue de l'obtention du

DOCTORAT DE L'UNIVERSITÉ DE TOULOUSE

Délivré par *Université Toulouse III Paul Sabatier*
Discipline ou spécialité : *Génie des Procédés et de l'Environnement*

Van Nhat PHAM

Le 13 Décembre 2016

Titre :
Development of high throughput microfluidic platforms for the measurement of the protein solution thermodynamic properties

---

JURY
Jacques LENG, Cr. LOF. (Rapporteur)
Paul MENUT, Mcf. Montpellier SupAgro (Rapporteur)
Beatrice BISCANS, DR LGC (Examinateur)
Christophe A. SERRA, Pr. Université de Strasbourgs (Examinateur)
Jean-Christophe REMIGY, Pr. Université Paul Sabatier (Directeur de thèse)
Sébastien TEYCHENE, Mcf ENSIACET (Co-Directeur de thèse)

Ecole doctorale : *Mécanique, Energétique, Génie civil et Procédés (MEGEP)*
Unité de recherche : *Laboratoire de Génie Chimique (LGC)*
Directeur(s) de Thèse : *Jean-Christophe REMIGY et Sébastien TEYCHENE*

Acknowledgments (1page)

The work presented in this thesis would not be possible without the huge support which I received during almost 4 years in Laboratoire de Genie Chimique(LGC), Toulouse. I would like to say thank to my supervisors: Jean-Christophe Remigy and Sebastien Teychene for all of the guidance they have provided over the years.
With large amount of knowledge and patience, they have helped me become a better researcher and professional all around. Especially to my co-supervisor Sebastien Teychene, who I spent most of the time with. We not only shared knowledge about my work, but also about our family which helped I felt better in far family life. I also to thank Professor Patrice Bacchin, who invited and showed all procedures when I started my thesis. He also gave me a lot of ideas and solutions for my thesis.

Additional gratitude goes to my thesis committee including Dr. Paul Menut, Dr. Jacques Leng and Beatrice Biscans for their insightful comments and encouragement, but also for the hard questions which incented me to widen my research from various perspectives. Funding for research in this thesis was provided by Vietnamese Government and University of Science and Technology Hanoi (USTH).

I would like to thank the past and present lab mates of LGC in Rangeuil as well as Labege site for all their help and discussions, for all the fun, for all the beers we have had in the last 4 years. And I also thank my Vietnamese friends who helped and supported me a lot for living in France. Without them the 4 past years for PhD in Toulouse would not be the same.

Last but not the least, I would like to thank my family: my parents, to my wife and my son and to my brother for supporting me spiritually throughout doing this thesis far away from Vietnam and my life in general.

Abstract

Colloidal interactions in solution are the core of many industrial processes. Knowledge of the nature and intensity of these interactions leads to better process control. This is particularly true for the crystallization process, still perceived as an art, despite the efforts made during the last twenty years on its rationalization. Due to an excessive product consumption and to the time required to acquire reliable thermodynamic data, trial and error approach is still the method of choice for drug and protein crystallization. This thesis is focused on the development of more efficient measurement protocols for the determination of phase diagrams and the equation of state of a model molecule through the measurement of molecular interactions in solution, by means of different microfluidic approaches.

Firstly, a simple and inexpensive mold-making process has been developed, avoiding the use of clean room facilities and standardized protocols, which are not normally affordable and accessible to all laboratories. Microfluidic chips were then built up using different UV cured polymers. Developed chips have the advantage of providing excellent resistance to most of organic solvents, acids and bases but also the ability of withstanding pressures of up to hundred bars. Furthermore, surface modification by chemical grafting of the microchannel walls enables to steadily change their wetting properties allowing the generation of water in oil or oil in water emulsions.

The study of protein solutions at the nanoscale has been performed by coupling these experimental devices to small angle X-Ray scattering from a synchrotron source. First, a parametric study to determine the optimal operating conditions for obtaining the best signal quality was carried out. This study provides a basis for a measurement protocol which can be standardized in the future for other applications. At the end of this study, the form factors of various proteins were measured. These curves provided information about the size, the oligomeric state and overall the shape of the protein molecules. Additionally, it was demonstrated neither the protein solutions nor the continuous phase were damaged by radiation and the chosen surfactant chosen for the study did not

interact with proteins. In addition, the study of protein interactions was performed by screening the charges of proteins by the continuous addition of a saline solution. The second virial coefficient was determined from the extrapolation of the structure factor at zero angle. The results are in good agreement with the results published in the literature but using few milligrams of protein.

The equation of state of lysozyme, relating the osmotic pressure to the volume fraction of protein, was also determined using a microfluidic device. The experimental setup was based on the mass transfer between a dispersed and a continuous phase. Drops of protein solution were generated in an organic solvent which is partially miscible with water and in which proteins are insoluble. Given the difference in chemical potential of water between the continuous and the dispersed phases, the water diffuses through the interface until thermodynamic equilibrium is reached. Knowing the chemical potential of the continuous phase (considered as an infinite medium due to the small size of the droplets generated as a dispersed phase), the activity of water in the disperse phase can be obtained. For a given range of water activity, the resulting equation of state was found to be in agreement with data reported in the literature. In contrast, when the transfer material is high, i.e. when the difference in activity is too high, the reorganization of the proteins within the drop is too slow leading the skin formation. To link the dynamic of the transfer to the thermodynamic properties of the system a first modeling approach is proposed. This approach aims to determine the equation of state of the protein using only one droplet.

Résumé en français

Les interactions de colloïdes en solution sont au cœur de nombreux procédés de génération de séparation de solides divisés. La connaissance de la nature ainsi que l'intensité de ces interactions engendre une meilleure maîtrise du procédé. Ceci est particulièrement vrai pour les processus de cristallisation, encore perçu comme un art, malgré les efforts effectués durant ces vingt dernières années concernant leur rationalisation. L'essai-erreur est encore à l'heure actuelle la méthode de choix pour la cristallisation de protéines ou d'actifs pharmaceutiques. La raison principale est essentiellement liée à la consommation excessive en produit ainsi qu'au temps nécessaire pour acquérir des données thermodynamiques fiables. L'objectif des travaux de cette thèse est de mettre en place des outils microfluidiques génériques permettant de déterminer les diagrammes de phases et l'équation d'état d'une molécule modèle au travers de la mesure des interactions moléculaires en solution.

Un procédé simple et peu onéreux de fabrication de moule a été développé à partir de films sec. Les puces microfluidiques ont ensuite été réalisées à l'aide de polymères photoréticulables aux UV. Les puces développées présentent l'avantage d'offrir une très bonne résistance aux solvants organiques, aux acides et bases couramment utilisée mais résistent également à des pressions allant jusqu'à la centaine de bars. En outre, la modification par greffage chimique de la surface des microcanaux permet de générer des émulsions eau dans huile ou huile dans eau.

L'étude des solutions de protéines à l'échelle nanométrique a été réalisée en couplant ces dispositifs expérimentaux à la diffusion de rayonnement X aux petits angles. Une étude paramétrique a permis de déterminer les conditions opératoires optimales en vue de l'obtention d'un signal de bonne qualité. A l'issue de cette étude, les facteurs de formes de différentes protéines ont été mesurés. Il a été mis en évidence que d'une part ni les solutions de protéines ni la phase continue n'étaient endommagées par les radiations et que le tensioactif retenu pour l'étude n'interagissait pas avec les protéines. En outre, l'étude des interactions faibles proteines-proteines a été réalisée en écrantant les charges

des protéines en solution par l'ajout en continue une solution de saline. Le second coefficient du viriel a été déterminé à partir de l'extrapolation à angle nul du facteur de structure. Les résultats obtenus sont en très bon accord avec les résultats publiés dans la littérature mais en utilisant seulement quelques milligrammes de protéines.

L'équation d'état du lysozyme, reliant la pression osmotique à la fraction volumique, caractéristique des interactions en solution a été également déterminé à l'aide d'un dispositif microfluidique basé sur le transfert de matière entre d'une phase dispersée vers une phase continue. Des gouttes de solution aqueuse de protéines sont générées dans un solvant organique partiellement miscible avec l'eau dans lequel les protéines sont insolubles. Etant donné la différence de potentiel chimique de l'eau entre la phase dispersée et la phase dispersée, l'eau diffuse au travers de l'interface jusqu'à l'équilibre thermodynamique. Connaissant le potentiel chimique de la phase continue (considérée comme un milieu infini), l'activité de l'eau dans la phase dispersée à l'équilibre peut être obtenue. Dans une certaine gamme de fraction volumique, l'équation d'état obtenu est en bon accord avec les données de la littérature. En revanche, lorsque le transfert de matière est trop important, lorsque la différence d'activité est trop importante, la réorganisation des protéines à l'intérieur de la goutte est trop lente et la formation d'une peau est observée. Afin de relier la dynamique du transfert aux propriétés thermodynamique du système une première approche de modélisation est proposée. Cette approche a pour but de déterminer l'équation d'état de la protéine avec une seule goutte.

Synthèse en français

INTRODUCTION

Les interactions colloïdales en solution sont au cœur de nombreux procédés industriels comme la filtration, la précipitation, le séchage et la cristallisation. La connaissance de la nature et de l'intensité de ces interactions conduit à une meilleure compréhension des processus élémentaires à l'origine des changements d'état de la matière et donc à un meilleur contrôle des procédés industriels. Cependant la détermination expérimentale des interactions colloïdales ainsi que la mesure des propriétés macroscopiques qui en découlent sont très consommatrice en produit et en temps. A l'heure actuelle, l'approche empirique essais-erreur (méthode de screening par des robots par exemple) est la méthode de choix dans l'industrie, mais cette approche ne permet pas de rationaliser l'étude des conditions opératoire en vue de la mise en place d'une méthodologie globale de dimensionnement d'un procédé ou de détermination des conditions optimales de cristallisation, de séchage ou de filtration par exemple.

Ainsi, l'objectif de cette thèse est de développer des techniques de mesure plus efficaces des propriétés thermodynamiques des solutions protéines en utilisant des outils microfluidiques. Les principaux objectifs de cette approche sont les suivants:

- de développer une technologie fiable, peu coûteuse, rapide et facile pour produire des systèmes microfluidiques polyvalent.

- de mesurer in-situ, à l'aide de ces outils, les interactions protéine-protéine.

- d'établir avec peu de produit dans un temps raisonnable l'équation d'état d'une solution de protéine.

Dans le premier chapitre, le processus de fabrication de puces microfluidiques est présenté. Tout d'abord, un moule rigide est conçu et préparé à l'aide de la méthode de photolithographie douce à l'aide de deux types de resines photosensibles : la SU-8 de MicroChem et film sec (série WBR2000) de chez DuPont.

Selon les buts des puces microfluidiques, le masque est conçu avec plusieurs composants tels que les structures de génération de gouttelettes, les structures de mélange et de stockage. Le processus de photolithographie typique est effectué étape par étape (nettoyage de substrat, revêtement, exposition, cuisson, développement). Pour chaque étape, les paramètres de la littérature ont été optimisés afin d'obtenir un moule avec la meilleure résolution possible. Les moules fabriqué à partir de la résine SU-8 possèdent de très bonnes propriétés physico-chimiques. Cependant, le procédé de production nécessite beaucoup de temps, des équipements coûteux et un environnement très propre (salle blanche). Ces contraintes ne sont pas ou peu satisfaites dans des laboratoires non spécialisés. En vue de mettre en place un procédé de fabrication peu onéreux et adapté a de nombreux laboratoires non spécialistes, un protocole de fabrication de moule a été mis en œuvre à partir de films sec photopolymérisables. Le protocole de fabrication développé pendant cette thèse a permis de fabriquer des moules dont la résolution est comprise entre 5 à 50µm, en fonction de l'épaisseur du moule.

A partir de ces moules, des puces microfluidiques ont été construite à partir de polymère de type Thiolène. Deux types de polymères ont été utilisés: la NOA 81 (Norland Optical Adhesive) de Norland Inc. et OSTEmer 322 de Mercene Lab (Suède). Les puces microfluidiques ainsi construites présentent des propriétés intéressantes en termes de résistance à une large gamme de produit chimiques, de résistance à la pression et des propriétés de surface ajustables.

Dans le deuxième chapitre de la thèse, ces puces microfluidiques ont été couplées à la diffusion de rayons X à petites angles (SAXS) afin d'étudier les interactions de protéines en solution. L'objectif de cette étude est :

(1) De mettre en place un dispositif expérimental fiable permettant d'étudier le facteur de forme et de structure de solutions de protéines

(2) d'étudier l'évolution des interactions faibles entre les molécules de protéines en solution en fonction des conditions opératoires.

Dans le dernier chapitre, un système microfluidique a été utilisé pour étudier le phénomène de transfert de masse au cours de la dissolution de gouttes d'eau pure ou de gouttes contenant un solution de protéines dans un solvant organique. À la fin du processus de dissolution, taille finale de la goutte dépend de l'équilibre thermodynamique de l'eau à l'intérieur et à l'extérieur de la goutte. Cet état d'équilibre dépend de l'activité de l'eau dans initialement présente dans la phase continue. Lorsque l'équilibre thermodynamique est atteint, la connaissance de l'activité de l'eau dans phase continue permet de déterminer l'activité de l'eau dans l'eau à l'intérieur de la gouttelette. À partir de l'état final de la gouttelette de la solution de protéines, plusieurs paramètres thermodynamiques tels que la pression osmotique, le potentiel d'hydratation peuvent être déterminés. Ainsi, les expériences réalisées dans ce chapitre ont trois objectifs principaux:

(1) de concevoir et valider un système microfluidique adaptée à l'étude de la déshydratation de de de solution de protéines.

(2) D'obtenir l'équation d'état de solution de protéines reliant l'évolution de la pression osmotique à la fraction volumique en protéine.

(3) Construire les premières bases d'un modèle de transfert basé sur les lois Fick (processus purement diffusif) pour prédire la dynamique de dissolution des gouttes.

CHAPITRE 1

Protocole de fabrication de masque et de puces microfluidiques low-cost et rapide

Partant du constat que les systèmes microfluidiques nécessitent à l'heure actuelle un investissement et un coût de maintenance conséquent pour les laboratoires, nous avons développé lors de ces travaux des protocoles de fabrication de moules et de puces microfluidiques rapide et peu onéreux à mettre en œuvre.

1. **Mise en place d'un protocole de fabrication de moules de puces microfluidique à partir de films secs.**

Dans un premier temps, les moules des puces microfluidiques sont réalisés à partir de films sec photosensibles de chez Dupont (film de type WBR 2000). Ce type de fil a été retenu, après avoir effectué différents test sur différents film sec, il est apparu que ce type de films offrent une résolution importante et un rapport d'aspect (dimension latérale / dimension verticale des motifs) de l'ordre de 3.

Après analyse systématique des conditions opératoires de fabrication des moules microfluidique (température de lamination, temps de repos, température de « bake », temps de développement et traitement de surface…) un protocole a été mis en place. Tout d'abord les films sec photosensibles sont laminés sur un substrat en verre à l'aide d'une lamineuse (XXXX) à une température de 95°C et une vitesse de 1.2m/min. Le film est ensuite placé dans une étuve à 65°C pendant 25min afin d'améliorer l'adhésion de la résine sur le substrat. L'exposition est réalisées

avec une insoleuse UV KUB 3 (λ = 365nm, P = 30W/cm²), l'énergie optimale d'exposition en fonction de l'épaisseur des films est donnée sur la Figure 1

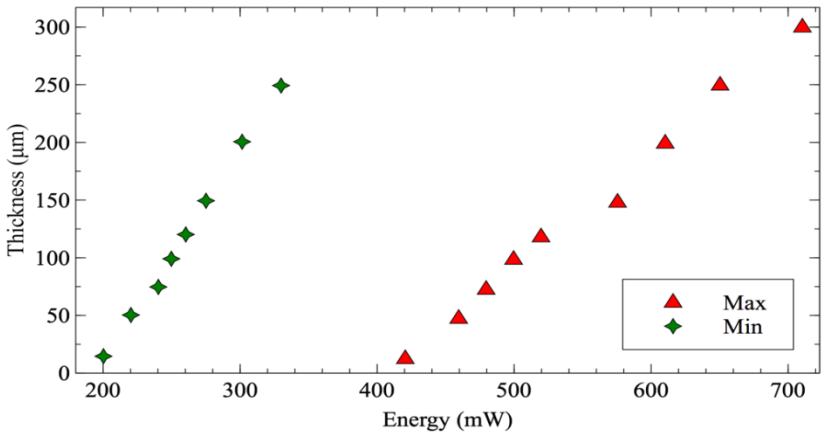

Figure 1 Evolution de l'energie d'exposition en fonction de l'epaisseur de la résine

Le développement des moules est ensuite réalisé à l'aide d'un développeur a spray avec un solution de K2CO3 à 1% massique à 25°C. Le temps de développement en fonction de l'épaisseur des films est donné dans le tableau XX. Les moules sont ensuite rincé puis séché à l'azote et laissé a température ambiante pour une durée de 6h afin d'achever le processus de réticulation de la résine.

Pour éviter l'adhésion des polymères (Polydimethyl siloxane, (PDMS), ou OSTEMER) il est nécessaire de traiter la surface des moules. Ce traitement est réalisé dans un premier temps par immersion des moules dans du toluène perdant 30s, puis dans dans une suspension de fluoropolymère (NOVEC 1720). Les moules ainsi obtenus sont parfaitement hydrophobes et lipophobes. Un exemple de moule est présenté sur la Figure 2.

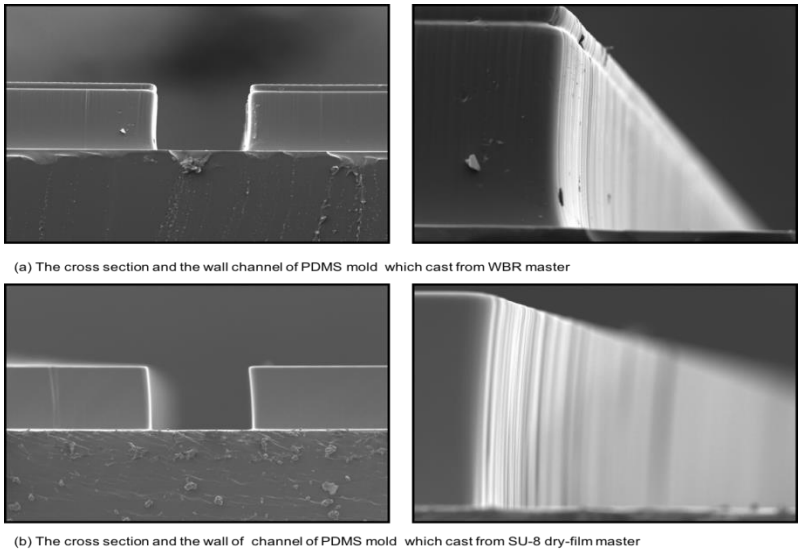

Figure 2 Exemple de moules en PDMS issue des deux technologie de fabrication (a) Films sec WBR 2000 (b) Résine liquide SU 8 2050

2. Protocole de fabrication des puces microlfuidiques polyvalentes.

Le Polydimethyl Siloxane (PDMS) est le matériau le plus utilisé pour la fabrication de puces microfluidiques. Il doit sa popularité a ses propriétés remarquables (parfaitement transparent dans l'UV et le visible, faible retrain, hydrophobe) et à sa facilité de mise en œuvre. Cependant, la principale faiblesse de se matériau est sa faible résistance à la plus part des solvants organiques (alcanes, cétone…). C'est la raison pour laquelle, ce matériau est assez peu utilisé en génie chimiques, par exemple, pour l'étude de réactions complexes impliquant l'utilisation de fluides organiques. Dans cette optique, nous avons développé des protocoles de fabrication de système microfluidiques (plus ou moins complexes) en utilisant des résines de type thiolène (NOA, OSTEMER). En outre, certaines de ces résines présentent l'avantage de contenir des groupements époxy permettant de fabriquer des plateformes de microfluidiques sur divers matériaux (acier, aluminium, polymères…).

Les protocoles mis en place lors de cette thèse ont permis de fabriquer des systèmes microfluidiques dont les propriétés de surface (la mouillabilité notamment) peut être ajustée en fonction des besoins de l'étude. Ainsi il a été possible de générer de gouttes d'eau dans l'huile ou de gouttes d'huile dans l'eau. En outre, il a été montré que ces systèmes microfluidiques peuvent résister à des pressions allant jusqu'à 50bar, permettant l'étude de réaction à haute pression et l'utilisation de fluides surpercritique.

Chapitre 2

Couplage microfluidique-diffusion de rayons X aux petits angles pour l'étude du facteur de forme et de structure des protéines en solution.

Dans ce chapitre, nous nous intéressons à la détermination des facteurs de formes et de structure de protéines étudiée grâce au couplage entre microfluidique et SAXS. Des dispositifs microfluidiques sont conçus et développés pour générer des gouttes de phase aqueuses monodisperses contenant des protéines dans une solution tampon avec un agent de cristallisation, le tout dispersé dans une phase porteuse huileuse contenant un surfactant pour stabiliser l'interface des gouttes. Les gouttes ainsi générées sont transportées vers le faisceau de rayons X pour obtenir des données SAXS. Des informations sur la structure, la forme et les interactions entre protéines à l'échelle du nanomètre peuvent ainsi être obtenues. En faisant varier les débits des différentes solutions, il est facile et rapide d'étudier un très grand nombre de conditions physico-chimiques

1. Matériel et méthode

a. Construction de la plateforme microfluidique.

Les puces microfluidiques ont été développées à l'aide des protocoles présentés dans le premier chapitre de la thèse. Le lien entre la puce microfluidique et le porte-échantillon SAXS est réalisé en connectant un capillaire en silice de verre (ID 320µm, OD 435µm, Postnova Analytics) directement en sortie de puce. Le capillaire est scellé hermétiquement dans le porte-échantillon afin de maintenir le vide autour de lui, nécessaire pour l'obtention de données de diffusion de de bonne qualité. Pour

acheminer les solutions à la puce, des seringues de 1mL (Hamilton, USA) sont connectées à la puce à l'aide de tubes en plastiques et de fines aiguilles métalliques (OD 300µM, Sigma-Aldrich, Allemagne) insérées dans la puce. Les débits sont contrôlés à l'aide de pousse-seringues haute précision (neMESYS Cetoni, Allemagne). Une illustration d'une puce est présenté en Figure 3.

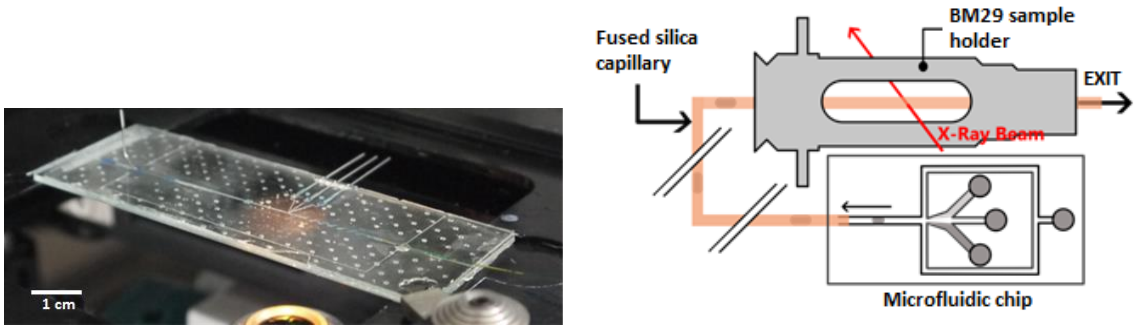

Figure 3 Puce microfluidique (gauche) et connexions au SAXS (droite)

b. Diffusion de rayons X aux petits angles par rayonnement synchrotron (SAXS)

Les mesures SAXS ont été réalisées sur la ligne de lumière BM29 à l'European Synchrotron Radiation Facility (ESRF) à Grenoble. Les images de diffusion en deux dimensions ont été obtenues avec un détecteur Pilatus 1M. La longueur d'onde des rayons X et la distance entre le capillaire et le détecteur étaient de 0,099 nm et 2,87 m respectivement couvrant une gamme allant de 0,03 à 4,5 nm-1 pour le vecteur de diffusion. La taille du faisceau de rayons X est ajustée avec des fentes pour atteindre une taille de 90µm horizontalement et 165µm verticalement. Le porte-échantillon peut être déplacé par rapport au faisceau de quelques millimètres avec une précision de 10µm. Dans notre dispositif microfluidique, des gouttes aqueuses contenant de la protéine, du tampon et un agent de cristallisation sont formées et transportées par une huile fluorée contenant un surfactant pour stabiliser les interfaces de goutte. Deux différents surfactants ont été étudiés, le Perfluorooctanol (PFO) de Sigma-Aldrich et

un copolymère à trois blocs (PFPE-PEG-PFPE) de Ran Biotechnologies, tous deux dissous à une concentration précise dans de l'huile Krytox (DuPont) pour former des gouttes stables sans affecter la stabilité biologique et les interactions entre protéines.

2. Résultats et discussion

a. Validation du dispositif expérimental

La plupart des composés utilisés lors de ces expériences SAXS (protéine, surfactant, huile etc.) peuvent être dégradés par l'intense faisceau de rayonnement synchrotron. Il est donc nécessaire de trouver la bonne combinaison de composés, qui donne un signal SAXS suffisant sans effet de radiation. De plus, le surfactant ne doit pas interagir avec la protéine dans les gouttes et la dénaturer. Pour valider notre couplage microfluidique/SAXS et identifier le meilleur surfactant, la protéine rasburicase de forme native tétramérique a été testée dans des gouttes avec un tampon Tris à pH 8.0 et 2%m de perfluorooctanol dans de l'huile Krytox GPL100. Les courbes SAXS de la rasburicase présentant l'intensité diffusée en fonction du vecteur de diffusion sont présentées dans la figure 2. Les points noirs sont les résultats expérimentaux et les courbes en pointillés éloignés et continue sont les intensités diffusées obtenues à partir des coordonnées atomiques avec CRYSOL (Svergun & al. (1995)) pour le dimère et le tétramère de rasburicase respectivement. La courbe en pointillés rapprochés obtenue avec OLIGOMER (Konarev & al. (2003)) représente la meilleure correspondance avec les résultats expérimentaux et indique que la protéine dans les gouttes est un mélange de 58% de tétramère et de 42% de dimère. Dans ces conditions expérimentales, la protéine est donc un mélange de la forme native tétramérique et d'une forme dissociée dimérique.

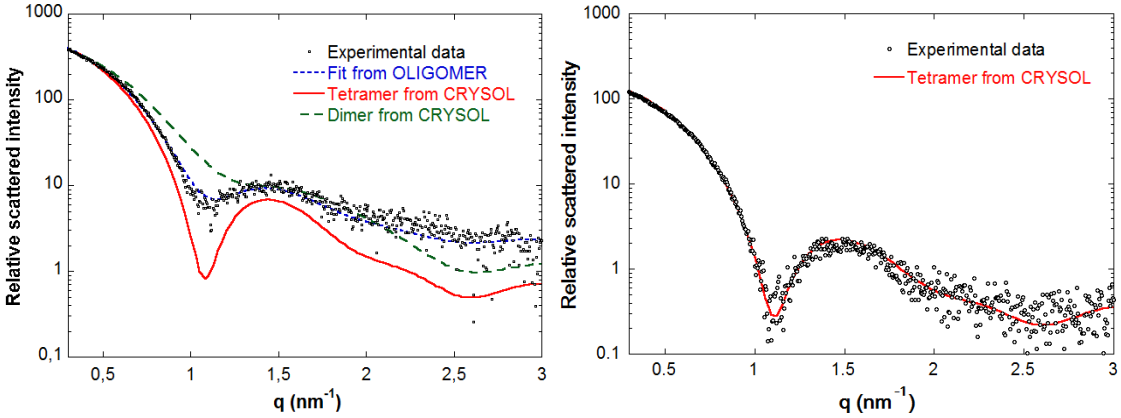

Figure 4 Courbes SAXS de la rasburicase avec dans l'huile un surfactant Perfluorooctanol (gauche) et copolymère trois blocs PEG-PFPE-PEF (droite)

Cela suggère que le surfactant à l'interface, en particulier les têtes polaires dans la goutte aqueuse, pourrait interagir avec les tétramères de protéine, les dissociant en dimères. Par conséquent, le perfluorooctanol semble pouvoir dénaturer les protéines ce qui limite considérablement son utilisation pour nos expériences microfluidiques.

Un autre surfactant a par conséquent été testé, un copolymère à trois blocs (PEG-PFPE-PEG) de Ran Biotechnologies dissous à 2%m dans l'huile Krytox. Les données SAXS avec ce surfactant et la rasburicase sont présentées dans la figure 2. Cette fois, la courbe CRYSOL pour le tétramère correspond parfaitement aux données expérimentales illustrant le fait que la protéine n'est pas dénaturée ce qui signifie que le surfactant est inerte vis-à-vis de la protéine. De plus, ces données illustrent qu'en utilisant notre système microfluidique, des données SAXS de bonne qualité, en accord avec les structures cristallographiques de macromolécules peuvent être obtenues.

b. Etude des interactions faibles entre protéines

L'objectif de la deuxième série d'expérience est l'étude de la variation des interactions faibles entre protéines en solution en variant la concentration en agent cristallisant. Afin d'induire un phénomène de

cristallisation, l'échantillon de protéine doit être dans un état d'interaction attractif. L'expérience est menée avec du lysozyme à une concentration stock de 130 mg/mL dans un tampon acétate à pH 4,4. L'huile et le tensioactif utilisés sont ceux précédemment retenus, le Krytox GPL100 et le copolymère à trois blocs respectivement. L'agent cristallisant utilisé est le sel NaCl à une concentration stock de 2M. Dans cette série d'expérience, les concentrations dans les gouttes pour la protéine sont de 21,7 – 52 – 86,7 mg/mL et pour le sel de 0 – 100 – 200 – 300 – 400 mM pour un total de 15 expériences. Des exemples de courbes SAXS correspondantes à deux concentrations en protéines sont présentées dans la Figure 5.

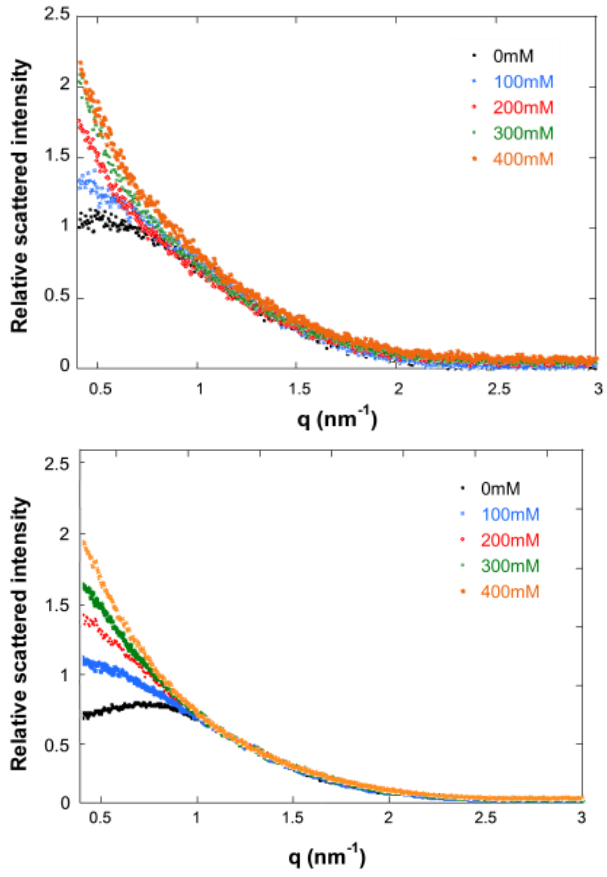

Figure 5 Courbes SAXS pour différentes concentrations en sel et lysozyme : 21,7 (gauche) 86,7 mg/mL (droite)

L'intensité diffusée d'une solution de macromolécules en interaction faible peut être écrite :

$$I(c,q)=I\_FF\ (c=0,q)\times S(c,q) \quad (1)$$

IFF représente l'idéalité de la solution, est appelé facteur de forme et ne dépend que de la macromolécule considérée (forme, taille, …). S est le facteur de structure et dépend des interactions faibles entre macromolécules en solution.

Les interactions peuvent être caractérisées à l'aide du second coefficient du viriel A2 qui est relié aux variations du facteur de structure en fonction de la concentration de macromolécules (Vivarés, Bonneté (2002)).

$$S(c,q=0)=1/(1+2MA\_2\ c) \quad (2)$$

Conformément à l'équation (2), la pente du tracé de S(c, q=0) en fonction de la concentration en protéine est -2MA2 ce qui donne accès à la valeur de second coefficient du viriel pour chaque concentration en sel. Ces valeurs sont présentées sur la figure 6. Les résultats illustrent qu'en l'absence de sel, la protéine est dans un état répulsif due à des répulsions électrostatiques causées par la charge nette positive du lysozyme à pH 4,4. Lorsqu'une faible quantité de sel est ajoutée dans les gouttes, les charges du lysozyme sont partiellement écrantées et la répulsion due aux forces électrostatiques est réduite entraînant une diminution du second coefficient du viriel. Quand il y a assez de sel pour écranter toutes les charges du lysozyme, il n'y a plus de répulsion entre les protéines et les interactions deviennent attractives. Cela se produit dans notre cas pour des concentrations en sel supérieures à 180mM. Ces résultats sont en accord avec d'autres obtenus en micro volumes (Bonneté & al. (1999)). Ainsi, notre dispositif microfluidique permet d'obtenir des données de bonne qualité qui permettent d'étudier les interactions entre macromolécules et de trouver des conditions optimales de cristallisation au travers de mesures du second coefficient du viriel, tout ceci en utilisant

une faible quantité de produit. Dans cette étude, seuls 12 mg de lysozyme ont été utilisés.

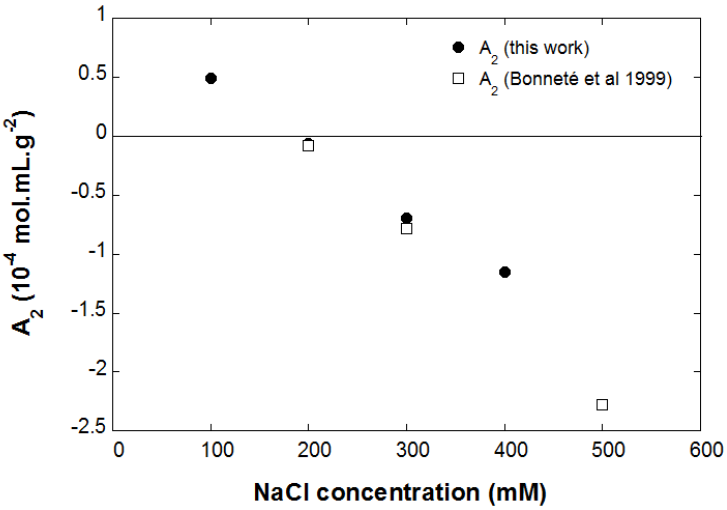

Figure 6 Second coefficient du viriel du lysozyme en fonction de la concentration en sel

Chapitre 3

Approche microfluidique pour la mesure de la déshydratation de protéines.

La détermination de l'équation de l'état de colloïdes est d'une importance primordiale dans l'industrie (aliments, peinture, chimie, cosmétiques ...) puisqu'il définit les conditions opératoires de nombreux procédés tels que le séchage, le mélange, la filtration et la cristallisation. Pour déterminer cette équation d'état l'approche la plus utilisée est la mesure de la pression osmotique à l'aide de procédés membranaires. Cette technique expérimentale a été largement utilisée pour étudier le comportement de la caséine (Bouchoux et al. 2009; Bouchoux et al., 2010; Bouchoux et al., 2014), du lysozyme (Coralie Pasquier et al., 2016; Grobelny et al., 2014), et de l'ovalbumine (C. Pasquier et al. 2012). Cependant, malgré sa pertinence, cette technique présente plusieurs inconvénients, dont par exemple le volume d'échantillon de la chambre de dialyse (quelques millilitres) et le faible flux de perméation à travers la membrane (en raison d'un ratio de volume de surface non optimisé).

Dans ce chapitre, une nouvelle méthode permettant de déterminer l'équation d'état d'une protéine modèle en solution est proposée. Cette méthodologie est basée sur le transfert de masse entre deux fluides partiellement miscibles. A l'aide d'un système microfluidique présenté sur la Figure 7 , des gouttes de phase dispersée (contenant le soluté et le solvant) sont générées dans une phase continue, dont les propriétés de mélanges telles que l'activité de l'eau sont connues.

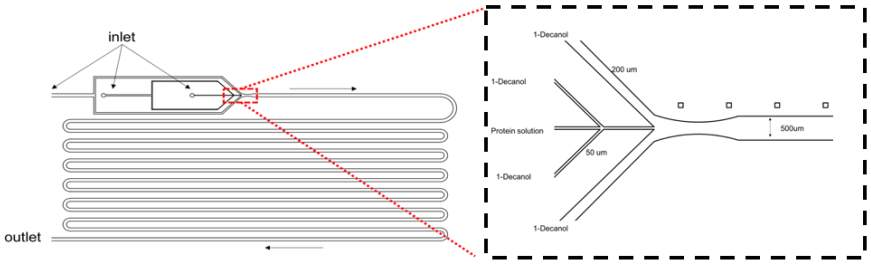

Figure 7 Puce microfluiidque retenue pour cette étude. Cette puce est constituée d'une zone de génération de gouttes (h=l=50µm) et d'un serpentin (h=l=500µm). Le serpentin permet d'assurer un temps de séjour suffisant afin d'atteindre l'équilibre thermodynamique

Dans cette étude la phase dispersée est constituée d'une solution aqueuse de protéine (lysozyme) et la phase continue est un solvant organique (1-décanol) avec une quantité connue d'eau. Dès que les gouttelettes sont générées, étant donnée la différence de potentiel chimique de l'eau dans la goutte et dans la phase dispersée, le transfert de masse se produit, l'eau transfère de la goutte vers la phase continue, jusqu'à ce qu'un équilibre thermodynamique soit atteint. En considérant que la protéine est immiscible avec le solvant organique, l'évolution temporelle du diamètre de la goutte permet de déterminer la quantité d'eau transférée. En outre, si le volume de phase continue est grand par rapport au volume de la goutte, la concentration en eau, et donc son activité, dans la phase continue loin de l'interface sont constante et égale à l'activité avant le transfert. Le dispositif expérimental permettant le suivi temporel de la taille de la goutte est présenté sur la Figure 8.

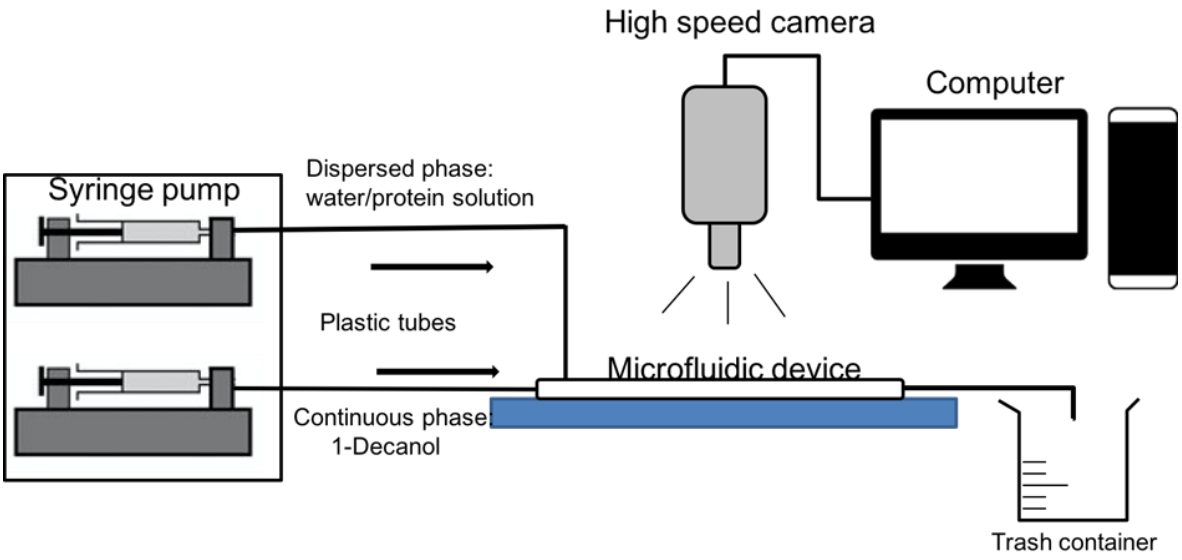

Figure 8 Dispositif expérimental permettant le suivi temporel de la dissolution de la goutte

Lorsque l'équilibre thermodynamique est atteint, l'égalité des potentiels chimiques de la phase continue et de la phase dispersée permet de déduire l'activité de l'eau dans la goutte. La pression osmotique de la solution est alors calculée à partir de la connaissance de l'activité de l'eau à l'équilibre par la relation :

$$\Pi_{oms} = k_B T / \nu_w \ln(a_w)$$

En réalisant ces expériences pour différentes teneurs en eau, l'évolution de la pression osmotique en fonction de la fraction volumique en protéine, peut être déterminée.

Un exemple de suive d'une goutte en fonction du temps est présenté sur la Figure 9.

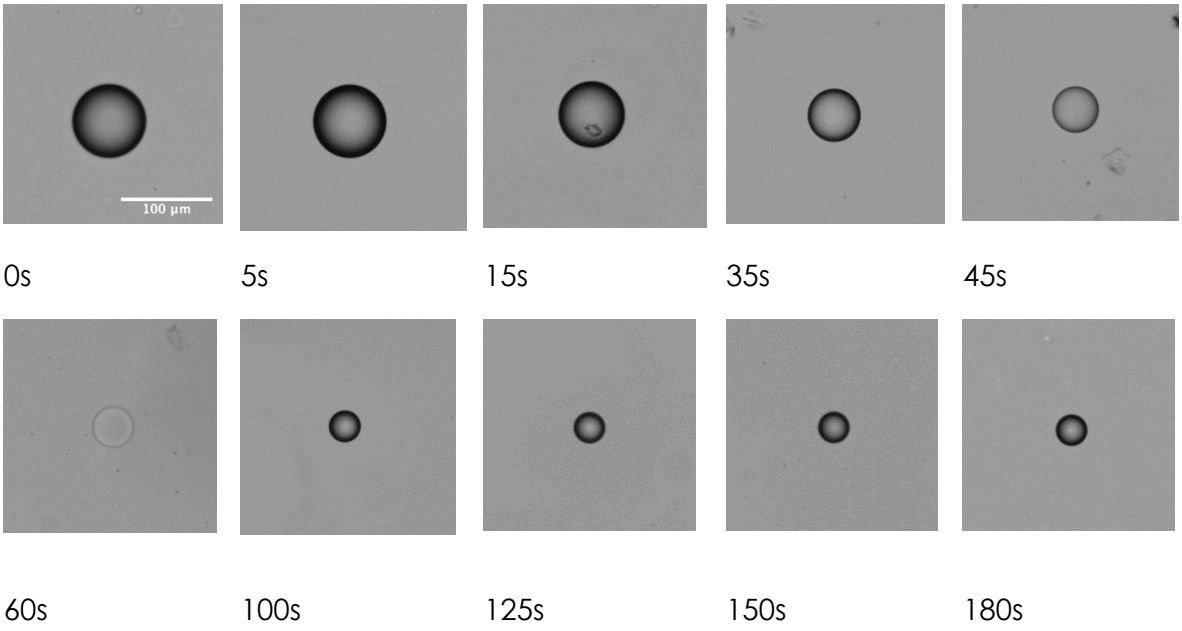

Figure 9 *Evolution de la goutte en fonction du temps et de la position dans le serpentin pour un rapport de saturation de* $f=C_{eau}/C_{sat}=0.4$

Sur la figure 10 est présentée la courbe caractéristique de dissolution d'une goutte contenant une solution de protéine.

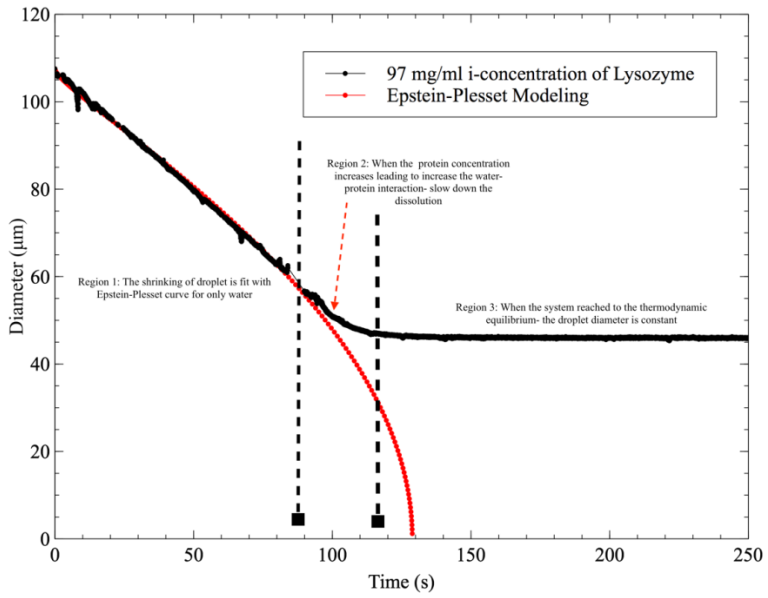

Figure 10 Evolution typique du diamètre de la goutte en fonction du temps (la courbe théorique de dissolution d'une goutte d'eau pure est donnée en rouge)

Il apparait clairement sur cette figure, que le processus de dissolution peut être divisé en trois étapes :

- Une première étape pendant laquelle la dissolution est rapide. Dans cette partie la goutte se comporte comme une goutte d'eau pure. La diminution du diamètre de la goutte est lié au transfert de l'eau qui n'est pas en interaction directe avec la protéine.
- Lors de la deuxième étape, le transfert est ralenti. C'est à partir de cet instant que la goutte est déshydratée.
- Dans la troisième partie, le diamètre de la goutte est constant et l'équilibre thermodynamique est atteint.

A partir des valeurs des plateaux obtenus pour différentes conditions opératoire, l'évolution de la pression osmotique en fonction de la fraction volumique en protéine, permettant la détermination de l'équation d'état, est présenté sur la figure 11.

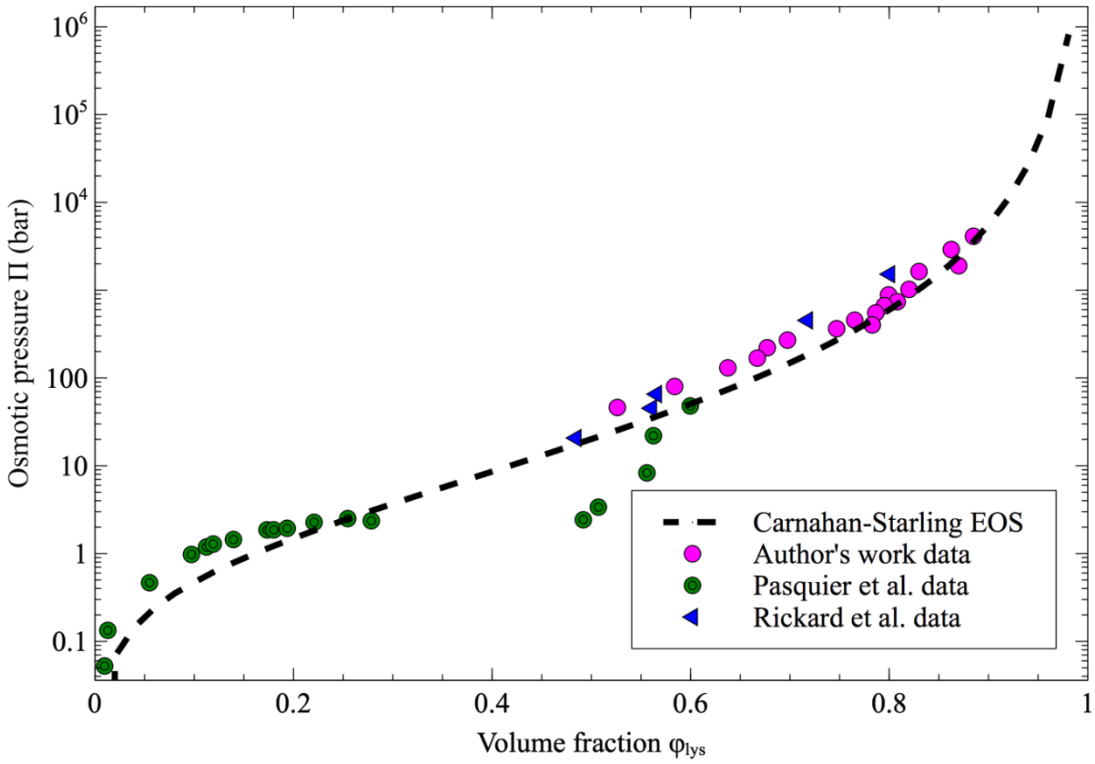

Figure 11 Evolution de la pression osmotique en fonction de la fraction volumique en protéine.

Comme présenté sur la figure 11, les données obtenues par cette approche sont en très bon accord avec les données de la littérature.

Dans cette étude, une nouvelle approche de détermination de l'équation d'état de protéine est proposée. Les résultats obtenus avec ce nouveau dispositif expérimental sont en très bon accord avec les données issues de la littérature.

En outre, cette approche permet également de suivre la dynamique du transfert. La mise en place d'une modélisation fine de la dissolution de la goutte (en couplant les deux lois de Fick) permettra la détermination de l'équation d'état de la protéine en utilisant une seule goutte.

CONCLUSION

Le travail présenté dans cette thèse comprend une approche originale pour le développement de nouvelles méthodologies plus efficaces pour l'étude du comportement de protéines en solution.

Tout d'abord, afin de fournir des outils nouveaux analytiques à haut rendement permettant une réduction drastique de la consommation de réactifs et du temps de mesure, un protocole rapide, peu coûteux et robuste de fabrication de puces microfluidiques a été développé. Le protocole développé, lors de cette thèse, présente les avantages suivants:

- Haute résolution, prototypage rapide et matériaux peu coûteux. Les structures 2D peuvent être fabriquées dans des laboratoires non spécialisé en microfabrication (en évitant les installations coûteuses de salle blanche). L'ensemble du processus, de la conception CAO à la fabrication de systèmes réels, prend moins de 24 heures et le coût unitaire pour la fabrication d'une puce est inférieur à 5 euros.
- Modification facile des propriétés de surface des microcanaux: Plusieurs techniques simples sont proposées pour modifier la chimie de surface des micro-canaux pour les rendre hydrophiles ou hydrophobes, selon leur utilisation prévue.
- Résistance aux produits chimiques et à la pression : les puces ainsi fabriquées résistent aux solvants usuels utilisés dans les laboratoires de chimie et biologie. En outre, ces systèmes microfluidiques résistent à des pressions allant jusqu'à 200 bars pendant plus de 20 minutes.

Deuxièmement, ce protocole de fabrication a permis de développer des plates-formes microfluidiques peu coûteuses pour deux applications différentes. Dans le chapitre III, les interactions moléculaires de protéines en solution en présence d'agents précipitants (sel) ont été étudiées en couplant la microfluidiques de gouttes à de la diffusion de rayons X aux petits angles issue d'un rayonnement synchrotron. Une optimisation complète des paramètres expérimentaux (matériaux, revêtement de surface, tensio-actifs, phase

porteuse…) a été menée afin de sélectionner les matériaux capables de résister aux dommages causés par les rayonnements intenses du synchrotron et tout en ne modifiant pas les propriétés structurales des protéines en solution. Les expériences ont été réalisées sur la ligne BM29 à l'ESRF avec plusieurs protéines modèles. La dispositif microfluidique a d'abord été testée avec de une protéine connue pour être particulièrement sensible à la dénaturation (Rasburicase). Le facteur de forme obtenu pour la Rasburicase est en bon accord avec les données rapportées dans la littérature, validant le nouveau protocole expérimental. Par la suite, Les interactions protéine-protéine ont été étudiées pour différentes concentrations de sel. Les expériences ont été menées avec succès en utilisant seulement quelques milligrammes de protéines et quelques dizaines de microlitres de solution. Les résultats ainsi obtenus sont en parfait accord avec les résultats issus de la littérature.

Enfin, l'étude présentée dans le chapitre IV fut dédié à la détermination de l'équation d'état d'une solution de protéine en diminuant drastiquement les temps de mesures ainsi que la consommation en produit (quelques mg de protéine). Cette nouvelle approche permet également de capter la dynamique du système. Une approche numérique a été mise en place pour prédire l'évolution du diamètre des gouttelettes au cours du processus de déshydratation. En première approche, on a supposé que l'activité de l'eau dans la phase continue était égale au rapport $aw = c / csat$, cette approche certes imprécise, a permis de capter les ordres de gradeurs de la cinétique de dissolution, mais reste relativement imprécise. Une étude, plus poussée, de modélisation des transferts (en couplant la première et la seconde loi de Fick pour des systèmes non idéaux) ainsi qu'une modélisation rigoureuse thermodynamique de la phase continue (par une approche a enthalpie libre d'excès, par exemple) permettrait d'obtenir l'équation d'état de la proteine en n'utilisant qu'une seule gouttelette, mais également de déterminer des loi de comportement pour certaines transition structurales observées (cristallisation, formation de peau).

Table of Contents

ACKNOWLEDGMENTS (1PAGE) I

ABSTRACT III

RESUME EN FRANÇAIS V

SYNTHESE EN FRANÇAIS VII

LIST OF FIGURES XXXIII

LIST OF TABLES XLI

CHAPTER I GENERAL INTRODUCTION 1

CHAPTER II DEVELOPMENT OF MICROFLUIDIC SYSTEMS 7

II.1. INTRODUCTION 9

II.2. MATERIALS AND METHODS 10

II.2.2. Microfluidic chip fabrication 10

II.3. MASTER DESIGN AND FABRICATION PROCESS 11

II.3.1. General aspects of photolithography process 11

Surface modification 19

II.4. PDMS MOLD FABRICATION FOR UV-SENSITIVE POLYMER CASTING 21

II.5. SOLVENT AND PRESSURE RESISTANT MICROFLUIDIC CHIPS 25

II.5.1. Norland Optical Adhesive (NOA) microfluidic chips 27

II.5.2. OSTEmer microfluidic chips fabrication process 29

II.5.3. Near zero dead volume interconnections 44

II.6. CONCLUSION 45

CHAPTER III PROTEIN INTERACTIONS STUDIED BY SAXS AND MICROFLUIDIC 47

III.1. INTRODUCTION 49

III.1.1. Theory background 51

III.1.2. Coupling microfluidics and Small Angle X-Ray Scattering. 61

III.2. MATERIALS AND METHODS 67

III.2.1. Microfluidic devices 67

III.2.2. Connection to the SAXS sample holder (POD) 68

III.2.3. Real time image analysis and data acquisition 72

III.3. RESULTS AND DISCUSSION 74

III.3.1. Validation of experimental setup 74

III.3.2. Study of weak interaction for crystallization conditions 78

III.4. CONCLUSION AND PERSPECTIVES 85

CHAPTER IV DEHYDRATION OF PROTEIN SOLUTION 87

IV.1. INTRODUCTION..... 89

IV.2. THEORETICAL BACKGROUND OF DROPLET DISSOLUTION 95

IV.2.1. The E-P equation for pure water droplet..... 95

IV.2.2. The modified E-P equation for a multicomponent mixture. 97

IV.2.3. Numerical approach for modeling the droplet dissolution. 98

IV.3. MATERIALS AND METHODS 103

IV.3.1. Materials 103

IV.3.2. Method for droplets dissolution in 1-decanol. 103

IV.3.3. Microfluidic chips preparation..... 105

IV.3.4. Analysis methods: refractive index and hydration analysis. 107

IV.3.5. Osmotic pressure and Equation of State (EOS) 109

IV.4. RESULTS AND DISCUSSION 111

IV.4.1. Validation of microfluidic designs 111

IV.4.2. Dissolution of pure water droplets 111

IV.4.3. Typical experiment of droplet dissolution with lysozyme solution..... 117

IV.4.4. From the influence of saturation fraction to the equation of state of the protein 124

IV.4.5. Modeling of the dissolution process. 130

IV.5. CONCLUSIONS AND PERSPECTIVES 135

CHAPTER V GENERAL CONCLUSION.....139

REFERENCES 143

APPENDIX 152

List of Figures

Figure I-1: Illustration of crystallization protein phase diagram. The plot, based on the concentration of protein as a function of an adjustable parameter which can be pH, temperature, concentration of precipitant and so on. 4 regions are mentioned: under-saturation, metastable zone, nucleation zone and precipitation zone. These arrows with black dots (initial conditions) are techniques to achieve crystals: (i) batch, (ii) vapor diffusion, (iii) dialysis and (vi) free interface diffusion(Chayen 2004). 2

Figure I-2: An example for complete OSTEmer microchip prepared by soft lithography..... 5

Figure II-1: Typical lithography process, containing spin coating, exposure and development. 11

Figure II-2 Example of Chrome mask (left) and transparency mask (right). 13

Figure II-3: (a) SU-8 photoresist molecule structure. (b) SU-8 made crosslinked by UV beam..... 14

Figure II-4: (a) Dry-film formulation: Polyethylene-Resist-Polyester. (b) Lamination of dry film photoresist using laminator..... 15

Figure II-5: Thickness versus Exposure energy for Dry film WBR 2000 series. Marker (closed star) for the required minimum energy and (closed up triangle) for maximum energy..... 18

Figure II-6: The silanization box is designed and built at LGC. 21

Figure II-7: The chemical formula of Polydimethyl Siloxane(PDMS) 22

Figure II-8 : Casting of PDMS mold from a resist rigid master 23

Figure II-9: Deformation of PDMS molds. 24

Figure II-10: The TEM images of PDMS molds which cast from WBR dry film master (a) and SU-8 photoresist (b). 25

Figure II-11: Micro-molding technique for fabrication of microfluidic systems..... 26

Figure II-12: Fabrication of microfluidic using OSTE+ and soft lithography method. 34

Figure II-13: Process to fabricate OSTEmer microfluidic chip using "quasi injection molding" technique 36

Figure II-14: Surface modification of OSTEmer chip using methacrylate monomers 38

Figure II-15: The contact angle of (left) nature, (middle) hydrophilic modification and (right) hydrophobic modification OSTEmer with contact angle are 80°, 88° and 110°, respectively. 39

Figure II-16: Water droplet generation in decanol without surfactant using NOA 81 microfluidic chip. 40

Figure II-17: Side views channel which tested by acetone, cyclohexane, ethanol and toluene by the period of time. 42

Figure II-18: Schematic diagram with dimension of microfluidic chips using for high pressure. 43

Figure II-19: The procedure for pressure test in OSTEmer microfluidic chip as a function of time. 43

Figure II-20: 2 types of connectors: Nanoports Upchurch (right) and typical needle structure (left) 44

Figure III-1: Schematic principle of SAXS setup at ESRF (Grenoble, France). 52

Figure III-2: Calculation of the phase difference δ between the waves from scatters at points O and P in a particle. In the draw s and $\mathbf{s0}$ are unit vectors in the direction of scattered and incident beams, respectively, and P is displaced from O by the vector $\mathbf{r}$, θ is denoted scattering angle and $\mathbf{q}$ scattering vector. 53

Figure III-3: Scattering curves of γ-crystallins in a 50 mM Na Acetate buffer at pH 4.5 and α-crystallins in a 150 mM Na Phosphate buffer at pH=6.8 with different salts. 61

Figure III-4: The second virial coefficient several proteins in various salts..... 61

Figure III-5: Photograph of Kapton microfluidic chips compatible with synchrotron radiations developed by Salmon and coworkers(Barrett et al. 2006) 63

Figure III-6: (a) Sketch of the microfluidic channel. The channel inlet is shallower than the side inlets and the outlet, preventing contact between assembling vimentin and the channel walls. (b) Sketch of the cross and measurement positions. The position 0 is indicated by the gray arrow. (c) Log-log plot of the scattering curves. (d) Kratky plot(Brennich et al. 2011a). 64

Figure III-7: Schematic of a glass micro- capillary device for on-chip droplet formation and SAXS analysis. 65

Figure III-8: X-ray scattering curves recorded on gold nanoparticles dispersed within W/O emulsion droplets in a droplet-based microfluidic SAXS implementation.(Stehle et al. 2013). Here, squares denote the raw signal, whereas diamonds denote the signal of plain W/O emulsion. The gold nano-particle scattering is obtained by subtraction of 2 signals above. 66

Figure III-9: Design for SAXS microfluidic chip. (Left) the chip design with 3 inlets for protein, buffer and crystallization agent and one inlet for continuous phase, here as fluorous oil. (Right) the real microfluidic chip is fabricated by the soft lithography technique based on NOA 81 material. 67

Figure III-10: The whole setup of the combination of microfluidic system and SAXS. 68

Figure III-11: Structure of sample holder (POD) and glued Kapton/Quartz capillary inside..... 69

Figure III-12: The connection of glass capillary from the outlet of microfluidic chip and Kapton capillary to POD 70

Figure III-13: Pilatus 1M at the moment is the best detector for solution SAXS-Beamline 29 ESRF Grenoble - France..... 71

Figure III-14: The scattering signal of the first set of experiment. Lysozyme 60mg/ml + salt 300mM(cyan), the interface of droplets (blue), the oil (red) and the buffer (green). 72

Figure III-15: Scheme of the synchronization process: Once the droplets are detected, knowing the speed of each droplet, the beam position and the distance between the window of detection and the beam position, a delay time is calculated (compatible with the opening and closing time of the shutter) and the acquisition is triggered. This approach allows us to get only the SAXS data within the droplets. 73

Figure III-16: The scattering signal of two different capillaries which were glued in the POD: Glass and Kapton capillary. 74

Figure III-17: SAXS curves of Rasburicase in the presence of surfactant PFO and triblock copolymer. (top) with PFO surfactant, the black dots are our experimental data, green and red curves are scattering curves from atomic. (bottom) with triblock surfactant, the red line is the scattering signal of tetramer of Rasburicase (1.5r1.pdb). 77

Figure III-18: SAXS curves for lysozyme with increasing crystallization agent concentration from 0 to 400 mM with 3 values of lysozyme 21.7, 52 and 86.7 respectively. 80

Figure III-19: Example of the Guinier plot for lysozyme at 52 mg/mL and salt about 300 mM 81

Figure III-20: Scattering intensity at the zero angle as a function of lysozyme concentration for different salt concentration. It can be extrapolated to give access to the value of the form factor $I0,0$. 82

Figure III-21: Linear regression for different salt (NaCl) concentration: 100, 200, 300 and 400 mM/L. The slope of straight line equal $2MA2$. 83

Figure III-22: Variation of second virial coefficient for Lysozyme as a function of salt (NaCl) concentration. 83

Figure IV-1: Dissolution of liquid droplet phase A into an immiscible liquid phase B.(left) for pure liquid and (right) for mixture liquid. 90

Figure IV-2: Water activity evolution of a pure water droplet (left) and a protein solution droplet (right) in a medium partially saturated by water. For the pure water droplet, the droplet's diameter decreases until its complete dissolution (i.e. $R = 0$) whereas the diameter of the protein droplet decreases until the equilibrium of water activity inside the droplet and the surrounding medium is reached (Rickard's PhD thesis 2011). 92

Figure IV-3: Comparison of the numerical model results and E-P equation for different water concentration in the continuous phase (f). The grid size was 150, time step $dt = 1e\text{-}4s$ and $dr = 0.05$ µm 101

Figure IV-4: Experimental setup for dissolution of single droplets using microfluidic system. 104

Figure IV-5: Illustrations of designs for microfluidic systems.(a) the design with the serpentine channel and (b) the design with big storage zone. These designs have the same dimension for generation structures 106

Figure IV-6: Water activity as a function of saturation fraction. 109

Figure IV-7: The evolution of pure water droplet size with initial diameter around 80 µm is dissolving in pure 1-decanol as a function of time from 0s to 83s. .. 112

Figure IV-8: Evolution of droplet's diameter by the time of water droplet in 1-decanol with saturation fraction $f = 0.2$. (black circle) is the experimental data and (red circle) is the E-P modeling data. 113

Figure IV-9: Flux of diffusion and diameter evolution by the time of 90 µm initial diameter water droplet in pure 1-decanol 114

Figure IV-10: Dimensionless plot of dissolution water droplet in various 1-decanol saturation fractions ($f = 0;\ 0.1$ and 0.2). 115

Figure IV-11: Diameter evolution for 2 droplets with different initial diameter dissolving in pure 1-decanol $f = 0$. 116

Figure IV-12: Flux of diffusion of 2 droplets with different initial diameter(90 µm and 135 µm) dissolving in pure 1-decanol ($f = 0$). 117

Figure IV-13: Dehydration process of a lysozyme solution droplet with initial concentration of 80 mg/mL in 1-decanol with saturation fraction $f = 0.4$ ... 118

Figure IV-14: Comparison between the experimental data obtained from the dehydration of a 97 mg/mL lysozyme droplet in 1-decanol ($f = 0.3$) and the E-P modeling data for a droplet of pure water with the same initial diameter. 119

Figure IV-15: Influence of initial diameter in the dehydration process of a 90 mg/mL lysozyme solution droplet in 1-decanol with saturation fraction $f = 0.4$. 120

Figure IV-16: Flux of diffusion of water to drying medium($f = 0.4$) with different droplet's initial diameter of Lysozyme droplets with 90 mg/mL..... 121

Figure IV-17: Relation between the mass diffusion flux and evolution of diameter in 1-decanol $f = 0.4$..... 121

Figure IV-18: Diameter evolution of 2 droplets with the same initial diameter (100 µm) but different initial lysozyme concentration (130 and 175 mg/mL, respectively) dehydrating in 1-decanol $f = 0.25$ medium. 123

Figure IV-19: Concentration change of droplets with the same initial diameter (100 µm) but different initial concentration of protein (130 mg/mL and 175 mg/mL) in 1-decanol $f = 0.25$..... 123

Figure IV-20: The mass flux of droplets with the same initial concentration 100 mg/mL and same initial diameter 70 µm at 3 different values of $f = 0.24$, $f = 0.35$ and $f = 0.5$. 124

Figure IV-21: Evolution of analogous droplets with 98 µm initial diameter and 100 mg/mL concentration at two different saturation fractions $f = 0$ and$f = 0.4$. Here, the skin formation is observed for case $f = 0$ leading the final diameter of droplet is larger than in $f = 0.4$. 125

Figure IV-22: The formation of skin on a droplet during its dehydration process at $f = 0$. The change of the droplet shape can be clearly observed..... 126

Figure IV-23: Equilibrium hydration levels at the end of the protein droplets dehydration process using 1-decanol are shown as a function of a_w compared to other data previously reported in the literature (Absorption isotherm(Lüscher-mattli and Rüegg 1982) and Single particle vapor sorption(Rickard, Duncan, and Needham 2010)) 129

Figure IV-24: Osmotic pressure Π as function of volume fraction of Lysozyme. The empirical data from this work is compared with osmotic pressure values previously reported in literature: (bullseyes)of Pasquier et al(Coralie Pasquier et al. 2016), (filled triangle) of Rickard(Rickard, Duncan, and Needham 2010) and (dash line) the Carnahan-Starling approximation..... 130

Figure IV-25: Evolution of droplet diameter versus modeling data for $f = 0.1$ 131

Figure IV-26: Experimental mass flux versus modeling data for $f = 0.1$ 131

Figure IV-27:Evolution of diameter (µm) versus modeling data for $f = 0.35$ and $f = 0.5$. 132

Figure IV-28: Experimental mass flux(g/m^{2}s) as a function of time versus modeling data for $f = 0.35$ and $f = 0.5$..... 133

Figure IV-29: Evolution of droplet diameter and water activity inside as a function of time. 134

Figure -1: Illustration of moving grid..... 161

Figure -2: Illustration of fixed grid..... 161

List of Tables

Table II-1: Typical properties of NOA 81 (NOA81, 2016) 27

Table II-2: Contact angle for coated FDTS(Gu, Duits, and Mugele 2010)..... 29

Table II-3: List of solvents and period of time for testing OSTEmer chips. Here, Y (yes) and N (no) is abbreviation of the experiments have been done or not. 41

Table III-1: Flow rates of the stock solutions and concentration of different compounds in droplets with Lysozyme, buffer and salt. 79

Table IV-1: Experimental conditions for each dehydration experiment performed 127

Chapter I

GENERAL INTRODUCTION

Colloids are fluids containing particles suspended in a liquid. The size of the dispersed molecule is larger than a simple molecule (having a diameter between 1 to 1000 µm) but small enough to remain suspended. So colloid is an intermediate state between suspensions and solutions. A representative example is milk, which is an emulsified colloid of liquid butterfat globules dispersed within a water-based solution. Colloidal particles give special physical properties of fluids and are therefore widely used in the industry to fine tune the physical-chemical properties of materials in which they are dispersed. Thousands of examples can be found in everyday life in which colloid are used: silica as a reinforcing filler in elastomer, as an abrasive in toothpaste, titanium oxide in glass, paint, drug dispersion… The overwhelmingly important property of colloids is their very large surface area. To some degree, they are all surface and their properties are those of their surface. Consequently, to control the properties of a colloidal suspension, intermolecular and surface acting forces are controlled: Van der Waals attractive force (leads to product instability), and electrostatic and steric repulsive forces (that stabilize the dispersion). These colloidal interactions in solution are the core of many industrial processes as filtration, precipitation, drying... Knowledge of the nature and intensity of these interactions leads to better process control.

This is particularly true for the crystallization process, still perceived as an art, despite the efforts made during the last twenty years on its rationalization. Thermodynamically, protein crystallization is not very different from the crystallization of salt and small molecules. In both cases, the solution needs to be brought into a supersaturated state after which the (macro)molecule will hopefully start to crystallize. The whole crystal growth process can be conveniently visualized in a two-dimensional phase diagram (Figure I-1) representing the stable states (liquid, crystalline, precipitate) as a function of two crystallization variables. When the concentration of a protein solution is brought above its solubility limit, the solution becomes supersaturated. Depending on the level of supersaturation, this zone of the diagram can be divided into three regions: very high supersaturation (“precipitation”), where molecules form amorphous aggregates , intermediate supersaturation (“labile”), where both growth and nucleation occur, and lower supersaturation (“metastable”), where

only growth is supported. Because these regions are related to kinetic parameters, the boundaries between them are not well defined. As stated earlier, this "sort of" phase diagram, mixing kinetic and purely thermodynamic parameter, is universal and suitable to describe salt, drug, colloids… crystallization processes.

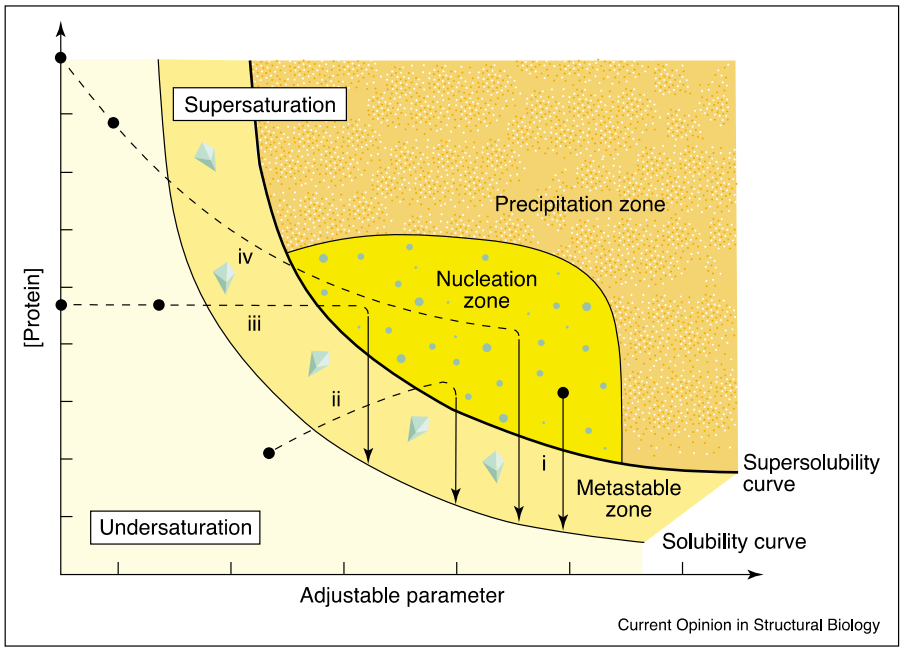

Figure I-1: Illustration of crystallization protein phase diagram. The plot, based on the concentration of protein as a function of an adjustable parameter which can be pH, temperature, concentration of precipitant and so on. 4 regions are mentioned: under-saturation, metastable zone, nucleation zone and precipitation zone. These arrows with black dots (initial conditions) are techniques to achieve crystals: (i) batch, (ii) vapor diffusion, (iii) dialysis and (vi) free interface diffusion(Chayen 2004).

However, from a microscopic point of view, protein crystallization is very different since the interactions between proteins and thus the "nature" of the solvent can be fine-tuned through the introduction of a crystallizing agent that induce more attraction (salt for instance) to promote aggregation or a polymer that induce a steric destabilization. The pioneers of protein crystallization rationalization Georges and Wilson(George and Wilson 1994) have proposed a thermodynamic explanation of how to perform protein crystallization experiments: the "solvent conditions which are known to promote protein crystallization are grouped in a narrow range of osmotic virial coefficient B_{22} values that are somewhat negative. These solvent conditions can be referred to

as being 'moderately poor', i.e. the solvent has to be poor enough (slightly negative B_{22} values) to eventually promote the formation of craggs at high enough protein concentration but not so poor (larger negative B_{22} values) that praggs are produced which lead to an amorphous structure. Thus, B_{22} is clearly a dilute solution parameter that has a predictive character regarding protein crystallization.

From these thermodynamic rules, many types of research have been conducted on the rationalization of protein crystallization, but due to an excessive product consumption and to the time required to acquire reliable thermodynamic data (i.e. virial coefficient, interactions in solution and protein equation of state), trial and error approach is still the method of choice for protein crystallization.

From 1990s, the microfluidic is a versatile tool to study fluid flows at the microscale and for microscale analytical chemistry techniques. A potential strength of microfluidic systems is that they can be performed with laboratory conditions using a very small amount of reagents due to reduced volume. By this way, not only the volume of reagents can be nano- to femtoliters. Thanks to advantages of microfluidic systems, they can be applied in many fields of applications such as drug delivery, diagnostic, organic synthesis and micro-reactors(Xu et al. 2009)(Frenz et al. 2008)(G. Jones et al. 2011). Recently, the development of microfluidic technique makes a huge (Zheng, Roach, and Ismagilov 2003; Zheng et al. 2004; Zheng, Gerdts, and Ismagilov 2005; Weigl and Sygusch 2002)breakthrough for protein crystallization studies. Thank to different behaviors of flow and mass transfer phenomenon at micro-scale, microfluidic systems allow to perform hundreds, evenly thousands of trails simultaneously on a single system. This helps to reduce the consumption of materials and time. However, all the aforementioned studies and most of the studies encountered in the literature deals with the reproduction in microfluidic systems of the high throughput screening experiments performed in batch or micro-wells experiments by robots.

Thus, the aim of this thesis is to develop a more efficient measurement techniques of thermodynamic properties of protein solutions by using microfluidic platforms. The main objectives of the approach are to:

- Develop versatile, reliable, low cost, fast and easy technology to produce microfluidic platforms.
- Measure in-situ the protein-protein interaction.
- Establish a protein equation of state in solution.

The development of such a technology and methodologies must be immediately transferrable to any nonspecialized laboratory and easy to use in order to contribute to the development of rationalization of protein crystallization experiments.

In the first chapter, the whole process of microfluidic fabrication is presented. It can be seen as the long process with three main steps. Firstly, a rigid master is designed and prepared using the photolithography method based on two different types of negative photoresists: SU-8 from MicroChem and dry film from DuPont. Depending on the purposes of microfluidic chips, the mask is designed with several components such as droplet generation structures, mixing and storage structures. The typical photolithography process is performed step by step (Substrate cleaning, coating, exposure, baking, development). For each step, the parameters from the literature are optimized to fit with our equipment to obtain better resolution of the rigid master. As the results, the SU-8 molds possess very good properties of physical/chemical resistances. However, the product process is time-consuming and required high-cost equipment and a very clean environment. In order to build the rigid master by a fast and cheap protocol, the use dry film photoresist is strongly recommended. Masters from dry film WBR series from DuPont were successfully fabricated in short time with simple and reasonable equipment which any laboratory can have. Moreover, even if the resolution of dry film master is lower than SU-8 master, it is enough for microchannel dimension ranging from 5 to 200 µm. Finally, the microchannel is built from UV-sensitive polymers using soft lithography technique. Two kinds of photosensitive materials were used: NOA 81 (Norland Optical Adhesive) of Norland Inc. and OSTEmer 322 from Mercene Lab (Sweden). The large range

(from 50 µm to 500 µm) of microchip dimension was successfully fabricated with very high resolution. Besides, the microfluidic chips fabricated have several excellent properties like chemical resistant, high-pressure resistance, and tunable surface properties. Depending on the purposes, the chips are modified to have a hydrophilic or hydrophobic surface.

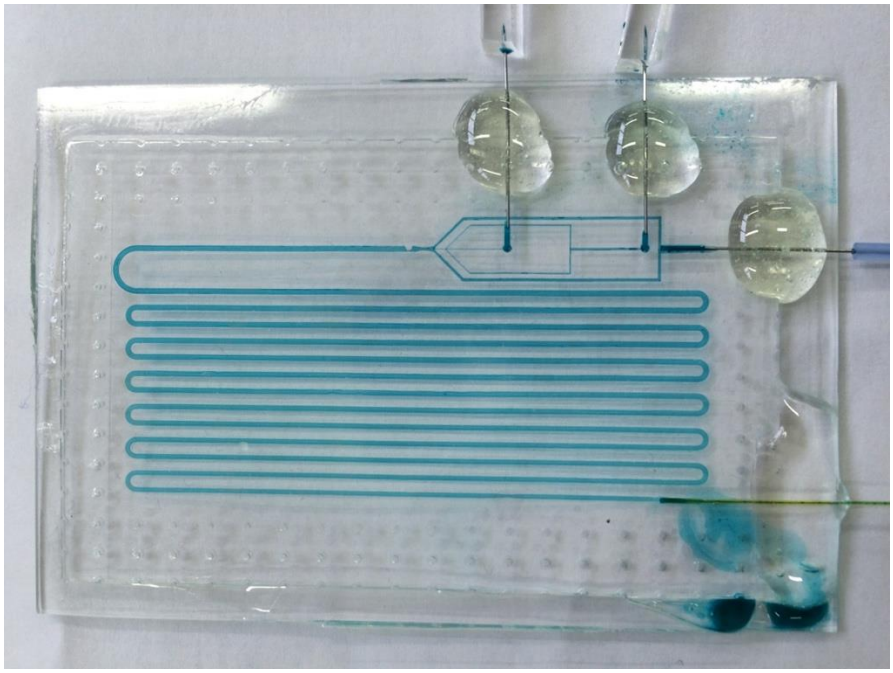

Figure I-2: An example for complete OSTEmer microchip prepared by soft lithography.

The coupling of Small Angle X-ray Scattering (SAXS) and microfluidic chips to study the interactions of protein in solution is presented and discussed in Chapter III. In this chapter, the basic principle of SAXS and method to analyze the obtained scattering intensity data is first shown. Then, the SAXS experiments performed at BioSAXS BM29 at ESRF presented in this chapter, have two goals:

(1) To validate the experimental setup by comparing the obtained data to data from the protein data bank. Moreover, other parameters such as the material of capillary, surfactant… were also determined to get a higher quality of SAXS data.
(2) To study the variation of weak interactions between protein molecules in solution by varying the concentration of crystallization agent.

In the last chapter, a microfluidic system was used to study mass transfer phenomenon happened during the dissolution of water or hydration of protein

solution droplets in an organic solvent. At the end of the dissolution process, the droplet reaches a final size that depends on the thermodynamic equilibrium, which depends on the water activity in the droplet and in the continuous phase. When the thermodynamic equilibrium is reached, the knowledge of the water activity in the continuous phase allows determining the water activity of water inside the droplet. From the final state of the protein solution droplet, several thermodynamic parameters such as the osmotic pressure, the hydration potential can be determined. Thus, the experiments performed in this chapter have three main goals:

(1) To design and validate a microfluidic setup suitable for the dehydration of micro-droplet in drying medium to ensure the system can reach to the thermodynamic equilibrium.
(2) To obtain the protein equation of state in the solution which relates the osmotic pressure to the volume fraction of protein.
(3) To build a model base on Fick laws (purely diffusive process) to predict the shrinking of the droplet.

Chapter II

DEVELOPMENT OF MICROFLUIDIC SYSTEMS

II.1. Introduction

In this chapter, the fabrication process for the microfluidic setups is presented. The microfluidic systems have been built by soft lithography methods following the subsequent main steps: firstly, fabrication processes of rigid masters made from photoresists (liquid and dry film) are presented. Then, the masters are used to fabricate solvent/pressure resistant microfluidic chips. These steps, in which some innovative techniques were applied to improve the process, will be discussed in more detail below. .

The first step of soft lithography method is to fabricate a patterned rigid master with the desired design. In the literature, numerous research groups have used SU-8 negative photoresist to fabricate this kind of master(Lorenz et al. 1997)(Hwang, Lo, and Chin 2001). Thanks to the properties of SU-8 resists, the obtained molds present a high resolution. Moreover, SU-8 also displays a high resistance tosolvents. However, the SU-8 master fabrication process requires a costly equipment and very critical conditions. Hence, the price for whole fabrication process is high and it requires a long time for fabrication.

In order to build a fast, reasonable and still reliable master mold, a novel negative photoresist of DuPont company was utilized. The photoresist is available as a thin film and widely utilized in the circuit board design industry. Because of its intrinsic properties, the dry film photoresist can be coated easily on the substrates (many types: glass, silicone, copper…) by simple lamination. After that, the dry film photoresist mold is finished just by following the lithography method with an inexpensive UV lamp and a non-toxic developer. The resolution of dry film is lower than SU-8, however, it is still acceptable to fabricate microfluidic systems with structures larger than 20 µm. In conclusion, depending on the purposes and requirements of the microfluidic systems, SU-8 technology can be applied for high definition master mold fabrication, with a high-cost and long-time process, and the dry film photoresist can be utilized for building fast, cheap and reliable microfluidic molds.

For the microfluidic chip fabrication, we proposed the use of UV curable materials (e.g. NOA 81, OSTEmer)…to manufacture solvent/pressure resistant

systemsby using the micro-molding technique.. In addition, several methods were tested and improved for microchannels surface modification. On this sense, depending on the offend use of the microfluidic chip, the surface can be modified to be hydrophobic or hydrophilic in order to form W/O or O/W emulsions, respectively.

II.2. Materials and methods

II.2.1.1. Master mold fabricationMaster mold fabrication

SU-8 2150 and SU-8 2050 (MicroChem, MA 02464 USA) were used as received. SU-8 2150 was used to fabricate thicker molds because of its higher viscosity. SU-8 was spin-coated using a Spin150 from POLOS-SPS EURO The Netherlands. Diacetone was used as developer of SU-8 photoresist. Dry film WBR series and MX 2000 series were purchased from DuPont with thicknesses ranging from 20 to 120 µm. Potassium carbonate, ACS, 99.0% (Alfa Aesar, Germany) and Magnesium Sulfate (anhydrous, reagent plus, >99.5 %) from Sigma – Aldrich were used to prepare the developer solution. Pouch laminator was purchased from MEGA Electronics to laminate thedry-film photoresists. This laminator can change the roller pressure, the rolling speed and temperature. A UV-KUB 1 equipment was used to mask-expose the master molds prior to their development.In oder to modify master molds surface to increase their nonsticking properties, 3M™ Novec™ 1720 (USA) Electronic grade coating (supplied by 3M and used as received) and Sigmacote (Sigma)were used as siliconizing reagents. Also toluene, anhydrous for analysis (Carlo Erba reagents, France) was applied with the same purpose.

II.2.2. Microfluidic chip fabrication.

NOA 81 and OSTEmer 322 Crystal Clear UV-curing polymers were purchased from Norland Products Inc. (USA) and Mercene Lab (Sweden), respectively. They were stored in a refrigerator for a dark and cold environment. The UV cure Station One (Mercene Labs, Stockholm, Sweden) and the previously mentioned UV-KUB 1 were used for polymer UV-curing . For microchannels surface modification,, the following reagents were used: Perfluorodecyltrichlorosilane (PDTS), 96% was used as received from Alfa Aesar (Germany). Isooctane, dried was purchased from

VWR (USA). Benzophenone ReagentPlus, 99%, Irgacure R819- Phenylbis(2,4,6-trimethylbenzoyl) phosphine oxide. 97%, powder, Allyl glycidyl Ether, Heptadecafluorodecyl methacrylate 97% and 2-hydroxyethyl methacrylate, 97% were purchased from Sigma-Aldrich.Finally, a Corona equipment (EasytreatBC 20, Boussey Control, Belgium) was used for surface cleaning using plasma treatment.

II.3. Master design and fabrication process

II.3.1. General aspects of photolithography process

Photolithography is a process of transferring of geometric shapes from a masks to a thin layer of radiation-sensitive materials (called as photoresists) which are deposited on a substrate (wafer). Depending on the purposes, several photoresists can be applied. Photoresists are classified as a function of their behavior when they are irradiated. If the radiation transferred to the photoresists through the transparent parts of a mask make them insoluble in the developer solution, they are considered as negative. Conversely, if they become soluble, they are considered positive. A general schematic presentation of photolithography process is shown in the **Erreur ! Source du renvoi introuvable.**.

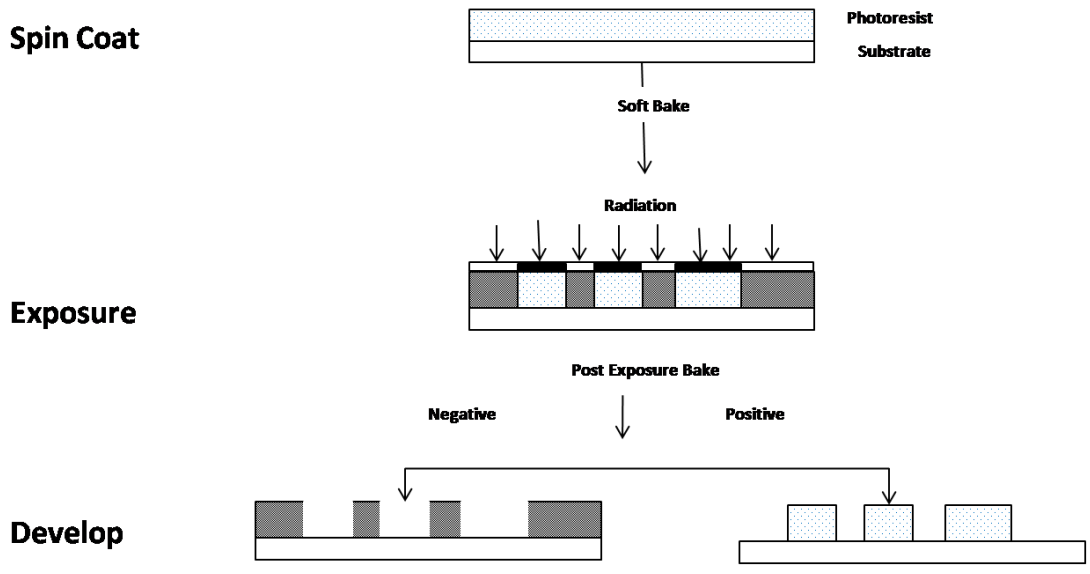

Figure II-1: Typical lithography process, containing spin coating, exposure and development.

A general photolithography procedure is described hereafter:

II.3.1.1. Contamination and cleaning

Substrates (wafers) can generally be polluted by several contamination sources, both organic and inorganic. This contamination must be prevented as much as possible, or cleaned following standardized protocols. Contamination sources on the wafer can arise from vapor depositions, photoresist, fingerprints, containers, chemicals and so on. There are several ways to clean organic contaminations but the easiest way is rinsing by acetone or alcohol. After rinsing, the wafer must be washed by deionized (DI) water and dried by nitrogen flow. To remove inorganic residues, a mixture containing strongly oxidize acid solution is generally used. Depending on the lab-ware conditions, using the Piranha solution is recommended. The Piranha solution is a mixture of sulfuric acid (H_2SO_4) and hydrogen peroxide (H_2O_2) in a 4:1 ratio. Using this solution, not only organic matter, but also inorganic residues on the surface of substrate can be removed. Additionally, the Piranha solution adds more OH groups and turns substrate surface into hydrophilic. Finally, rinsing using DI water must be carefully carried out to ensure that all of Piranha solution is completely removed from wafers.

II.3.1.2. Wafer pre-conditioning

After cleaning the substrates, a heating process is recommended to improve the adhesion of photoresist by two ways:

- At 100°C, all of water present on the wafers surface is desorbed. Hence, few minutes at 100°C are recommended.

- An Increase of temperature up to 150°C also makes that all OH bonds present on the surface of oxidized substrates (e.g. glass, silicon…) are thermally cracked. These OH radicals form a hydrophilic surface which improve the wetting and contact with photoresists.

The photoresist can be applied directly after heating to avoid absorbing water again. However, the wafer temperature should be tempered to room temperature in order to get a better homogeneity of the resist layer.

II.3.1.3. Photomask fabrication

A typical process to fabricate photo-mask begins by a CAD design which is subsequently transferred to a physical support. Typically, a chrome-mask is generally used in the photolithography procedure because of its high resolution (Müllenborn, Dirac, and Petersen 1995). The size of the patterns in a chrome mask can go down to a few nanometers. However, the chrome masks are typically fabricated by using e-beam and laser writing which require specific and expensive facilities, and hence they are expensive. An alternative method to prepare a photo-mask with an inexpensive and rapid process was proposed by Xia et al (Xia and Whitesides 1998) and other researchers(Deng et al. 2000; Duffy et al. 1998; Anderson et al. 2000) . Here, printings from office printer with high or normal resolution on transparent films are used as masks for the lithography method. However, the smallest features which can be fabricated by using this low cost approach is around 20 µm, provided by the limitation of printer resolution (Deng et al. 2000).

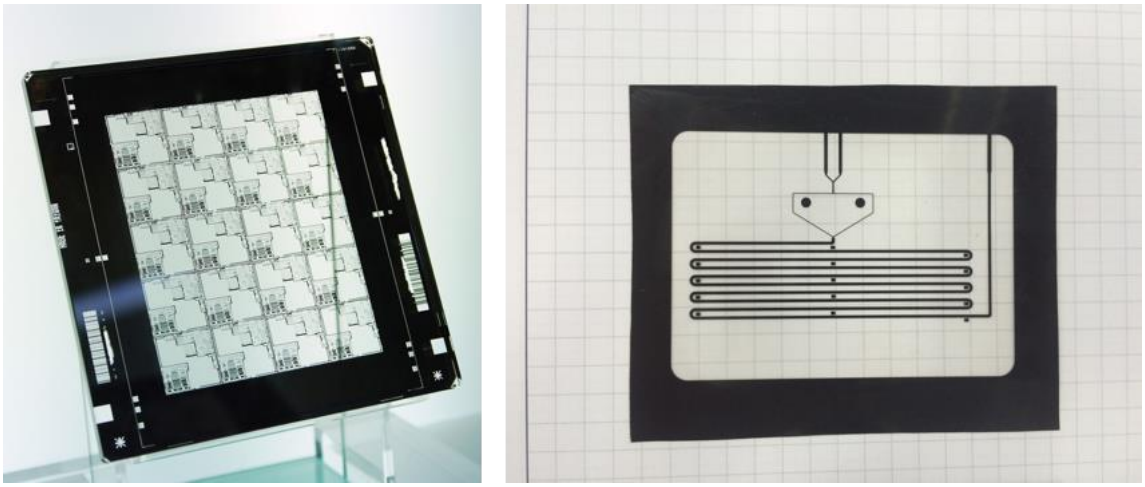

Figure II-2 Example of Chrome mask (left) and transparency mask (right).

II.3.1.4. Rigid master mold fabrication

For master mold fabrication, the most widespread fabrication protocol is based on SU-8, a widespread epoxy–based negative photoresist. Here, the word "negative" means that the exposed parts become cross-linked and non-exposed parts are soluble in developer solution. The name of SU-8 refers that in the

molecule structure, there are eight epoxy groups. These epoxies will make cross-links to the final structures.

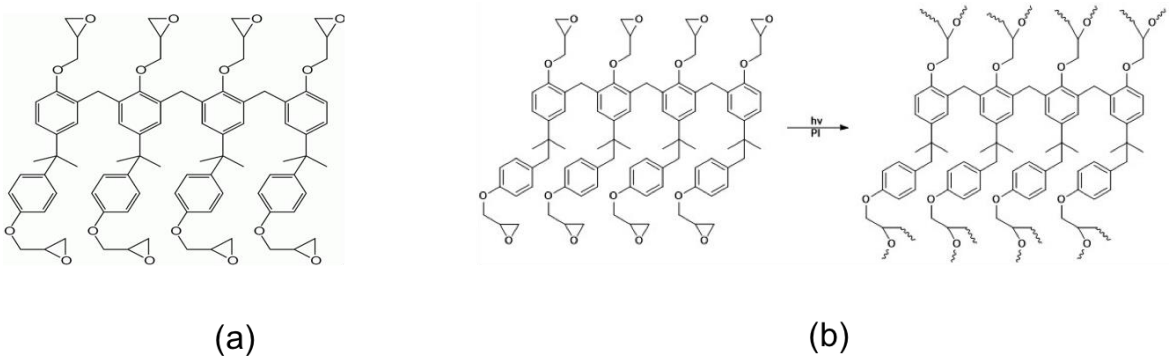

Figure II-3: (a) SU-8 photoresist molecule structure. (b) SU-8 made crosslinked by UV beam

With these particular properties, the SU-8 photoresist presents some interesting features for microfabrication: (i) a high ratio aspect (15:1); (ii) Bio-compatible; (iii) high mechanical and chemical properties, as SU-8 has good solvent resistance. Additionally, the nature of SU-8 surface is hydrophobic. Hence, it is easy to directly obtain PDMS replicas by direct cast molding on the SU-8 structures, thus obtaining PDMS chips or PDMS masters. However, SU-8 requires extremely clean operating conditions (i.e. the use of clean room facilities is highly recommended), which are not easily achievable in a common laboratory, the fabrication protocol for a SU-8 mold comprises several time-consuming steps and the material itself is very expensive. For that reason, we have developed a more simple and low cost master mold fabrication protocol, based on dry film technology.

The dry film photoresists were originally developed more than 30 years ago. Initially, dry film were applied for printed circuit boards (PCB), but nowadays they are also applied for MEMS and microfluidic systems fabrication (Tsai et al. 2006; Stephan et al. 2007; Garland, Murphy Jr, and Pan 2014; Chuan et al. 2004). A typical dry film resist is generally purchased with three-layer presentation: a thin negative photoresist layer is sandwiched between a bottom polyester layer and a top polyolefin sheet (usually 25 µm thick poly-ethylene). The polyethylene is coated to prevent sticking of photoresist on preceding polyester layer during roll

production. In this work, two types of negative photoresist dry film WBR series 2000 and MX from DuPont incorporation are utilized:

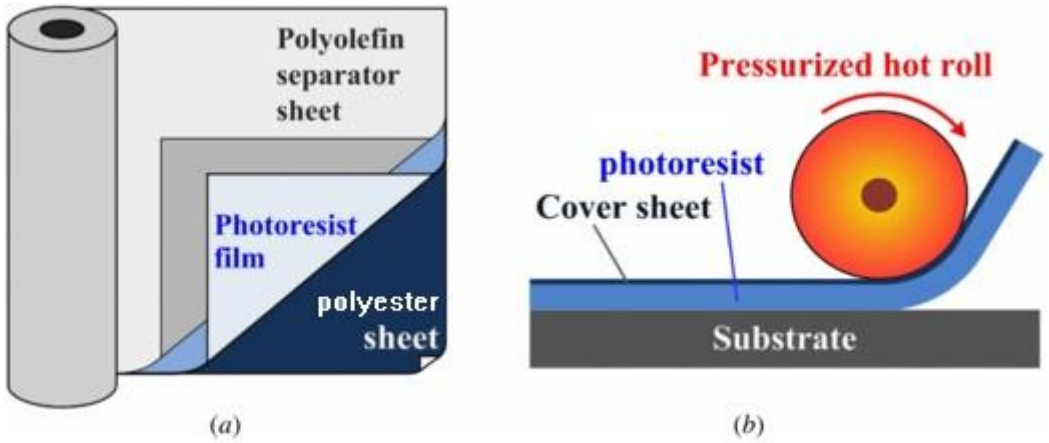

Figure II-4: (a) Dry-film formulation: Polyethylene-Resist-Polyester. (b) Lamination of dry film photoresist using laminator

DuPont Dry film WBR 2000 series, which present high resolution, and multi-purpose applications, compatible with lead-free electroplating and stencil printing. They are blue dry films with several available thicknesses: 50, 75,100 and 120 microns.

DuPont Dry film MX series, which are transparent and present higher resolution than WBR series, so they can be used to fabricate smaller scale structures.

Both dry film based photoresists present several advantages for fast prototyping compared to conventional methods using liquid photoresists as the previously mentioned SU-8:

(1) Easy to implement.
(2) Not require cleanroom equipment, consequently, the process can be performed at standard laboratories.
(3) Low-cost because dry film photoresist are produced at large scale for industrial applications.
(4) A significant reduction of fabrication time (the whole fabrication process for a microfluidic structure can be reduced to less than 24h)
(5) Homogeneous thickness for the whole wafer.
(6) Have a good adhesion to several substrates.
(7) No bead edge.

(8) Low exposure energy.

However, they still present some drawbacks. Firstly, the adhesion of dry film on glass substrates is not optimal. To improve it, a carefully cleaning process or preparation a dry film seed layer is recommended. This step will take more time. Secondly, unlike the SU-8 with hydrophobic surface, the dry films present a hydrophilic surface. Thus, in the PDMS casting process, dry film surface should be modified to hydrophobicity by silanization/ anti adherence processes. However, these processes cause side effects, as reducing the resolution of dry film and the adhesion as well.

II.3.1.4.a. Dry film lithography process steps

The lithography process for dry film is almost the same to other photosensitive materials like SU-8. However, because of their low content in solvents, the time of procedure is significantly reduced.

Lamination (coating)

In contrast to the typical spin coating processes for liquid photoresists, like SU-8, the dry film photoresist is directly laminated on a substrate using a pouch laminator. The substrate is cleaned using the cleaning process described above. In order to improve the adhesion between the photoresist and the substrate, a plasma treatment is also recommended. It was shown that the dry film can be applied to many types of materials such as copper and isolated mainboard for electronics industry, glass for laboratory… However, only glass substrates from Corning (Sigma-Aldrich, USA) were used in this work.

The main advantage in this coating process is that the lamination equipment do not need special requirements. Hence, a typical office laminator can be used. With such laminators, the temperature and speed can be adjusted to fit with the thickness of laminated dry films. These factors play a very important role to obtain a good lamination. For instance, small air bubbles can be trapped during lamination when the temperature is too high and, in contrary, if low temperatures are applied, the adhesion between film and substrate or between film layers is reduced. Thus, temperature operational parameters need to be optimized. To

work with the WBR dry film from DuPont, the temperature of roller in a range from 95°C to 100°C is recommended.

Before lamination, the polyethylene layer is peeled off to allow the contact between the resist layer and the substrate. The hot rolls on the laminator provide a smooth and internal dry contact between resist and substrate. After each lamination step, the dry film wafer should be checked to make sure there are no air bubbles or winkles on the surface before removing the polyester protection layer and applying another film afterwards. Depending on the desired total dry film thickness, the lamination can be repeated several times. Since the dry film contains less solvent inside than liquid-type resists, a soft bake step is only optional. However, baking the laminated dry film in the oven at 65°C for 20 minutes is proposed to improve the adhesion.

Exposure

As other negative photoresists, the dry film crosslinking is activated by UV exposure. Any 365 nm wavelength UV lamp can be used, however in order to get better resolution, a high intensity light source is highly recommended. The last film protection layer is kept until in the end of exposure to avoid contamination during the process. This protection layer is removed before the development.

During exposure, the two most important factors are the intensity of light source and the exposure time, configuring the exposure dose. According to the datasheet from DuPont, an intensity >20 mW/cm^2 or >10 mW/cm^2 is required, respectively for high or low resolution structures. For example, the UV-Kub irradiation equipment, with a power intensity of 25 mW/cm^2 is good to work with high resolution. On the other hand, the time of exposure depends on the thickness of dry film. The relationship between the two parameters is shown in the Figure II-5 below.

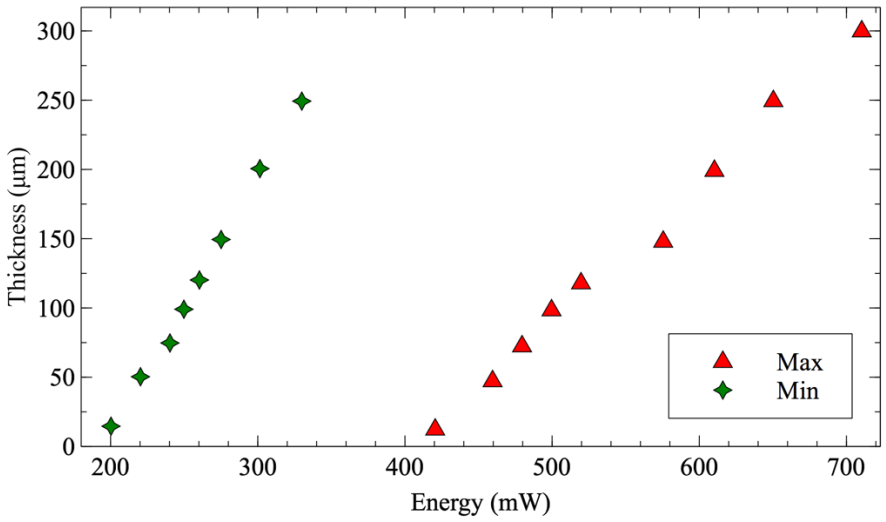

Figure II-5: Thickness versus Exposure energy for Dry film WBR 2000 series. Marker (closed star) for the required minimum energy and (closed up triangle) for maximum energy.

The Figure II-5 shows the maximum and minimum energy required to effectively expose a certain dry film thickness. The range between min and max values is suitable to get high resolution structures without over/under exposure. There is no significant difference for applying max and min value of energy.

Post Exposure Bake (PEB)

This is an optional step which can be applied to improve film resolution and development latitude, leading to complete development and a straight side wall by improving the crosslinking of the resist. Normally, the exposed dry film is baked on a hot plate at 100°C for 55 seconds. Subsequently, the dry film is cooled down gradually to ambient temperature before continuing with the development step.

Development

The dry film is dipped in/sprayed with a Potassium/Sodium Carbonate solution 1% wt. to remove the unexposed regions. The time of development not only depends on the thickness of dry film but also of the temperature of developer. With higher temperature, the development rate is higher. So, it is important to determine the good value of time and temperature for development. The optimal development temperature is around 28°C. If the development is too long, the exposed structures can be attacked by developer, leading to lower

adhesion. If it is too short, some parts of unexposed patterns remain, leading to lower resolution.

According to the presented steps for the preparation of a dry film master, a recommended protocol for obtaining structures larger than 200 µm is shown below:

1. Clean the glass substrates by acetone.
2. Clean by acid or Piranha solutions and rising by water.
3. Use plasma gun Corona for 20 s.
4. Laminate a 50-100 µm thickness dry film layer at 95°C as a seed layer.
5. Soft bake at 65°C for 30 minutes.
6. Let seed layer cool down to ambient temperature.
7. Full exposure for seed layer by UV-KUB 3 for 9 s.
8. Using plasma gun Corona for seed layer for 20 s.
9. Laminate 2-3 layers of 100 µm thickness to reach desired thickness.
10. Depending on the thickness, apply the necessary time for exposure to ensure a correct exposure dose. For instance, 300 µm channel needs 16 s for 25 mW/cm^2 UV-source.
11. Post exposure bake at 100°C for 55 s.
12. Develop for 10 minutes by K_2CO_3/Na_2CO_3 1% and rinse with $MgSO_4$ 1% solution at least for 3 minutes.
13. Dry by using an air flow and keep the dry-film at room temperature before a surface modification step.

Surface modification

Prior to PDMS casting, the dry film molds are silanized to prevent sticking. In the literature, lots of silanization processes have been reported, and most of them used silane compounds such as Perfluorodecyltrichlorosilane (PDTS)(Sandison et al. 2007; Bass and Lichtenberger 2004; Jones et al. 2011; Lee et al. 2007) or trimethoxysilanes (Labit et al. 2009). The detailed protocol for each method is briefed below.

- Vapor phase surface modification: The procedure is carried out by vapor phase deposition. The dry film master is placed on a sample holder (petri dish, for

example) inside a vacuum desiccator with some drops of PDTS. By changing the pressure inside the desiccator, the liquid PDTS becomes vapor phase and forms a very thin layer on top of the dry film master. The silanization process is performed for 30 minutes. Afterwards the master is baked at 100°C for 1 hour.

- Liquid phase surface modification: This protocol uses liquid phase deposition of silane in an organic solvent (acetone, n-heptane, ethanol…). All steps of silanization are performed in full nitrogen glove box to avoid exposure to atmosphere humidity. The silanization box is shown in the Figure II-6. Briefly, the silanization box contains two gloves, an injection/withdraw system for nitrogen and air, and an input chamber with two doors. Initially the air is removed by means of a vacuum pump. When the pressure inside the box is low enough, the nitrogen is injected. Both injection and vacuum pumps are carefully controlled to keep the humidity inside the box below 5%.

The silane solution is prepared by diluting 100 µL of Trimethoxysilane into 100 mL of n-heptane or other solvents before use. The samples (microchips – discussed below – or dry-film master) are directly dipped in the silane solution (or the solution is injected in the microchips) and incubated for 30 minutes. Subsequently, samples are carefully rinsed with heptane and dried under a nitrogen flow. Finally, samples are baked at 65°C for 1 hour.

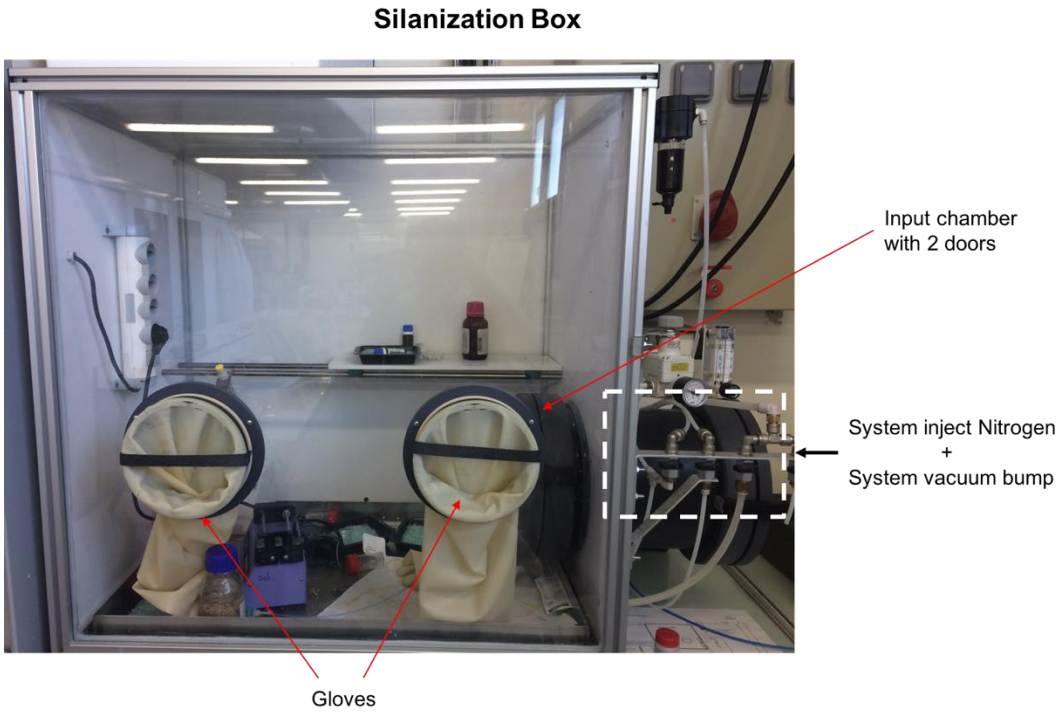

Figure II-6: The silanization box is designed and built at LGC.

- Deposition of a monolayer of fluorous nanoparticles: Using 3M NOVEC1720 Electronic Coating is a simple protocol to improve the anti-adherent properties of the dry film master. The dry film master is dipped in NOVEC solution for 20 minutes and baked at 150°C by hot plate for a few minutes. We have tested that the deposited hydrophobic layer displays long-term stability.

- Toluene treatment: Dipping the WBR 2000 series dry films on Toluene after photolithography is another way to improve its surface properties. After development, on the dry film surface can still remain small unexposed particles which can be dissolved by using Toluene. However, if the dipping time is too long, Toluene starts to dissolve the exposed dry film as well, reducing both the adhesion to the substrate and resolution of the master.

II.4. PDMS Mold fabrication for UV-sensitive polymer casting

Polydimethyl Siloxane (PDMS) is a mineral-organic polymer (containing carbon and silicon) of the siloxane family (name derived from silicon, oxygen and alkane). The chemical formula of PDMS is $CH_3[Si(CH_3)_2O]_n$-$Si(CH_3)_3$ where *n* is the number of repeating monomer $[Si(CH_3)_2O]$ unit as illustrated in the Figure II-7

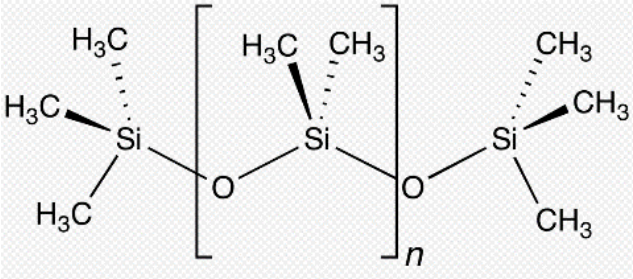

Figure II-7: The chemical formula of Polydimethyl Siloxane(PDMS)

In the soft photolithographic method, elastomer materials are used because of their ability to make a conformal contact with surfaces over large areas, and they can be released easily from rigid masters or complex structures (e.g. quasi-three-dimensional structures). The PDMS possesses a low interfacial free energy and good chemical and thermal stability; this means that PDMS cannot bond easily with any materials, and it can be used from low to high temperatures without losing resolution (shrinking). Furthermore, thank to its UV transparency, can down to 250 nm, PDMS molds can be used to mold a variety of UV-curable polymers.

To prepare PDMS mold, first the pre-polymer and curing agent are mixed with ratio 10:1, respectively. The mixture is then degassed in a desiccator to remove air bubbles. Next, the PDMS mixture is poured on a rigid master (SU-8 or dry film master, for instance). The PDMS is degassed again to remove air bubbles trapped after pouring. This step can enhance the resolution of PDMS stamp as well. The PMDS is cured by oven at 60°C for more than 2 hours or at 100°C for 1 hour. Finally, the PDMS stamp is gradually peeled off from the master.

The natural surface property of PDMS is hydrophobic with the contact angle around 80°. However, the PDMS is proposed to silanize to obtain higher hydrophobicity which important in the PDMS replication process with polymers. Using NOVEC 1720 (3M, USA) is shown a good silanization result for PDMS as well. The PDMS mold is dipped in NOVEC solution for 20 minutes before curing in oven for 1 hour at 150°C.

The schematic illustration for PDMS casting process is shown in the Figure II-8.

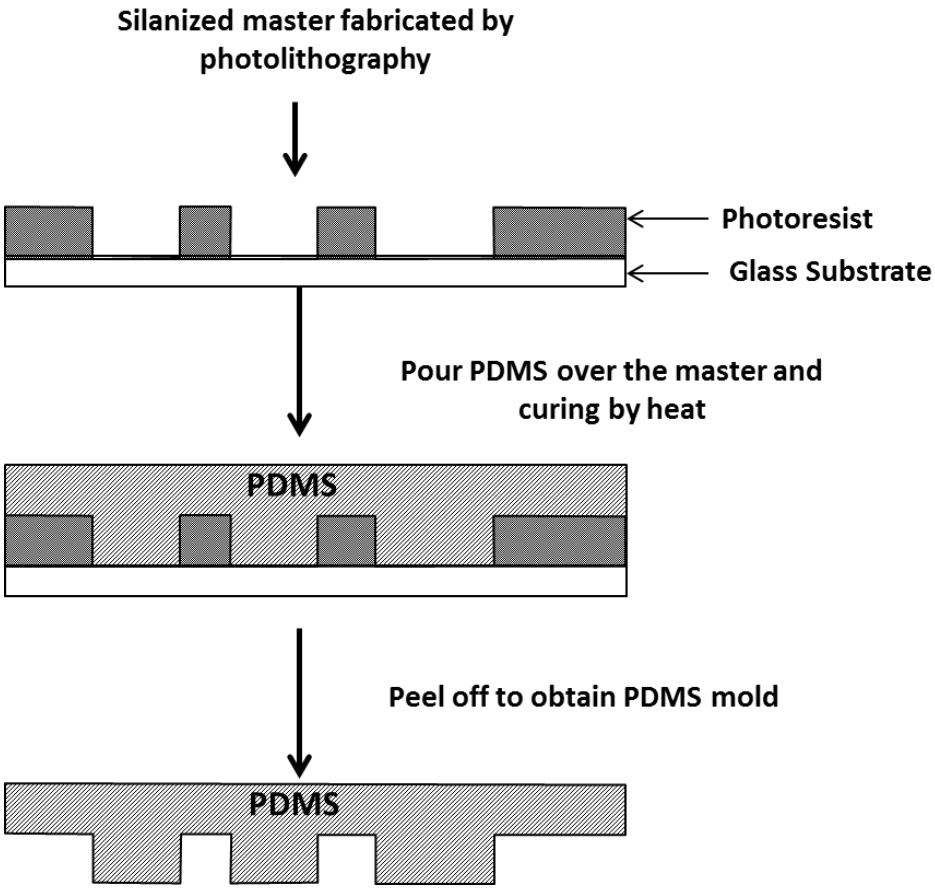

Figure II-8 : Casting of PDMS mold from a resist rigid master

In contrast, PDMS elastomers have been showed some technical problems for soft lithography. The first is the swelling of cured PDMS molds caused by some nonpolar solvents such as toluene and hexane. The softness of PDMS mold reduces the aspect ratio of microstructures. If the ratio of height and width of desired features (aspect ratio h/w) is too large (illustrated in the Figure II-9), it duplicated by PDSM own weight. However, the aspect ratio is too small, insufficient relief structures can withstand and collapse to each other. The range of aspect ratio from 0.2 to 2 can produce good relief structures on PDMS (Delamarche et al. 1997).

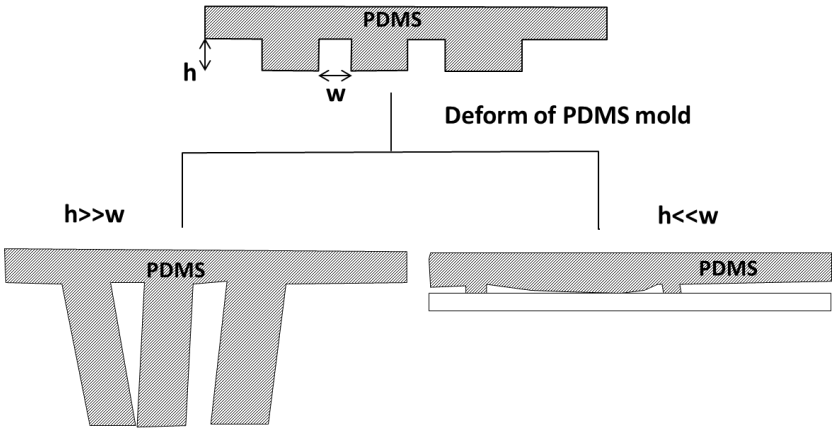

Figure II-9: Deformation of PDMS molds.

In fact, the PDMS can be used directly as a material for microfluidic chip. The PDMS microfluidics are built via PDMS-PDMS (Eddings, Johnson, and Gale 2008), and/or PDMS bonding with other materials (e.g. glass)(Zheng et al. 2004). The popular technique to modify the surface of PDMS is using oxygen plasma (Bhattacharya et al. 2005b). They showed that as the contact angle decreases, the bonding strength increases. In addition, four differently inexpensive methods to bond PDMS/PDMS were tested by Eddings et al. to determine the relative bond strength. The methods based on partial curing and uncured PDMS adhesive techniques which have a significant increasing on bonding compared to oxygen plasma and corona discharge method.

Thank to vapor permeability of PDMS elastomer, the PDMS channels was used as tools to study protein crystallization conditions by vapor-diffusion (Zheng et al. 2004). However, in our case working in free vapor permeability, so PDMS microfluidic chips are not concerned. We only used PDMS as a mold to fabricate microfluidic systems using other materials such as UV-curable pre-polymers.

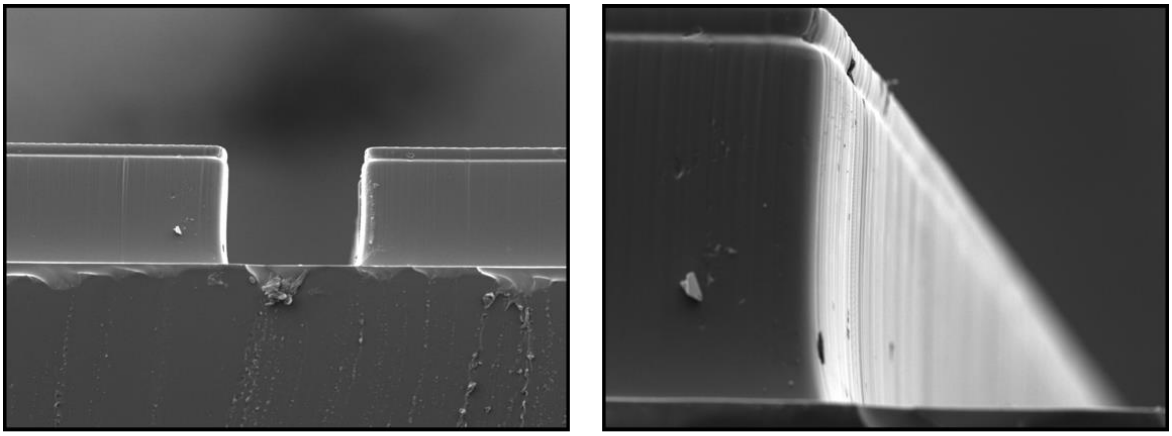

(a) The cross section and the wall channel of PDMS mold which cast from WBR master

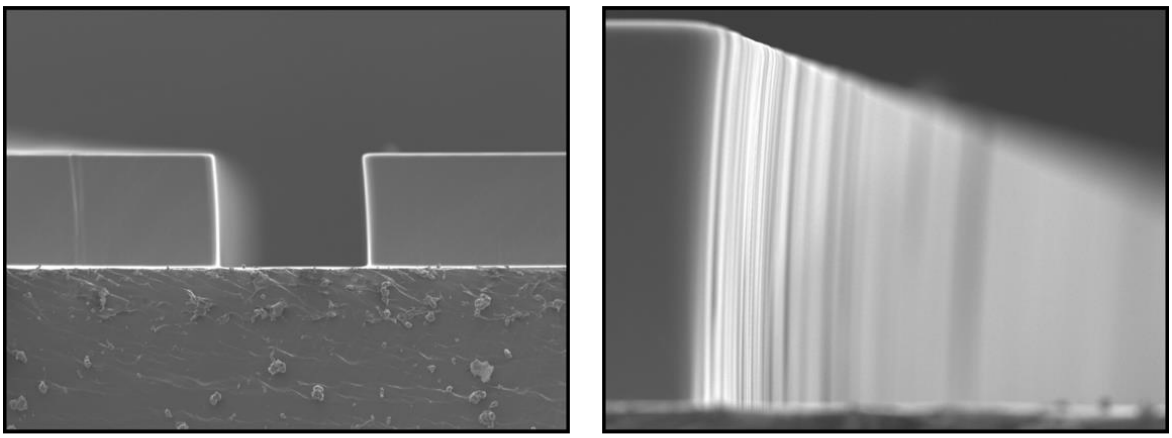

(b) The cross section and the wall of channel of PDMS mold which cast from SU-8 dry-film master

Figure II-10: The TEM images of PDMS molds which cast from WBR dry film master (a) and SU-8 photoresist (b).

The Figure II-10 shown the cross section and the wall channel of PDMS molds which were cast from SU-8 and WBR dry-film master, respectively. It is clearly to see that both cases were shown the straight wall of channel with smooth surface. This means that with the cheap materials as WBR dry-film for rigid master, a high quality of PDSM mold and evenly microfluidic chips were obtained.

II.5. Solvent and pressure resistant microfluidic chips

To fabricate microfluidic system, the micro-molding technique is applied on UV- curable or thermal-curable pre-polymers. As discussed above, PDMS stamps are fabricated by casting from rigid masters (SU-8 or dry film) with relief structures on their surfaces. These structures on PDMS molds are used as a mold for forming structures in the UV or thermally curable pre-polymers. The typical process of micro-molding technique is illustrated in the Figure II-11.

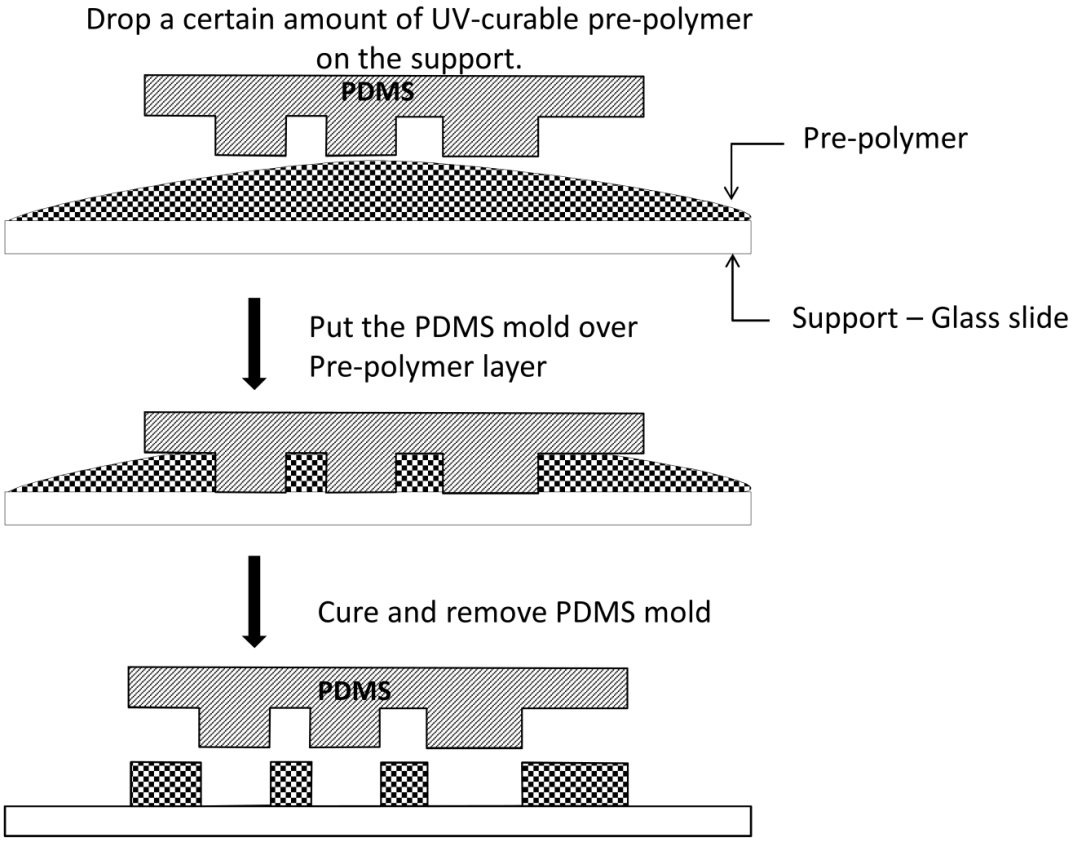

Figure II-11: Micro-molding technique for fabrication of microfluidic systems

Firstly, a certain amount of pre-polymer is dropped on a substrate; here the substrate is a clean glass slide. Afterward, the PDMS mold is placed over the pre-polymer. A light pressure is applied on the PDMS mold in order to remove trapped air bubbles and to excess pre-polymer. The sandwich system PDMS- polymer-substrate is exposed by UV chamber to cure the pre-polymer. The pre-polymer is polymerized into solid phase during the curing procedure. The PDMS mold is gradually lifted off and left the polymer structures on the substrate. The complete microfluidic system is finished by closing the channel by a glass cover slip and injecting inlets and outlets.

In this work, two UV curable materials to fabricate microfluidic platforms are discussed. These materials have been used in a wide range of micro-fabrication: ***Norland Optical Adhesive 81*** (NOA 81) and ***OSTEmer*** polymer.

II.5.1. Norland Optical Adhesive (NOA) microfluidic chips

NOA 81, a single component liquid adhesive thiol-ene based resin, are cured by UV irradiation. It is used generally as glue for very fast and effective way to precise bonding optical components. NOA 81 is sensitive to entire long wavelength from 320 nm to 380 nm and the peak sensitive is around 365 nm. Thus, the UV irradiation source to cure NOA 81 with wavelength 365 nm is required. Some typical properties of NOA 81 are provided by Norland Inc. and showed in Table II-1.

Table II-1: Typical properties of NOA 81 (NOA81, 2016)

Typical properties of NOA 81

Solids	100%
Viscosity at 25°C (non-cured)	300 cps
Refractive Index of Cured Polymer	1.56
Elongation at Failure	25%
Modulus of Elasticity (psi)	200,000
Tensile Strength (psi)	4,000
Hardness - Shore D	90

II.5.1.1. Protocol of fabrication chip using PDMS master

The process to fabricate NOA 81 microfluidic chip is fast and simple(Philip Wägli et al. 2010)(Bartolo et al. 2008)(Hung, Lin, and Lee 2008). Following the soft photolithography method, the NOA 81 liquid is poured on a clean glass slide before applying PDMS mold. A light press is performed on the PDMS mold to fill NOA 81 over all of PDMS mold and remove air bubbles which trapped between PDMS mold and glass slide. The system is kept in ambient condition for few minutes before UV curing. Thank to the gas permeability of PDMS mold, small trapped air bubbles are absorbed. After then, the PDMS and NOA 81 system are exposed in UV chamber for few s or few minutes to cure NOA 81 depending on

the thickness of NOA 81 chip. The PDMS mold is lifted off from NOA 81 solid layer. An uncured thin layer of NOA 81 remains on surface of cured NOA 81 solid. A cover slip is put on to close the channel. A full exposure (i.e. longer time) is performed to cure the uncured layer which bonds NOA 81 and glass cover slip. The optimum bonding of NOA 81 and glass cover is accelerated at 65°C for 12 hours before use.

For example, a 300 µm rectangular channel microchip is prepared by the protocol bellow:

(1) Drop 1-2 mL of NOA 81 on the glass slide. Spread the NOA 81 as much as possible to cover almost the glass slide.
(2) Gradually put the PDMS master on the NOA 81 layer. If there are some air bubbles, try to remove by pressing lightly the PDMS mold.
(3) Expose by UV lamp. In this case, with the UV intensity by 25 mW/cm^2, the 300 µm thickness channel is exposed for 45 s. It is noticed that if the exposure takes so long, the NOA chip will be over cured leading a lower adhesion. And if not, the NOA 81 remains a layer of liquid NOA 81. Consequently, the liquid-NOA 81 can come into and block the channel during full exposure.
(4) Cover a glass cover slip on the top of NOA 81 channel. A small pressure over the surface of microchip to ensure that the cover is in contact with NOA 81. Next, the closed chip is fully exposed by 2 minutes.
(5) The complete microchip is kept in the oven at 65°C at least before connectors assembly and surface modification process.

II.5.1.2. Surface treatment of microfluidic chips

To form a hydrophobic surface for NOA 81 microfluidic chips, several methods have been studied such as using Ag nanoparticles (M. Xu et al. 2010), modified formulation using APTES (Ph Wägli, Homsy, and de Rooij 2011), deposition of molecular monolayer (Gu, Duits, and Mugele 2010). Except the deposition method, other methods are complicated protocols and expensive cost. Hence, the deposition method is proposed to silanize the NOA 81 microfluidic devices. Following Gu et al, the FDTS solution was prepared under nitrogen and low humidity environment which contains 1.5% (v/v) FDTS in isooctane. The whole

process was carried out in the silanization box, described above, to avoid the effect of humidity in the air. Next, the FDTS solution was injected into closed NOA 81 chips and incubated for at least 20 minutes. After then the excess FDTS was removed by rinsing carefully by isooctane and IPA. The NOA 81 chip is dried using nitrogen and kept at ambient temperature for overnight. The long lived of hydrophobic coating is shown in Table II-2.

Table II-2: Contact angle for coated FDTS(Gu, Duits, and Mugele 2010)

		Coated FDTS – NOA 81		
Contact angle	**Native NOA 81**	*Right after treatment*	*3 days after*	*10 days after*
In air	70°±1°	112°±1°	100°±1°	111°±2°
In oil*	96°±2°	156°±1°	155°±2°	155°±1°

* Mineral oil with 5% wt. span 80

II.5.2. OSTEmer microfluidic chips fabrication process

As discussed above, NOA 81 is a potential material for microfluidic system. However, its price is expensive and it is difficult for bonding to any surface. In addition, the surface modification chemistry for NOA 81 is complicated protocol. Thus, an alternative material using thiol-ene click chemistry is proposed. This is Off-Stoichiometry Thiol-ene (OSTE) polymer which had been developed in 2010 by Carlborg et al (C. F. Carlborg et al. 2011).

II.5.2.1. Thiol-ene click chemistry

During the twentieth century, there are two click reactions of thiol and allyl groups have been shown: (a) thiol-ene free radical and (b) thiol-ene catalyzed Michael reaction (Hoyle and Bowman 2010).

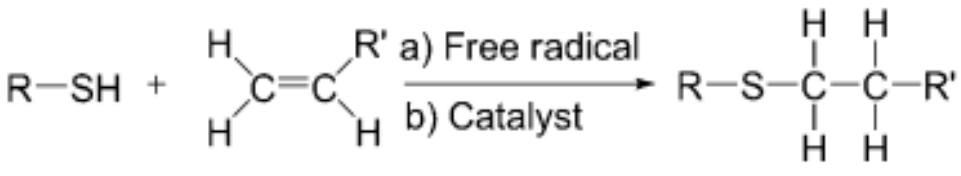

Generally, the thiol-ene click reactions are induced by photo-polymerization which had presence of photo initiation. In initiation step, a thiyl radical is formed, R-S•, under irradiation treatment (i.e. the abstraction of hydrogen from thiol group).

Initiation

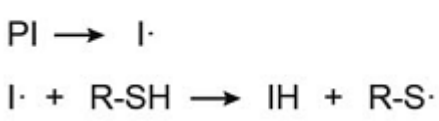

After that, the thiyl radical can propagate through a direct addition to a carbon-carbon double bond of terminal -ene, consequently a centered carbon radical is formed.

Propagation

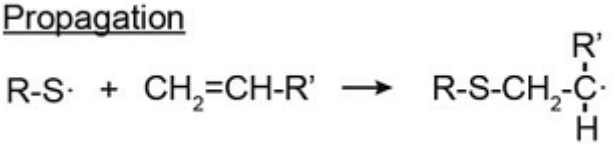

On the chain transfer step, the centered carbon radical abstracts a Hydrogen atom from free thiol groups which becomes thiyl groups.

Chain transfer

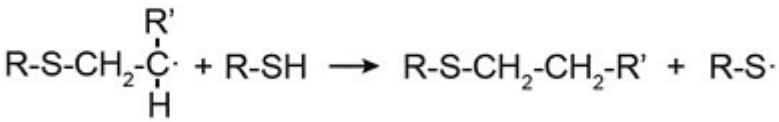

The propagation and chain transfer can repeat several times and generate thiol-ene reactions which mainly occur via different radical-radical combinations.

Termination

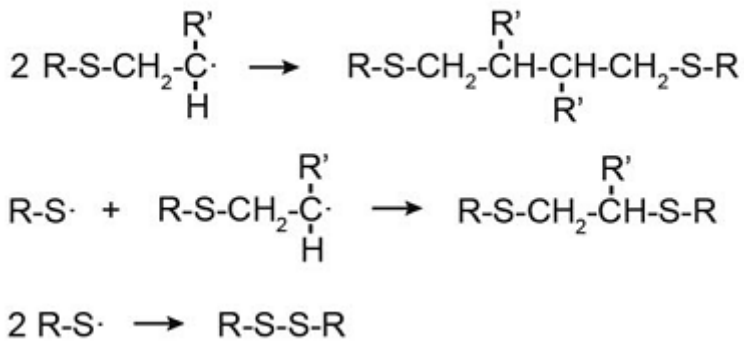

Based on UV-initiated thiol-ene click chemistry, the OSTE can apply to fabrication high resolution micro-features using direct lithography (Pardon et al. 2014) or duplicating on defined mold. Karlsson et al indicated that an aspect ratio (1:8) was obtained (Karlsson et al. 2012). Furthermore, OSTE polymer has been showed as a polymer possesses tunable mechanical properties (C. F. Carlborg et al. 2011), biocompatibility (Errando-Herranz et al. 2013), tunable chemistry surface (F. Carlborg et al. 2012) which can modify OSTE surface property to hydrophobic or hydrophilic using fluorinated or hydroxylated methacrylate, respectively. The OSTE polymer also shows very fast and facile bonding protocol at room temperature (C. F. Carlborg et al. 2011; Niklas Sandström et al. 2011). However, OSTE polymer has some drawbacks: (a) the bonding of OSTE layers is performed only one layer with excess thiol groups and one layer with excess allyl groups. (b) Some studies report a leaching of unreacted monomers as contaminations in micro-fluidic devices (Cramer et al. 2010). (c) Limited high temperature performance with low glass transition temperature.

In order to overcome these limits of OSTE polymer, a novel, superior ternary, dual cure, thiol-ene-epoxy (OSTE+) polymer system has been introduced. By the combination of epoxy groups with thiol-ene chemistry, new polymer is polymerized by two stages of UV activation. First UV curing provides thiol-ene networks with an intermediated, soft solid material which can be seen as an ideal surface for bio/chemical modification and bonding. Second UV curing results excess thiol and epoxy reactions which presented as an inert polymers with excellent engineering plastics properties (C. F. Carlborg et al. 2014; Haraldsson, Carlborg, and van der Wijngaart 2014). A typical platform of OSTE+ contains thiol, ene, epoxy groups and radical and anionic initiators. The chosen anionic initiator is often a tertiary amine which enhances the formation of thiyl radical from thiol groups; subsequently open the epoxy groups via anionic addition reactions.

Initiation I

Propagation I

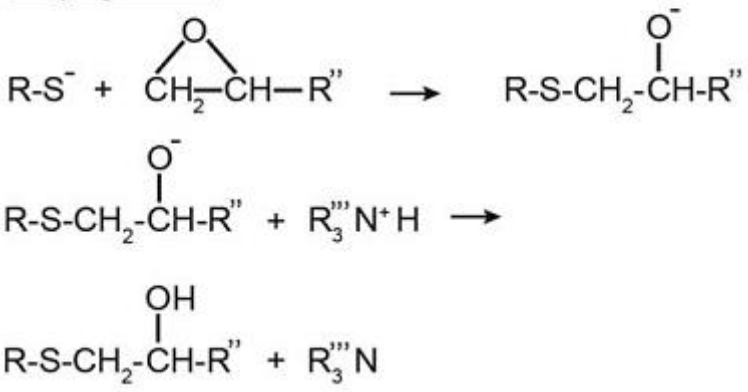

On the other hands, the tertiary amines also react with epoxy groups to form zwitterions, which subsequently enable nucleophilic displacement in the presence of thiol groups. And the zwitterions also participate in epoxy homo-polymerization.

Initiation II

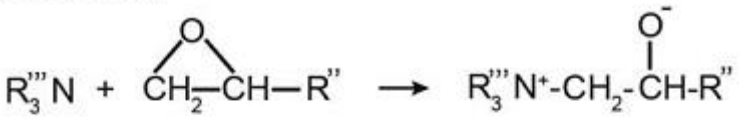

Propagation II

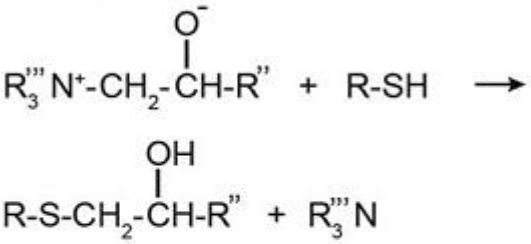

Propagation III (homopolymerization)

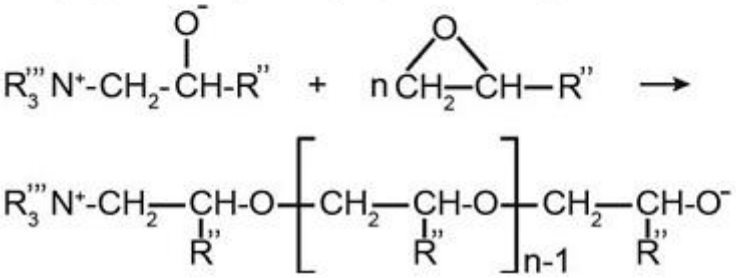

II.5.2.2. Protocol of fabrication using PDMS master

The combination of thiol-ene and thiol-epoxy reactors makes OSTE+ polymer useful for microfluidic fabrication(N. Sandström et al. 2015) and adhesive-free bonding (Vastesson et al. 2013; C. F. Carlborg et al. 2014; Zhou et al. 2014). A typical fabrication process of microfluidic device is shown in the Figure II-12. The OSTE+ is a commercial OSTEmer 322 40 Clear Crystal from Mercene Labs (Sweden). The kit pack contains 2 components: A and B. The mixture of A and B component with ratio 1:0.87 respective is well mixed for 2 minutes and degassed in desiccator. Then, the mixture OSTEmer containing thiol, epoxy and allyl monomers is filled in between PDMS molds and glass slides. The first exposure is performed with 365 nm UV light to establish thiol-ene networks and still remain excess thiol and epoxy monomers on the surface. The top and bottom layer are aligned precisely before the second UV exposure. The thiol-epoxy reaction happens to bond two polymer layers and close the microfluidic chip.

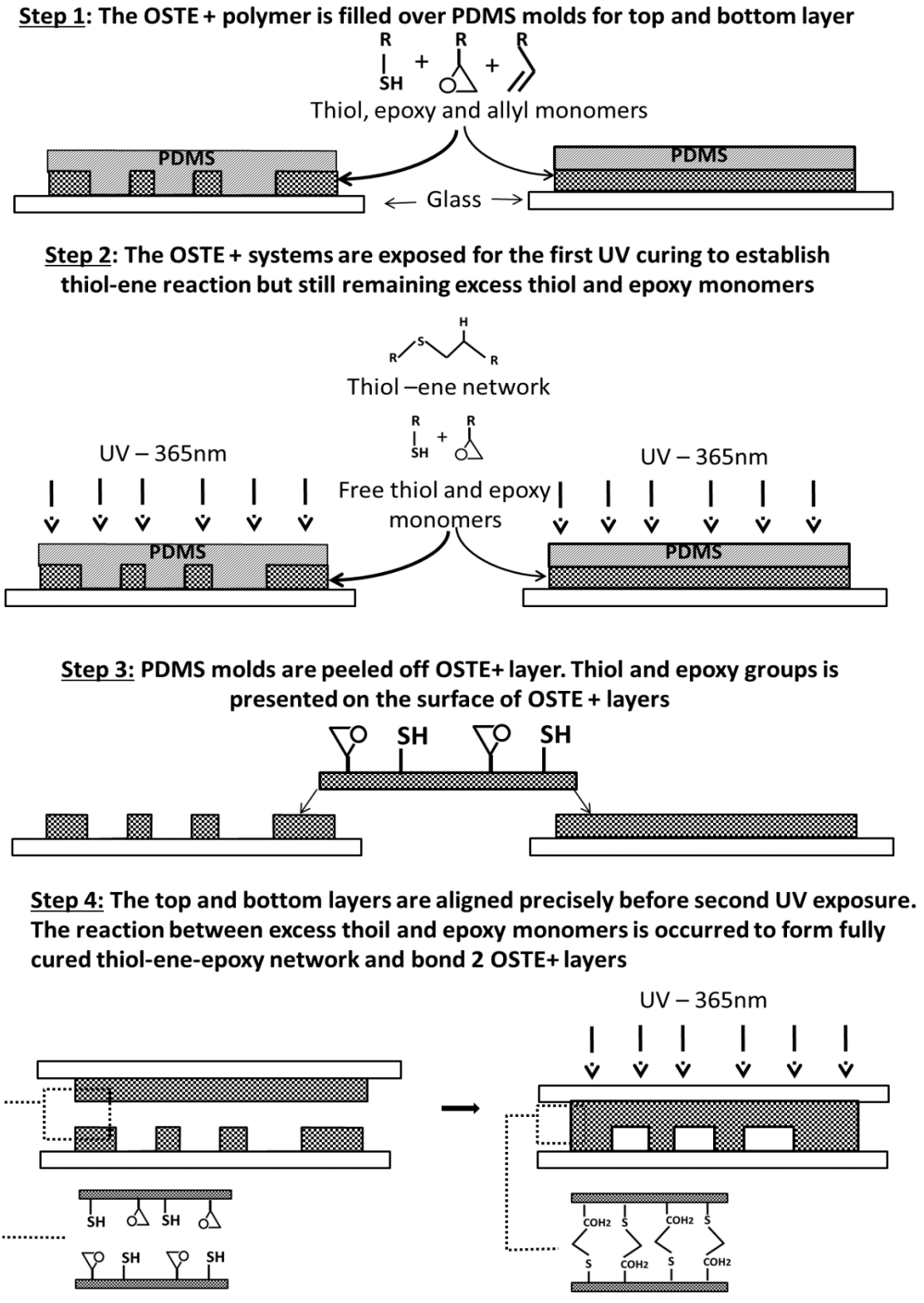

Figure II-12: Fabrication of microfluidic using OSTE+ and soft lithography method.

II.5.2.3. Protocol of fabrication using "quasi-injection molding"

The injection molding is very effective method to fabricate microfluidic systems(Chandekar et al. 2008; N. Sandström et al. 2015). In general, the system contains two molds for the cover and the patterns which made by aluminum. For the case of OSTEmer, the mold for the cover is glass slide which transparent property for exposure by UV light. Both of molds are aligned together perfectly before injecting OSTEmer through an inlet. The air space inside two molds is replaced by OSTEmer during the injection, the air is removed through out a ventilation port. The UV light was applied on the transparent side of the mold (i.e. the side of glass slide) to cure OSTEmer. The two parts of the microfluidic chip are prepared with one for the cover and one for the channel. After peeling off from molds, the two parts of OSTEmer will be aligned together to complete the chips. The injection molding is very useful with many benefits such as the aluminum mold can use for many times, saving the materials... However, to design the patterns on the aluminum mold is quite difficult and expensive as well. Hence, a novel way to build the mold is use of PDMS mold instead of aluminum mold. The method is called "quasi-injection molding" due to the similar way to the injection molding technique when using the two different molds. The detailed protocol to build the microfluidic chip is shown in the Figure II-13 below.

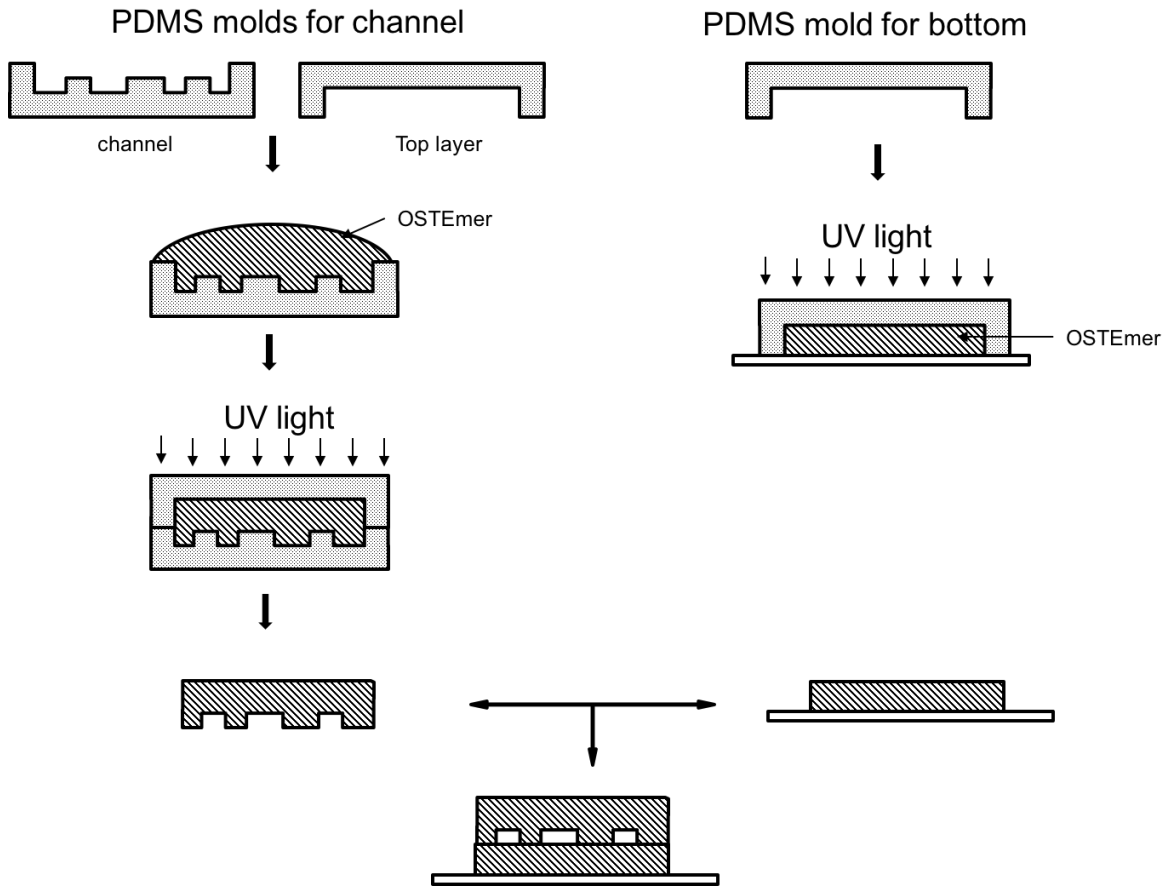

Figure II-13: Process to fabricate OSTEmer microfluidic chip using "quasi injection molding" technique

The protocol can be split into two parts: preparing the channel layer and the bottom layer. *Preparation of the channel*: a PDMS mold with channel patterns and a flat PDMS mold to make cover are used. Firstly, the OSTEmer after degassing by vacuum chamber is poured directly to the channel PDMS mold. The air bubbles trapped in the PDMS mold are removed by the tweezer. Next, the cover PDMS mold is put gradually on the channel PDMS mold with OSTEmer to avoid trapping more air bubbles. The UV light with 365 nm wavelength is used to expose the paired mold systems for 90 s with UV intensity 10 mW/cm^2.

Preparation of bottom layer: the aim is to build a flat OSTEmer layer on a glass slide. Firstly, the OSTEmer is poured on the glass slide before covering by PDMS mold. The PDMS mold is put gradually on the OSTEmer to avoid air bubbles. Finally, the system is exposed to UV light in 30 s with UV intensity 25 mW/cm^2.

Assembling the final chip: The PDMS molds are kept until finishing both parts of the chip. The first step, the PDMS mold of bottom layer is removed to get a flat OSTEmer layer on the glass substrate. And for the channel molds, at the beginning the PDMS mold for the channel is peeled off and still kept the PDMS mold of top layer. Two OSTEmer layers are precisely aligned under microscope. Press all of surface to ensure that two layers are well contacted. The last PDMS mold is removed and the OSTEmer chip is ready for next step: Surface Modification.

II.5.2.4. Surface treatment of microfluidic chips

The surface modification process for OSTEmer microfluidic devices has been showed in few studies (F. Carlborg et al. 2012; Pardon et al. 2014). They also used the same protocol to spatially modify surface properties which radical mediated reaction of thiol and methacrylate monomers. Depending on fluorinated or hydroxylated methacrylate monomers is used, the surface is modified into hydrophilicity or hydrophobicity, respectively. The methacrylate solution is a mixture of hydroxylated/fluorinated methacrylate monomer, two photo initiators Benzophenone (BP) and TPO-L in toluene. Briefly, after UV curing, BP will promote conversion of thiol groups into active thiyl radicals via the abstraction of hydrogen atoms. After that, the methacrylate monomers are added to thiyl radical via chain –wise reaction until the chain terminated. Because BP only abstracts hydrogen atoms from the thiol groups on surface, consequently the methacrylate molecules only graft on surface of OSTE layer. Carlborg et al (F. Carlborg et al. 2012) also showed that more excess thiol groups on formulation of OSTEmer polymer, higher density of methacrylate chains on the surface, so higher degree of hydrophobicity or hydrophilicity. Both studies indicated that the distinct of the contact angle between hydrophobic and hydrophilic region is 95°.

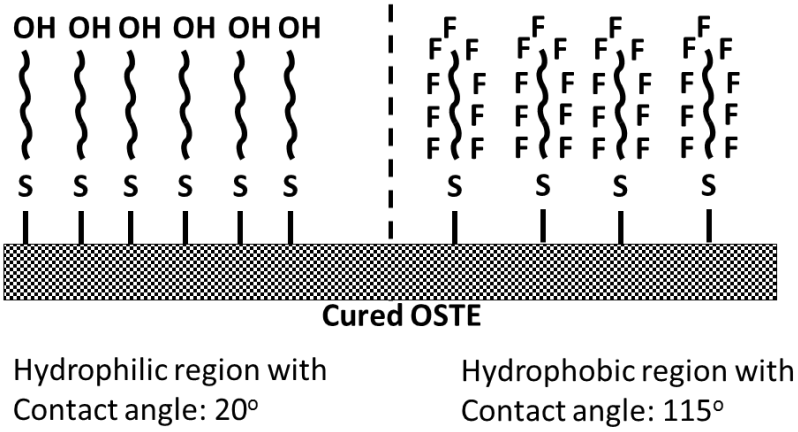

Figure II-14: Surface modification of OSTEmer chip using methacrylate monomers

II.5.2.4.a. Hydrophobic and hydrophilic surface modification

As introduced above, the OSTEmer chip is modified the surface properties using mixture of hydroxylated/fluorinated methacrylate monomers. So, in order to change the nature surface property of OSTEmer chip into hydrophobic, the hydroxylated methacrylate solution is applied. The mixture is prepared by protocol which presented more detailed here: Heptadecafluorodecyl methacrylate 2% wt. is dissolved in Toluene with 2% wt. Benzophenone, 1% wt. Allyl glycidyl Ether and 0.5% wt. Irgacure R819 (initiator). The solution is mixed well and stored in dark area before use. The solution is injected in OSTEmer chip by a syringe and exposed for 2 minutes with a 365 nm UV light source at 25 mW/cm^2 intensity. After that, the chip is slowly rinsed by Isopropanol for at least 3 minutes and dried by nitrogen. With this step, the chip is rid off almost excessed fluorinated methacrylate. Finally, the chip is stored in the oven at 100°C for at least 1 hour.

The mixture and protocol to change the surface of OSTEmer channel into hydrophilic are almost the same as the hydrophobic modification method, except that instead of using Heptadecafluorodecyl methacrylate, 2-hydroxyethyl methacrylate is used. All percentages of other components are kept the same as well.

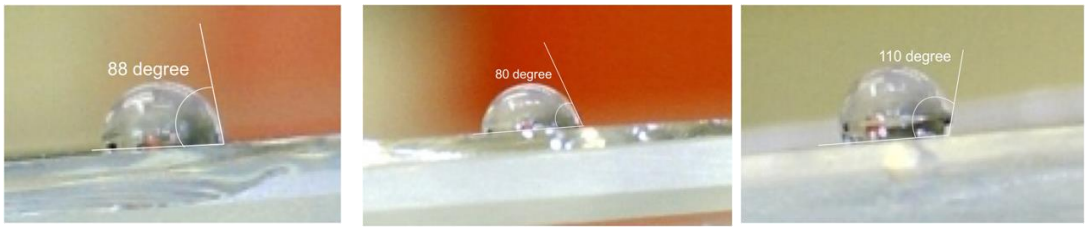

Figure II-15: The contact angle of (left) nature, (middle) hydrophilic modification and (right) hydrophobic modification OSTEmer with contact angle are 80°, 88° and 110°, respectively.

The Figure II-15 shown the contact angles of the nature, the hydrophilic modification and the hydrophobic modification OSTEmer. It is noticed that the nature surface property of OSTEmer is hydrophilic with contact angle by 88°. After the hydrophilic modification, the contact angle was decreased down to 80°. This was not so good result but still good enough for generation O/W droplets. For the hydrophobic modification was better with contact angle around 110°. The results are strongly agreed with results of methods mentioned in the literature(Zhou et al. 2014).

II.5.2.5. Chip testing

II.5.2.5.a. Aqueous and non-aqueous droplet generation

To test the surface modification, the droplet generation of aqueous/non-aqueous is carried out. The generation water droplet in decanol and the hexadecane droplet in water were tested for hydrophobicity and hydrophilicity of surface channel, respectively.

The Figure II-16 shown the generation of droplet water in decanol without surfactant. Normally, the surfactant is used to increased the interface tension of water in decanol and lead the forming droplet more easily and stable. The silanized OSTEmer structure enabled to form the water droplet without surfactant proving that the surface of channel was hydrophobic enough.

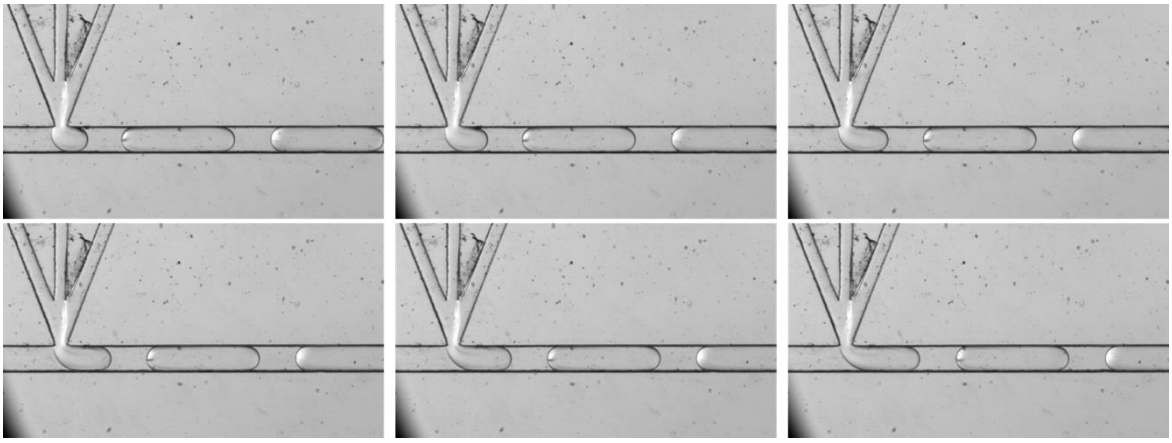

Figure II-16: Water droplet generation in decanol without surfactant using NOA 81 microfluidic chip.

The work of testing non-aqueous droplet generation was carried out by Christina Wegner, a German internship student for her bachelor degree in Karlsruhe Institute of Technology (KIT), Germany. System goals are to study nucleation and crystallization process of hexadecane which depended on the temperature and volume of droplets. A microfluidic chip was designed to generate droplets of hexadecane in aqueous continuous phase (water) with or without the presence of surfactant. In this work, two types of surfactant Tween 20 and Tween 60 were used. In the results, the modified surface of channel was hydrophilic enough to form hexadecane droplets in the water however the life-time was under expectation. After one day working, the hydrophilicity is lowered causing hexadecane droplets stuck easily to the surface of channel.

II.5.2.5.b. Common solvent resistance

To test the solvent resistance of OSTEmer chip, several of solvents have been used. Small pieces of OSTEmer with channel pattern were dipped in several solvents at different period of time. Afterward, the samples were observed on a microscope to see any difference on the straight of channel walls. The Table II-3 shown the list of solvents and period of time for resistance testing.

Table II-3: List of solvents and period of time for testing OSTEmer chips. Here, Y (yes) and N (no) is abbreviation of the experiments have been done or not.

Solvents/Time	**1h**	**24h**	**1 week**	**Observation**
Acetone	Y	Y	Y	Slightly swelling after a week
Cyclohexane	Y	Y	Y	No difference
Ethanol	Y	Y	y	No difference
Heptane	Y	Y	Y	No difference
Toluene	Y	Y	N	No difference
Nitric acid	Y	Y	Y	Destruction occurred after 5 minutes.

As the results, the OSTEmer chips had a good resistance to all common solvents such as acetone, cyclohexane, ethanol, heptane and toluene but the nitric acid. In the nitric acid, the OSTEmer dissolved rapidly even at few minutes and completely destroyed at 24 hours.

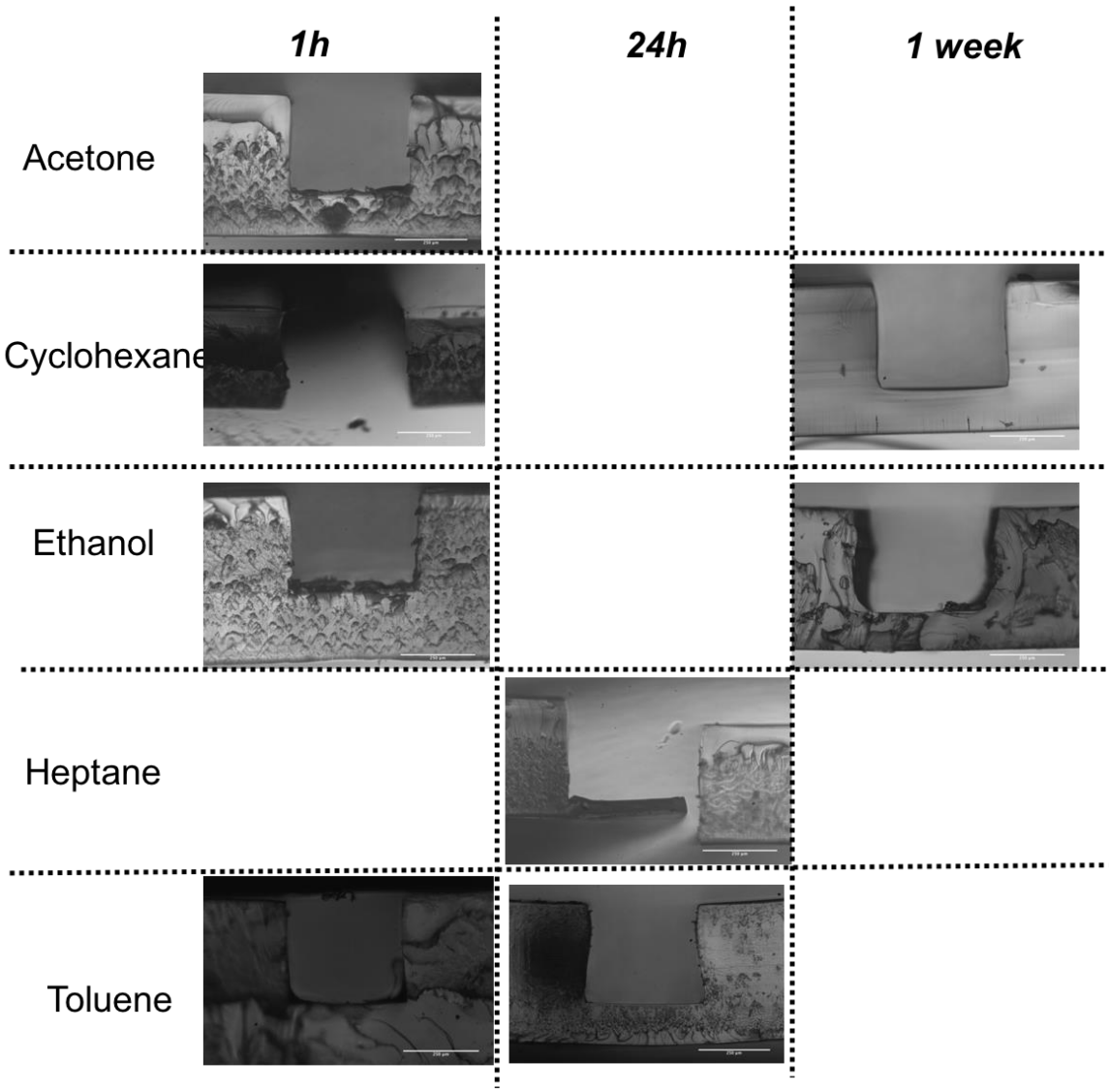

Figure II-17: Side views channel which tested by acetone, cyclohexane, ethanol and toluene by the period of time.

The Figure II-17 shown the side views of each sample which contains channel patterns tested with some solvents for different period of time. For all of tested solvents, no significant damage was observed. The walls of channels were kept straightly from the beginning to the end. This means that the original OSTEmer chip can stand to these solvents for a long time.

II.5.2.5.c. High pressure testing

There is a lack of publication in the literature which mentioned about high pressure resistance of OSTEmer chips. However, Alexandre Martin's publication on 2016 shown that OSTEmer microchips can stand for high pressure environment

(A. Martin et al. 2016). They indicated that the OSTEmer chips with the structures are illustrated in the Figure II-18, can stand for 20 minutes at the maximum pressure by 200 bar.

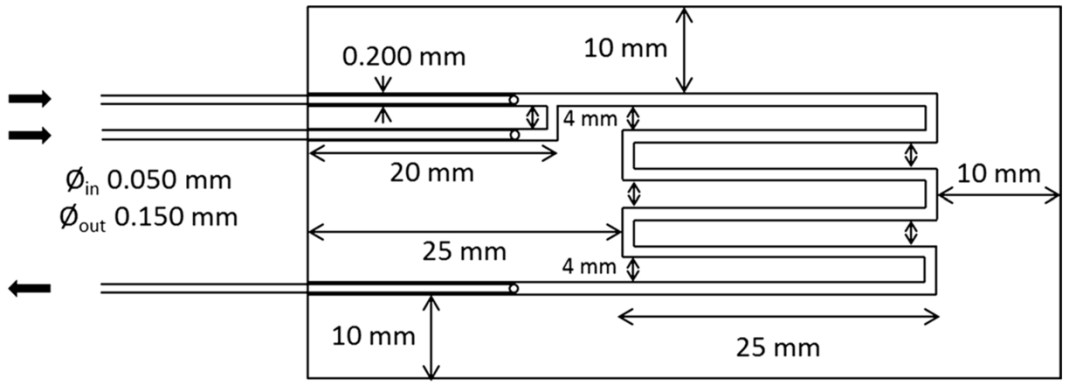

Figure II-18: Schematic diagram with dimension of microfluidic chips using for high pressure.

The preparation of microchips is followed the same protocol presented in Section II.5.2. However, in order to enhance the bonding, 2 mm thickness glass slides were used as a supporter and a cover. The pressure test for several OSTEmer chips was shown identical results, as shown in the Figure II-19.

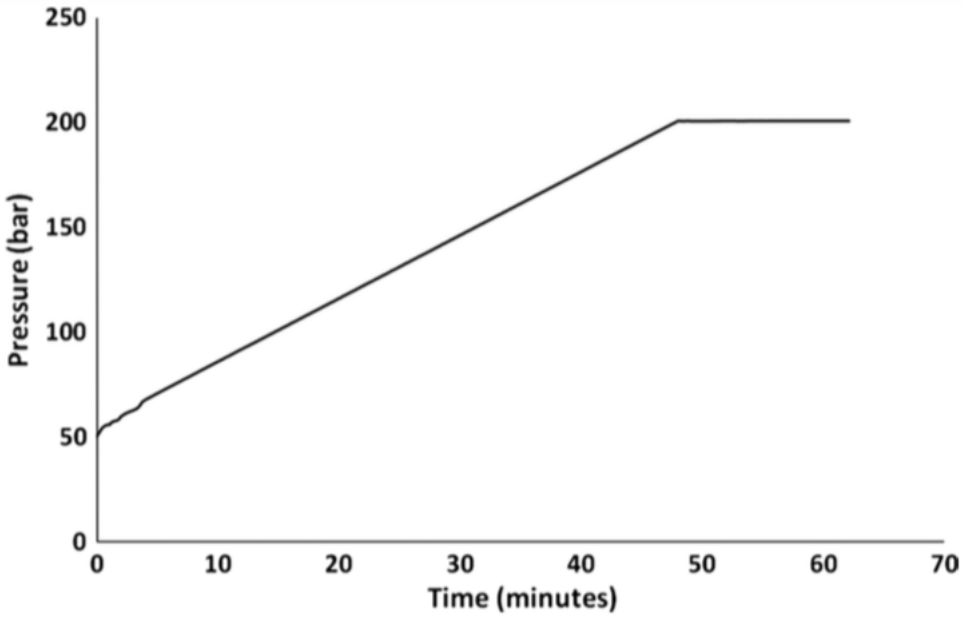

Figure II-19: The procedure for pressure test in OSTEmer microfluidic chip as a function of time.

The microchip is stood successfully at 200 bar without rupture of the glass or delamination of the different glass and polymer layers within the chip for approximately 20 minutes. In conclusion, besides other advantages of OSTEmer chip such as: easy to fabrication, easy to surface modification and high solvent-resistance, it also owns the pressure-resistance property which will be versatile for many purposes.

II.5.3. Near zero dead volume interconnections

In order to create inlets and outlets for microfluidic devices, the connectors are used through two approaches: vertical and horizontal way. A vertical one, connector named Nanoports from Upchurch (USA) are proposed because of their advantages such as a lot of size of connector which fitted with various kinds of chips, easy to use, reusable…etc. However, the Nanoports also possesses itself some drawbacks. The first thing is its own expensive cost. Moreover, because of original design of Nanoports, death zones occur and causing unstable flow rate. It becomes a severe problem when tiny flow rates applied to generate nano-litter volume scale droplets.

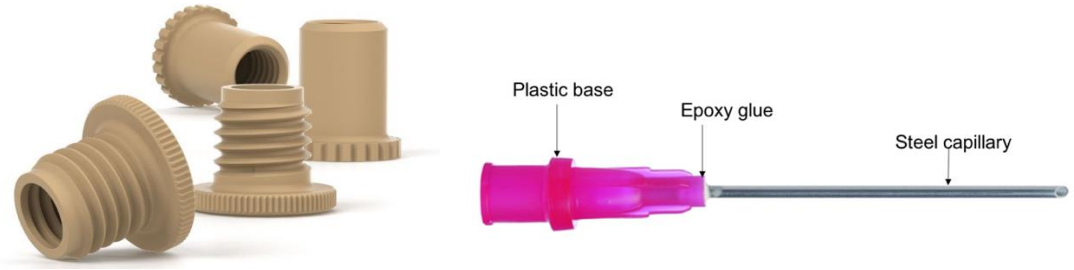

Figure II-20: 2 types of connectors: Nanoports Upchurch (right) and typical needle structure (left)

By using the horizontal approach, the drawback of Nanoports connectors is eliminated. A small steel tubing with few hundred micrometers inner diameter can be used as connectors. These steel capillaries were obtained by removing from needles (Sigma). Normally, the needle contains three components: plastic base, epoxy glue and steel capillary(illustrated in the Figure II-20). The epoxy glue was easily dissolved by utilizing chloroform and afterward, the steel tubes were

carefully picked up from plastic bases with tweezer. With these steel capillaries, the dead zone in the connection is approximately by zero. However, after gluing in the microfluidic system, the steel capillaries are rarely reusable.

For both cases, connectors are assembled on the microfluidic chips by an epoxy glue. Depending on the design of microfluidic chip, the Nanoports and steel capillary can be used separately or together.

II.6. Conclusion

In this chapter, a cheap and fast protocol for fabrication a versatile microfluidic system is presented. The microfluidic platforms are based on the soft lithography method for UV-sensitive materials shown a bunch of advantages than other techniques. The fast and low-cost protocol is proposed to build high throughput in 24 hours with less than 10 euros for each chip. The microfluidic chips are also proved to stand at high pressure around 200 bar for at least 20 minutes and for several common solvents. Moreover, easy modification surface of channel is the most valuable for different purposes dealing with W/O or O/W emulsions. According to these successes, microfluidic chips are fabricated to suitable for further experiments such as combination with SAXS and to study the mass transfer in dehydration of micro-droplets which discussed in the following Chapters.

Chapter III PROTEIN INTERACTIONS STUDIED BY SAXS AND MICROFLUIDIC

III.1. Introduction

Small Angle X-ray Scattering (SAXS) has become a powerful technique in colloidal science for determining size, shape and internal structure of polymer particles in the size range from a few nanometers up to about 100 nm(Fournet and Guinier 1955; Glatter and Kratky 1982; D. I. Svergun and Feigin 1986; Lindner and Zemb 1991; Kaler and Brumberger 1995; Hunter 1989) . SAXS is mainly applied to systems of randomly oriented and statistically distributed structures of colloidal dimensions, such as latexes (e.g. (Ballauff et al. 1996; Dingenouts, Norhausen, and Ballauff 1998; Dingenouts et al. 1999), supramolecular aggregations (e.g. micelles (e.g. (Hickl, Ballauff, and Jada 1996; Kratky and Müller 1982), proteins (Pilz 1982), natural and synthetic high polymers dispersed in solutions (e.g. (Kratky and Müller 1982; Kirste and Oberthur 1982; Hickl et al. 1997; Kholodenko, Ballauff, and Granados 1998; Dingenouts, Norhausen, and Ballauff 1998) or precipitates in amorphous materials (e.g. (Bergmann, Fritz, and Glatter 2000; Jörg Bolze et al. 2000; J. Bolze et al. 2004). Small-Angle X-ray scattering has also been proved to be a powerful technique to investigate the structure of soft matter and biological macromolecules at the nanometer-scale (Kratky 1982; Feigin and Svergun 2016). It has demonstrated its potential for diverse applications, from nucleation studies (i.e. glycine crystals(Chattopadhyay et al. 2005) or colloidal silica(Pontoni, Narayanan, and Rennie 2004) to the determination of proteins molecular weight(Fischer et al. 2010) or to study protein interactions in solution prior to crystallization(Ducruix et al. 1996), protein structure(Mertens and Svergun 2010), or even conformational changes(Durchschlag et al. 1996). SAXS measurements have also been used to determine the second virial coefficient A_2, a thermodynamic parameter characterising protein interaction which has been proved as a powerful tool to predict crystallization conditions, and therefore protein solubility.

However, the required volume for each measurement (a few mL), together with a large number of experiments necessary to obtain reliable statistical information at each studied condition, makes this technique less convenient when working with high value compounds. To partially solve this issue, few studies are reported in literature proposing the coupling of single-phase continuous flow

microfluidics and SAXS in order to screen phase behaviours(Khvostichenko et al. 2013), to study self-assembly of surfactants(H. P. Martin et al. 2010) or biological macromolecules(Brennich et al. 2011a) or also to investigate nucleation and growth of gold nanoparticles(Polte et al. 2010). But this approach presents a major drawback: A continuous flow can be unfavourable when fluids modify their characteristics after being mixed, as components are able to diffuse in the channels and, in the case of crystallization studies, a nucleating phase can inhibit the precipitation and growth of other different phases. In this sense, the use of droplet-based microfluidics seems to be more convenient. A dispersed phase can be created by mixing several miscible compounds and subsequently periodically separated by a continuous phase, generating monodisperse droplets, which are suspended in an external carrier phase thus behaving as isolated micro-reactors, as the immiscibility of the two phases prevents diffusion from one droplet to another. With this technique hundreds/thousands of independent experiments can be generated with ease in a short period of time and using a very low quantity of reagents. So far, the promising combination of continuous flow droplet-based microfluidics and SAXS has been sparsely reported for very few and different approaches in the literature dealing with gold nanoparticles(Stehle et al. 2013) and liquid crystals(Otten et al. 2005).

In this chapter, low cost microfluidic platforms presented will prove the convenience of combining high throughput droplet-based microfluidics and SAXS for the study of protein shape factor and weak interactions in solution.

This chapter is divided into three parts. First, in order to state the fundamental basis of the study, basic principle, theoretical and practical aspect of SAXS dedicated to biological macromolecules are reviewed. Then a short bibliographic report of the coupling of microfluidics and SAXS from synchrotron source will be discussed. In a second part of the chapter, the experimental setup will be presented and discussed. The experimental setup consists of a microfluidic platform, a sample holder (POD) and a real-time image acquisition routine used to improve data acquisition. The last part of this chapter is dedicated to the determination of a protein (Lysozyme) interactions in solution for different experimental conditions (e.g. salt concentration).

III.1.1. Theory background

Small Angle X-ray Scattering (SAXS) is a non-destructive analytical technique to investigate structures of soft matter and biological macromolecules at the nanometer-scale(Glatter and Kratky 1982)(D. I. Svergun and Feigin 1986). An X-ray beam is sent through or onto a sample containing nanostructures, such as proteins, macromolecules or quantum dots. The beam interacts with the electrons of the sample and is scattered. The detected scattering pattern is characteristic of the nanostructures and can be used to determine their size, shape, internal structure and more. This method is extensively used for diverse applications, to study the nucleation of glycine crystals(Chattopadhyay et al. 2005), colloidal silica aggregation(Pontoni, Narayanan, and Rennie 2004), or to study proteins to determine their interactions in solution (Ducruix et al. 1996), their molecular weight(Fischer et al. 2010), their structure(Mertens and Svergun 2010), or even their conformational changes(Durchschlag et al. 1996).

In synchrotron rings (as illustrated in the Figure III-1) electrons or positrons are accelerated to relativistic speeds and guided through devices inserted into the ring structure, e.g., bending magnets, wigglers, or modulators, to facilitate the emission of X-rays. Depending on the setup of these insertion devices, the characteristic properties of the emitted X-ray beam, such as flux, energy spectrum, coherence, and divergence, may be controlled(Als-Nielsen and McMorrow 2011). A beamline tangential to the synchrotron storage ring following such an insertion device then shapes and filters the initial X-ray beam to defined characteristics suitable for a particular experiment.

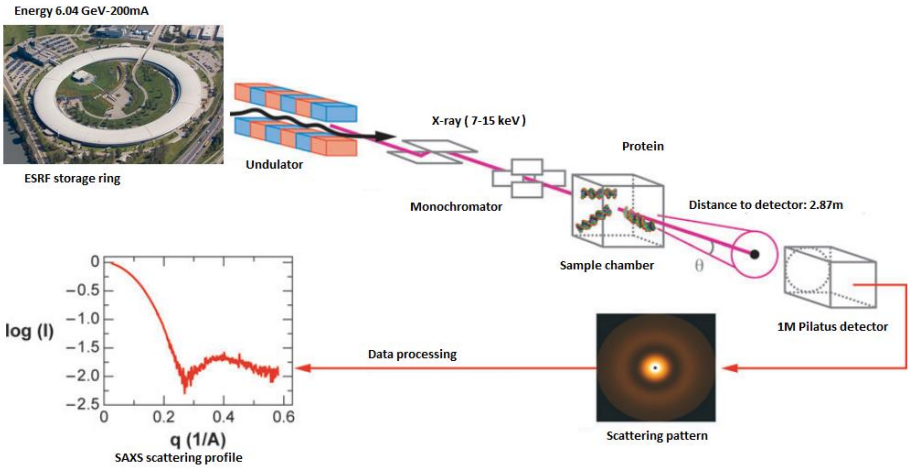

Figure III-1: Schematic principle of SAXS setup at ESRF (Grenoble, France).

In the case of biological SAXS, the reduction of parasitic and background scattering is a high importance as biological samples scatter only very weakly in comparison to other materials(Kirby et al. 2013). Moreover, biological materials are prone to radiation damage due to free radicals, leading to nonspecific aggregation in proteins and degradation in polynucleotides. An ideal SAXS beamline will strive to optimize photon delivery, focus, sample flow, and exposure times. A temperature-controlled environment for sample storage and exposure keeps proteins stable during data collection. As proteins come in all sizes, adjustable detector distance or user configurable energy changes are important.

III.1.1.1. Basic aspect of SAXS

In a typical SAXS experiment (shown in the Figure III-2), a monochromatic beam of incident wave vector $\overrightarrow{s_0}$ is selected and falls on the sample.

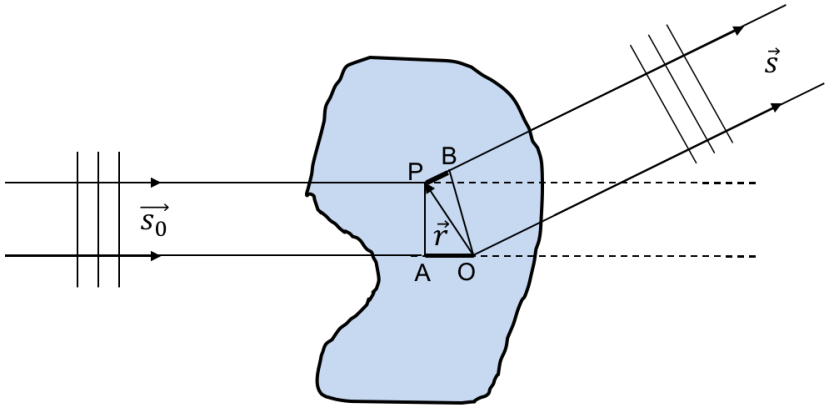

$$\delta = |\overline{PB}| - |\overline{AO}| = \vec{r}.(-\overrightarrow{s_0}) + \vec{r}.\vec{s} = \vec{q}.\vec{r}$$

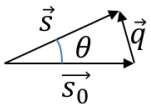

$$\vec{q} = \vec{s} - \overrightarrow{s_0}$$

$$q = |\vec{q}| = 2|\vec{s}|.\sin(\theta/2) = \frac{4\pi}{\lambda} sin(\theta/2)$$

Figure III-2: Calculation of the phase difference δ between the waves from scatters at points O and P in a particle. In the draw $\vec{s}$ and $\overrightarrow{s_0}$ are unit vectors in the direction of scattered and incident beams, respectively, and P is displaced from O by the vector $\vec{r}$, θ is denoted scattering angle and $\vec{q}$ scattering vector.

The scattered intensity is collected as a function of the so-called scattering angle 2θ. Elastic interactions are characterized by zero energy transfers, such that the final wave vector $\vec{s}$ is equal in modulus to $\overrightarrow{s_0}$. The relevant parameter to analyze the interaction is the momentum transfer or scattering vector $\vec{q} = \vec{s} - \overrightarrow{s_0}$, defined by:

$$q = |\vec{q}| = \frac{4\pi}{\lambda} sin\frac{\theta}{2} \qquad \text{Eq. III-1}$$

In SAXS experiments, the characteristic size of the sample is inversely proportional to the modulus of the scattering vector.

The angle dependent scattering amplitude is related to the electron density distribution $\rho(\vec{r})$ of the scatterer by a Fourier transformation. $\rho(\vec{r})$ is the number of electrons per unit volume at the position $\vec{r}$. An element of volume dV at $\vec{r}$ contains $\rho(\vec{r})dV$ electrons. The scattering amplitude of the whole irradiated volume V is given by:

$$A(\vec{q}) = A_e \int_V \rho(\vec{r}) e^{-i\vec{q}\vec{r}} d\vec{r} \qquad \text{Eq. III-2}$$

Where A_e is the scattering amplitude of one electron.

The scattering intensity of one single particle $I_0(\vec{q})$ is the absolute square given by the product of the amplitude $A(\vec{q})$ and its complex conjugate $A^*(\vec{q})$

$$I_0(\vec{q}) = A(\vec{q}).A^*(\vec{q}) = I_e \int_V \int_V \rho(\vec{r})\rho(\vec{r}')e^{-i\vec{q}(\vec{r}-\vec{r}')}d\vec{r}d\vec{r}' \qquad \textit{Eq. III-3}$$

with I_e the single electron scattering intensity (von Laue 1960).

In most case of SAXS performed on proteins, the following hypothesis is formulated:

1. The particles are statistically isotropic and no long-range order exist (no correlations between particles for large spatial distances)
2. The particles are embedded in a matrix (buffer, solvent...). The matrix is considered as an homogeneous medium with a constant electron density ρ_0. Thus, the electron density in equations (Eq. III-2) and (Eq. III-3) should be replaced by the difference in electron density $\Delta\rho = \rho - \rho_0$.

In this case, the average over all orientations leads to the fundamental formula of Debye:

$$\langle e^{-i\vec{q}\vec{r}} \rangle_\Omega = \frac{\sin(qr)}{qr} \qquad \textit{Eq. III-4}$$

Thus, equation (Eq. III-3) can be reduced to:

$$I_0(\vec{q}) = 4\pi \int_0^\infty \gamma(r) \frac{\sin(qr)}{qr} r^2 dr \qquad \textit{Eq. III-5}$$

Equation (Eq. III-5) is the most general formula for the scattering pattern of any systems, which obey the above two restrictions. $\gamma(r)$ is the correlation function(Debye and Bueche 1949), or characteristic function(Porod 1951). It can be obtained by the inverse Fourier transform with

$$\gamma(r) = \frac{1}{2\pi^2} \int_0^\infty I_0(\vec{q})\, q^2 \frac{\sin(qr)}{qr} dq \qquad \textit{Eq. III-6}$$

For $q = 0$ and $r = 0$, as the Debye factor equals to unity, equation (Eq. III-5) and (Eq. III-6) are simplified to:

$$I_0(0) = 4\pi \int_0^\infty \gamma(r)\, r^2 dr \qquad \text{Eq. III-7}$$

$$\gamma(0) = \frac{1}{2\pi^2} \int_0^\infty I_0(\vec{q})\, q^2 dq = V_p \Delta\rho^2 \qquad \text{Eq. III-8}$$

For equation Eq. III-7 at $q = 0$, all secondary waves are in phase, so that $I_0(0)$ may be expected to be equal to the square of the total number of electrons in the irradiated volume V_P (volume of one single particle). However, this quantity is experimentally not available (i.e. due to the presence of the beam). So, it should be regarded as an extrapolated value through Guinier approximation or Zimm plot.

III.1.1.2. Guinier's Law and radius of Gyration:

At low q region, i.e., for $qr \ll 1$ the Debye factor $\frac{\sin(qr)}{qr} = 1 - \frac{(qr)^2}{3!} + \cdots$ equation (Eq. III-5) reduces to(Guinier 1939) :

$$I_0(\vec{q}) = 4\pi \int_0^\infty \gamma(r)\,(1 - \frac{(qr)^2}{6} + \cdots) r^2 dr \cong I_0\left(1 - \frac{q^2 R_g^2}{3}\right) \qquad \text{Eq. III-9}$$

As $e^{-x} \cong 1 - x$ equation (Eq. III-9) can be expressed as follows :

$$I_0(\vec{q}) \cong I_0 exp\left(-\frac{q^2 R_g^2}{3}\right) \qquad \text{Eq. III-10}$$

This is the so-called Guinier's law, which is a most useful relation in SAXS analysis for proteins since it allows to obtain R_g and $I_0(0)$ from scattering data in the region of smallest angles without any prior assumption on the shape and internal structure of the particles under investigation. R_g the radius of gyration of the scatterer. For spherical particles with a radius R, the gyration radius is:

$$R_g = \sqrt{\frac{3}{5}} R$$

III.1.1.3. Inter-particle Interference

In the whole discussion in previous section has focused on the scattering of single particle or in very dilute regime (i.e. $c \to 0$). For this kind of solution, it is assumed that the intensities are simply added to give the total scattering pattern, but with increasing concentration the inter-particle interference effects should be expected. This interference comes from two sources: pure geometric influence (impenetrability of the particles) and electrostatic Coulomb interaction.

III.1.1.4. Definition of the structure factor

In the case of a system of a volume V, containing N identical quasi-spherical particles, the scattering intensity is a convolution of the "particle identity" term, $I_0(q)$, (the intra-particle interference), and an inter-particles term that must define all the possible arrangements of all the particles in the solution. This term is represented by the structure factor $S(q)$. Consequently, for non-diluted system the scattering intensity can be expressed as follows:

$$I(q) = \frac{N}{V}.I_0(q).S(q) = \frac{N}{V}.\Delta n_e^2 P(q).S(q) \qquad \textit{Eq. III-11}$$

Where $P(q)$ is the form factor of the particle, corresponding to the scattering intensity of one single particle, but normalized to the number of excess electrons of one particle:

$$P(q) = \frac{I_0(q)}{I_0(0)} = \frac{I_0(q)}{\Delta n_e^2} \qquad \textit{Eq. III-12}$$

For system containing identical quasi-spherical particles of radius R, the structure factor $S(q)$ has been given by Guinier and Fournet (Fournet and Guinier 1955):

$$S(q) = 1 + \overline{\sum_k \sum_{j \neq k} \cos\left(\vec{q}\,\vec{r}_{jk}\right)} \qquad \textit{Eq. III-13}$$

with j and k represent scattering centers in different particles. In order to calculate the structure factor, a radial distribution function (or pair correlation function), $g(r)$ should be introduced. In a system of identical particles, this

function describes how density varies as a function of distance from a reference particle. The function $g(r)$ is a measure of the probability of finding a particle at a distance r away from a particle taken as reference. One property of this function is that:

- For $r < 2R, g(r) = 0$.
- For $r \gg 2R, g(r) = 1$.

Guinier and Fournet used this pair correlation function to express the average term in equation (Eq. III-13), which give the usual form of the structure factor:

$$S(c,q) = 1 + (N/V)\int 4\pi r^2 (g(r) - 1).\frac{\sin(rq)}{rq} dr \qquad \textit{Eq. III-14}$$

The pair correlation function $g(r)$ can then be calculated with help of the statistic mechanics, while the theory for simple liquids(Hansen and McDonald 1969a) can be applied to the colloidal systems.

III.1.1.5. Protein – protein interactions

In the solution, macromolecules interact through weak interaction forces: electrostatic and Van der Waals components but also more complicated forces like hydrogen bonds, hydration and hydrophobic interactions. These forces are medium range, from few angstroms up to few tens of angstroms and each term depends on physicochemical conditions such as pH, temperature, solvent… According to Curtis et al(Curtis, Prausnitz, and Blanch 1998), the interaction potential $U(r)$ for a pair of protein molecules in a salt solution with a center-to-center distance, r, can be expressed by the sum of the following spherically symmetric potentials:

$$U(r) = U_{hs}(r) + U_c(r) + U_{VdW}(r) + U_{os}(r) + U_{SA}(r) \qquad \textit{Eq. III-15}$$

Where:

- $U_{hs}(r)$ is the hard sphere potential related to excluded volume effect. This potential is the expression that molecules cannot interpenetrate. With compact proteins, the excluded volume fraction is equal to vc where $v = 0.74ml/g$ for most proteins.

- $U_c(r)$ is the screened Coulomb potential. With monodisperse solutions, the charges are the same for all particles and the resulting potential is negative.
- $U_{VdW}(r)$ is the Van der Waals attractive potential.
- $U_{os}(r)$ is the depletion potential caused by the excluded-volume effect of salt ions.
- $U_{SA}(r)$ is a potential that take into account the self-association of proteins.

A general structure factor should consider all of the potentials described above. However, studies on the total interaction potential of proteins in salt solution indicate that, depending on the salt concentration, the interaction is dominated by only one or two of these potentials at any particular salt concentration. Therefore, the total potential can be simplified(Tardieu et al. 1999). For the sake of simplicity, $U_{hs}(r)$, $U_c(r)$, $U_{VdW}(r)$ will be written as a hard core Yukawa potential, characterized by three parameters : the diameter of the hard core d , the range σ and the depth J of the potential well.

$$(r) = \begin{cases} +\infty, & r < d \\ J\left(\frac{d}{r}\right)\exp\left(-\frac{r-d}{\sigma}\right), & r > d \end{cases} \qquad \textit{Eq. III-16}$$

For repulsive Coulomb interaction(Derjaguin, Landau, and others 1941; Verwey and Overbeek 1948)

$$J = \frac{\left(\frac{Z_p^2}{d}\right)L_B}{(1+0.5\kappa d)^2} \qquad \textit{Eq. III-17}$$

where $L_B = \frac{e^2}{4\pi\varepsilon\varepsilon_0 k_B T}$ the Bjerrum length, $\kappa = \sqrt{4\pi L_B I}$ is the inverse of Debye-Hückel screening length, I denotes ionic strength and Z_P the charge of one particle.

With large spherical particles in aqueous solvent, the Van der Waals potential can be written as (Israelachvili 1992):

$$U_{VdW}(r) = -\frac{A}{12}\left[\frac{1}{x^2-1} + \frac{1}{x^2} + 2ln\left(1+\frac{1}{x^2}\right)\right] \qquad \textit{Eq. III-18}$$

Where $x = r/d$ and A is the Hamaker constant. This potential diverges when r is equal to the diameter, so a steric protection must be added to suppress this

divergence. For proteins like lysozyme, the Hamaker constant is calculated to be $2.86K_BT$.

For one component fluid, the Ornstein-Zernicke equation(Hansen and McDonald 1969b):

$$h(r_{12}) = c(r_{12}) + \frac{N}{V}\int_V h(r_{13})c(r_{23})d\,r_3 \qquad \textit{Eq. III-19}$$

links the total correlation function $h(r) = 1 - g(r)$ and the direct correlation function $c(r)$. By using a closure relation of Percus-Yevick that links the correlation functions and the pair potential the structure factor can be calculated by:

$$S(q) = \frac{1}{1 - \frac{N}{V}FTc(q)} \qquad \textit{Eq. III-20}$$

Where $FTc(q)$ is the Fourier transform of the direct correlation function $c(r)$.

For dilute solutions, or when only binary interactions are significant, $g(r)$ is directly related to the pair potential (r) :

$$g(r) \cong \exp\left(\frac{-U(r)}{k_BT}\right) \qquad \textit{Eq. III-21}$$

At low q region for $qr \ll 1$ the Debye factor $.\frac{\sin(rq)}{rq} \cong 1 - (qr)^2/3!$, equation (Eq. III-14) is reduced to (Fournet and Guinier 1955; Pötschke and Ballauff 2002) :

$$S(c, q \to 0) = 1 + 4\pi\left(\frac{N}{V}\right)\int\left(\exp\left(\frac{-U(r)}{k_BT}\right) - 1\right).\left[1 - \frac{(qr)^2}{6}\right]r^2dr$$
$$= 1 - 2\phi A_2(1 - \frac{1}{6}q^2d_{eff}^2) \qquad \textit{Eq. III-22}$$

Where:

$$A_2 = \left(\frac{2\pi}{V_p}\right)\int\left(\exp\left(\frac{-U(r)}{k_BT}\right) - 1\right)r^2dr$$

And

$$d_{eff}^2 = \frac{\int\left(\exp\left(\frac{-U(r)}{k_BT}\right) - 1\right)r^4dr}{\int\left(\exp\left(\frac{-U(r)}{k_BT}\right) - 1\right)r^2dr}$$

Since the structure factor at $\rightarrow 0$, $S(c, q \rightarrow 0)$ (i.e. the osmotic compressibility) is also related to the osmotic pressure Π of the solution by (Fournet and Guinier 1955):

$$S(c, q \rightarrow 0) = \frac{RT}{M}\left(\frac{\partial \Pi}{\partial c}\right)^{-1}$$

Where R is the gas constant and Π is the osmotic pressure described by:

$$\Pi = c\,\frac{RT}{M}(1 + A_2 c + A_3 c^2 + \cdots) \qquad \textit{Eq. III-23}$$

The second virial coefficient may be experimentally determined from the extrapolation at the q origin of the scattering curves according to:

$$\frac{1}{S(c, q \rightarrow 0)} = 1 + 2MA_2 c + o(c^2) \qquad \textit{Eq. III-24}$$

In slightly attractive regimes, the extrapolation can be done with Guinier plots or Zimm plots.

Experimentally, the structure factor is obtained as the ratio of the scattering intensity at finite concentration (c) and that at vanishing concentration $(c \rightarrow 0)$. Of course, the scattering intensity should be at first normalized to the concentration:

$$S(c, q) = \frac{I(q)/c}{(I(q)/C)_{c \rightarrow 0}} \qquad \textit{Eq. III-25}$$

This approach has been used extensively for determining phase diagrams and the interactions of proteins in solution as a function of salt concentrations for different salts. As for example, the group of Tardieu et al. where the pioneers in using this approach for determining the possible domain of crystallization of various proteins(Finet et al. 2004). Finet et al. had made a series of experiments with -crystallins and γ-crystallins proteins. The results obtained in terms of scattering curves are presented in the Figure III-3. For the γ-crystallins in a 50 mM Na Acetate buffer at pH 4.5, as well as for the a-crystallins in a 150 mM Sodium Phosphate buffer at pH=6.8, the interactions are repulsive. In both cases, the addition of salt screens the charge, and induces an additional attraction but for the γ-crystallins, the salt is able to induce an attractive regime (the scattered intensity is above the form factor), which is not the case of the a-crystallins for 1 M

salt. The author also shown from this study that the efficiency of the anions follows the inverse (thiocyanate>chloride>acetate), or direct (acetate>chloride>nitrate) order of the Hofmeister series for the γ-crystallins, respectively, the a-crystallins.

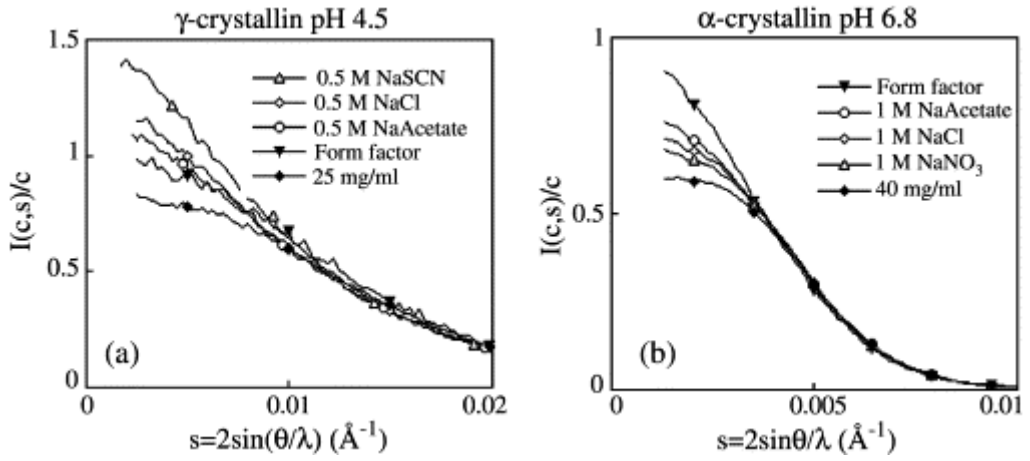

Figure III-3: Scattering curves of γ-crystallins in a 50 mM Na Acetate buffer at pH 4.5 and a-crystallins in a 150 mM Na Phosphate buffer at pH=6.8 with different salts.

Furthermore, in the same study, with the help of equation (Eq. III-22) the authors have determined the second virial coefficient, for various proteins (lysozyme, a-crystallins and γ-crystallins) and for various salts. These data were used to screen the possible region of crystallization of each protein.

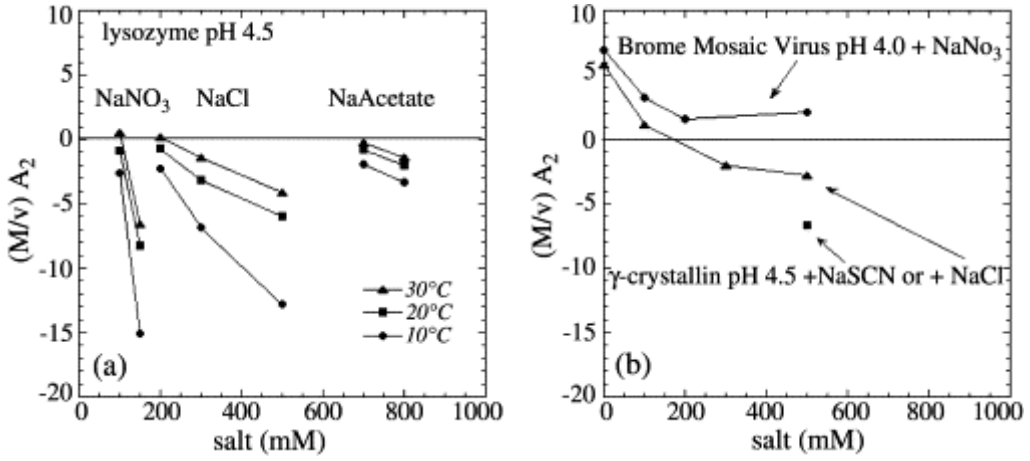

Figure III-4: The second virial coefficient several proteins in various salts

III.1.2. Coupling microfluidics and Small Angle X-Ray Scattering.

During the past decade, given the growing interest of the microfluidic community to use in-situ characterization techniques, significant progress has been made in the use of microfluidic and X-ray scattering. Pollack et al (L. Pollack

et al. 2001; Lois Pollack et al. 1999)pioneered the combination of a simple microfluidic diffusion-based mixer with SAXS measurements in a flow-through cell to measure the dynamic of proteins and RNA folding after a pH jump. In this work, the authors used a pink X-ray beam focused onto the microfluidic mixer to record scattering patterns in the $0.04 - 0.5$ nm^{-1} range. The size of the focused beam onto the chip is 10×40 µm^2. To avoid background scattering from the micro-device, they sealed their microfluidic mixer with silicon nitride membranes as windows for the X-ray beam(Lois Pollack et al. 1999). Greaves and Manz reviewed all the problems related to X-ray analysis on microfluidic device(Greaves and Manz 2005). They also showed successful X-ray fluorescence measurements using on chip X-ray generation. For X-ray scattering measurements, they reported diffraction data of weak intensities using a polycarbonate of bisphenol chip, and using a 1mm wide X-ray beam. The authors also indicated some recommendations in how to perform on-chip X-ray scattering measurements: (i) low absorption materials, (ii) thin chip thicknesses, (iii) high energies for small angles.

Otten et al. have used Kapton windows (polyimide polymer made by DuPont) in microfluidic chips to investigate soft matter by SAXS(Otten et al. 2005). This material is well suited to perform X-ray scattering experiments using intense micro-focused beams, as Kapton is both relatively resistant to the high intensities generated by a synchrotron, and almost transparent to X-rays. From this study, Barrett and coworkers(Barrett et al. 2006) fabricated by laser ablation thin microfluidic devices in Kapton in the Figure III-5. By studying the shear-induced transition of a complex fluid in a microchannel, they have demonstrated during these experiments that both large and small angle X-ray scattering can be performed for structural analysis, in the $0.03 < q < 6$ nm^{-1} range, with a spatial resolution of a few microns.

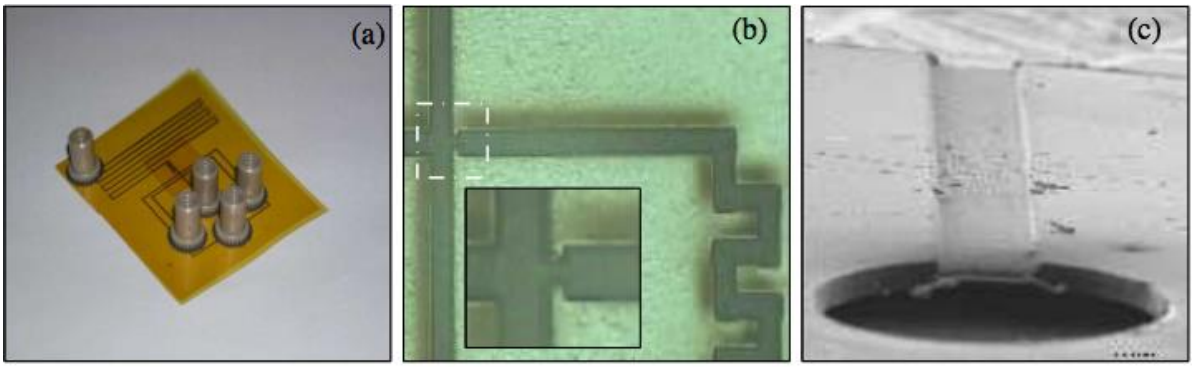

Figure III-5: Photograph of Kapton microfluidic chips compatible with synchrotron radiations developed by Salmon and coworkers(Barrett et al. 2006)

Akiyama et al(Akiyama et al. 2002) and Uzawa et al(Uzawa et al. 2006; Uzawa et al. 2004) have also developed a continuous-flow mixing device to study the folding dynamics of several proteins by SAXS. Panine et al.(Panine et al. 2006) reviewed the status and limitations of these continuous-flow microfluidic-mixing devices for SAXS. Marmiroli et al. (Marmiroli et al. 2009) used a free-jet micromixer to study the kinetics of gold nanoparticle formation using time-resolved SAXS. All these rapid-mixing devices were designed specifically to study folding events or reaction kinetics with sub-millisecond time resolution. Microfluidic devices can also be used to perform very specific functions. For example, Martel and co-workers(Martel et al. 2008; Martel et al. 2008) have studied silk fiber assembly by SAXS in a concentric flow microfluidic cell designed to mimic the geometry of the spinning duct of the silkworm.

Toft et al.(Toft et al. 2008) and La fleur et al.(Lafleur et al. 2011) reported a lab-on-chip high-throughput device for protein structural analysis on a microfluidic front-end named the bioXTAS chip. This chip enabled to automate mixing of samples by diffusion and featured a 500 nL X-ray chamber. Protein consumption was limited to 36 µL, with a total cycle time of 28 minutes.

With the exception of the work of Salmon and coworker(Leng and Salmon 2009), who used millifluidic in-tube geometry, all the microfluidic chips presented above are based on a really expensive or needs complex fabrication procedures and specifics equipment (hot embossing, high energy laser, etching...). The

following publication is a real breakthrough in combination of SAXS experiments and microfluidics.

Brennich and coworkers(Brennich et al. 2011b) have developed a multi-layer microfluidic (see in the Figure III-6) device to follow the dynamics of intermediate filament assembly by coupling microfluidics and SAXS. This multi-layer device prevents proteins from adsorbing to the channel walls by engulfing the protein jet with a fluid layer of buffer. To ensure compatibility with SAXS, the device is fabricated from UV-curable thiol-ene polymer. In that paper, the authors show that the weak background SAXS signal of these devices allow for the detection of molecular scattering profiles at low additional noise. SAXS data were collected at different positions in the jet, corresponding to different salt concentrations, and they reveal distinct differences between the earliest assembly states. They found that the mean square radius of gyration perpendicular to the filament axis increases from 13 nm^2 to 58 nm^2 upon assembly.

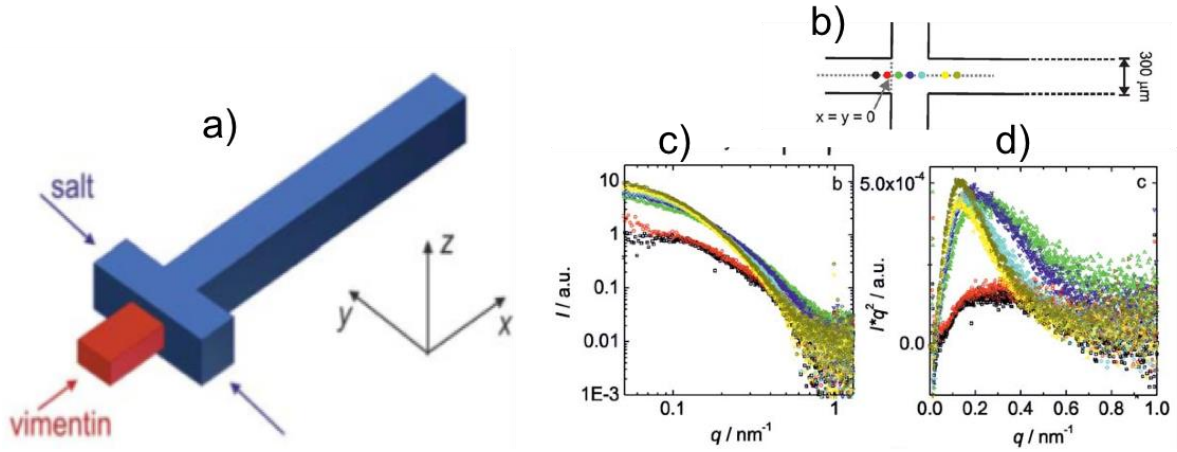

Figure III-6: (a) Sketch of the microfluidic channel. The channel inlet is shallower than the side inlets and the outlet, preventing contact between assembling vimentin and the channel walls. (b) Sketch of the cross and measurement positions. The position 0 is indicated by the gray arrow. (c) Log-log plot of the scattering curves. (d) Kratky plot(Brennich et al. 2011a).

In this direction, Stehle et al(Stehle et al. 2013) have done a very interesting study dealing with the determination of size and concentration of gold nanoparticles in aqueous suspension and also to probe *in situ* formation of gold nanoparticles by coupling droplet microfluidics and SAXS. In their work, the

droplets are generated either in capillary or using a PDMS chips. The droplets are then pumped through a thin-walled detection glass tube that is exposed to the X-ray beam (as shown in the Figure III-7). This experimental setup is inexpensive and presented some flexibilities.

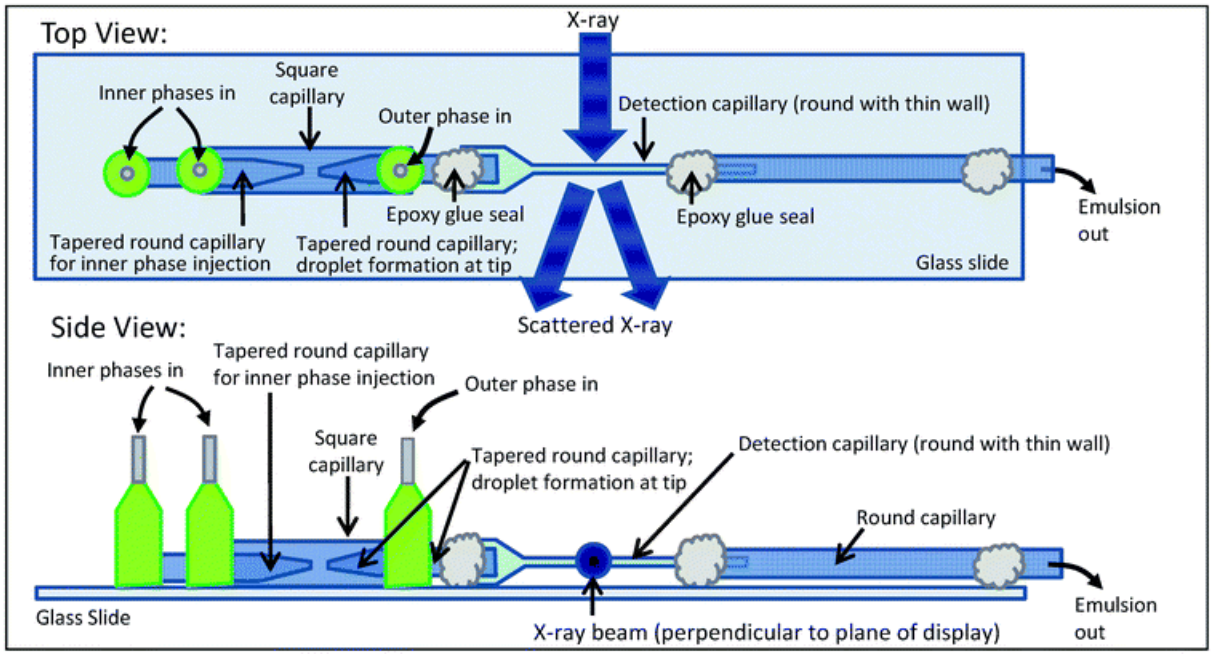

Figure III-7: Schematic of a glass micro- capillary device for on-chip droplet formation and SAXS analysis.

With a droplet formation rate of about 10 Hz and a measurement time of 900s, one SAXS experiment samples an average of about 9000 droplets. When SAXS is performed on a plain water-in-oil emulsion that does not host any additional load inside its droplets, the author observed scattering with $d\sigma/d\Omega \approx 0.05$ cm^{-1} in the range of $q = 0.5 - 2.5$ nm^{-1}, whereas the scattering at $q = 0.1 - 0.5$ nm^{-1} is up to one order of magnitude stronger, as shown in the Figure III-8(diamond). This scattering can be addressed to several parasitic effects, including scattering by the detection micro-capillary, refraction at the droplet interfaces, and scattering due to surfactant micelles in the emulsion. However, if analytes are encapsulated within the droplets, all these contributions superimpose to the analyte scattering in an independent fashion. Thus, the plain-emulsion scattering can be subtracted from the scattering that is obtained from analyte-less emulsions, thereby isolating the scattering of the analyte alone. When this approach is performed on droplets that contain a dilute suspension of gold

nanoparticles, the scattering is about one order of magnitude stronger than the scattering of the plain water-in-oil carrier emulsion in the range of $q = 0.1 - 0.5$ nm^{-1}, whereas the two scattering curves converge at $q > 1$ nm^{-1}, as shown in the Figure III-8 (squares and diamonds). Subtraction of the plain-emulsion scattering from the scattering of the emulsified gold-nanoparticle suspension yields a curve that corresponds to the form factor of spherical nanoparticles with a Gaussian size distribution, as also shown in the Figure III-8 (filled circles).

This approach seems to be successful for characterizing strong scatterer, like gold nanoparticles, but this methodology cannot be applied for polymers or proteins due to the low electronic contrast between the solute and the solvent.

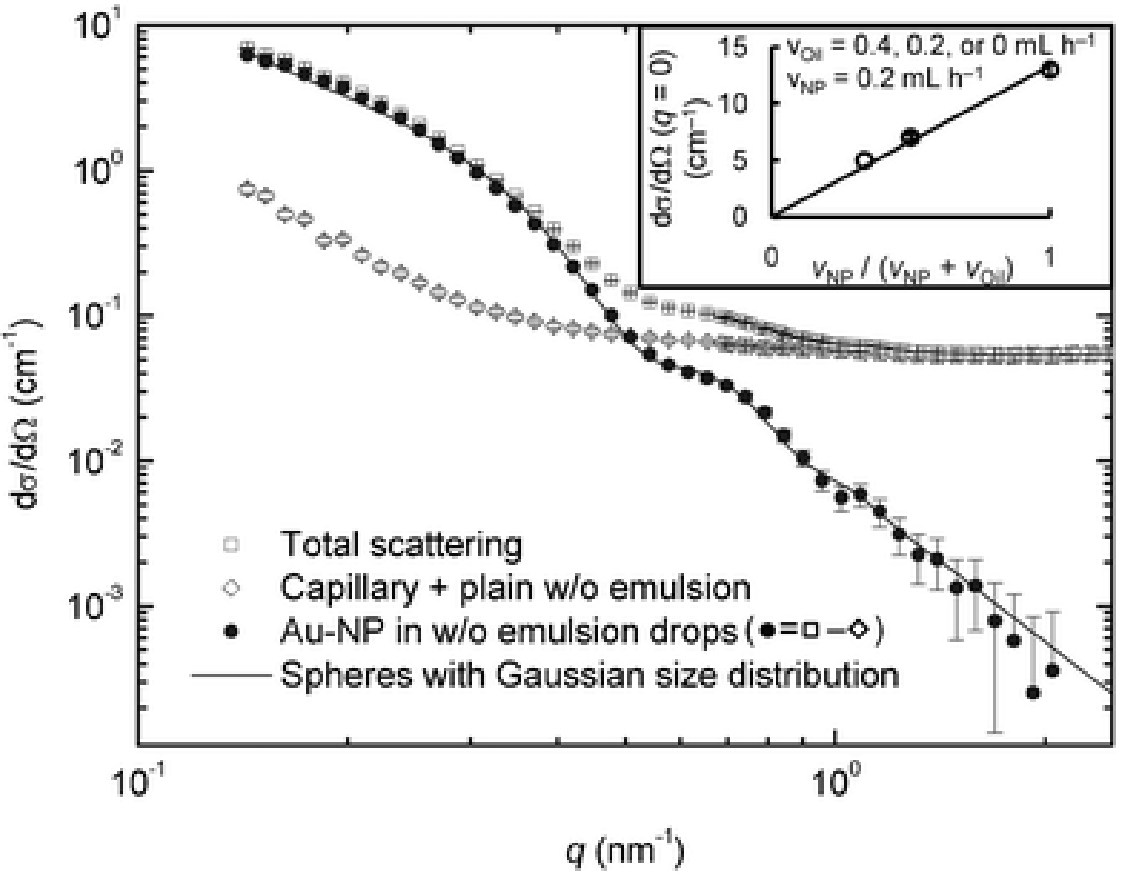

Figure III-8: X-ray scattering curves recorded on gold nanoparticles dispersed within W/O emulsion droplets in a droplet-based microfluidic SAXS implementation.(Stehle et al. 2013). Here, squares denote the raw signal, whereas diamonds denote the signal of plain W/O emulsion. The gold nano-particle scattering is obtained by subtraction of 2 signals above.

III.2. Materials and methods

III.2.1. Microfluidic devices

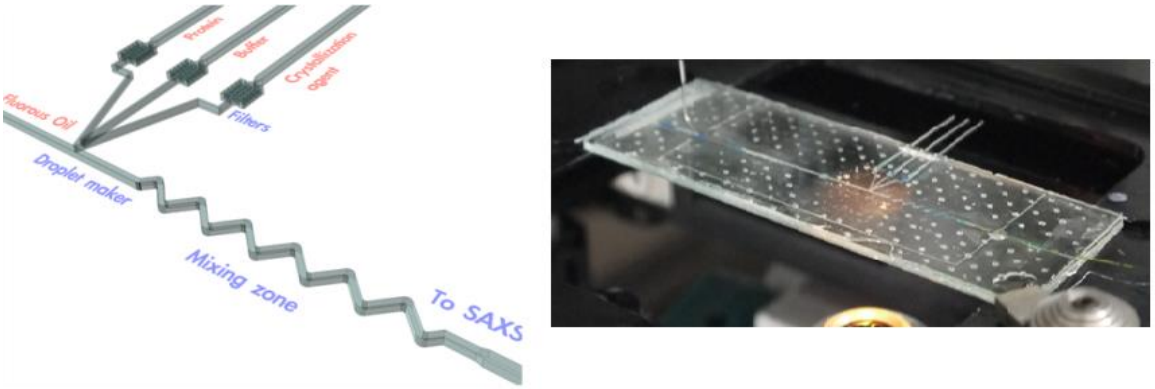

Figure III-9: Design for SAXS microfluidic chip. (Left) the chip design with 3 inlets for protein, buffer and crystallization agent and one inlet for continuous phase, here as fluorous oil. (Right) the real microfluidic chip is fabricated by the soft lithography technique based on NOA 81 material.

NOA 81 microfluidic devices with 200 µm deep, rectangular channels were fabricated using typical soft lithography methods as discussed in the previous section (illustrated in the Figure III-9). Following whole the fabrication process from rigid dry-film master, PDMS casting and soft lithography using NOA 81, the open channel was covered by cover slip (25x50x0.1mm, cover slips Menzel-Glaser, Germany) in order to form a closed channel. Afterward, the surface of NOA 81 channel was modified using FDTS (Sigma- Aldrich) to achieve hydrophobic surface.

III.2.2. Connection to the SAXS sample holder (POD)

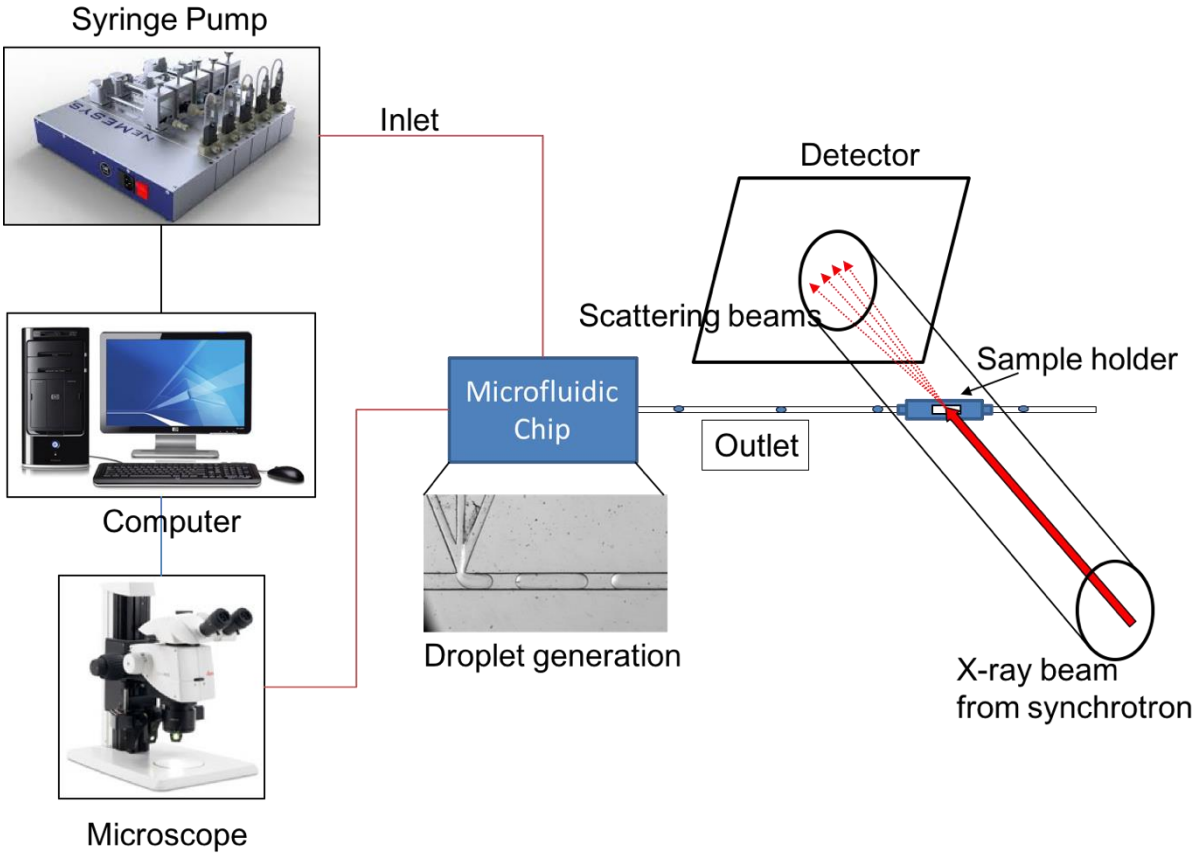

Figure III-10: The whole setup of the combination of microfluidic system and SAXS.

The Figure III-10 shown the whole setup of combination of microfluidic system and SAXS at synchrotron. It is noticed that there were two mains parts: microfluidic part and SAXS part. Firstly, the goal for the microfluidic part was the generation of droplets using a T-junction structure which contains three elements: protein, buffer and salt as the same order respectively. These elements are injected by a syringe pump system (neMESYS) controlled by a computer software in order to obtain the certain ratio among these elements. In addition, the generation process was observed by a microscope (Leica M250C) to check again the stability of the flow rate, the distance between droplets and the droplet size… After their formation in microfluidic chip, droplets are transferred to SAXS via a capillary which is connected with SASX sample holder, called POD. The POD has windows that the X-ray beam can expose to a specific region of the capillary.

The connection between the microfluidic chip and the SAXS sample holder were made by connecting capillaries (with internal diameters ranging from 250 to 300 µm) to the exit of the microfluidic chip. The capillary was then hermetically sealed to the pod in order to keep vacuum level around the capillary required for high-quality SAXS data (illustrated in the Figure III-11). With this setup, SAXS experiments can be performed at a residual pressure of about 10^{-2} mBar. The capillaries were made of fused silica (ID 320 µm, OD 435 µm, Postnova analytics) or Kapton (ID 320 µm, Good-fellows). For the case of fused silica capillary, the capillary was glued to POD directly from the exit of microfluidic chip, hence droplets can be easily transferred to POD without leakage.

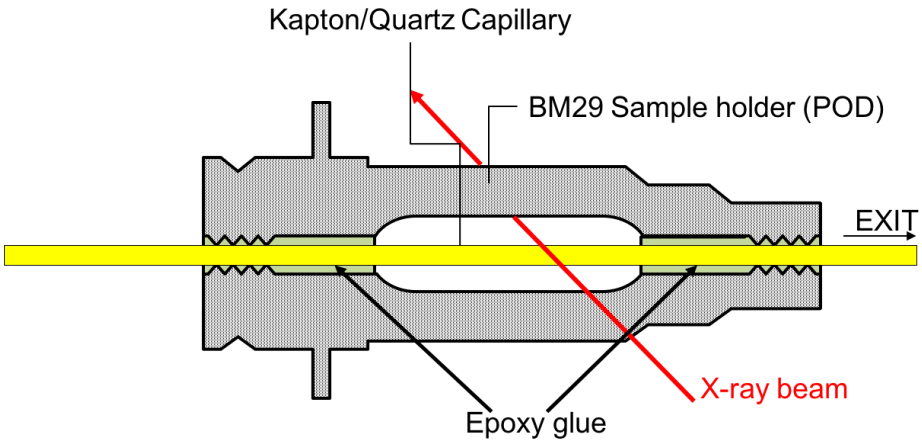

Figure III-11: Structure of sample holder (POD) and glued Kapton/Quartz capillary inside.

In another case with Kapton capillary, the capillary was glued to POD as shown in the Figure III-11. However, in order to connect to microfluidic chip one more connection device was required. The Figure III-12 shown the connection of two different capillaries : glass and Kapton. Normally, the glass capillary is glued at the outlet of microfluidic chip with ID 300 µm and OD 360 µm and the Kapton capillary is glued inside the POD. The connection (Upchurch) contains two parts: two crews and the body which presented in the Figure III-12. In order to be sure that no leakage happened, the sleeve tubes were placed inside. When the two crews went in the body, the tips of crews kept tightly the sleeve to two capillaries and made them in the same position. By testing the connection, the droplets are moved to connection and no droplet breaks is observed.

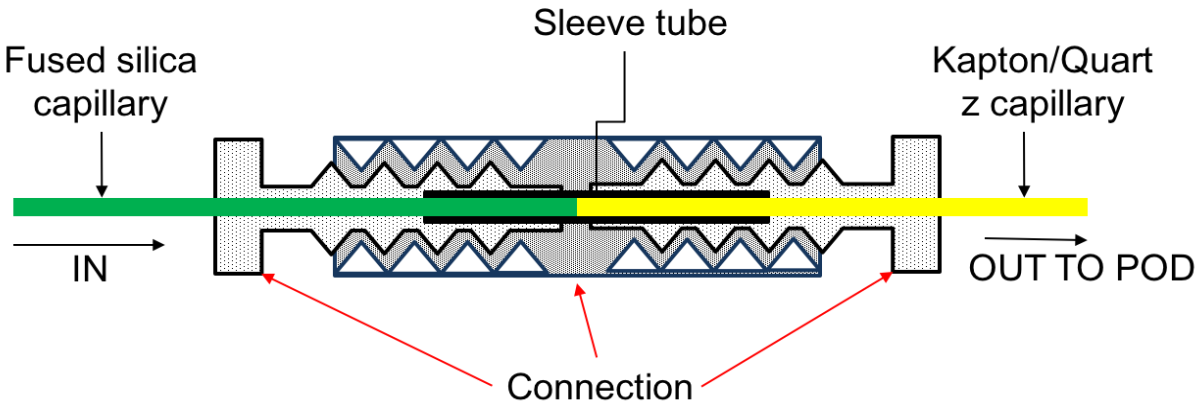

Figure III-12: The connection of glass capillary from the outlet of microfluidic chip and Kapton capillary to POD

To deliver the fluids to the chip, 1mL syringes (Hamilton, USA) were connected with the microchip via glass capillaries with inner diameter of 250 µm and outer diameter of 365 µm (Postnova analytics, Germany). The flow rates were controlled by the high precision syringe pumps neMESYS from Cetoni, Germany.

Synchrotron sourced SAXS measurements were performed on the beamline BM 29 at the European Synchrotron Radiation Facility (ESRF) in Grenoble, France. The working energy of BM29 is set between 7 and 15 KeV. The two-dimensional SAXS patterns were recorded with a 1M Pilatus detector, as shown in the Figure III-13. The experimental X-ray wavelength and the sample to detector distance were respectively 0.0991 nm and 2.87 m, covering a range of $0.03 - 4.5$ nm^{-1} for the scattering vector $q = 4\pi \sin\theta/\lambda$ and the beam cross-section is 90 µm x 165 µm. The sample in capillary can be moved horizontally and vertically by a few millimeters with a precision of ten microns.

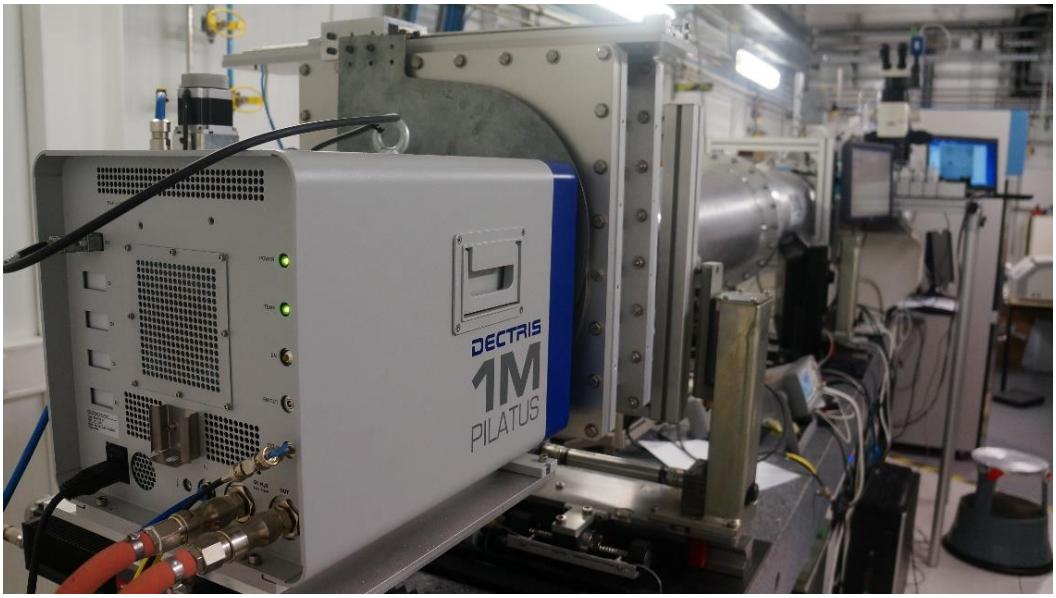

Figure III-13: Pilatus 1M at the moment is the best detector for solution SAXS- Beamline 29 ESRF Grenoble - France

Thanks to microfluidic design, water-in-oil droplets containing the protein, buffer and crystallization agent were formed and carried by fluorous oil containing surfactant in order to stabilize the droplets interface. In our work, two different surfactants were used: 1H,1H,2H,2H-Perfluorooctanol (PFO – $C_8H_5F_{13}O$) (Sigma) and a lab-made tri-block copolymer (PFPE-PEG-PFPE). Both surfactants were dissolved at a precise concentration in fluorous oil Krytox (DuPont) to make stable droplets without affecting biological stability and interactions between proteins.

Three different proteins with different molar mass, oligomeric states, isoelectric point and crystallization agents were used in this study, Lysozyme (Sigma), Rasburicase (Sanofi). Firstly, in order to validate the setup of SAXS-microfluidic and to choose the more suitable surfactant that stabilizes droplets but does not interact with proteins, an active and native tetrameric form of Rasburicase was injected in droplets with Tris buffer at pH=8.0. After validation of the suitable surfactant to use, Lysozyme was used as a model protein to measure interaction between proteins in solution.

III.2.3. Real time image analysis and data acquisition

In this device, the droplets pass through the detector and if the SAXS images are acquired "continuously". Since the exposure time should be reduced to decrease radiation damage, a high number of images is achieved. The recorded SAXS curves result from the contribution of the scattering signal of the continuous phase, the interface, and the protein inside the droplet. As proteins are weak scatterer, the acquired SAXS signal of protein solution is very close to the one obtained for the continuous phase and of the interface as shown in the Figure III-14.

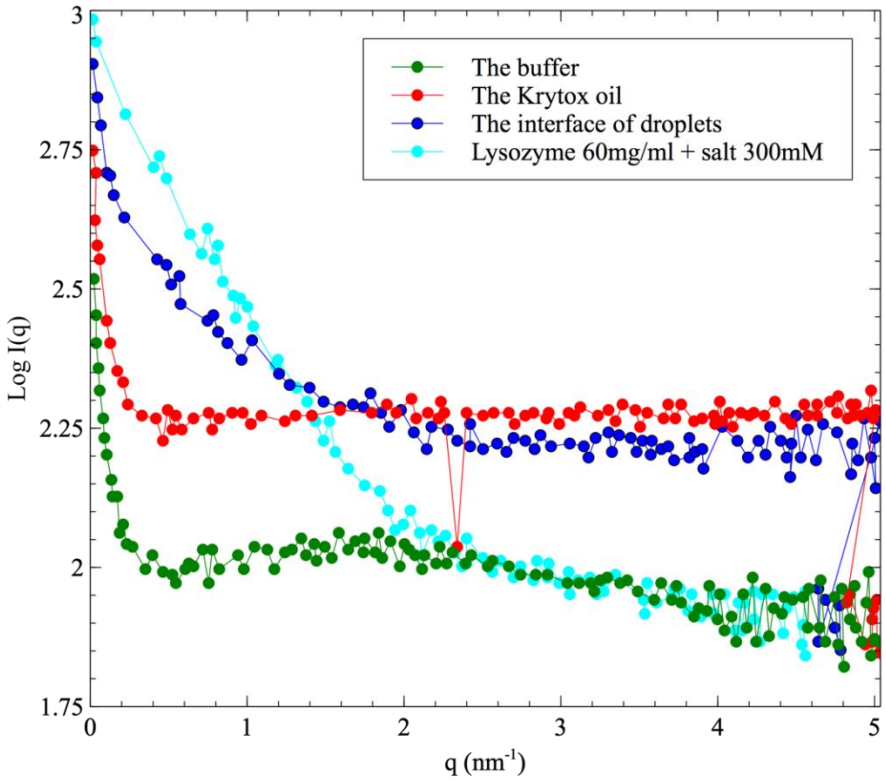

Figure III-14: The scattering signal of the first set of experiment. Lysozyme 60mg/ml + salt 300mM(cyan), the interface of droplets (blue), the oil (red) and the buffer (green).

Consequently, the approach of Stehle et al (Stehle et al. 2013) cannot be used and the SAXS signals have to be acquired and/or treated only with the aqueous solution.

To acquire clean SAXS data (comparable to the one obtained with 1.5 mm capillaries) it is necessary to average the data on 3 to 10 SAXS curves. If the data are acquired continuously, it is necessary to acquire up to 300 frames per

experiments to get enough data. This approach gives satisfactory results, but data treatment is really time consuming. In addition, when using continuous data acquisition, the capillary and the oil are exposed to intense X-ray radiation which can induce radiation damage of the capillary surface coating. To solve these problems, an acquisition system based on a real time image treatment software has been developed. This "macro" developed using open CV and Matlab, allows synchronizing the SAXS image acquisition on the Pilatus camera, the shutter that allows that open or close the X-ray beam and the detected droplets. A principle scheme of the acquisition setup is given on Figure III-15.

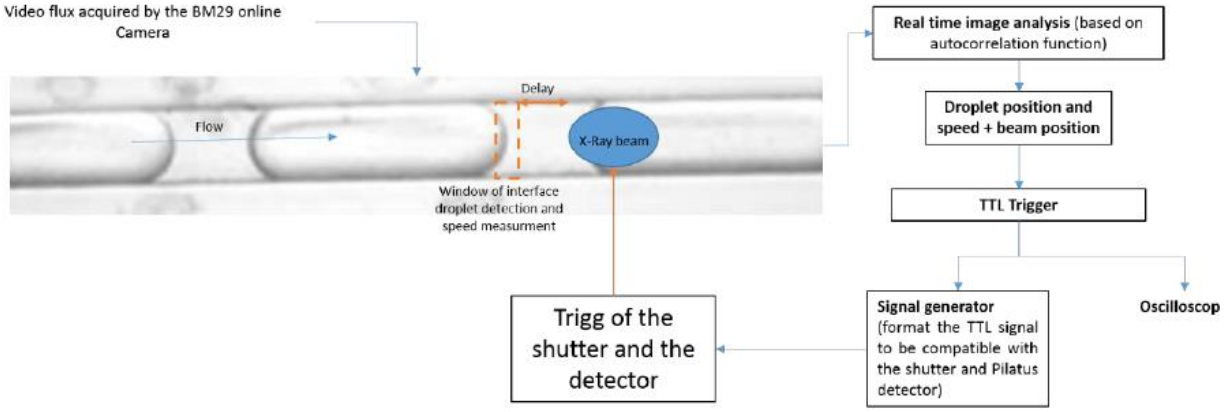

Figure III-15: Scheme of the synchronization process: Once the droplets are detected, knowing the speed of each droplet, the beam position and the distance between the window of detection and the beam position, a delay time is calculated (compatible with the opening and closing time of the shutter) and the acquisition is triggered. This approach allows us to get only the SAXS data within the droplets.

The principle of the image treatment function is based on the fact that in microfluidic system, all the generated droplets have the same interface (either at the nose or at the tail of the droplet). Consequently, by using a simple autocorrelation function in Matlab or developed in open CV (to accelerate the procedure), it is possible to detect all the droplets passing in a defined position on the capillary. By defining different position inside the capillary, this approach allows determining the number of detected droplets, their instantaneous velocity, and the time when they reach the detection area. When this area is reached by a droplet, a transistor-transistor logic (TTL) signal is send to the fast shutter of the beam line and to the Pilatus camera. The TTL signal is generated using a USB-RS232 converter (FTDI232, Future Technology International Device Ltd) able to

send a 1bit signal of 3V, compatible with the Pilatus and the shutter. The measured timing of the detection (i.e. between the detection to the generation of the signal) is from 10 to 15ms allowing to track more 40 images per second (which is the maximum frame rate of the Proscillica camera mounted on the beamline).

III.3. Results and Discussion

III.3.1. Validation of experimental setup

III.3.1.1. Selection of the capillary materials

In order to test the influence of the capillary material on SAXS data, two kinds of capillaries were tested: Kapton capillaries and surface modified quartz capillaries. The inner diameter of the capillaries was 250 µm. Their scattering signal is shown in the Figure III-16.

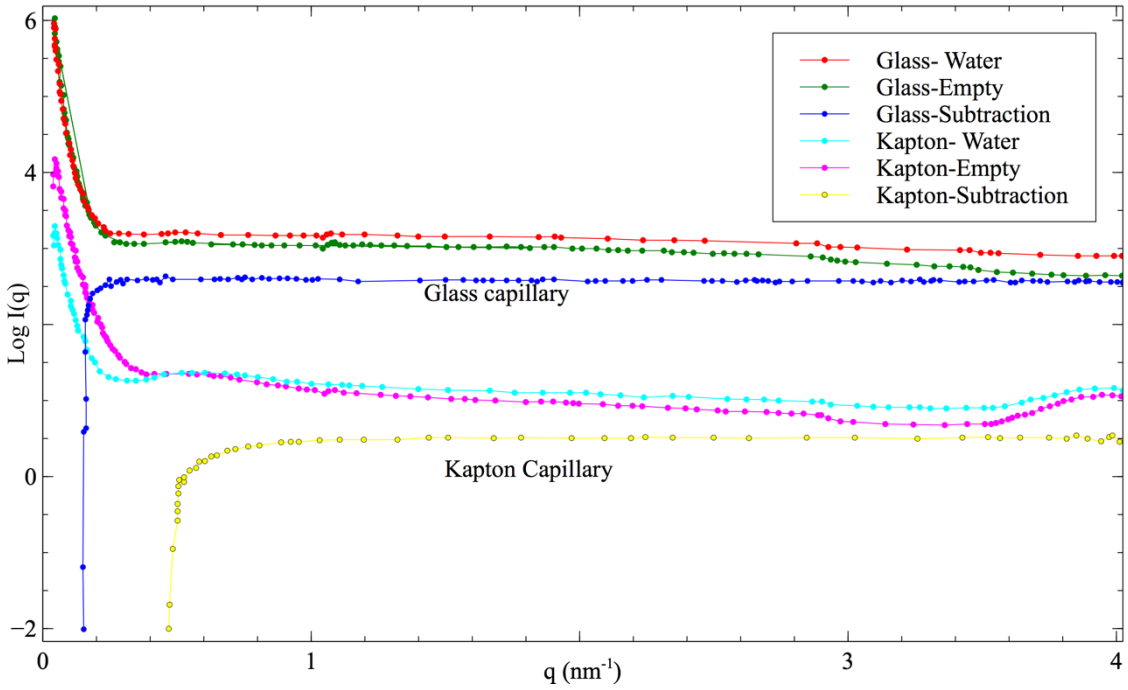

Figure III-16: The scattering signal of two different capillaries which were glued in the POD: Glass and Kapton capillary.

The own scattering signal of Glass/Kapton capillary was determined by subtraction the scattering signal when capillary filled with and without water. The important result here is that both capillaries do not show the same adsorption characteristic. The minimum q-range are 0.1 and 0.5 for glass and Kapton

respectively. It should be noted that for quartz capillaries, the surface has been modified by silane solution using Sigmacote (Sigma-Aldrich) in order to render the surface hydrophobic and thus compatible with water in oil droplets. It is also important to notice that for Kapton, the features observed at low and high q disappear after subtraction. With both capillaries, a standard protein, BSA (bovine serum albumin), was tested with success in the glass capillary without oil in static for scattering/absorption ratio. For the rest of the study, quartz capillaries were used because of the better resolution obtained at low angles.

III.3.1.2. Selection of the surfactant and oil

The objective of the first experiment was to validate the pertinence of our experimental set-up. Indeed, most of the compounds used in these SAXS experiments (protein, surfactant, oil …) can be damaged by the X-ray beam. Therefore, a good combination of compounds in order to have a decent SAXS signal and to avoid radiation damage is required. Moreover, the surfactant can interact with the protein within the droplet and probably denature it, so we also had to be sure that the surfactant is inert for the protein. For this experiment Rasburicase, a homo-tetrameric protein at a concentration of 15 mg/mL in Tris buffer at pH = 8 was used.

All classical fluorous oil used in microfluidic experiments (FC77, FC40, perfluorodecalin, HC220…) were irradiated in the same conditions as of the future experiments. Unfortunately, none of these oils were compatible with the high energy of X-ray generated at BM29. Indeed, after few millisecond of exposure, radiation damage of the oils was observed even in flow conditions. Radiation damages of the oil generate free radicals that interact with the surface of the capillary (i.e. react with the silane group at the quartz capillary surface or adsorb on the surface of the capillary). The modification of the surface capillary induced modification of the surface properties of the capillary and generated different SAXS signal for the same experiment. After testing of several commercial fluorous oils, it was found that Krytox GPL 100 (DuPont) oil as the best compromise between radiation damage and physicochemical properties.

The first experiment was performed with PFO at 2% wt. in Krytox GPL100. The corresponding SAXS curves describing the scattered intensity as a function of the

scattering vector are presented in the Figure III-17(top). The black dots correspond to our experimental results whereas the green and red curves are respectively the scattering intensities obtained from atomic coordinates with CRYSOL which invented by Svergun et al. (D. Svergun, Barberato, and Koch 1995) for the tetramer and the dimer of Rasburicase (*1r51.pdb*). Finally, the blue curve obtained with OLIGOMER (Vivares and Bonneté 2002) which represents the best fit for our experimental result shows that the protein solution in the droplet is a mixture of 58% tetramer and 42% dimer. Under these experimental conditions (oil, surfactant), Rasburicase is in either native tetrameric form or completely dissociated dimeric form. It means that the surfactant at the interface of the droplet may interact with tetramers of Rasburicase. Some tetramers are dissociated into two dimers and thus, we can affirm that the PFO denatured proteins that limited its use for our microfluidic experiments.

To avoid denaturation and interaction of surfactant with proteins in droplets, we synthetized a biocompatible surfactant, a tri-block copolymer PFPE-PEG-PFPE that has been described somewhere else (D. Svergun, Barberato, and Koch 1995) and used it at a concentration of 2% wt. in Krytox GPL100. SAXS experiment with Rasburicase is presented in the Figure III-17 (bottom). With this surfactant, it appears that the CRYSOL curve for the tetramer of Rasburicase perfectly fits our experimental data, which means that the protein is not denatured/dissociated and therefore that the surfactant is inert for the protein.

Moreover, this shows that thanks to our microfluidic set-up, we can obtain experimental SAXS data that are in good agreement with crystallographic structures of macromolecules in solution. PFPE-PEG-PFPE and Krytox GPL100 have been proved as a good combination of compounds to study protein structure in droplets as they behave exactly as in usual SAXS experiments in micro-volume.

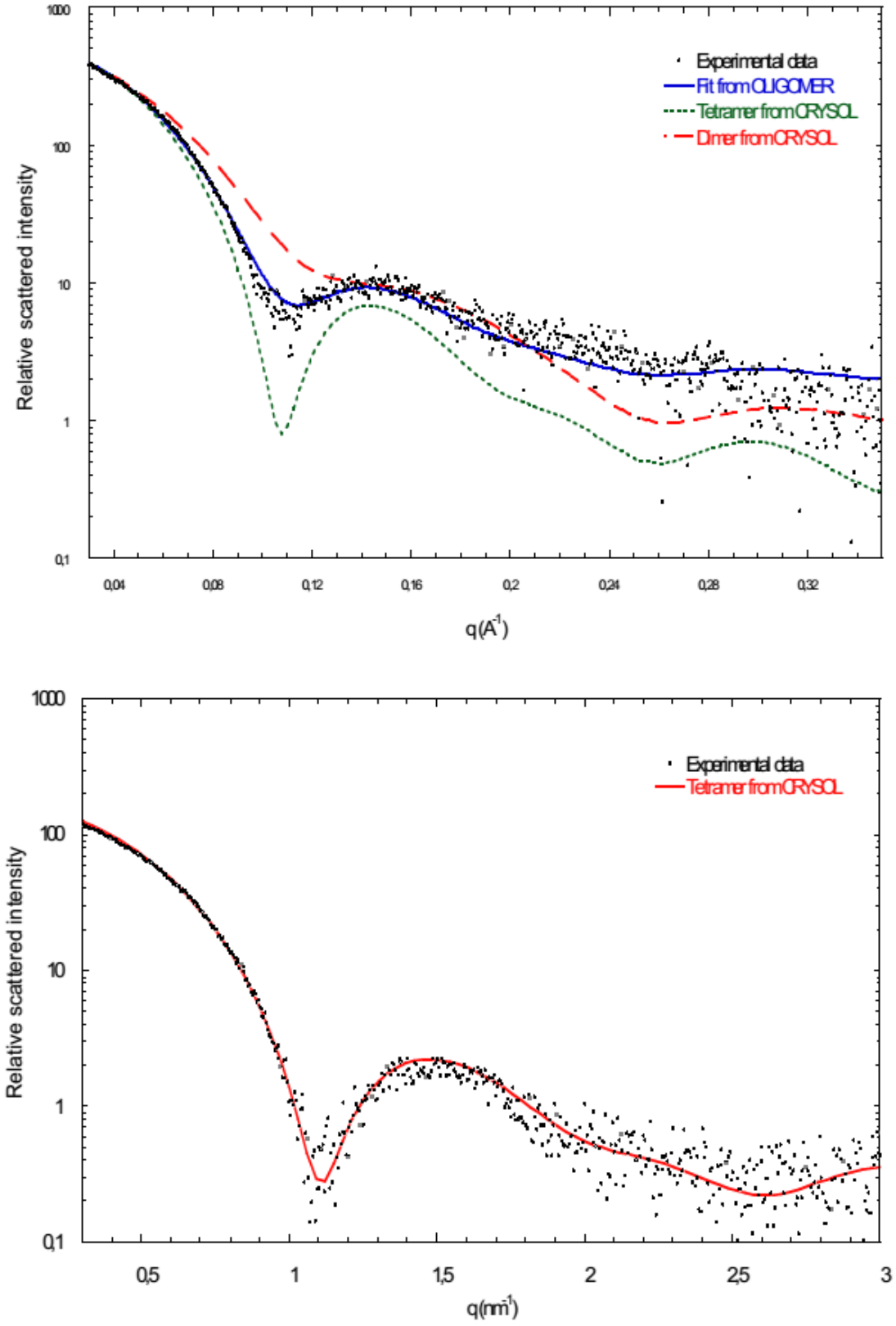

Figure III-17: SAXS curves of Rasburicase in the presence of surfactant PFO and triblock copolymer. (top) with PFO surfactant, the black dots are our experimental data, green

and red curves are scattering curves from atomic. (bottom) with triblock surfactant, the red line is the scattering signal of tetramer of Rasburicase (1.5r1.pdb).

III.3.2. Study of weak interaction for crystallization conditions

Weak interactions between protein molecules in solution was suited by varying the concentration of crystallization agent. This experiment was done with the Lysozyme at a stock concentration of 130 mg/mL with a sodium acetate buffer at pH=4.4. The mixture of the oil and surfactant were the same as previously, respectively Krytox GPL100 and tri-block copolymer PFPE-PEG-PFPE. We utilized NaCl as crystallizing agent at a stock concentration of 2 mol/L. The droplets generation structure is Y-junction with the oil in the left channel, salt, buffer and protein in the top left, top middle and top right channel respectively. One of the advantages of the design of this microfluidic device is that we can screen several concentrations of crystallization agent (e.g. salt) just by changing the flow rate of the incoming solutions. For example, if we want to increase salt concentration, we have to increase salt flow rate but we also have to decrease buffer flow rate to generate droplets of the same volume. The following Table III-1 describes the different experimental conditions. The SAXS curves of the scattering intensity as a function of the scattering vector are represented in the Figure III-18.

Table III-1: Flow rates of the stock solutions and concentration of different compounds in droplets with Lysozyme, buffer and salt.

Flow Rates (µL/min)				Concentrations	
Oil	**Lysozyme**	**NaCl**	**Buffer –NaAc**	**Lys(mg/mL)**	**NaCl(mmol/L)**
4	0.5	0	2.5	21.7	0
4	0.5	0.15	2.35	21.7	100
4	0.5	0.3	2.20	21.7	200
4	0.5	0.45	2.05	21.7	300
4	0.5	0.6	1.9	21.7	400
4	1.2	0	1.8	52	0
4	1.2	0.15	1.65	52	100
4	1.2	0.3	1.5	52	200
4	1.2	0.45	1.35	52	300
4	1.2	0.6	1.2	52	400
4	2.0	0	1.0	86.7	0
4	2.0	0.15	0.85	86.7	100
4	2.0	0.3	0.7	86.7	200
4	2.0	0.45	0.55	86.7	300
4	2.0	0.6	0.4	86.7	400

The relation between the scattered intensity and A_2 the virial coefficient is discussed previously. The coefficient can describe the interaction state between the macromolecules. If $A_2 > 0$, macromolecules are in a repulsive state and if $A_2 < 0$, the interactions are attractive.

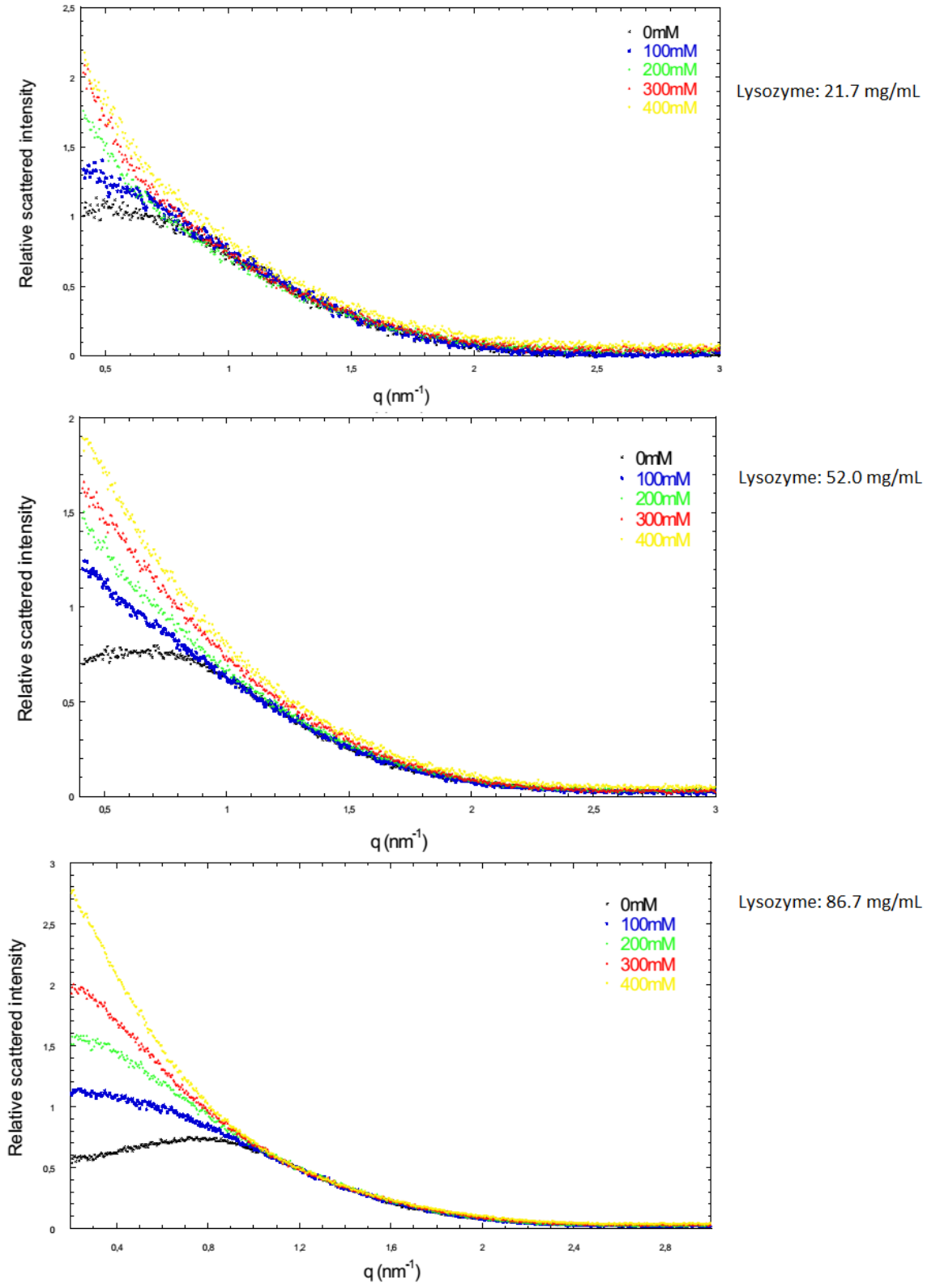

Figure III-18: SAXS curves for lysozyme with increasing crystallization agent concentration from 0 to 400 mM with 3 values of lysozyme 21.7, 52 and 86.7 respectively.

To go further into details, we can calculate this second virial coefficient A_2 for the different salt concentration. In fact, for a given SAXS curve with fixed protein and salt concentration, we can estimate the intensity when the scattering vector tends to zero thanks to Guinier plot as shown previously. The Guinier approximation can be re-written:

$$I(c \to 0, q) = I(0,0).exp\{-(4\pi^2/3){R_g}^2 q^2\}$$

This approximation is only valid at low scattering angles (i.e. $qR_g < 1.3$). By plotting $Ln(I) = f(q^2)$ for values of q such as $qR_g < 1.3$ we can estimate the intensity when the scattering vector tends to zero $I(c, q \to 0)$. An example of Guinier plot for lysozyme concentration of 52 mg/mL and salt concentration of 300 mM is shown in the Figure III-19.

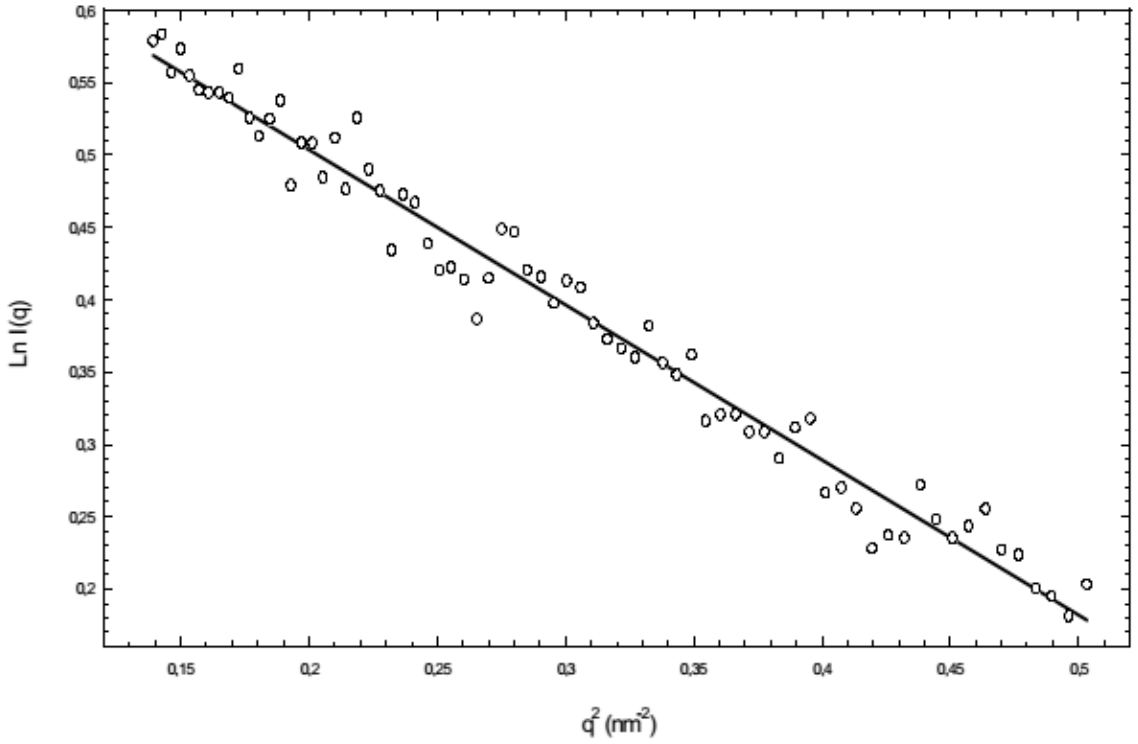

Figure III-19: Example of the Guinier plot for lysozyme at 52 mg/mL and salt about 300 mM

For a given salt concentration, the approximation can be applied for each protein concentration and plotted the scattered intensity at q-origin $I\,(c, 0)$ as a function of the protein concentration. These results are shown in the Figure III-20. By extrapolation, this graph gives access to the value of the scattered intensity at zero angle and at the zero protein concentration, the form factor $I\,(0,0)$.

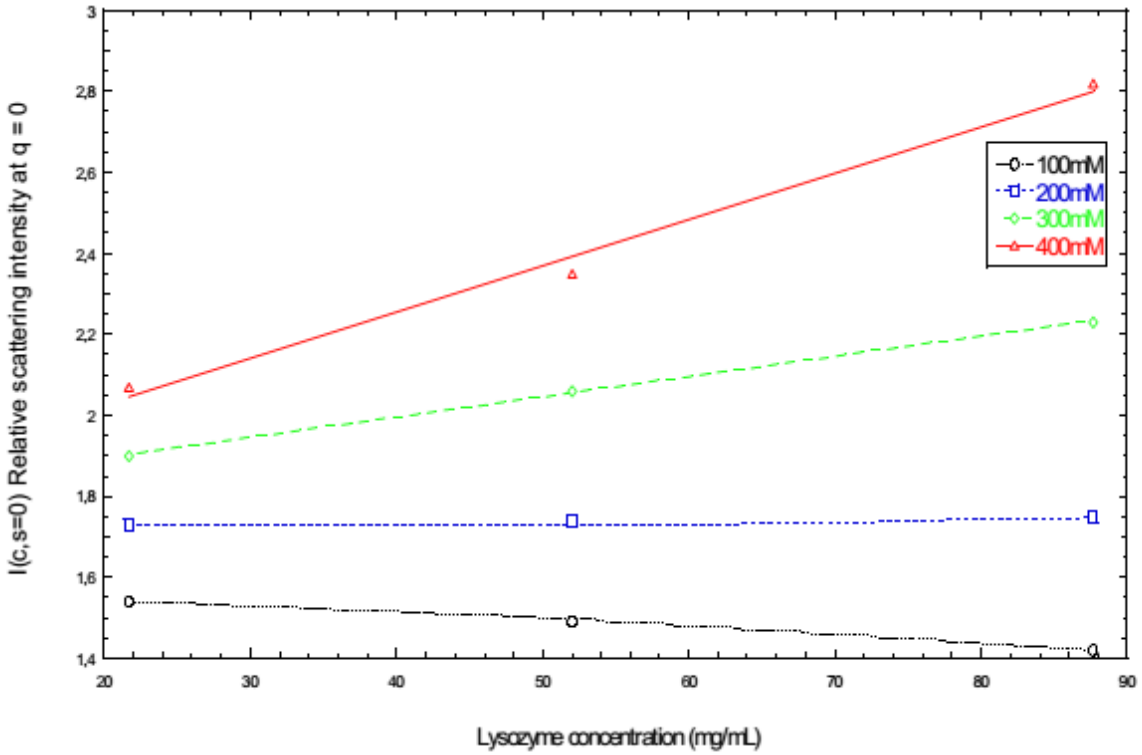

Figure III-20: Scattering intensity at the zero angle as a function of lysozyme concentration for different salt concentration. It can be extrapolated to give access to the value of the form factor $I(0,0)$.

Once we know the value of this form factor, we can get back to the previous relation:

$$I(c,0) = I(0,0) \times \frac{1}{1 + 2MA_2c}$$

At a given salt concentration, if we plot $\frac{I(0,0)}{I(c,0)} - 1$ as a function of the protein concentration c, we are supposed to have a straight line whose slope equals $2MA_2$ and thus give access to the value of the second virial coefficient A_2. These curves are illustrated in the Figure III-21.

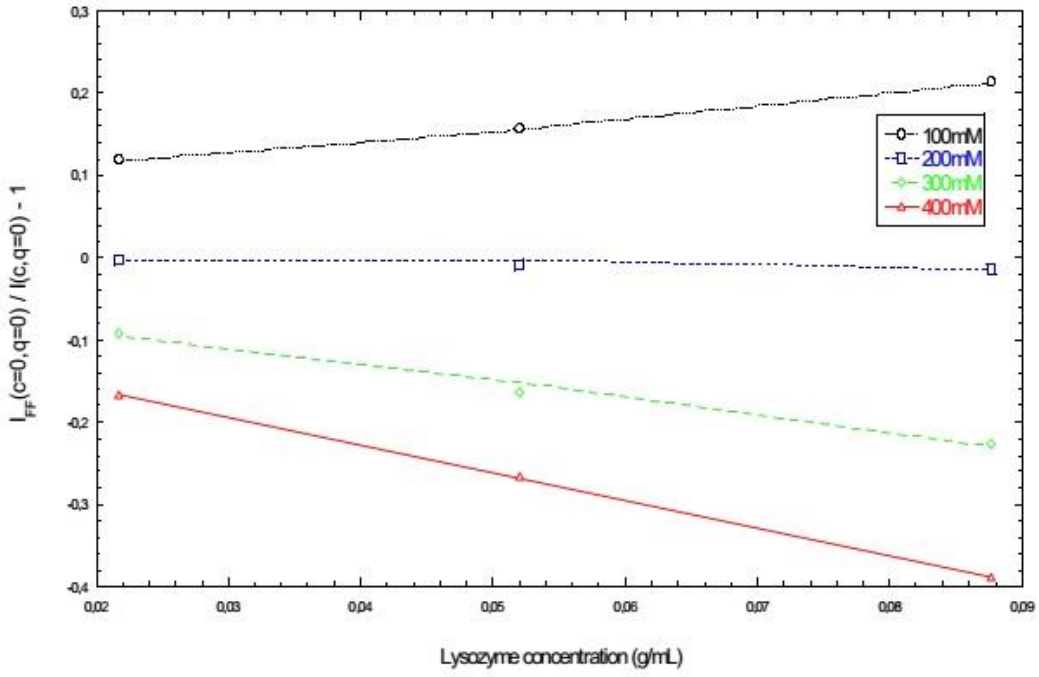

Figure III-21: Linear regression for different salt (NaCl) concentration: 100, 200, 300 and 400 mM/L. The slope of straight line equal $2MA_2$.

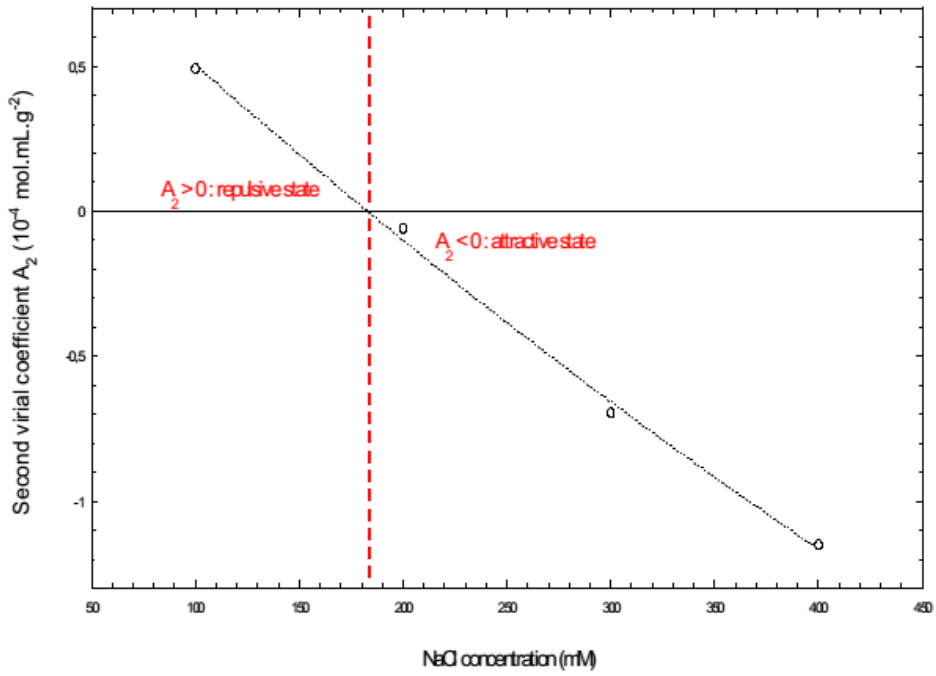

Figure III-22: Variation of second virial coefficient for Lysozyme as a function of salt (NaCl) concentration.

We finally have access to the second virial coefficient A_2 values for each crystallization agent concentration and can plot them as a function of the

concentration to know the interaction state between molecules as shown in the Figure III-22. The interactions between proteins molecules have been investigated by several researcher groups (Ducruix et al. 1996; Bonneté et al. 2004). This graph highlights the fact that without salt, because of the positive charges net around lysozyme molecules at pH 4.4, the protein in a repulsive state. The addition of salt, the protein interaction potential changes smoothly from repulsive to attractive state due to a progressive screening of the charges at the Lysozyme surface. The attractive state was illustrated in the plot for salt concentration above 180 mM/L.

These results are in really good agreement with previous results obtained in micro-batch volumes (Bonneté, Finet, and Tardieu 1999) that have been achieved quickly and with a few of products. Therefore, it is concluded that obtaining a good data quality with our experimental microfluidic setup allows studying the interactions between macromolecules for crystallization condition screening via second virial coefficient measurements.

III.4. Conclusion and perspectives

In this work, the combination of droplet based microfluidic system and SAXS is applied successfully for characterization of two proteins: Rasburicase and Lysozyme. In the first experiment, the coupling between microfluidic set-up and SAXS was validated underlining the fact that the protein in droplets have the same behaviours as in usual solution and all the data in the literature can be used as reference. In addition, in this first set of experiment, other serious technical problems were solved. For instance, some kinds of capillary which used for POD were tested to obtain the high quality of data (less noise from the wall of capillary and without radiation damage). In the results, for further experiments the Sigmacote modified surface glass capillary was chosen because of its better resolution at lower angles. Moreover, the tri-block copolymer surfactant also shown that was the good surfactant (i.e. no denatured protein was observed) which presented no interaction with the protein molecule within droplets.

For the second set of experiment, the interaction of Lysozyme molecule in the presence of salt (NaCl) at various concentration was studied using SAXS. The results shown that the interaction between protein molecule in the solution can be described by the second virial coefficient A_2. If $A_2 > 0$, macromolecules are in a repulsive state and if $A_2 < 0$, the interactions are attractive. At the beginning, the protein solution without salt, the positive charges net around lysozyme molecules at pH 4.4, the protein in a repulsive state. By adding of salt (i.e. increasing the ionic strength), the protein interaction potential changes smoothly from repulsive to attractive state.

Once again, the combination of SAXS and microfluidic have been shown the promised ability for studying the behavior of proteins as well as their interaction. Besides, because of system's success, more perspectives for technique as well as methodology can be expected in the future. Firstly, in order to improve the precise and high quality of SAXS data, better quality of capillary in the POD will be applied (e.g. the wall of capillary thinner is better to limit noise). The synchronization process will be improved more precisely to achieve the SAXS signal of protein within droplet.

In the further experiment, the interaction of protein molecule in the nucleation/crystal growth process will be more focused. By integrating the temperature control system to microfluidic chips, the temperature of the whole system can be adjusted easily. By this method, the droplets containing three components can be reached to critical points by decreasing and keeping at low temperature before send to shoot. By this way, the scattering signal for each moment of nucleation/crystal growth can be observed.

Chapter IV

DEHYDRATION OF PROTEIN SOLUTION

IV.1. Introduction

In the previous chapter, the protein-protein interaction in the presence of crystallization agents (e.g. salt) was characterized using Small Angle X-ray Scattering method. Interactions of colloids in solution can also be studied through the determination of the equation of state which relates the osmotic pressure to the volumetric properties of the solution. The equation of state of colloids is of paramount importance in the industry (food, paint, chemistry, cosmetics…) since it defines the operating conditions of several processes such as drying, filtration mixing… One quite common, but not widely spread yet, approach for determining this thermodynamic property of the polyphasic system is based on the exchange of solvent by dialysis between the dispersion under study and a reservoir with a known osmotic pressure (or water activity if the solvent is water). In particular, this technique has been widely used for studying the behavior of casein(Bouchoux et al. 2009; Bouchoux et al. 2010; Bouchoux et al. 2014), of lysozyme (Coralie Pasquier et al. 2016; Grobelny et al. 2014), and ovalbumin(C. Pasquier et al. 2012) under compression. However, despite its relevancy, this technique suffers from several drawbacks : the sample volume of the dialysis chamber (few milliliters), and very permeation flux through the membrane (due to a no optimized surface volume ratio). In this chapter, a novel method to determine the equation of state of a model protein in solution is proposed. This methodology is based on the mass transfer between two partially miscible fluids. In order to understand this new approach, it is necessary to briefly introduce the experimental setup: In a microfluidic platform, monodispersed droplets of the dispersed phase are generated in a continuous phase. Here, the dispersed phase is an aqueous solution of protein (lysozyme) and the continuous phase is an organic solvent (1-decanol) in which water is partially miscible and the protein is not. As soon as the droplets are generated, mass transfer occurs, and water is continuously dissolved in the continuous phase, considered as an infinite reservoir, until a thermodynamic equilibrium is reached.

The basic principles of droplet dissolution process for two cases, (a) a pure liquid droplet and (b) a multicomponent droplet are shown in the Figure IV-1 below.

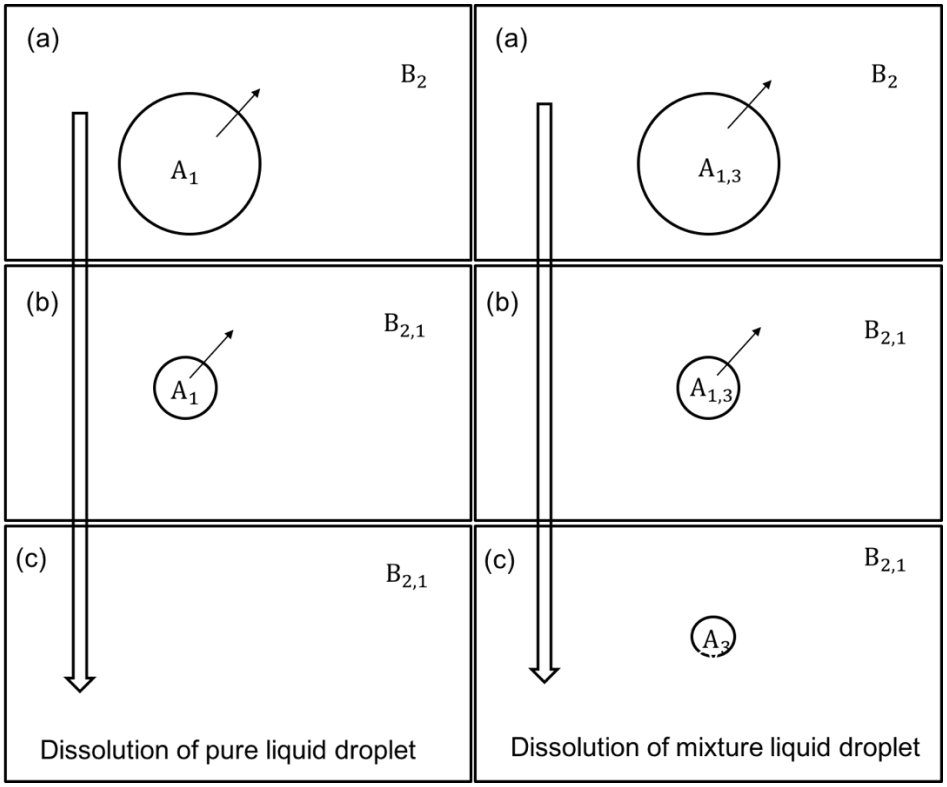

Figure IV-1: Dissolution of liquid droplet phase A into an immiscible liquid phase B.(left) for pure liquid and (right) for mixture liquid.

Here, A and B correspond to the liquid phase inside the droplet and the surrounding medium, respectively. The components 1, 2 and 3 are designated by numerical subscripts. For example, the $A_{1,3}$ means that the droplet phase A has two components 1 and 3. For the simplest case, let us consider that only component 1 can be dissolved in component 2 and that the phase B with component 2 is infinite (i.e. the component 1 in droplet can be totally dissolved in component 2 at the end of dissolution process without any significant modification of the concentration of liquid B). Based on these assumptions, the dissolution process of both cases can be separated into three main steps as represented in the Figure IV-1. For pure liquid droplet, (the scheme on the left), as soon as the phase A droplet with component 1 is generated and placed in the liquid phase B with component 2, the mass transfer starts and component 1 is dissolved into component 2 in the surrounding medium. Due to the loss of mass of

component 1, the droplet's volume decreases and thus the shrinking of droplet diameter occurs as a function of time. Consequently, at the end of the process when the component 1 is totally dissolved, the droplet disappears.

In contrast, the dissolution of a liquid mixture droplet presents two differences compared to pure droplets. The dehydration process is longer and the droplet does not disappear at the end. In this case, the droplet containing components 1 and 3 is formed and placed in the surrounding medium containing component 2. Taking the assumption that only component 1 can be dissolved in component 2, the loss of mass is thus only due to component 1 dissolution. At the end of the process, the component 1 is completely dissolved, and component 3 remains inside the droplet at a very high concentration. From this moment, the droplets size becomes steadily constant. Depending on the properties of component 3, the final phase of the droplet can be crystalline (Sivaji 1989), or glassifed micro-beads(Rickard, Duncan, and Needham 2010).

The Figure IV-2 shows a schematic depicting the evolution of water activity during droplet dehydration. Here, two cases are presented: a droplet of pure water and a protein solution droplet.

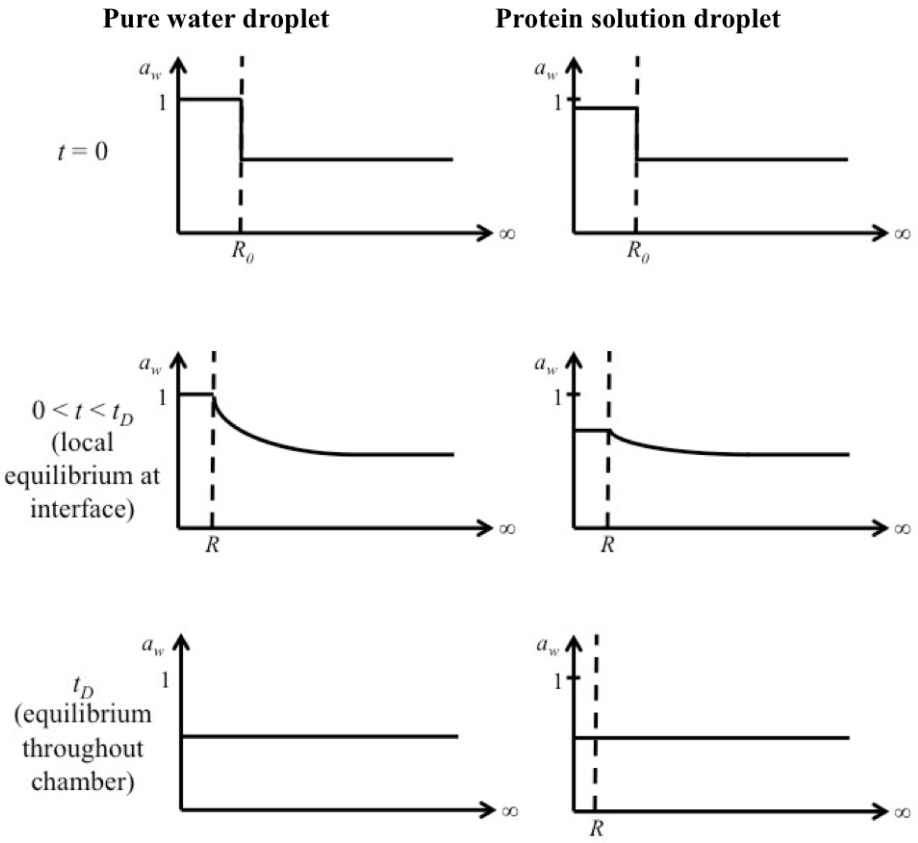

Figure IV-2: Water activity evolution of a pure water droplet (left) and a protein solution droplet (right) in a medium partially saturated by water. For the pure water droplet, the droplet's diameter decreases until its complete dissolution (i.e. $R = 0$) whereas the diameter of the protein droplet decreases until the equilibrium of water activity inside the droplet and the surrounding medium is reached (Rickard's PhD thesis 2011).

The dissolution process can be divided into three different time steps. In the pure water droplet case, the water activity is always 1. At $t = 0$, the droplet with radius R_0 is formed and placed in a chamber partially saturated by water ($a_w \approx 0.5$). A local thermodynamic equilibrium at the interface is assumed, so the water activity inside droplet is equal to water activity at the interface. Between $0 < t < t_D$, (t_D is the time required to dissolve the droplet) the water inside the droplet starts diffusing into the surrounding medium and this causes a decrease of the droplet diameter ($R < R_0$). However, the activity of pure water is equal to 1 and the water activity of surrounding medium with $r \gg R_0$ equals 0.5 as since the surrounding medium can be considered as an infinite medium. At the end of the process, at $t = t_D$, the droplet totally disappears ($R = 0$) .

For a protein solution droplet, at the initial time $t = 0$, the droplet has an initial diameter, R_0 . In this case, the water activity of the protein solution droplet is smaller than 1 due to the presence of protein. By the time $0 < t < t_D$, analogously to the pure water case, the water inside the droplet diffuses into the surrounding medium, the droplet loses water and thus, its size decreases. However, in this case, the water activity in the droplet also decreases due to the increase in protein concentration. Using the same assumption about the local thermodynamic equilibrium, the water activity inside droplet is equal to the water activity at the droplets interface. However, the difference between the water activity at $r \gg R_0$ (i.e. at the infinite medium), and the activity at the interface and at infinite is smaller and therefore droplets diameter shrinking rate is lower. At the end of the dehydration process, when $t = t_D$, the water activity inside the droplet is equilibrated with the water activity of the surrounding medium (i.e. $a_{w.in} = a_{w.out}$). Consequently, although there is still some water inside the droplet, there is no diffusion anymore and the droplets diameter,R_D, remains constant. Hence, the protein concentration inside the droplet will increase from an initial value up to a critical point which depends on the relative humidity in the surrounding medium.

The first protein solution dehydration experiments were performed by Rickard et al. In their work, the authors created single droplets of lysozyme solutions with an average diameter around 50 µm, using the micropipette technique and dipping them in 1-decanol media with a controlled water activity. Knowing the water activity of the surrounding medium, the initial concentration of protein inside the droplet, and the final diameter of the aqueous droplet, the remaining amount of water inside the droplet and the protein concentration was calculated. The authors made the link between this amount of water and the hydration potential of the proteins. However, compared to microfluidics the micropipette technique displays some disadvantages: it takes some time to prepare single droplets individually, the droplets generated are not perfectly monodispersed and all the droplets cannot be monitored during the entire dissolution process.

One major assumption of this approach, which is based on mass transfer, is that the solute molecules (lysozyme in this case) are evenly distributed within the

droplet (i.e. the redistribution of protein molecule should be faster than the shrinking of droplets interface). The diffusion of water through the interface induces a diffusional flux of solute in the reversed direction – from the interface to the center of the droplet. If the diffusion of the solute molecule within the droplet is slow compared to the shrinking of the interface, a concentration gradient is formed inside the droplet. The high concentration of solute near the interface causes a local reduction of the water activity and a skin composed of a highly concentrated solute precipitates/aggregates formed at the droplet surface. Maki *et. al.* reported that the skin formation is induced by the weak water diffusion compared to the convective flow within the droplet (Maki and Kumar 2011).

The relationship between diffusion and convection of solute within the droplet is usually represented by means of the Peclet number:

$$\mathrm{Pe} = \frac{\mathrm{Jh_0}}{\mathrm{D}} \qquad \textit{Eq. IV-1}$$

where J is the flux diffusion which is calculated by the loss of volume, h_0 is the initial height of droplet – in case of the experiments reported here, the value is equal to $2R_o$, the initial diameter of droplet – and D is the diffusion coefficient of the solute. Other investigations (Baldwin et al. 2011; Manukyan et al. 2013 for instance) agreed that with a low $Pe < 1$, the diffusion is controlling the process and induces a low gradient at the interface. In reverse, with high $Pe > 1$ the convection is the governing factor and causes a high gradient at the interface. Consequently, the water activity at the interface will be affected.

In this chapter, the influence of the experimental conditions in pure water and protein solution droplets dissolution/dehydration (saturation fraction, initial concentration, and initial droplet diameter) were studied. At the end of the dissolution/dehydration process (i.e. when the equilibrium is reached), the osmotic pressure and the hydration potential of protein molecules were calculated from the value of the final water activity inside the droplet, which equals the known water activity in surrounding medium. The results were compared and discussed with other results found in the literature, and with the Carnahan-Starling approximation. Additionally, the dehydration process of

lysozyme solution droplets in 1-decanol is predicted by modeling the multicomponent droplets dissolution. Results are presented and discussed below.

IV.2. Theoretical background of droplet dissolution

The Epstein-Plesset (E-P) model has been applied to study the stability of gas bubbles in the liquid-gas bubbles since 1950 (Epstein and Plesset 1950). It showed that the evolution of gas bubble diameters was related to an under/over-saturated amount of gas in the liquid. Following that theory, the group of D. Needham studied the dissolution of micro-droplets containing a single phase: air (Duncan and Needham 2004), liquid (Duncan and Needham 2006) or multi-phase (Su and Needham 2013) in an immiscible liquid medium. Su et al (Su et al. 2010) applied the Epstein- Plesset equation to investigate the effect of hydrogen bonding in water diffusion in liquid surrounding media with/without hydrogen bonds. They showed that the diffusion coefficient of water in alcohols is slower than in the corresponding alkane liquid with the same viscosity. In this way, they also explained why small solutes in large solvents have more quickly diffusion than the one predicted by the Stokes-Einstein equation.

IV.2.1. The E-P equation for pure water droplet

In their paper, Epstein and Plesset (Epstein and Plesset 1950) proposed to approximate the solution of the equation for the rate of dissolution of a gas bubble in an under-saturated liquid-gas solution. They considered a case that a spherical bubble with radius R is placed at $t = 0$ in a liquid-gas solution owning a uniform concentration of dissolved gas C_i. In a more recent paper, Duncan et al. (Su and Needham 2013) successfully tested this model for the dissolution of droplet in a well-defined liquid environment, proving that this theory can also be generalized to describe the dissolution of pure liquid droplets in an infinite isotropic solvent or solution.

As in the case of bubble dissolution, for liquid droplet dissolution, the main variables are the concentration gradient from the droplet surface and the pressure gradient across the interface. The concentration gradient is caused by the difference between the concentration at the thermodynamic equilibrium at the interface of the droplet ($C = C_{sat}$) and the concentration of the solution far

away from the droplet interface ($C_{infi} = C_0$). The pressure gradient arises from the interfacial tension and curvature of the droplet-medium interface which creates a Laplace overpressure in the droplet. In contrast to what obtained by Epstein-Plesset for gas bubble dissolution, Duncan et al. have shown that the pressure gradient is negligible in the case of droplet dissolution, especially for large droplets (few tens of microns). Hence, based on this work, the droplet dissolution is only governed by diffusion of the liquid forming the droplet to the continuous phase. In the case of water diffusion in an organic solvent, the total flux of water at the boundary of spherical droplet is given by the Flick's first law:

$$\frac{\mathrm{dm_w}}{\mathrm{dt}} = 4\pi \mathrm{R}^2 \mathrm{J} = 4\pi \mathrm{R}^2 \mathrm{D} \left(\frac{\partial \mathrm{c}}{\partial \mathrm{r}}\right)_{\mathrm{R}} \qquad \textit{Eq. IV-2}$$

where m_w is the mass of water,J is the flux per unit area and c the concentration of water at $t > 0$ and at a distance $r > R$ from the center of droplet. The temporal evolution of water concentration at a point $r > R$ in the solution is given by the second Fick's law:

$$\frac{\partial \mathrm{c}}{\partial \mathrm{t}} = \mathrm{D} \left(\frac{\partial^2 \mathrm{c}}{\partial \mathrm{r}^2}\right) \qquad \textit{Eq. IV-3}$$

The resolution of both equations proposed by Epstein and Plesset gives the following equation for the temporal evolution of the concentration of water in the continuous phase:

$$\left(\frac{\partial \mathrm{c}}{\partial \mathrm{r}}\right)_{\mathrm{R}} = (\mathrm{c}_0 - \mathrm{c}_\mathrm{s}) \left\{\frac{1}{\mathrm{R}} + \frac{1}{\sqrt{\pi \mathrm{Dt}}}\right\} \qquad \textit{Eq. IV-4}$$

The mass flow of water out from the droplet is:

$$\frac{dm}{dt} = 4\pi R^2 D \left(\frac{dc}{dr}\right)_R$$

Since the mass of a spherical water, droplet is $m = \frac{4}{3}\pi R^3 \rho$ (with ρ is the density of water) its temporal evolution is given by :

$$\frac{\mathrm{dm}}{\mathrm{dt}} = \frac{\mathrm{d}(\rho \mathrm{V})}{\mathrm{dt}} = 4\pi \mathrm{R}^2 \rho \left(\frac{\mathrm{dR}}{\mathrm{dt}}\right) \qquad \textit{Eq. IV-5}$$

Solving Eq. IV-4 for $\left(\frac{dR}{dt}\right)$, we obtain

$$\left(\frac{\mathrm{dR}}{\mathrm{dt}}\right) = \frac{1}{\rho}(\mathrm{c_0} - \mathrm{c_s})\mathrm{D}\left\{\frac{1}{\mathrm{R}} + \frac{1}{\sqrt{\pi \mathrm{Dt}}}\right\} = -\frac{\mathrm{c_s}}{\rho}(1-\mathrm{f})\mathrm{D}\left\{\frac{1}{\mathrm{R}} + \frac{1}{\sqrt{\pi \mathrm{Dt}}}\right\} \qquad \textit{Eq. IV-6}$$

where $f = c_0 / c_s$ is the saturation fraction of surrounding medium (in this case, 1-decanol). The term in the bracket $\frac{1}{R} + \frac{1}{\sqrt{\pi D t}}$ can be separated into two terms: the steady-state condition $(1/R)$ and the transient condition $(1/\sqrt{\pi D t})$ respectively.

IV.2.2. The modified E-P equation for a multicomponent mixture.

In order to adapt the previous model for the dissolution of a multicomponent droplet in a continuous phase, Su and Needham (Su and Needham 2013) proposed a modification of the Epstein Plesset equation. The main hypothesis of this approach is that all the components in the droplet are perfectly mixed and homogeneously distributed, including at the interface.

The total mass flux of the liquids in the droplet into the surrounding area is the sum of the mass flux of each component i, of the droplet:

$$\mathrm{J_{tot}} = \sum_{\mathrm{i}} \mathrm{J_i} \qquad \textit{Eq. IV-7}$$

The concentration at the edge of the droplet is given by Eq. IV-4.

Following the first Fick's law, the mass flux from the droplet is proportional to the concentration gradient via the diffusion coefficient. The mass of component i transferred by this flux is proportional to the surface area through which the flux occurs. To develop their model, the authors assumed that the surface fraction is proportional to the volume fraction. Thus, the mass flux of component i is given by:

$$\frac{\mathrm{dm_i}}{\mathrm{dt}} = \vartheta_\mathrm{i}\mathrm{D_i}(\mathrm{c_i} - \mathrm{c_s})\left\{\frac{1}{\mathrm{R}} + \frac{1}{\sqrt{\pi \mathrm{D_i t}}}\right\} \qquad \textit{Eq. IV-8}$$

where ϑ_i is the area fraction of component i at the interface and D_i is the diffusion coefficient of component i. The mass flux can be related to the volume changes via the density of each component, which can be related to the droplet radius.

In their paper, the definition of the surface fraction is vague and seems to be an adjustment parameter (proportional to the volume fraction). In addition, this approximation is a way of dealing with the condition of equality of chemical potential at the interface, but it has no fundamental basis. Moreover, Su and Needham assume that the equilibrium concentration is constant at the interface during dissolution but it cannot be.

IV.2.3. Numerical approach for modeling the droplet dissolution.

IV.2.3.1. Definition of the problem

Given a non-ideal system, where diffusion occurs as a result of the disturbance of an equilibrium state characterized by a non-uniformity of the chemical potential, μ, of the diffusion species, the first Fick's law can be written as follows:

$$\mathrm{J_i} = -\frac{\mathrm{DC_i}}{\mathrm{kT}}\left(\frac{\partial \mu_\mathrm{i}}{\partial \mathrm{r}}\right) \qquad \textit{Eq. IV-9}$$

where D is the diffusion coefficient, C the concentration of the diffusing species, and μ the chemical potential of the diffusing species. Eq. IV-9 may be rewritten in terms of activity:

$$\mathrm{J_i} = -\frac{\mathrm{DC_i}}{\mathrm{kT}}\left(\frac{\partial \ln \mathrm{a_i}}{\partial \mathrm{r}}\right) = -\frac{\mathrm{DC_i}}{\mathrm{a_i}}\left(\frac{\partial \mathrm{a_i}}{\partial \mathrm{r}}\right) \qquad \textit{Eq. IV-10}$$

With $\mu_i = {\mu_i}^0 + kT \ln a_i$, μ^0 being the standard chemical potential.

The second Fick's law becomes:

$$\frac{\partial \mathrm{C_i}}{\partial \mathrm{t}} + \frac{1}{\mathrm{r^2}}\frac{\partial \mathrm{J_i r^2}}{\partial \mathrm{r}} = 0 \qquad \textit{Eq. IV-11}$$

In the case of droplet dissolution, a droplet which contains pure water or a solute (protein for instance), the mass flux across the interface at $r = R$ is given by:

$$-\frac{\mathrm{dm_i}}{\mathrm{dt}} = -\rho_\mathrm{i}\frac{\mathrm{dV_i}}{\mathrm{dt}} = 4\pi \mathrm{R^2 J_i} \qquad \textit{Eq. IV-12}$$

With $dV_i = 4\,\pi R^2 dR$ and equation Eq. IV-9, the equation Eq. IV-12 can be re-written as:

$$\frac{dR}{dt} = -\frac{1}{\rho}J_i = -\frac{DC_i}{\rho a_i}\left(\frac{\partial a_i}{\partial r}\right) \qquad \textit{Eq. IV-13}$$

IV.2.3.2. Assumptions and boundary conditions

In order to numerically solve the problem, several assumptions have been made:

H1: a lumped system is assumed in the droplet (i.e. every variable at the surface of the droplet are the same as the one inside the droplet)

H2: Fluid is unbounded in extent and quiescent.

H3: in the case of an aqueous solution in an organic solvent, only water diffuses through the interface (the solute do not dissolve in an organic solvent, and the organic solvent do not diffuse in the droplet).

H4: There is no slip velocity between the droplet and the continuous phase (the convection is neglected).

H5: Since the droplets are generated by a flow-focusing microfluidic structure and flowed along the channel which its dimensions are larger than droplet's diameter, hence it can be assumed that the droplets were spherically symmetric.

Initially, at $t = 0$, the droplet has a known initial concentration and the surrounding medium has a uniform water concentration of $C_0 = f.C_{sat}$. At any time, far away from the droplet, the concentration of water in the organic solvent is $C_\infty = f.C_{sat}$.

IV.2.3.3. Discretization of the problem

Different discretization schemes have been used (explicit, implicit and Crank-Nicolson), however, for the sake of clarity, only the explicit scheme will be presented in this manuscript (the other numerical schemes and the grid definition are given in the **Appendix A**).

The combination of Eq. IV-10 and Eq. IV-11 gives:

$$\frac{\partial C_i}{\partial t} - \frac{D}{r^2}\left(2r\frac{C_i}{a_i}\frac{\partial a_i}{\partial r} + r^2\frac{1}{a_i}\frac{\partial C_i}{\partial r}\frac{\partial a_i}{\partial r} - r^2\frac{C_i}{a_i^2}\left(\frac{\partial a_i}{\partial r}\right)^2 + r^2\frac{C_i}{a_i}\frac{\partial^2 a_i}{\partial r^2}\right) = 0 \qquad \textit{Eq. IV-14}$$

The term $\frac{\partial C_i}{\partial r}\frac{\partial a_i}{\partial r}$ in this equation is non-linear (as the concentration and the activity are interdependent) and cannot be discretized using finite elements. To solve the

equation, as the solubility of water in the organic solvent is low, it is assumed that at $r > R$ the solution behaves ideally (i.e. $\frac{\partial C_i}{\partial r} = \frac{\partial a_i}{\partial r}$). Hence, the Eq. IV-14 can be simplified as:

$$\frac{\partial \mathrm{C_i}}{\partial \mathrm{t}} - \frac{\mathrm{D}}{\mathrm{r}^2}\left(2\mathrm{r}\frac{\mathrm{C_i}}{\mathrm{a_i}}\frac{\partial \mathrm{a_i}}{\partial \mathrm{r}} + \mathrm{r}^2\frac{\mathrm{C_i}}{\mathrm{a_i}}\frac{\partial^2 \mathrm{a_i}}{\partial \mathrm{r}^2}\right) = 0 \qquad \textit{Eq. IV-15}$$

As the surrounding solution is considered ideal, the activity can be calculated using the Henry law:

$$\lim_{x\to 0}\frac{a}{C} = \mathrm{H}_{wo}$$

with C being the molar fraction of water in the organic solvent. In the case of water in 1-decanol, the Henry law constant is $\mathrm{H}_{wo} = 6.22 \pm 0.2$(Šegatin and Klofutar 2004). The activity is then calculated by:

$$\mathrm{a}_i = \mathrm{C}_i\mathrm{H}_{wo}$$

Using the implicit scheme, for $r > R$ the discretization of Eq. IV-14 equation is:

$$C_r^{t+1} = C_r^t + D\cdot\Delta t\cdot\frac{C_r^t}{a_r^t}\cdot\left(\frac{2}{r}\frac{a_{r+1}^t - a_{r-1}^t}{2\Delta r} + \frac{2}{\Delta r}\left(\frac{a_{r+1}^t - 2a_r^t - a_{r-1}^t}{\Delta r}\right)\right)$$

Knowing, C_r^{t+1} at $r = R^+$, the radius and the volume of the droplet can be calculated respectively from : (so-called equation radX)

$$\mathrm{R}_{t+1} = R_t + DC_2\frac{M}{\rho}\Delta t\frac{a_{r=R^-}^t - a_{r=R^+}^t}{\Delta r}$$

and

$$V|_{t+1} = \mathrm{V_p} + V_w = C_p|_{t=0}\cdot V|_{t=0}\cdot M_p\cdot V_{sp,p} + \frac{C_i|_{t+1}\cdot V|_{t+1}\cdot M_i}{\rho_w}$$

where the subscript i and p are for the water and protein respectively, $V_{sp,p}$is the specific volume of the protein. The concentration of water inside the droplet at $t = t+1$, can then be calculated by:

$$\mathrm{C}_{i,in}|_{t+1} = \frac{\rho_\mathrm{i}}{M_i} - \frac{\rho_i\cdot V_{sp,p}\cdot M_p\cdot C_p|_{t=0}\cdot V|_{t=0}}{V|_{t+1}\cdot M_w}$$

The activity of water or the droplet osmotic pressure can then be calculated either using a fitting of experimental data or from an equation of state (Carnahan-Starling EOS for instance).

IV.2.3.4. Comparison between the E-P equation and the numerical code

To test the validity of the numerical modeling, the result of equation RadX is compared to the results obtained using the E-P equation (Eq. IV-6), for the dissolution of a water droplet of 97µm in 1-decanol. The solubility of water in 1-decanol was taken from the literature (Šegatin and Klofutar 2004) is $m = 2.4112$ mol.kg^{-1} and the diffusion coefficient of water in 1-decanol $D = 6e - 10$ m^2/s (Lin, Lu, and Hwang 1995). A comparison, in term of the temporal evolution droplet radius, between the E-P equation and the numerical model is given in the Figure IV-3.

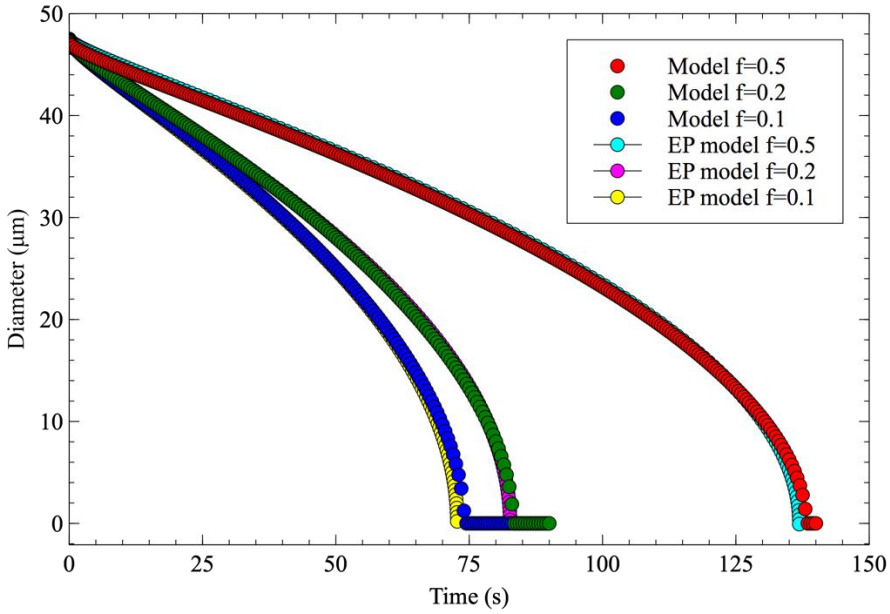

Figure IV-3: Comparison of the numerical model results and E-P equation for different water concentration in the continuous phase (f). The grid size was 150, time step $dt = 1e^{-4}s$ and $dr = 0.05$ µm

The results obtained with the numerical code are in good agreement with the E-P equation. However, a difference in terms of diameter is observed at the end of the dissolution process (i.e. when the droplet radius is lower than 7µm). This could be attributed to the numerical scheme. However, different numerical

schemes, grid size, meshing methods have been tested and no improvements can be found.

IV.3. Materials and Methods

IV.3.1. Materials

Lysozyme from chicken white egg (dialyzed, lyophilized, powder, ~100000 U/mg, Sigma-Aldrich) was used as received. The ultra pure water was filtered by PURELAB machine (USA Resistivity of 18.18 MΩcm^{-1}). Pure 1-decanol grade (≥ 99%, Sigma-Aldrich) was used and keep dry using 3A molecule sieves (Sigma-Aldrich) before used to prepare solutions with different water saturation fractions.

The 1-decanol was chosen because of its solubility properties with water. The solubility of 1-decanol in water is low enough (approximately 0.01% volume) which allows us neglecting decanol diffusion into micro-droplets with initial volumes of tens of picoliters. On the other hand, the solubility of water into decanol is high enough to ensure that the amount water in the droplet is much lower than the dissolution capability of the surrounding medium. For example, for a channel of 125 µm width, 500 µm depth and a length between two droplets of 0.5 cm, the continuous phase enables to dissolve at least approximately 3500 droplets of water which have the diameter around 50 µm. This means that with this configuration the 1-decanol surrounding medium can be considered as an infinite medium.

Microfluidic platforms (made in OSTEmer 322) for droplet dissolution experiments were built according to the procedure described in Chapter II.

IV.3.2. Method for droplets dissolution in 1-decanol.

Two different sets of experiment were carried out: (1) to validate the experimental setup, dissolution experiments of pure water droplets in 1-decanol with various saturation fraction of water, $f = 0$, $f = 0.25$, and $f = 0.5$, were performed. The results obtained in terms of temporal evolution of the droplet radius were compared with E-P equation. (2) Determination of Lysozyme EOS in water: the dissolution of aqueous lysozyme solution droplets with different initial concentrations of Lysozyme in 1-decanol with different saturation fractions (f in a range from 0 to 0.9) were performed.

The experimental setup, shown in the Figure IV-4, contains a microfluidic chip with inlets and outlets connected to a syringe pump system (neMESYS, Cetoni GmbH, Germany) by means of PFA tubes (Upchurch, ID250µm; OD1/16"). The continuous and dispersed phase are transferred to the flow-focus structure in a microfluidic system in order to generate single droplets of the aqueous solutions. The droplets are kept and flowed in 1-decanol through the whole channel length of the microfluidic chip. The evolution and movement of the droplets are recorded by an inverted Zeiss Axio Observer microscope coupled to a high-speed camera (Miro M120, Vision Research). The microscope is set by 10x magnification. The fast camera is set up at 40 frames per second and a resolution of 1200x800 pixels. The embedded memory of camera allows recording movies ranging from 3 to 15 minutes depend on the duration of the dissolution process. Finally, the movie is moved to a computer to be able to analyze the evolution of the size of the droplet. A Matlab program is utilized to automatically detect the diameter of droplets as a function of time. This program is based on a first autocorrelation function that detects the presence of the droplet in the channel. The diameter of the detected droplet is calculated either using a circle Hough function of Matlab or using a gray scale gradient induced by the presence of the droplet in the channel (the Matlab program is given in the **Appendix B**).

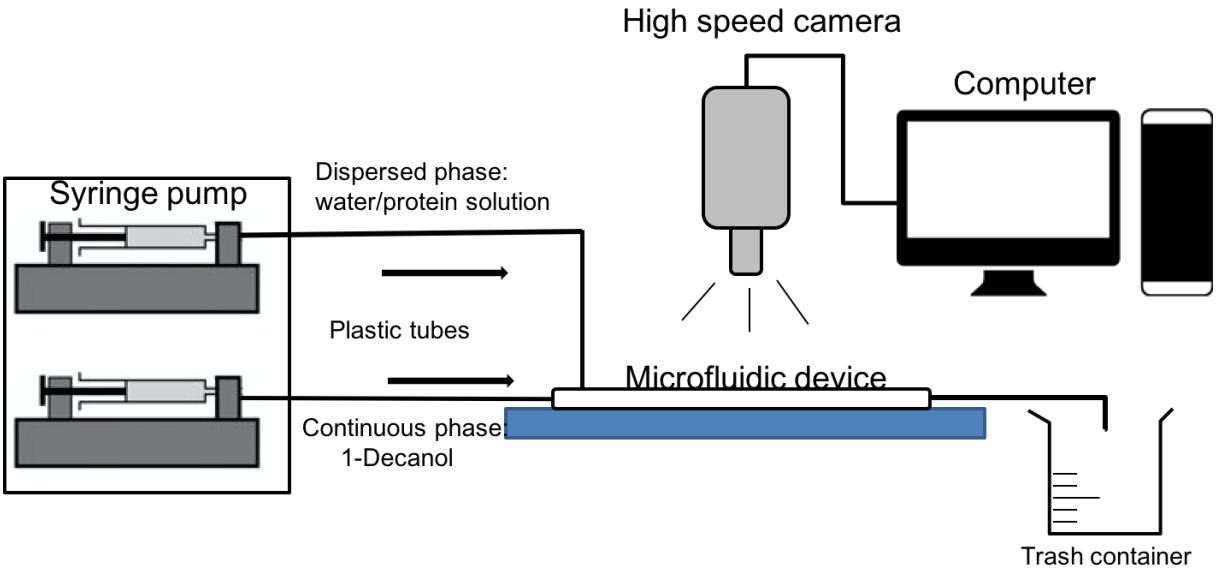

Figure IV-4: Experimental setup for dissolution of single droplets using microfluidic system.

IV.3.3. Microfluidic chips preparation

To study the diffusion of water from the protein solution droplet into the surrounding environment, several requirements for the microfluidic chip design are required:

A) Generation of single droplets with homogeneous diameter.
B) The distance between 2 droplets in a row should be large enough to satisfy the condition of an infinite dissolution environment.
C) The geometry of the channel has to be long to ensure that the residence time of the droplet in the microfluidic chip is greater than the dissolution process duration.

From these requirements, two types of microfluidic chips were designed with rectangular channels, as shown in the *Figure IV-5*. The first design consists of a flow-focusing structure to generate droplets and a long serpentine channel to store and to observe droplets dissolution. The height of the channel ranges from 120 to 240 µm and the width of the serpentine is 500 µm. The total length of the serpentine channel is 84 cm. For the flow-focusing structure, the width of the channel is 50 µm to ensure the generation of small droplets.

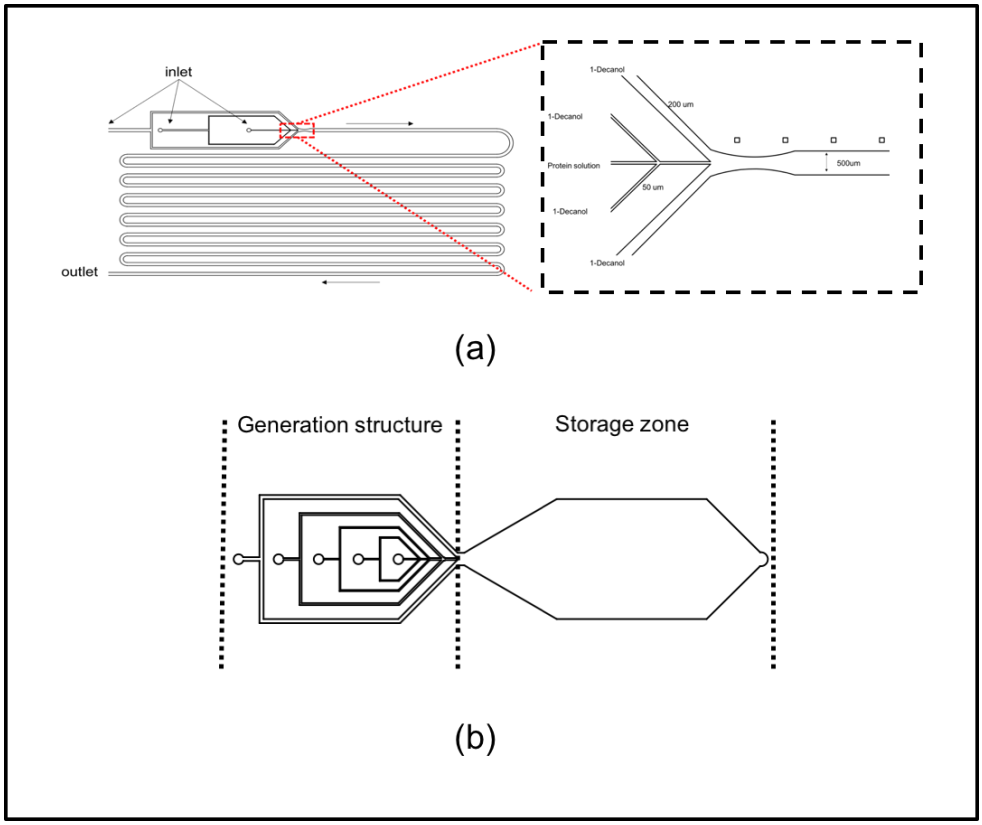

Figure IV-5: Illustrations of designs for microfluidic systems.(a) the design with the serpentine channel and (b) the design with big storage zone. These designs have the same dimension for generation structures.

In the second tested design, the droplet generation is the same as previously, but the storage part was modified to include a Hele-Shaw cell configuration to store the droplets as illustrated in the *Figure IV-5*b. The large storage zone is designed with a funnel shape nozzle in order to gradually slow down the speed of the droplets before entering the big area. Due to the large volume of organic solvent which can be stored in the Hele-Shaw cell, it is possible to dissolve thousands of water droplets. Both of designs were fabricated to test the configuration and the results are presented in the section *Results and Discussion*.

1-decanol solutions with different water concentrations were prepared before starting the experiments by mixing, off-chip the dry 1-decanol and the water saturated decanol. 1- decanol was dried by storing it in 3$\mathring{A}$ molecular sieves to absorb all dissolved water. In contrast, the full water saturated decanol was prepared by adding an amount of water, much higher than the water solubility in 1-decanol, and aging the solution for at least 1 week before use. The term

saturation fraction f is defined by the ratio of initial concentration of water in the solution over the saturated water concentration. Hence, f ranges from 0 to 1. Given the very low solubility of Lysozyme in decanol <0.002 mg/mL (Rickard, Duncan, and Needham 2010), the diffusion of Lysozyme into 1-decanol can be neglected within the time scale of the experiments.

IV.3.4. Analysis methods: refractive index and hydration analysis.

IV.3.4.1. Refractive index matching: in-situ lysozyme concentration measurement.

During the dehydration experiment, the concentration of protein solution within droplet increased due to the loss of water. By this way, the refractive index of protein solution evolves as well. At a certain time, the droplet has the same refractive index with the 1-decanol in the surrounding medium, called $n-match$. And then it becomes invisible. From $n-match$ value, the protein concentration at this time can be calculated. According to Rickard et al(Rickard, Duncan, and Needham 2010), the Lysozyme concentration at $n-match$ is by 518 mg/mL . If the initial diameter and the $n-match$ diameter of droplet are known, the initial protein concentration can be determined as well.

However, it is a quite serious problem to determine the $n-match$ diameter because of the invisibility of droplet. The temporal evolution of the droplet diameter is recorded for the whole dissolution process and the diameter at $n-match$ is determined by interpolation between the diameter before and after the droplet disappearance. The error of initial concentration calculation is in range 10-20 mg/mL.

IV.3.4.2. Hydration analysis

Let consider that the droplets containing water and Lysozyme are dissolving in the 1-decanol medium, just only water diffuses from droplet to outside. Obviously, the protein mass within the droplet is constant and determined by an initially given value. The water volume fraction is determined as:

$$\phi_w = 1 - \frac{C\nu_p}{1000} \qquad \textit{Eq. IV-16}$$

where C is the initial concentration of protein, ν_p is the protein specific volume which assumed to be constant by 0.7 mL/g. The water in the protein solution includes the water in the hydration water (i.e. the water molecule directly interacting with the surface of protein molecules) and the water presented in the interstitial space of the protein. Hence the water volume fraction can be written as: $\phi_w = \phi_{hyd} + \phi_{int}$. Here, the ϕ_{int} can be theoretically calculated using a term of packing efficiency and the random jammed state of hard core objects. It equals to 0.36 for spheres and 0.29 for ellipsoids (aspect ratio 1.5) (Chaikin et al. 2006). However, Rickard et al (Rickard, Duncan, and Needham 2010) calculated the interstitial space in vacuum and shown that the Lysozyme molecule can be packed more efficiently with $\phi_{int} = 0.07 \pm 0.01$.

The hydration potential of Lysozyme at the end of dehydration process in this work is presented by amount of hydration water, h, (g of water per g of Lysozyme) as a function of the water activity inside droplet (equal the water activity in the surrounding medium), whereas the amount of hydration water is calculated:

$$h = \frac{\text{weight of water}}{\text{weight of Lysozyme}} = \frac{1000\rho_w\phi_{hyd}}{C} \qquad \textit{Eq. IV-17}$$

where ρ_w (g/m^3)is the density of water and C(g/L) the initial concentration of protein.

According to the experimental data of water solubility in 1-decanol(Šegatin and Klofutar 2003), the water activity as a function of saturation fraction is presented in the Figure IV-6.

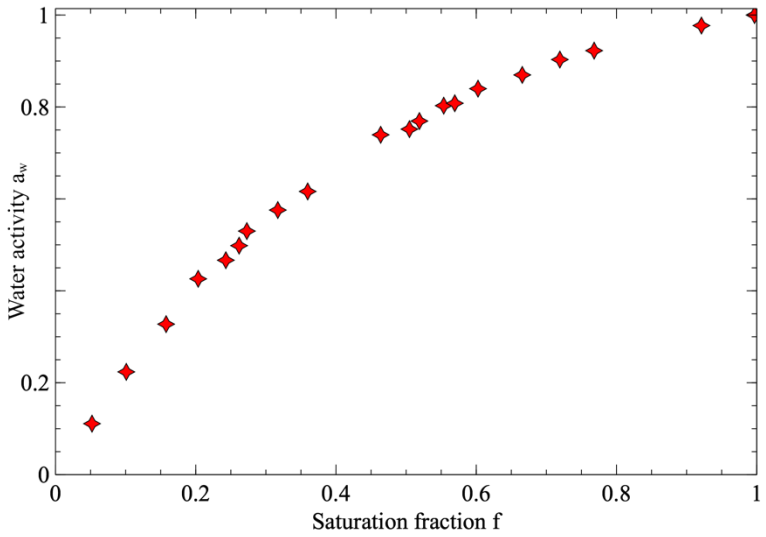

Figure IV-6: Water activity as a function of saturation fraction.

IV.3.5. Osmotic pressure and Equation of State (EOS)

Many studies have shown that in the solution, the water molecules in contact with protein molecules in solution have different properties compared to the ones in the bulk (Halle et al. 1981; Otting and Wuethrich 1989). They need more energy to be removed than water molecules surrounded by other water molecules. This energy in the dehydration process can be seen as a needed energy to remove a water molecule in contact with Lysozyme to its ideal state. And it is expressed as a function of water activity:

$$\mu_w = \mu_0 + k_B T \ln(a_w) \qquad \textit{Eq. IV-18}$$

where μ_w is the chemical potential of water in the solution. μ_0 is the chemical potential of pure water.

By dividing by molecule volume of water ν_w, the osmotic pressure can be obtained:

$$\Pi_{oms} = k_B T/\nu_w \ln(a_w) \qquad \textit{Eq. IV-19}$$

Where $T = 298\ K$ and k_B is the Boltzmann's constant.

Let assume that dissolved protein molecules in water can be described as non-attractive rigid spheres and all the laws of physics can be applied. It is

considered the case of hard sphere fluids with a sphere radius a, where the structure of fluid is determined by a radial distribution function $g(r)$, describing the probability of finding a neighboring particle. Here, r is the distance from the center of the reference particle (i.e. the location origin). If normalized, $g(r) = 1$ presents a randomly distributed suspension of non-interacting point particles. In the case of $r < 2a, g(r) = 0$ as the particles can not interpenetrate. At low concentration, when $r = 2a, g(r) = 1$, particles are arranged randomly. At high concentration, when $r = 2a, g(r)$ value is very high however, this value decays rapidly.

The pressure tensor in the thermodynamic which absence of hydrodynamic interactions is expressed:

$$\sigma^{\mathrm{thermo}} = -\frac{1}{\mathrm{V}}\langle\sum_{\mathrm{i=1}}^{\mathrm{N}} \mathrm{r_i F_i^{thermo}}\rangle \qquad \textit{Eq. IV-20}$$

where: r_i is the location of particles as given by the vector, F_i is the force acting on that particle and N and V are particles and volume, respectively.

Conceptually, as the simplest case, the interaction between hard-sphere particles is excluded volume: the point particle gives a way to other take up space and cannot overlap. Consequently, this stress expression can be used to recalculate the osmotic pressure. The osmotic pressure can be derived from the stress due to the excluded volume of hard sphere where ϕ_{hs} is the volume fraction of hard sphere molecule:

$$\Pi_{\mathrm{osm}} - \mathrm{nk_B T} = -\sigma_{\mathrm{ii}} = 4\mathrm{nk_B T}\phi_{\mathrm{hs}}\mathrm{g(2a)} \qquad \textit{Eq. IV-21}$$

This means that the osmotic pressure caused by molecule interactions in suspension can be determined by the value of the radial distribution function $g(2a)$ from Carnahan-Starling approximation(Carnahan and Starling 1969) which can be expressed as:

$$\mathrm{g(2a)} = \frac{1 - (\phi_{\mathrm{hs}}/2)}{(1 - \phi_{\mathrm{hs}})^3} \qquad \textit{Eq. IV-22}$$

So the equation of state for hard sphere molecules can be expressed as:

$$\frac{\Pi_{osm}}{nk_BT} = \frac{1 + \phi_{hs} + {\phi_{hs}}^2 - {\phi_{hs}}^3}{(1 - \phi_{hs})^3} \qquad \textit{Eq. IV-23}$$

For the case of Lysozyme, the $\phi_{hs} = \frac{4}{3}\pi r^3$, whereas r is the gyration radius of Lysozyme.

IV.4. Results and Discussion

IV.4.1. Validation of microfluidic designs

The designs presented in the *Figure IV-5* were tested for droplets generation and the study of the dissolution process. It was possible to achieve in both designs very homogenous and stable droplet generation with constant droplets diameter and frequency. However, droplet dissolution could only be tested successfully in the first design. In the second design, as the dimension of storage Hele-Shaw cell was huge compared to the flow rates of the continuous phase, droplets collided and coalesced easily. In addition, at lower flow rates, the droplets stuck to the walls. In contrast, if the flow rates were high enough to avoid sticking, the length of the cell was too short to observe total droplet dissolution.

In conclusion, the first design satisfied all conditions to perform dissolution experiments. Thus, this design was used for all the experiments presented in this chapter.

IV.4.2. Dissolution of pure water droplets

The experiments of dissolution of pure water droplets were carried out in three different saturation fraction 1-decanol media. These experiments were performed not only to test the E-P equation, but also to study the effect of water saturation fraction in 1-decanol in droplets dissolution. The evolution of droplet size is shown in the Figure IV-7.

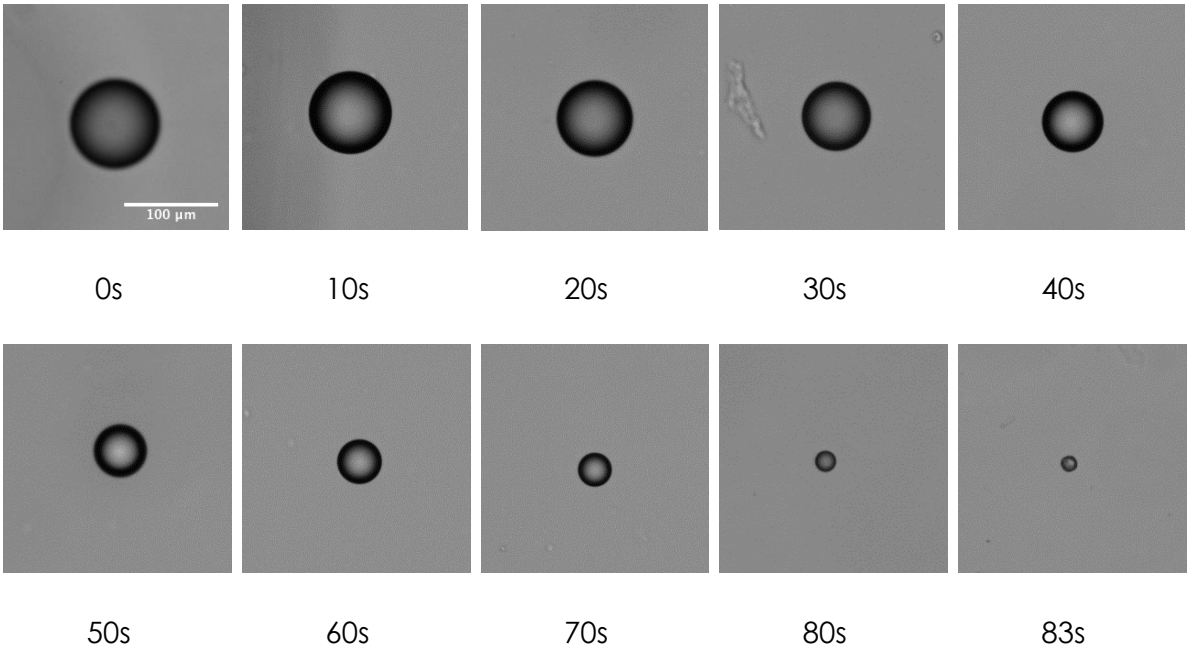

Figure IV-7: The evolution of pure water droplet size with initial diameter around 80 µm is dissolving in pure 1-decanol as a function of time from 0s to 83s.

The experimental data are in good agreement with the E-P model (see the Figure IV-8). In addition, using a flow rate of 0.03 µL/min for the dispersed phase and 5 µL/min for the 1-decanol, the droplet frequency is 16 droplets/min. In this case, the volume of 1-decanol surrounding the droplet was large enough to be considered as an infinite medium to small droplets, so the water droplets were completely dissolved. With this constraint, a water droplet with an initial diameter about 80 µm was generated in the pure decanol ($f = 0$) in the Figure IV-7. By the time($t > 0$), the size of droplet decreased due to diffusion of water from the droplet to the surrounding medium. When the droplet was totally dissolved, it disappeared (around 83s represented in the Figure IV-7). However, the droplets dissolution time depends on the initial volume/diameter and the saturation fraction (i.e. water activity). For example, for the 1-decanol with $f = 0.2$ the dissolution time for a 100 µm diameter droplet is around 94s as shown in the Figure IV-8. These influences are more deeply discussed below.

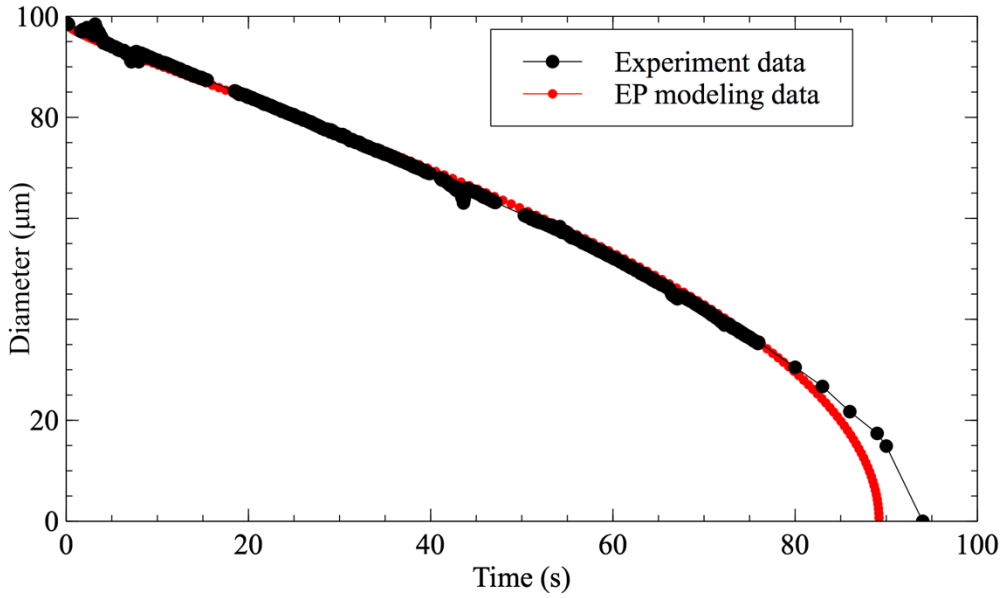

Figure IV-8: Evolution of droplet's diameter by the time of water droplet in 1-decanol with saturation fraction $f = 0.2$. (black circle) is the experimental data and (red circle) is the E-P modeling data.

The E-P modeling was applied to the case of a pure water droplet dissolution in 1-decanol with a saturation fraction $f = 0.2$ (Figure IV-8) and considering a water diffusion coefficient $D = 6e - 10$ m²/s. It is worth noting here that the empirical data perfectly fit with the modeling until the diameter of droplet goes below less than 20 µm. The difference observed might be explained by the sensitivity of the detection in the Matlab program. Below 15 µm, the program could not detect properly the droplet anymore. The fitting of experimental and modeling data also showed that the dissolution of pure water in 1-decanol is dominated just by diffusion of water.

In order to investigate the dissolution kinetics, the mass flux of water diffusion in 1-decanol was calculated. This flux is defined by the mass flow m in the time t through the droplet surface area S. In that case, it is calculated from variation of droplet's volume (ΔV) in Δt divided by the surface area of droplet S. By this way, the flux is determined from measured droplet diameters through the following expression:

$$F_i = -D\frac{dm}{dt}\left(\frac{1}{S}\right) = -D\frac{(V_{i+1} - V_i)}{(t_{i+1} - t_i)}\left(\frac{1}{S_i}\right) \qquad \textit{Eq. IV-24}$$

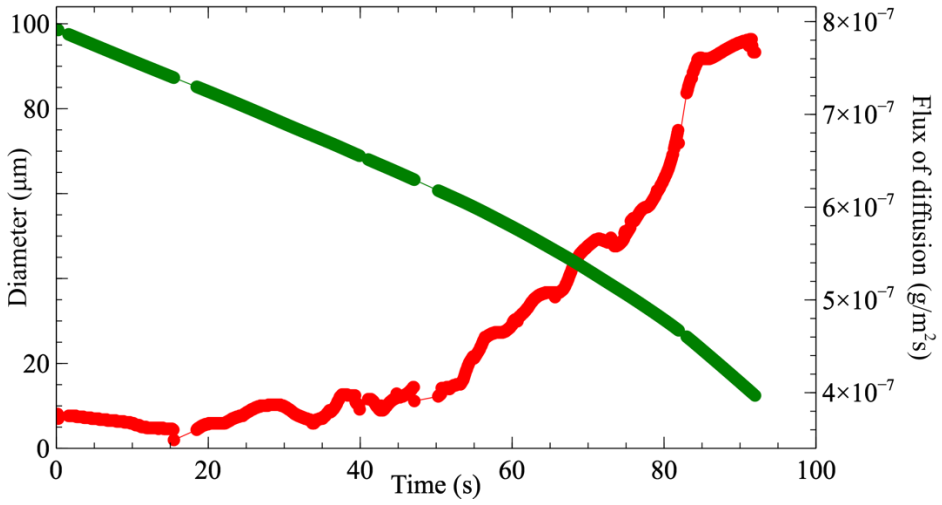

Figure IV-9: Flux of diffusion and diameter evolution by the time of 90 µm initial diameter water droplet in pure 1-decanol.

The relationship between the droplet diameter and flux of diffusion is depicted in the Figure IV-9. The experiments were carried out with a 90 µm initial diameter droplet diffusing in pure 1-decanol. The diameter of the droplet was automatically measured using the Matlab program and then the flux of diffusion was calculated based on these data as mentioned in the Eq. IV-24. According to the graph, at the beginning, $0 < t < 50s$ the flux can be seen as constant at $\sim 4e^{-10}$ (g/m²s). Subsequently, the flux starts to increase when the droplet diameter or time of dissolution reach a certain value. This means that at the final stage of dissolution, the dissolution rate becomes significantly faster. The rate increases to a maximum value when the diameter is minimum just before its complete dissolution.

IV.4.2.1. Influence of saturation fraction of surrounding medium.

The effect of the saturation fraction of surrounding media by the time of complete dissolution is studied for different saturation fractions f of 1-decanol.

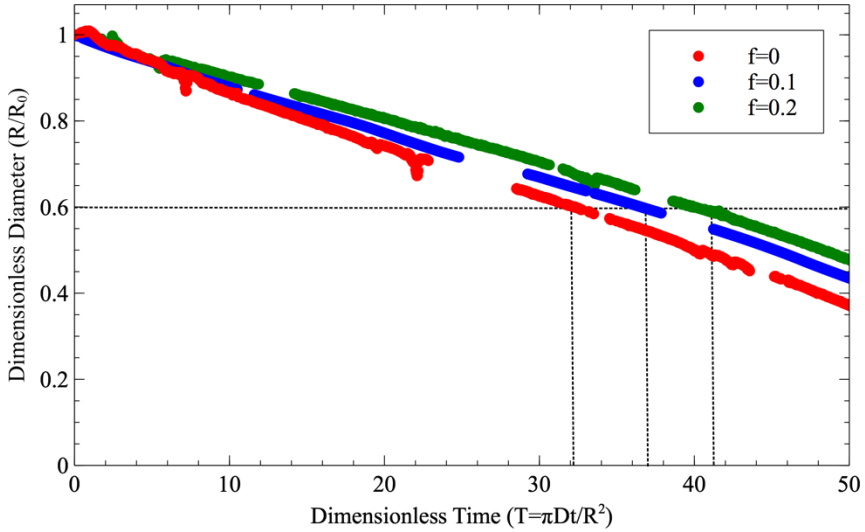

Figure IV-10: Dimensionless plot of dissolution water droplet in various 1-decanol saturation fractions ($f = 0;\ 0.1\ and\ 0.2$).

The dissolution kinetic of water droplets in 1-decanol was studied by generating single water droplets dissolved into drying 1-decanol media at three different water saturation levels $f = 0$, $f = 0.1$ and $f = 0.2$ (shown in the *Figure IV-10*). Since the droplet size affects its dissolution time, in order to compare the shrinking rate of the droplets, a dimensionless form of the E-P equation, independent to initial diameter and diffusion coefficient, was expressed. The terms $\mathrm{A} = R/R_0$ and $T = \pi Dt/{R_0}^2$ were employed and the E-P equation in dimensionless form was re-written as:

$$\frac{\mathrm{dA}}{\mathrm{dT}} = -\frac{\mathrm{c_s}}{\pi\rho}(1-\mathrm{f})\left\{\frac{1}{\mathrm{A}} + \frac{1}{\sqrt{\mathrm{T}}}\right\} \qquad \textit{Eq. IV-25}$$

The *Figure IV-10* shows the dissolution rates of water droplets in the 1-decanol solutions. When the saturation fraction increases (higher amount of water in decanol medium), the dissolution rate decreases. It is clearly shown in the graph that the dimensionless diameter decreased down to 0.6 for $f = 0$, $f = 0.1$ and $f = 0.2$ when the dimensionless time increased with $T = 32$, $T = 37$ and $T = 41$, respectively. Consequently, at a constant droplet initial diameter, the dissolution time at higher saturation fraction was longer.

IV.4.2.2. Influence of initial droplet diameter.

Here, the dissolutions of droplets with different initial diameters in the same surrounding media were performed in order to reveal the influence of initial diameter. In this case, droplets with initial diameters of 90 µm and 135 µm were dissolved into pure 1-decanol medium ($f = 0$).

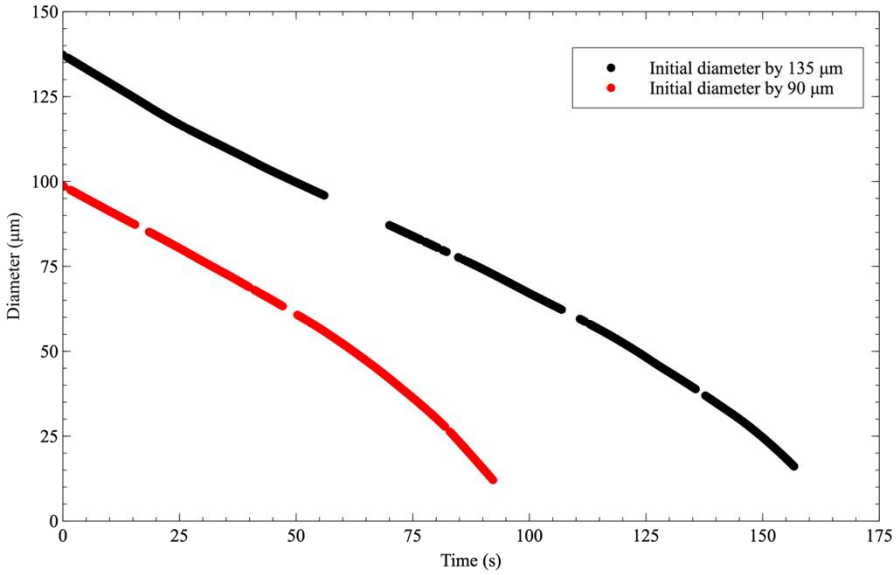

Figure IV-11: Diameter evolution for 2 droplets with different initial diameter dissolving in pure 1-decanol $f = 0$.

As expected, the droplet with bigger diameter took a longer time to dissolve (~ 160 s) compared to the smaller one (90 s).

The variation of diffusion flux as a function of time for the two droplets is illustrated in the Figure IV-12.

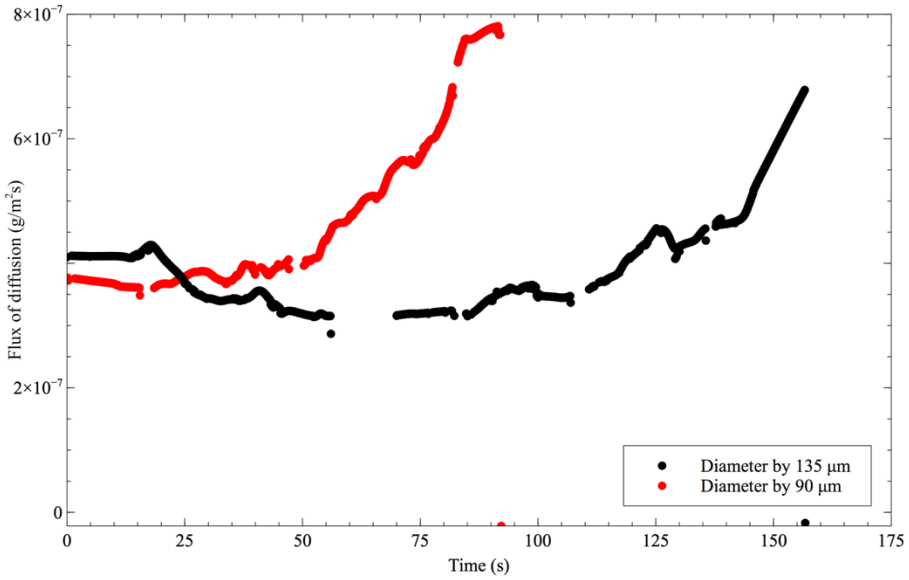

Figure IV-12: Flux of diffusion of 2 droplets with different initial diameter(90 µm and 135 µm) dissolving in pure 1-decanol ($f = 0$).

Firstly, the temporal evolution of the mass flux curve of a 135 µm droplet is considered. Since the diameter of the droplet is bigger than the depth of microchannel (120 µm), the droplet is confined between the top and the bottom of the channel. The flux of diffusion at the beginning of the process ($0 < t < 24s$) is larger than expected due to the higher velocity of 1-decanol at the top and bottom channel. However, when the droplet diameter is smaller than 120 µm (t around 24 s), the flux decreases and starts to keep a constant value, for a certain time, before increasing again. The shrinking of the droplet was compared again with the E-P modeling and a good agreement was found between the experimental and the E-P equation. This means that the dissolution process for oversize droplet is still in agreement with theory and no other factors but diffusion is involved in dissolution process. However, only lower than 120 µm diameter droplets are considered in the protein dehydration experiments to ensure the dissolution rate low enough to avoid skin formation.

IV.4.3. Typical experiment of droplet dissolution with lysozyme solution

As described above, single spherical Lysozyme solution droplets were formed and transported into 1-decanol to investigate the dehydration process of

lysozyme solution. Here, the concentration of Lysozyme solution explored ranges from 50 to 150 mg/mL, the size of initial diameter ranges from 60 to 120 µm and the saturation fractions of 1-decanol ranges from 0.1 to 0.9.

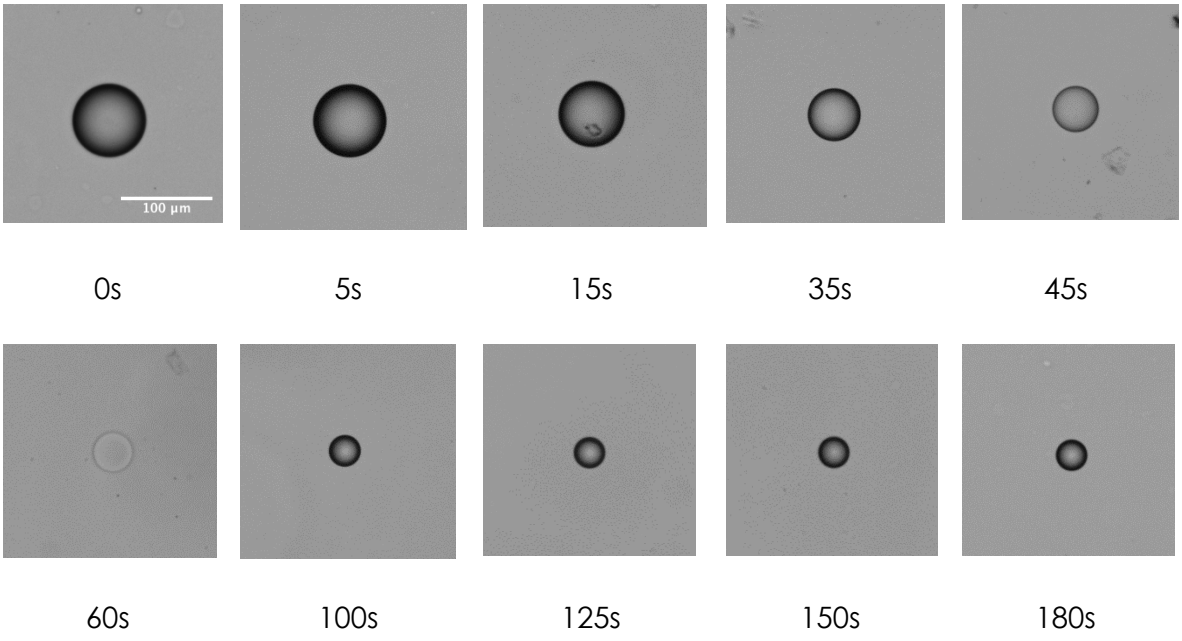

Figure IV-13: Dehydration process of a lysozyme solution droplet with initial concentration of 80 mg/mL in 1-decanol with saturation fraction $f = 0.4$

The general dehydration process of Lysozyme solution droplets in the 1-decanol medium with saturation fraction $f = 0.4$ is illustrated in the Figure IV-13. According to the picture sequence, the droplet disappeared at a certain time due to refractive index matching of protein solution and 1-decanol (e.g. in case $f = 0.4$, $t_{n-match} = 57$ s). When the chemical potential of water in the droplet and of water in the continuous phase are equal, i.e. when the thermodynamic equilibrium is reached, the diffusion of water stops and the droplet diameter remains constant as shown in the *Figure IV-14*.

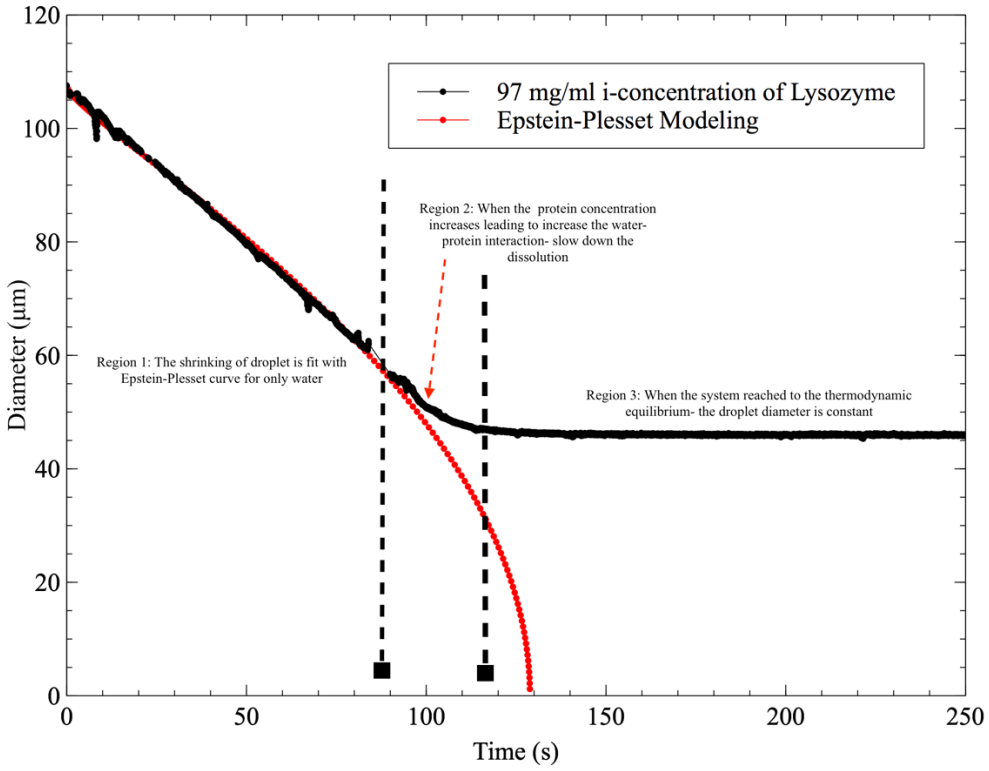

Figure IV-14: Comparison between the experimental data obtained from the dehydration of a 97 mg/mL lysozyme droplet in 1-decanol ($f = 0.3$) and the E-P modeling data for a droplet of pure water with the same initial diameter.

The use of microfluidic systems to study the dissolution of droplets has been rarely investigated in the literature. Hence, in order to test the dehydration process of a lysozyme solution droplet in 1-decanol using a microfluidic system, a comparison was performed between the evolution of a Lysozyme droplet with an initial concentration of 97 mg/mL in 1-decanol with $f = 0.3$ and the E-P modeling data of a droplet of pure water with the same initial diameter. The dehydration process can be divided into three parts. The first part, the shrinking of the diameter perfectly fits with the modeled curve for the pure water droplet. This means that in the first part of the dissolution process, the system behaves as an ideal system. The protein solution is diluted enough so that the water and protein interactions are negligible. The water removed in this part can be considered as bulk water (with water activity always equal 1). When the concentration of protein inside the droplet increases, protein-water interactions increase as well, the difference in chemical potential becomes less important and the dissolution is slowed down. In that case, as shown in the *Figure IV-14* the droplet diameter decreases from 57 µm down to 43 µm in 50 seconds. When the water activity on

both sides of the droplet interface are equilibrated, the diffusion of water stops and thus the droplet diameter stops shrinking.

IV.4.3.1. The influence of initial diameters

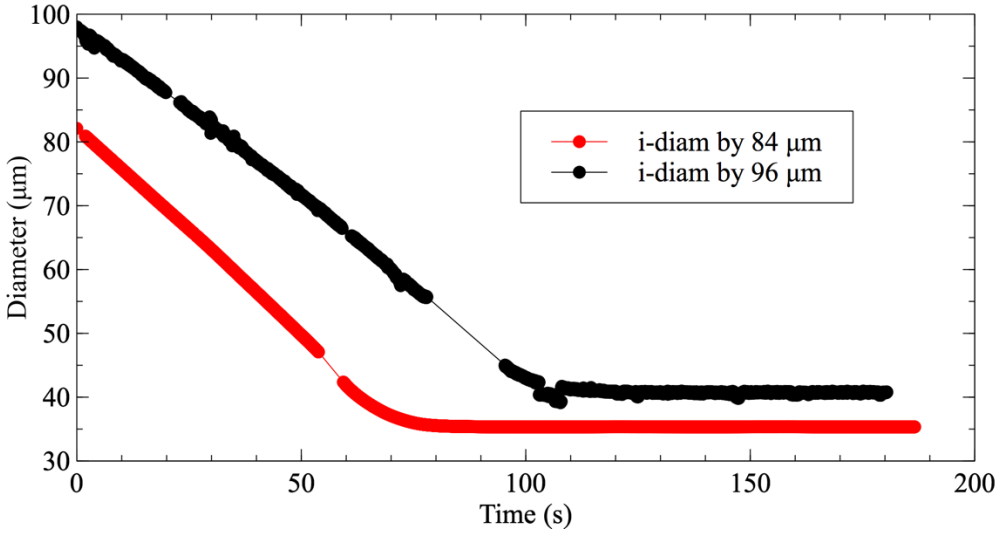

Figure IV-15: Influence of initial diameter in the dehydration process of a 90 mg/mL lysozyme solution droplet in 1-decanol with saturation fraction $f = 0.4$.

To illustrate the influence of the initial diameter on the dehydration process, let consider the case of dehydration of two droplets with the same initial concentration 90 mg/mL in 1-decanol ($f = 0.4$) with two different diameters (84 µm and 96 µm). The results obtained in terms of diameter evolution as a function of time are given in the Figure IV-15 and the corresponding mass flux are presented in the *Figure IV-16*. As expected, larger droplets take more time to dehydrate and the final diameter is proportional to the initial diameter. The most interesting observation in this experiment is depicted in the *Figure IV-16*. Indeed, the mass flux of the larger droplet is almost constant (even if a small increase is observed, which can be attributed to an experimental error due to the measurement method) during the first part of the dissolution process and then decreases down to 0 at the thermodynamic equilibrium. For the smaller droplet, a different behavior is observed. After a period during which the mass flux is almost constant, an important increase is observed before the flux starts to decrease. The formation of this flux peak could initially be attributed to the formation of a skin of protein (aggregated proteins at the interface), this kind of peak in the flux can be characteristic of a skin breakage.

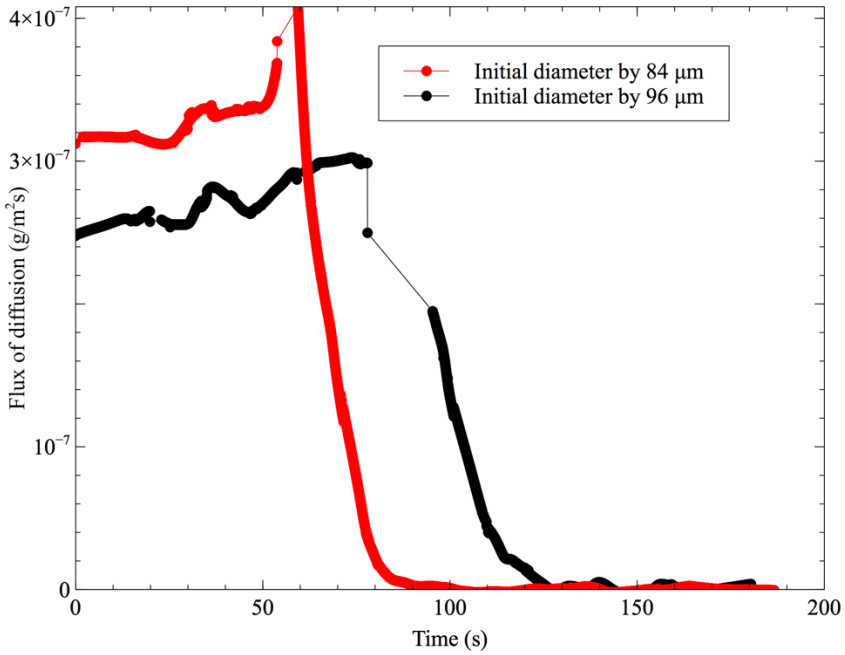

Figure IV-16: Flux of diffusion of water to drying medium($f = 0.4$) with different droplet's initial diameter of Lysozyme droplets with 90 mg/mL.

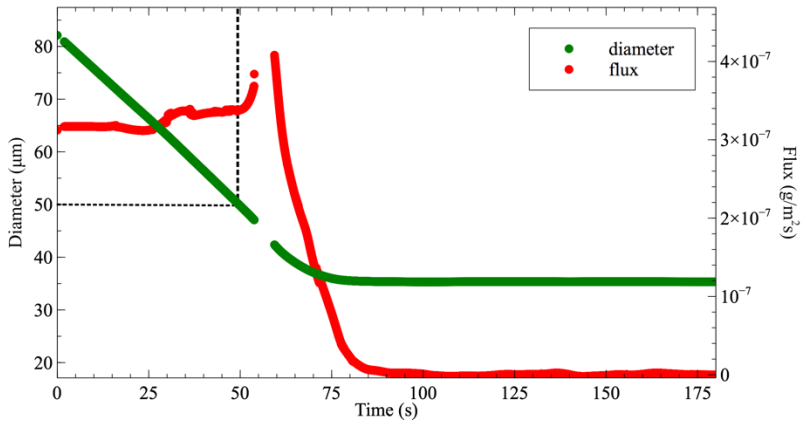

Figure IV-17: Relation between the mass diffusion flux and evolution of diameter in 1-decanol $f = 0.4$.

However, in all the experiment performed when f was greater than 0.05, no skin formation was observed during the droplet dehydration (Rickard and coworker made also this observation)(Rickard, Duncan, and Needham 2010). In addition, if a skin is formed at the droplet interface, the mass flux should first decrease, due to the skin formation. The skin at the interface is an additional barrier for the diffusion of water through the interface. When the skin breaks, as

the chemical potential of water inside the droplet is much higher than at the outside, a "fast" diffusion is observed to reach the thermodynamic equilibrium. This induces a fast increase (peak) of the mass flux. From this observation and from the observation of the temporal evolution of the flux of pure water shown in the Figure IV-12, which presents the same behavior as the protein solution, the increase of the flux can be attributed both to the lower size of the droplet and to the increase of the surface to volume ratio, which favor the diffusion process. As shown in the Figure IV-17 in the case of the protein solution dehydration, the increase of the mass flux is obtained when the droplet diameter is below 50 µm. Similar results are obtained for the dissolution of the pure water droplets of 90 µm presented in the Figure IV-9. In that case, the mass flux increases when the droplet diameter is lower than 50 µm.

These later observations are also supported by the simulation of the dissolution of Lysozyme solution droplets (presented in section IV.2.3).

IV.4.3.2. The influence of initial protein concentration

In order to study the influence of the initial concentration of lysozyme, experiments of droplets dehydration were carried out with the same initial droplet diameter at different initial concentrations, in1-decanol with a saturation fraction $f = 0.25$. The evolution of the droplet diameter by the time is plotted in the Figure IV-18. As previously observed, no matter the lysozyme concentration used, the first part of the dehydration curve perfectly fits with the E-P model, (i.e. the dissolution of pure water). In addition, the higher initial concentration, the higher final diameter and the faster final state are reached. It can be explained that the flux of both droplets has the same magnitude and behavior and it is independent to the initial concentration. The temporal evolution of protein concentration inside the droplet was calculated using the temporal evolution of the measured diameter. The variation of Lysozyme concentration inside the droplet as a function of time is presented in the Figure IV-19. In both cases with the saturation fraction $f = 0.25$ 1-decanol medium, the final concentration is 1100 mg/mL.

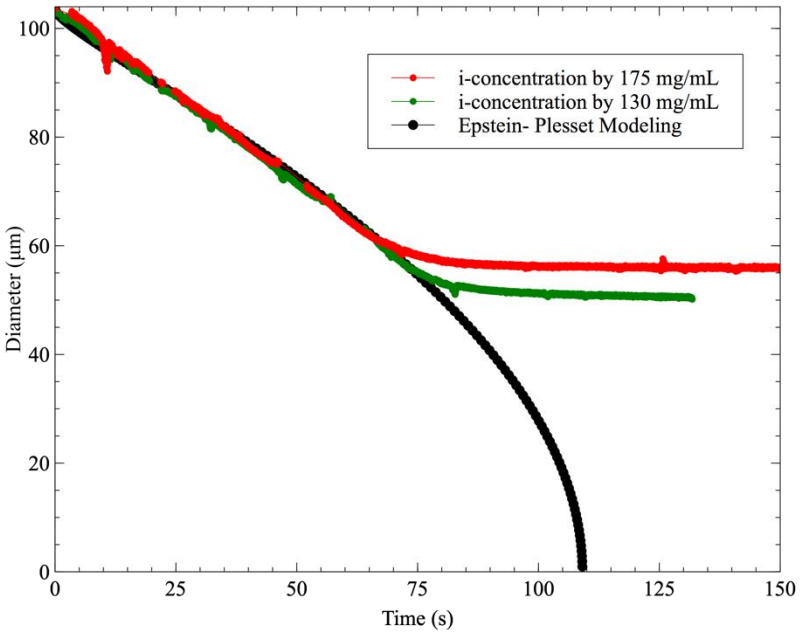

Figure IV-18: Diameter evolution of 2 droplets with the same initial diameter (100 µm) but different initial lysozyme concentration (130 and 175 mg/mL, respectively) dehydrating in 1-decanol $f = 0.25$ medium.

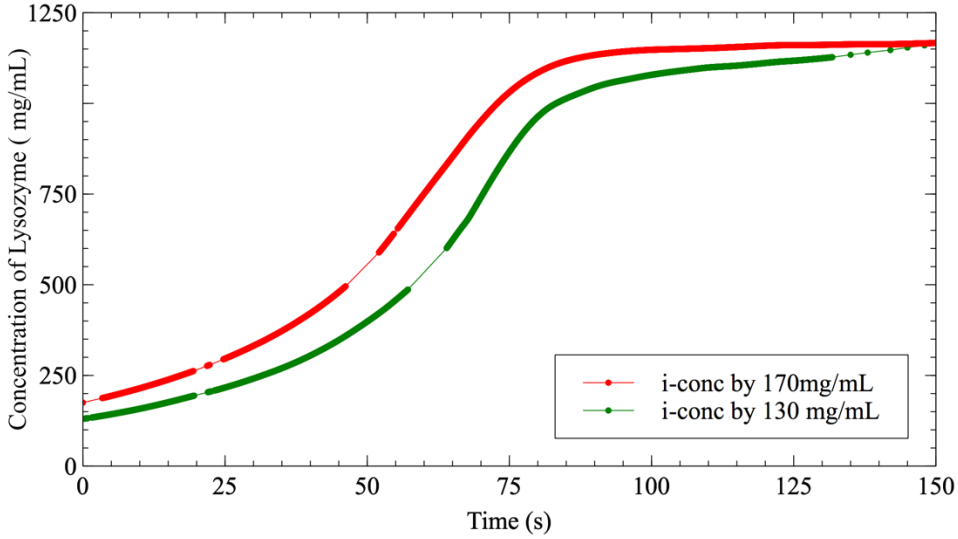

Figure IV-19: Concentration change of droplets with the same initial diameter (100 µm) but different initial concentration of protein (130 mg/mL and 175 mg/mL) in 1-decanol $f = 0.25$

Finally, some conclusions are extracted from this set of experiments. First, the protein concentration in the droplets reaches a constant value at the end of the process when the whole system reaches the equilibrium state. This value only depends on the saturation fraction of the drying medium. Consequently, higher

initial concentrations the droplets will reach the equilibrium faster. Second, from this preliminary results, some conclusions about the droplet dissolution process in a microfluidic system can be drawn:

- If the initial diameter is smaller than the channel height and the droplet generation frequency is low enough, the continuous phase can be considered as infinite compared to the droplet size.
- The initial diameter and the initial droplet concentration have no effect on the final state of the droplet
- At high initial protein concentration, the final state can be reached faster without affecting the mass flux and the final concentration.

IV.4.4. From the influence of saturation fraction to the equation of state of the protein

IV.4.4.1. Influence of the saturation fraction

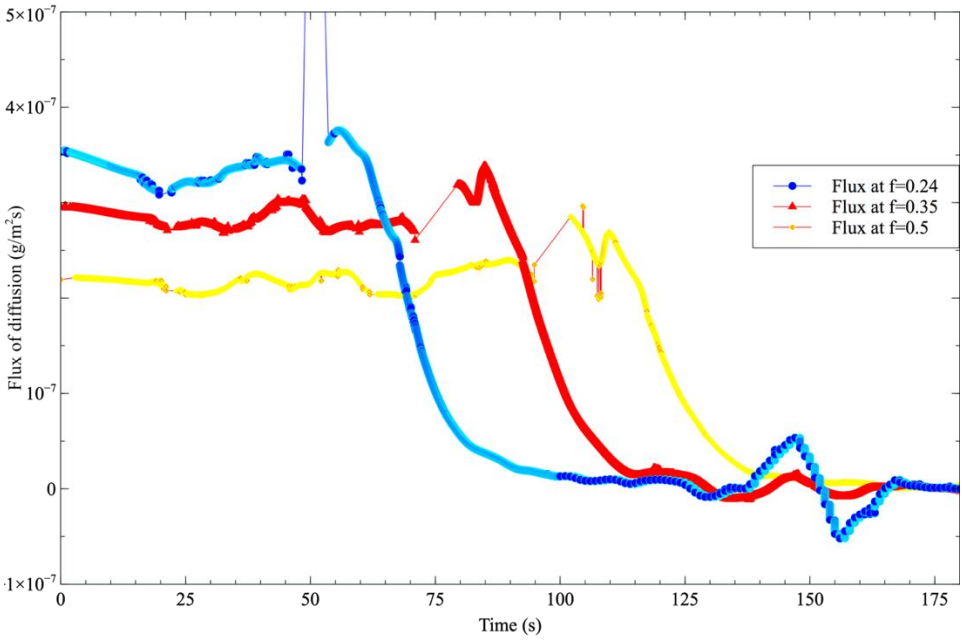

Figure IV-20: The mass flux of droplets with the same initial concentration 100 mg/mL and same initial diameter 70 µm at 3 different values of $f = 0.24$, $f = 0.35$ and $f = 0.5$.

To test the influence of the saturation fraction of water in 1-decanol, protein droplets with the same initial diameter and the same initial concentration were dehydrated in 1-decanol with different saturation fraction. For instance, in the case of droplets with an initial diameter of 70 µm and initial protein concentration of 100 mg/mL the final diameters were 28 µm, 31 µm and 35 µm for $f = 0.24$, 0.35

and 0.5 respectively. The temporal evolution of the water flux in these experiments are presented in the Figure IV-20. At the beginning of the experiment, the flux is constant. Then due to the decrease of the droplet size, the flux increases and then decreases until the system reaches the thermodynamic equilibrium. It is worth noting that when the saturation fraction increases, the flux is lower as the driving force (i.e. the difference in the chemical potential between the water inside and outside the droplet) of the transfer is lowered.

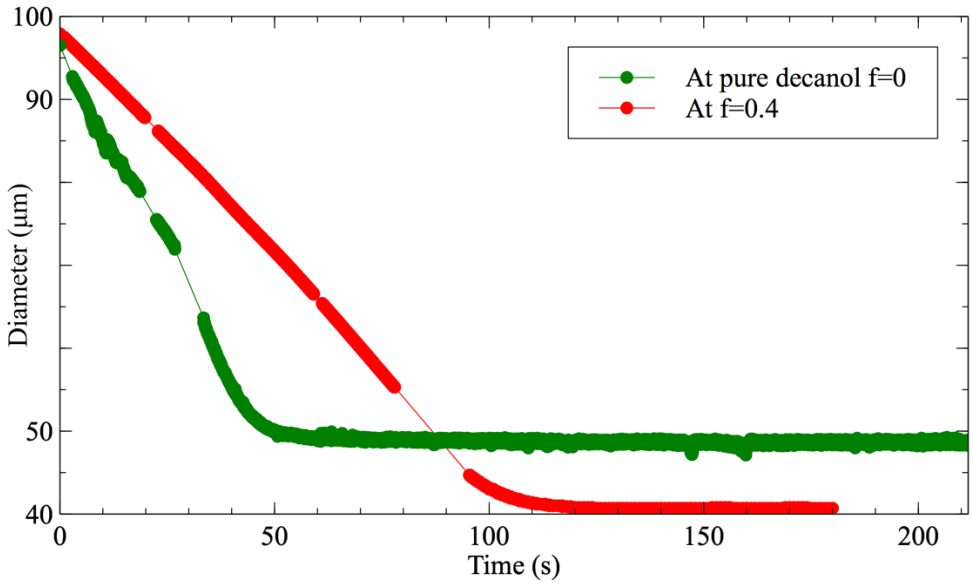

Figure IV-21: Evolution of analogous droplets with 98 µm initial diameter and 100 mg/mL concentration at two different saturation fractions $f = 0$ and$f = 0.4$. Here, the skin formation is observed for case $f = 0$ leading the final diameter of droplet is larger than in $f = 0.4$.

The Figure IV-21compares the dehydration of a lysozyme solution droplet (with a 98 µm initial diameter and 100 mg/mL initial concentration) in the pure decanol to the dehydration of an analogous droplet in decanol with $f = 0.4$. It is noticed that the final diameter in dehydration by pure 1-decanol is higher than in decanol which water is introduced. As shown in the Figure IV-22, the aqueous droplet loses its spherical shape, clearly showing that a skin is formed during the dissolution process. This skin on the surface of the droplet prevents the mass transfer of water and leads a larger amount of water in the droplet at the end of the dissolution process.

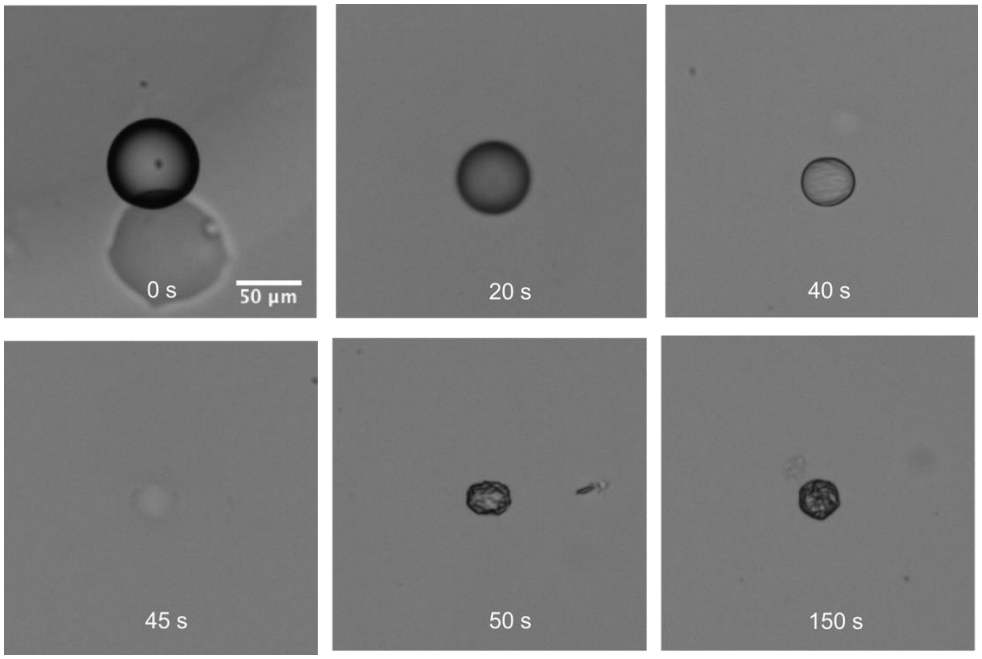

Figure IV-22: The formation of skin on a droplet during its dehydration process at $f = 0$. The change of the droplet shape can be clearly observed.

IV.4.4.2. The hydration of protein solution.

As observed in the previous experiments, as long as the droplet diameter is smaller than the height of the microfluidic channel in which droplets are generated, the final state of the protein solution droplet is only affected by the saturation factor. To study the influence of the saturation factor, and thus the relation between the hydration state of the protein in the solution and the water activity, several experiments were performed with a saturation factor ranging from $f = 0.1$ to $f = 0.84$, corresponding to a water activity ranging from 0.12 to 0.95. Some experimental conditions used during the dehydration experiments are given in Table IV-1.

Table IV-1: Experimental conditions for each dehydration experiment performed

Initial concentration (mg/mL)	***Initial diameter (µm)***	***n-matched diameter (µm)***	***End-diameter (µm)***	***Saturation fraction***	***Water activity***	***Mean a_w***	***STD a_w***	***Mean h***	***STD h***	***Mean φ_{Lys}***	***STD φ_{Lys}***	***Mean Π(bar)***	***STD Π(bar***
150.5-176.28	*90.11-95.45*	*66.64-67.6*	*48.62-51.17*	*0.02*	*0.05*	*0.05*	*0.00*	*0.05*	*0.06*	0.88	0.07	4113.07	0
109.37	*104.69*	*62.34*	*46.70*	*0.05*	*0.12*	*0.12*	*0.00*	*0.07*	*0.00*	0.86	0.00	2906.65	0.00
106.58 - 139.29	*102.85-109.5*	*61.47- 68.16*	*46.07-50.5*	*0.11*	*0.25*	*0.25*	*0.01*	*0.06*	*0.03*	0.87	0.03	1898.76	42.72
122.04 -140.96	*66.09-98.93*	*40.82-64.11*	*30.97-48.58*	*0.15*	*0.30*	*0.30*	*0.03*	*0.10*	*0.00*	0.83	0.00	1632.8	118.25
99.99-156.68	*69.49-108.28*	*42.29 -72.53*	*31.96-53.93*	*0.22-26*	*0.44-0.5*	*0.47*	*0.02*	*0.11*	*0.03*	0.82	0.03	1021.93	54.39
83.54-174.27	*69.65103.48*	*44.71-67.34*	*34.56-50.40*	*0.27-0.3*	*0.51-0.55*	*0.52*	*0.02*	*0.13*	*0.04*	0.80	0.04	883.73	40.25
90.74-147.25	*66.46-106.3*	*41.07-60.48*	*31.8-45.9*	*0.31-0.33*	*0.56-0.59*	*0.58*	*0.01*	*0.12*	*0.03*	0.81	0.02	739.73	33.71
90.74-118.95	*66.01-106.08*	*36.94-64.96*	*28.41-50.41*	*0.35*	*0.61*	*0.61*	*0.00*	*0.13*	*0.02*	0.8	0.02	666.74	0
57.67-89.16	*71.3-97.98*	*34.3-52.25*	*26.23-40.77*	*0.40*	*0.67*	*0.67*	*0.00*	*0.14*	*0.03*	0.79	0.03	550.79	0
67.11-80.25	*83.69-96.37*	*42.35-50.61*	*33.8-39.3*	*0.45*	*0.72*	*0.72*	*0.00*	*0.17*	*0.06*	0.77	0.05	455.29	0
85.67-146.52	*90.34-107.98*	*49.59-70.88*	*38.3-53.14*	*0.48*	*0.74*	*0.74*	*0.00*	*0.15*	*0.08*	0.78	0.07	401.98	7.68
95.27-148.75	*66.31-100.92*	*37.7166.58*	*29.8-53.10*	*0.5-0.52*	*0.76-0.77*	*0.77*	*0.01*	*0.19*	*0.04*	0.75	0.04	364.22	10.68
74.29-108.59	*67.44-99.26*	*36.07-58.84*	*29.08-46.68*	*0.56-0.59*	*0.80-0.83*	*0.82*	*0.0075*	*0.26*	*0.04*	0.88	0.07	4113.07	0

The obtained results were analyzed using equation Eq. IV-17, for the determination of the ratio of the mass of water to the mass of the protein. In addition, according to equation Eq. IV-23 and Eq. IV-19, the osmotic pressure has been calculated from the water activity and the volume fraction of the protein concentration. The Table IV-1 presents the mean value and the corresponding standard deviations for the amount of water per amount of Lysozyme h, the water activity a_w and the volume fraction of Lysozyme φ_{Lys}. At least 5 droplets were analyzed for each experiment to attain a meaningful average value. It should be noticed that for high values of the saturation factor, the time needed to reach the equilibrium state is longer than the residence time of the droplet in the microfluidic channel. For these experiments, the droplets were generated in the microfluidic channel and then stored in a petri dish in order to measure the final state of the droplet. Only the initial diameter and the final diameter were measured. The equilibrium hydration levels at the end of the dissolution process are shown as a function of a_w in the *Figure IV-23* along with data published in the literature, (Rickard, Duncan, and Needham 2010)(Lüscher-mattli and Rüegg 1982). In all cases, a higher a_w in the surrounding medium resulted in a higher water content in the final protein phase. At a_w > 0.8, the decanol dehydration data is in good agreement with the desorption isotherm and with single-particle vapor sorption data obtained from Rickard et al. However, for a_w < 0.8 the experimental protein beads show lower levels of hydration than the one obtained by Rickard technique although they are in agreement with the absorption data.

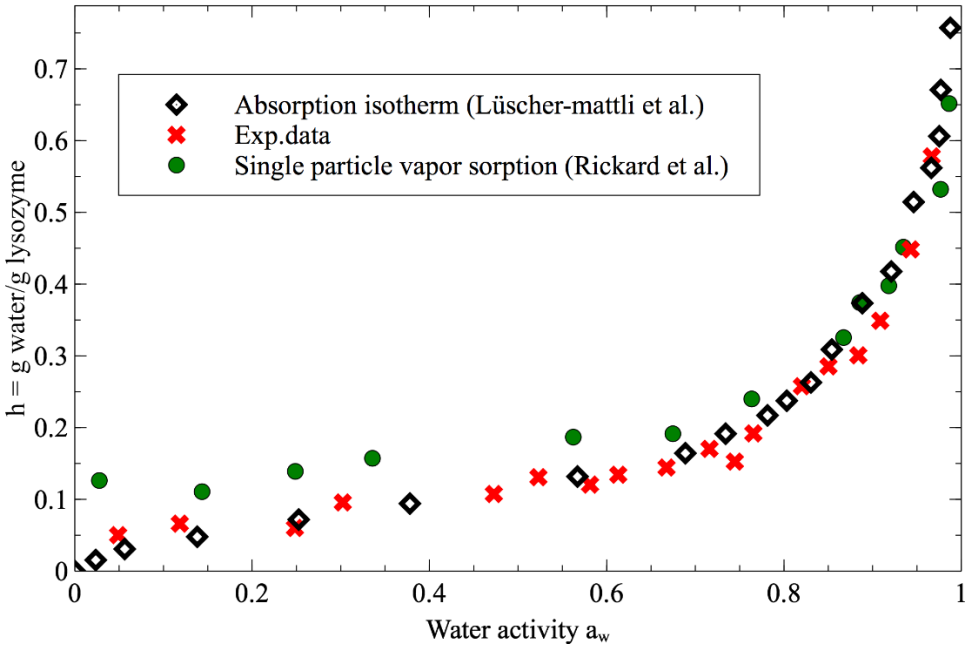

Figure IV-23: Equilibrium hydration levels at the end of the protein droplets dehydration process using 1-decanol are shown as a function of a_w compared to other data previously reported in the literature (Absorption isotherm(Lüscher-mattli and Rüegg 1982) and Single particle vapor sorption(Rickard, Duncan, and Needham 2010))

IV.4.4.3. The equation of state of the protein.

The evolution of the osmotic pressure as a function of the volume fraction of protein inside the droplets are plotted in the Figure IV-24 Together with the data obtained by Rickard et al. and the work Pasquier et al. (Coralie Pasquier et al. 2016). A good agreement between the experimental data in this work and the data from the work of Pasquier *et. al.* is observed. In their work, the osmotic pressure was determined using a dialysis membrane from the experimental procedure of Bouchoux et al.(Bouchoux et al. 2010). Their method is a complementary method since it provides less "dried" protein solutions compare to the dehydration process in an organic solvent. As mentioned above, the main reason rises from the fact that at high amount of water in 1-decanol, the dissolution process takes much more time to reach the thermodynamic equilibrium than the residence time of the droplet in the microfluidic chip.

The Carnahan-Starling equation of state is also plotted in the Figure IV-24 for a Lysozyme with a gyration radius of 14.64 Å(Torre, Huertas, and Carrasco 2000). It is worth noting that all the experimental data (for the present work and from

literature) are in good agreement with the trend given by the equation of state. However, in contrast to the data obtained by Pasquier et al. no crossover of the Carnahan-Starling equation is observed in our data. This could probably due to a different organization of the proteins molecules during between our experiments and their experiments. In addition, as no crossover of the equation of state is observed, during protein dehydration, the protein seems to remain in a repulsive state. However, this supposition needs to be confirmed by subsequent analysis (by SAXS for instance).

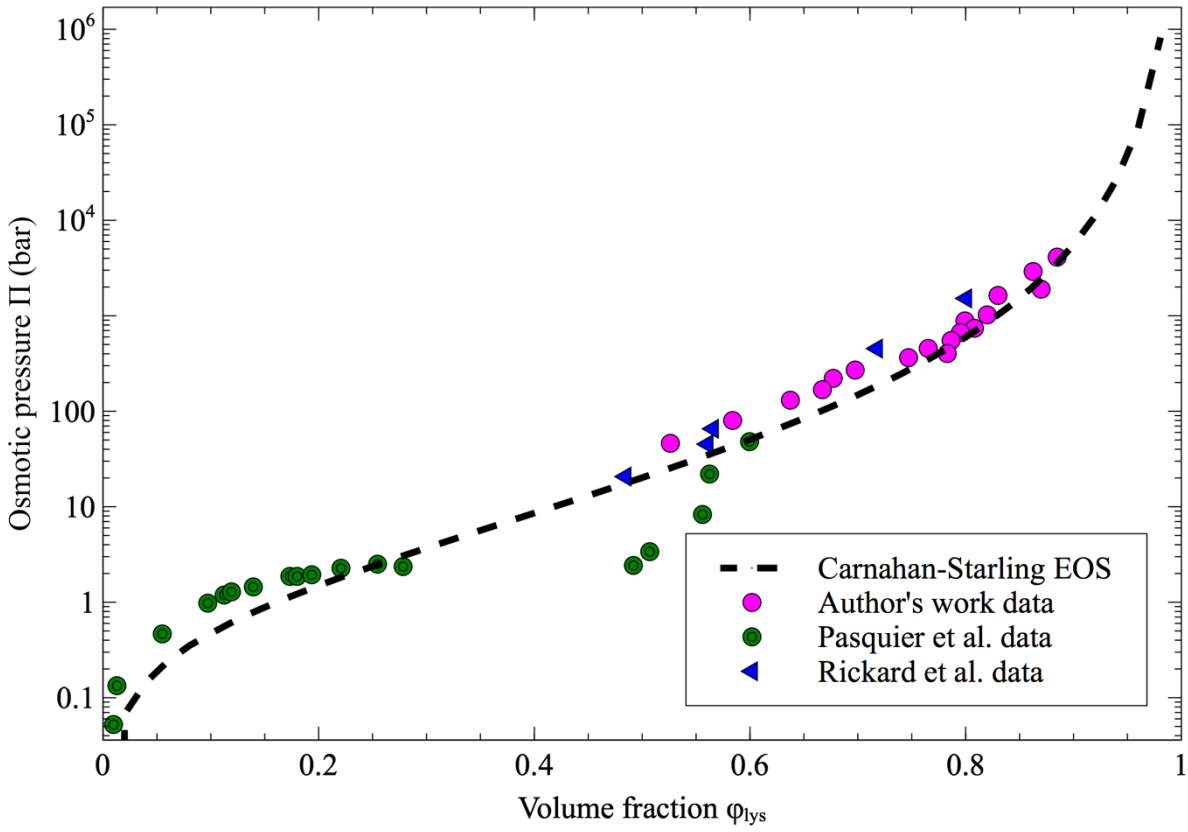

Figure IV-24: Osmotic pressure Π as function of volume fraction of Lysozyme. The empirical data from this work is compared with osmotic pressure values previously reported in literature: (bullseyes)of Pasquier et al(Coralie Pasquier et al. 2016), (filled triangle) of Rickard(Rickard, Duncan, and Needham 2010) and (dash line) the Carnahan-Starling approximation.

IV.4.5. Modeling of the dissolution process.

As the Carnahan-Starling equation of state describes well the data obtained for the final state of the protein, it has been implemented in the modeling presented in section IV.2.3. A comparison between modeling and empirical data

in the dehydration process by 1-decanol with $f = 0.1$ is presented in the Figure IV-25 for the temporal evolution of the droplet size and in the Figure IV-26 for the mass flux. It is clearly observed that the model is in good agreement with the experimental data for the diameter. But the final diameter is over estimated with an inaccuracy of around 5 to 7µm.

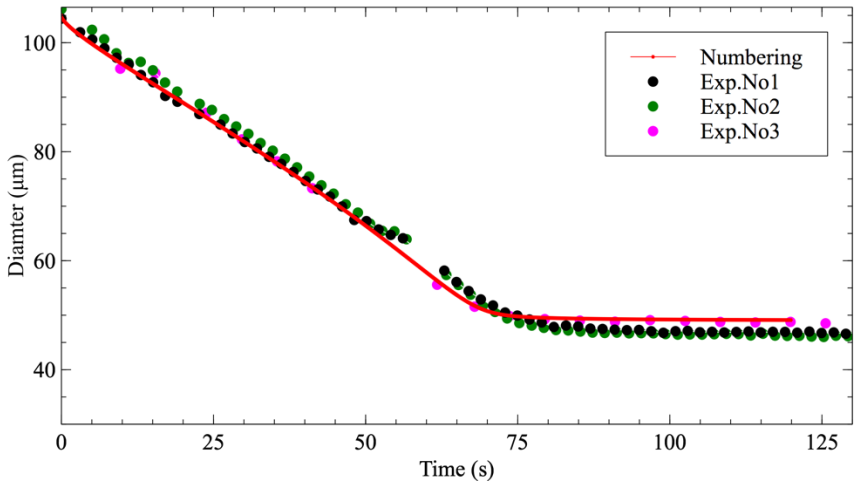

Figure IV-25: Evolution of droplet diameter versus modeling data for $f = 0.1$

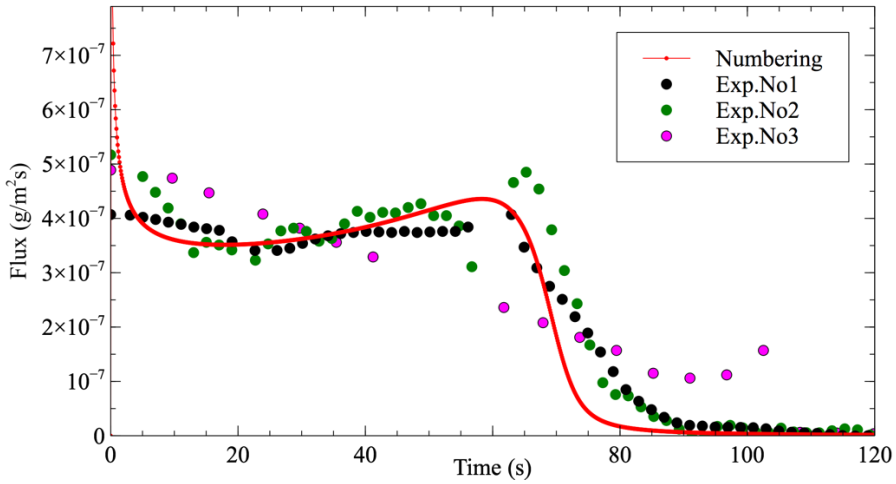

Figure IV-26: Experimental mass flux versus modeling data for $f = 0.1$

In the case of the flux, a less quantitative agreement is obtained, but the general experimental trend is respected. As mentioned above in the experiments, after a nearly constant value of the flux at the beginning of the dissolution process, the mass flux increases significantly and decreases afterward. In the case of the modeling results, the increase of the mass flux happens at $t = 60$ s

corresponding to diameter of 55 μm, which is in good agreement with the increase observed in the experiments.

Some important differences between the modeling and the experiments should be noticed. Firstly, at the beginning, it is noticed a huge decrease of the mass flux (probably due to a numerical error in the estimation of the initial diameter) which is not observed experimentally. The end of the dehydration process predicted by the numerical model is 20 s faster than in the experimental process. In addition, the mass flux decrease predicted by the model is faster than the mass flux obtained experimentally. Similar trends are observed for the modeling of the dehydration process at higher saturation fractions. In the Figure IV-27 and the Figure IV-28, the results of the modeling and the corresponding experimental data are presented for the evolution of the droplet diameter and the mass flux with time. Again, the correlation in general lines is preserved and well described by the numerical model and the final diameter is still overestimated by the model. However, the decrease of the mass flux obtained in this case agrees well with the experimental data.

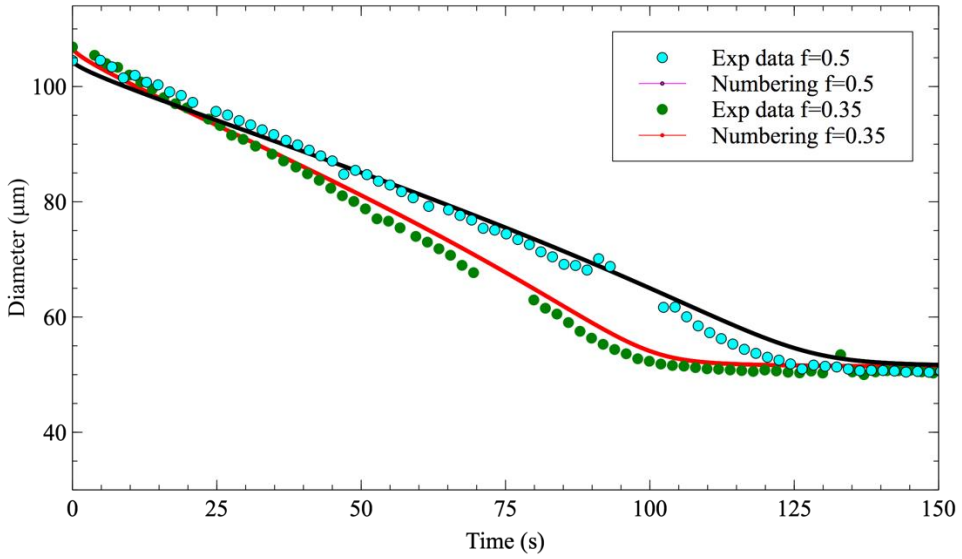

Figure IV-27:Evolution of diameter (μm) versus modeling data for $f = 0.35$ and $f = 0.5$.

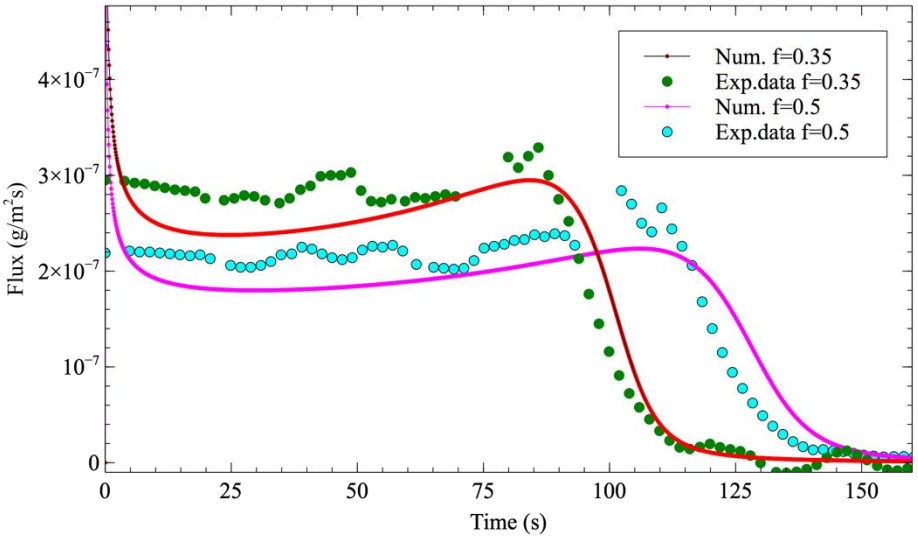

Figure IV-28: Experimental mass flux(g/m²s) as a function of time versus modeling data for $f = 0.35$ *and* $f = 0.5$

The differences between the experimental data and the modeled data can be attributed to different issues in the model. First, as stated in section IV.2.3, in the continuous phase a strong assumption (due to the numerical method used and due to the non-linearity of the equation to be solved) was made on the fact that the diffusion in the continuous phase behaves as in an ideal system. In addition, in order to satisfy the condition that at $c = c_{sat}$, $a_w = 1$, and at $c = 0$, $a_w = 0$, it was postulated that $a_w = c/c_{sat}$ meaning that the activity coefficient is constant and equal to $\gamma_w = \frac{1}{c_{sat}}$. Different modeling of the thermodynamic properties of the 1-decanol / water solution were tested, using the relation proposed by Segatin et al.(Šegatin and Klofutar 2004), but due to the uncertainty of the experiments (from the water activity in decanol and water activity in lysozyme solution), the results were not satisfactory. The main reason is that, at the beginning of the dissolution process, as soon as the water start to dissolve in the continuous phase, the calculated water activity inside the droplet becomes lower than the water activity in the continuous phase, which stops the dissolution process. In order to improve the modeling, a more detailed thermodynamic model is needed for the description of the continuous phase (i.e. using a PC-SAFT model for instance).

The main purpose of our modeling approach is that if it is possible to follow the entire dissolution process of a colloidal solution. Then by taking the assumption

that the dissolution process is slow enough, at each time steps, the droplet is in a "quasi" equilibrium state with the surrounding medium. This means that the colloidal solution in the droplet goes through all the equilibrium states from a water activity of 1 to the final water activity. In that way, if the modeling is sufficiently precise, the equation of state of the colloidal solution can be obtained in a single experiment with a single droplet. To illustrate this, the evolution of a lysozyme droplet and the water activity as a function of time is given in the Figure IV-29 for a droplet with an initial diameter of 95 µm and a saturation fraction $f = 0.2$.

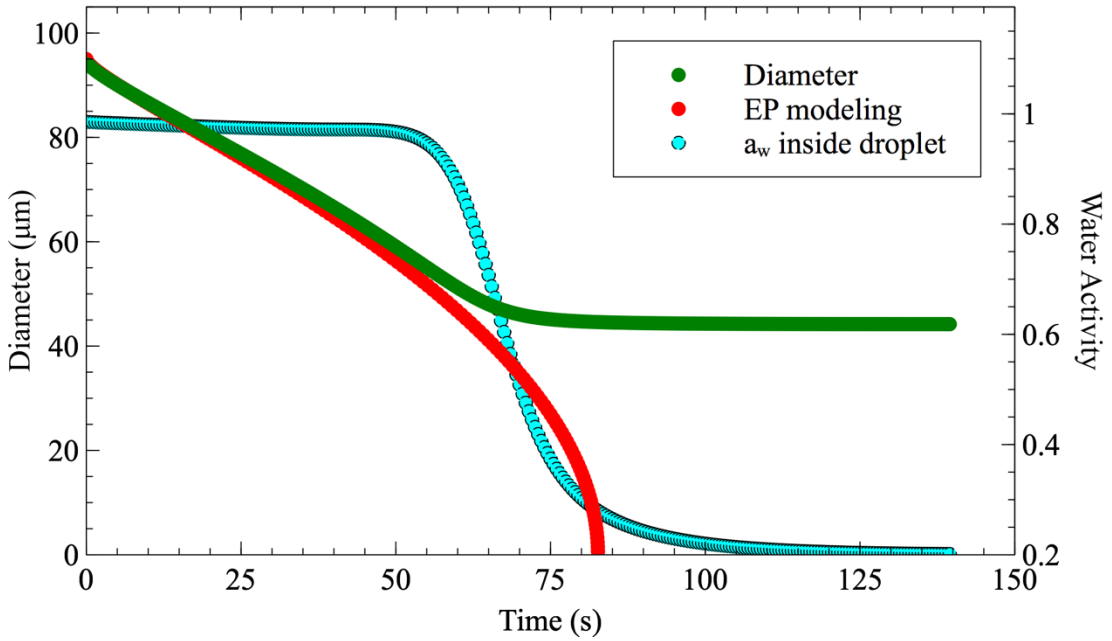

Figure IV-29: Evolution of droplet diameter and water activity inside as a function of time.

As it is qualitatively seen in this figure, at the beginning of the dissolution process, the activity of the water remains close to 1 and therefore the temporal evolution of the droplet diameter agrees well with the E-P model. Then the activity of water inside the droplet slowly decrease and the evolution of the diameter is no more in agreement with E-P modeling. At the end of the process, the activity coefficient reaches a constant value. The coupling of this experimental setup with an improved version of the numerical model (i.e. with no assumption of the continuous phase and a good thermodynamic model of the continuous phase),

can be a highly efficient method for the determination of the equation of state of colloidal systems.

IV.5. Conclusions and Perspectives

In this chapter, the use of microfluidic platforms is proposed to study the colloidal droplets dissolution in an organic solvent. Some important remarks are extracted from this work:

A microfluidic platform was successfully fabricated based on soft lithography method. The fabricated microfluidic chips satisfied all the requirements for following the entire dissolution/dehydration of water/Lysozyme solution droplets in 1-decanol media: achieving the generation of stable aqueous droplets and a large enough channel for being considered as infinite.

The experimental data of water droplet dissolution in the microfluidic chip were compared to E-P modeling data. The data were found in good agreement, thus validating the microfluidic setup in which the dissolution process was dominated by the diffusion of water molecules without the presence of convection.

The influence of different factors, namely initial protein concentrations, initial droplet diameters, and the saturation fraction of the surrounding medium, were investigated. However, only the saturation fraction was found to play a significant role in the dissolution/dehydration process as long as the diameter of the droplet is smaller than the height of the channel. At the same saturation fraction, the final state of lysozyme concentration will be the same no matter the value of mass flux nor the initial concentration of protein.

The hydration isotherms of lysozyme in aqueous media were obtained. Results were found to be in good agreement with the data previously reported in the literature. Moreover, the residence time to reach the isothermal equilibrium was significantly shorter than the one required using the other methods reported in the literature such as using dialysis membranes.

The first approach of modeling that describes the behavior of droplet dissolution is developed and proposed. In this case, the modeling result agrees quite well with the experimental data for the droplets diameter evolution. However, the dissolution time predicted by the model was faster than the one observed experimentally. Nevertheless, the general experimental trend was preserved and well described by the numerical model. On the other hand, the numerical modeling for the flux displayed a lower quantitative agreement, although the general experimental trend is still respected. These deviations can be explained by differences coming from the model related to the initial assumptions which are not satisfied.

However, several questions in this study are subject to improvement. First of all, some perspectives for technical issues are worth to be mentioned. The flow-focusing structure operation, for droplet generation, depends on the syringe pump system. Unfortunately, the syringe pump system reached its operational limit when very small droplet was generated leading to instability in droplet generation. To improve this, the use of a pressure controlled system, able to generate isolated droplets on demand in a more reproducible way is proposed.

During the dissolution process of protein solution, the refractive index of protein solution inside droplet changes as a function of protein concentration. When the two refractive indexes of organic phase and protein solution droplet matched, the droplet became invisible, causing important errors in the detection of droplet size. Thus, a special technique such as the Schlieren method can be coupled with the microfluidic system in order to present a more sensitive technique to monitor the refractive index variation.

With these improvements, an automatic tracking of the droplets flowing in the channel can easily setup. This would allow recording the entire dissolution process with higher precision.

Concerning the modeling, a complete thermodynamic model should be developed to describe the activity of water in decanol. The perturbed-chain statistical associating fluid theory (PC-SAFT) is proposed for developing this model

in the future. Additionally, the numerical model should be improved to solve non-linear partial derivative equations.

Chapter V GENERAL CONCLUSION

The work presented in this thesis spans a bottom-up approach for the development of new and more efficient methodologies for the study of the behavior of protein molecules in solution.

First, in order to provide new and high-throughput analytical tools allowing a dramatic improvement on reagent consumption and experimental time, a fast, low-cost and robust protocol for microfluidic chips fabrication was developed. This protocol, based on cast molding over master molds fabricated with inexpensive dry film photoresists presents the following advantages:

High resolution, fast prototyping and cheap materials: 2D structures can be fabricated in normal laboratory conditions (avoiding expensive clean room facilities) with low resolution film masks obtaining operative microfluidic channels down to 30 µm wide. The whole process from CAD design to real systems fabrication takes less than 24 hours, and the unit cost for the fabrication of a chip is less than 5 euros.

Easy modification of microchannel surface properties: Several simple techniques are proposed to change the surface chemistry of the micro-channels to make them hydrophilic or hydrophobic, depending on their planned use.

High chemical and pressure resistance: The chips fabricated in NOA 81 and OSTE materials were proven to stand some common organic solvents demonstrating a very good resistance without showing any significant damage of the fluidic structures. Additionally, microfluidic systems were also demonstrated to stand pressures up to 200 bar for more than 20 minutes maintaining their operability.

Second, the fabrication protocol presented in Chapter II of the thesis allowed us to develop low-cost microfluidic platforms for two different applications. In Chapter III, protein molecular interactions in solution in presence of precipitant agents (salt) were studied by combining high-throughput droplet-based microfluidics and small angle X-ray scattering techniques. A complete optimization of experimental parameters was performed in terms of materials selection able to resist radiation damage and to not to affect protein structural properties in solution. The experiments were carried out at beamline 29, ESRF

Grenoble, France with two model proteins. The special microfluidic setup configuration was firstly tested with Rasburicase enzyme, which is known to be especially sensitive to denaturation. The results presented as a function of scattering intensity versus scattering vector, shown a strong agreement with data previously reported in the literature, validating the novel experimental protocol. Subsequently, the interaction of lysozyme molecules at the various concentration of salt NaCl was studied. It was shown that in absence of salt the protein displays a repulsive state. By means of a screening of conditions increasing salt concentration (i.e. increasing the ionic strength), it was shown that the protein interaction potential changed smoothly from a repulsive to an attractive state, giving an indication on protein solubility and suggesting an optimal range of conditions in which protein crystallization could be successfully performed. Experiments were successfully carried out using just a few milligrams of protein and few tens of microliters of solution.

Finally, in Chapter IV, a second droplet-based microfluidic platform was developed to generate lysozyme solution droplets in 1-decanol continuous media. Droplets dehydration (occurring due to the diffusion of water molecules into the unsaturated continuous phase) was monitored at various initial saturation fractions of 1-decanol, and the equation of state of lysozyme in solution was determined through the relation of the osmotic pressure between protein molecules and the volume fraction of protein inside the droplets. In addition, the influences of all factors affecting dehydration process (i.e. initial droplet diameter, initial lysozyme concentration of and 1-decanol saturation fraction) were investigated. At the end of the dehydration process (i.e. when the system reaches the thermodynamic equilibrium), the water activity inside droplet equals the given water activity in 1-decanol. Hence, the hydration isotherms can be obtained. The equation of state found by this approach showed a good agreement with data reported in the literature as well as with the Carnahan-Starling approximation. Additionally, a numerical approach to predict the evolution of droplets diameter during the dehydration process was also presented. In order to satisfy the model assumptions, water activity was assumed to be $a_w = c/c_{sat}$. The modeling results revealed small discrepancies with the

experimental data but preserved and well described the general trends. To improve the model, a more detailed thermodynamic model is required.

References

Akiyama, Shuji, Satoshi Takahashi, Tetsunari Kimura, Koichiro Ishimori, Isao Morishima, Yukihiro Nishikawa, and Tetsuro Fujisawa. 2002. “Conformational Landscape of Cytochrome c Folding Studied by Microsecond-Resolved Small-Angle X-Ray Scattering.” *Proceedings of the National Academy of Sciences* 99 (3): 1329–1334.

Als-Nielsen, Jens, and Des McMorrow. 2011. “X-Rays and Their Interaction with Matter.” *Elements of Modern X-Ray Physics, Second Edition*, 1–28.

Anderson, Janelle R., Daniel T. Chiu, Rebecca J. Jackman, Oksana Cherniavskaya, J. Cooper McDonald, Hongkai Wu, Sue H. Whitesides, and George M. Whitesides. 2000. “Fabrication of Topologically Complex Three-Dimensional Microfluidic Systems in PDMS by Rapid Prototyping.” *Analytical Chemistry* 72 (14): 3158–3164.

Baldwin, Kyle Anthony, Manon Granjard, David I. Willmer, Khellil Sefiane, and David John Fairhurst. 2011. “Drying and Deposition of Poly (Ethylene Oxide) Droplets Determined by Péclet Number.” *Soft Matter* 7 (17): 7819–7826.

Ballauff, Matthias, Jörg Bolze, Nico Dingenouts, Peter Hickl, and Dominic Pötschke. 1996. “Small-Angle X-Ray Scattering on Latexes.” *Macromolecular Chemistry and Physics* 197 (10): 3043–3066.

Barrett, Ray, Marc Faucon, John Lopez, Galder Cristobal, Fanny Destremaut, Arash Dodge, Pierre Guillot, Philippe Laval, Chloé Masselon, and Jean-Baptiste Salmon. 2006. “X-Ray Microfocussing Combined with Microfluidics for on-Chip X-Ray Scattering Measurements.” *Lab on a Chip* 6 (4): 494–499.

Bartolo, Denis, Guillaume Degré, Philippe Nghe, and Vincent Studer. 2008. “Microfluidic Stickers.” *Lab on a Chip* 8 (2): 274–279.

Bass, Robert B., and Arthur W. Lichtenberger. 2004. “Microcontact Printing with Octadecanethiol.” *Applied Surface Science* 226 (4): 335–340.

Bergmann, AGGO, G. Fritz, and O. Glatter. 2000. “Solving the Generalized Indirect Fourier Transformation (GIFT) by Boltzmann Simplex Simulated Annealing (BSSA).” *Journal of Applied Crystallography* 33 (5): 1212–1216.

Bolze, J., D. Pontoni, M. Ballauff, T. Narayanan, and H. Cölfen. 2004. “Time-Resolved SAXS Study of the Effect of a Double Hydrophilic Block-Copolymer on the Formation of CaCO 3 from a Supersaturated Salt Solution.” *Journal of Colloid and Interface Science* 277 (1): 84–94.

Bolze, Jörg, Tetsuro Fujisawa, Takashi Nagao, Kazushi Norisada, Hazime Saitô, and Akira Naito. 2000. “Small Angle X-Ray Scattering and 31 P NMR Studies on the Phase Behavior of Phospholipid Bilayered Mixed Micelles.” *Chemical Physics Letters* 329 (3): 215–220.

Bonneté, F., N. Ferté, J. P. Astier, and S. Veesler. 2004. “Protein Crystallization: Contribution of Small Angle X-Ray Scattering (SAXS).” In *Journal de Physique IV (Proceedings)*, 118:3–13. EDP sciences. http://jp4.journaldephysique.org/articles/jp4/abs/2004/06/jpiv411801/jpiv411801.html.

Bonneté, F., S. Finet, and A. Tardieu. 1999. “Second Virial Coefficient: Variations with Lysozyme Crystallization Conditions.” *Journal of Crystal Growth* 196 (2): 403–414.

Bouchoux, Antoine, Pierre-Emerson Cayemitte, Julien Jardin, Geneviève Gésan-Guiziou, and Bernard Cabane. 2009. “Casein Micelle Dispersions under Osmotic Stress.” *Biophysical Journal* 96 (2): 693–706.

Bouchoux, Antoine, Geneviève Gésan-Guiziou, Javier Pérez, and Bernard Cabane. 2010. “How to Squeeze a Sponge: Casein Micelles under Osmotic Stress, a SAXS Study.” *Biophysical Journal* 99 (11): 3754–3762.

Bouchoux, Antoine, Peng Qu, Patrice Bacchin, and Geneviève Gésan-Guiziou. 2014. “A General Approach for Predicting the Filtration of Soft and Permeable Colloids: The Milk Example.” *Langmuir: The ACS Journal of Surfaces and Colloids* 30 (1): 22–34. doi:10.1021/la402865p.

Brennich, Martha Elisabeth, Jens-Friedrich Nolting, Christian Dammann, Bernd Nöding, Susanne Bauch, Harald Herrmann, Thomas Pfohl, and Sarah Köster. 2011a. “Dynamics of Intermediate Filament Assembly Followed in Micro-Flow by Small Angle X-Ray Scattering.” *Lab on a Chip* 11 (4): 708–716.

———. 2011b. “Dynamics of Intermediate Filament Assembly Followed in Micro-Flow by Small Angle X-Ray Scattering.” *Lab on a Chip* 11 (4): 708–716.

Carlborg, Carl Fredrik, Tommy Haraldsson, Kim Öberg, Michael Malkoch, and Wouter van der Wijngaart. 2011. “Beyond PDMS: Off-Stoichiometry Thiol–ene (OSTE) Based Soft Lithography for Rapid Prototyping of Microfluidic Devices.” *Lab on a Chip* 11 (18): 3136–3147.

Carlborg, Carl Fredrik, Alexander Vastesson, Yitong Liu, Wouter van der Wijngaart, Mats Johansson, and Tommy Haraldsson. 2014. “Functional Off-stoichiometry Thiol-ene-epoxy Thermosets Featuring Temporally Controlled Curing Stages via an UV/UV Dual Cure Process.” *Journal of Polymer Science Part A: Polymer Chemistry* 52 (18): 2604–15. doi:10.1002/pola.27276.

Carlborg, Fredrik, Francesca Moraga, Farizah Saharil, Wouter van der Wijngaart, and Tommy Haraldsson. 2012. “Rapid Permanent Hydrophilic and Hydrophobic Patterning of Polymer Surfaces via off-Stoichiometry Thiol-Ene (OSTE) Photografting.” In *Micro Total Analysis Systems (muTAS) 2012, The 16th International Conference on Miniaturized Systems for Chemistry and Life Sciences October 28-November 1, 2012, Ginowan City Okinawa, Japan*, 677–679. http://www.diva-portal.org/smash/record.jsf?pid=diva2:570338.

Carnahan, Norman F., and Kenneth E. Starling. 1969. “Equation of State for Nonattracting Rigid Spheres.” *The Journal of Chemical Physics* 51 (2): 635–36. doi:10.1063/1.1672048.

Chaikin, P. M., Aleksandar Donev, Weining Man, Frank H. Stillinger, and Salvatore Torquato. 2006. “Some Observations on the Random Packing of Hard Ellipsoids.” *Industrial & Engineering Chemistry Research* 45 (21): 6960–6965.

Chandekar, Amol, Michael Alabran, Sandip K. Sengupta, Jun S. Lee, Joey L. Mead, Carol M. F. Barry, James E. Whitten, Sivasubramanian Somu, and Ahmed A. Busnaina. 2008. “Fabrication of Stamps for Microcontact Printing by Injection Molding.” *Microelectronic Engineering*, ’Including Selected papers from the Advanced Gate Stack Technology (ISAGST)’Selected and extended papersThe Third IEEE International Symposium on Advanced Gate Stack Technology, 85 (1): 187–94. doi:10.1016/j.mee.2007.05.008.

Chan-Park, Mary B., Jun Zhang, Yehai Yan, and C. Y. Yue. 2004. “Fabrication of Large SU-8 Mold with High Aspect Ratio Microchannels by UV Exposure Dose Reduction.” *Sensors and Actuators B: Chemical* 101 (1): 175–182.

Chattopadhyay, Soma, Deniz Erdemir, James MB Evans, Jan Ilavsky, Heinz Amenitsch, Carlo U. Segre, and Allan S. Myerson. 2005. "SAXS Study of the Nucleation of Glycine Crystals from a Supersaturated Solution." *Crystal Growth & Design* 5 (2): 523–527.

Chayen, Naomi E. 2004. "Turning Protein Crystallisation from an Art into a Science." *Current Opinion in Structural Biology* 14 (5): 577–83. doi:10.1016/j.sbi.2004.08.002.

Chuan, Shan Xue, Jin Yufeng, Lu Haijing, and Wong Chee Khuen. 2004. "Process Development of Negative Tone Dry Film Photoresist for MEMS Applications." In *Solid-State and Integrated Circuits Technology, 2004. Proceedings. 7th International Conference on*, 1:575–578. IEEE. http://ieeexplore.ieee.org/xpls/abs_all.jsp?arnumber=1435072.

Chuang, Y.-J., F.-G. Tseng, and W.-K. Lin. 2002. "Reduction of Diffraction Effect of UV Exposure on SU-8 Negative Thick Photoresist by Air Gap Elimination." *Microsystem Technologies* 8 (4–5): 308–313.

Cramer, Neil B., Charles L. Couch, Kathleen M. Schreck, Jacquelyn A. Carioscia, Jordan E. Boulden, Jeffrey W. Stansbury, and Christopher N. Bowman. 2010. "Investigation of Thiol-Ene and Thiol-Ene–methacrylate Based Resins as Dental Restorative Materials." *Dental Materials* 26 (1): 21–28.

Curtis, R. A., J. M. Prausnitz, and H. W. Blanch. 1998. "Protein-Protein and Protein-Salt Interactions in Aqueous Protein Solutions Containing Concentrated Electrolytes." *Biotechnology and Bioengineering* 57 (1): 11–21.

Debye, Peter, and A. M. Bueche. 1949. "Scattering by an Inhomogeneous Solid." *Journal of Applied Physics* 20 (6): 518–525.

Delamarche, Emmanuel, Heinz Schmid, Bruno Michel, and Hans Biebuyck. 1997. "Stability of Molded Polydimethylsiloxane Microstructures." *Advanced Materials* 9 (9): 741–46. doi:10.1002/adma.19970090914.

Deng, Tao, Hongkai Wu, Scott T. Brittain, and George M. Whitesides. 2000. "Prototyping of Masks, Masters, and Stamps/Molds for Soft Lithography Using an Office Printer and Photographic Reduction." *Analytical Chemistry* 72 (14): 3176–3180.

Derjaguin, B. V., L. Landau, and others. 1941. "Theory of the Stability of Strongly Charged Lyophobic Sols and of the Adhesion of Strongly Charged Particles in Solutions of Electrolytes." *Acta Physicochim. URSS* 14 (6): 633–662.

Dingenouts, N., J. Bolze, D. Pötschke, and M. Ballauff. 1999. "Analysis of Polymer Latexes by Small-Angle X-Ray Scattering." In *Polymer Latexes-Epoxide Resins-Polyampholytes*, 1–47. Springer. http://link.springer.com/chapter/10.1007/3-540-68384-4_1.

Dingenouts, N., Ch Norhausen, and M. Ballauff. 1998. "Observation of the Volume Transition in Thermosensitive Core-Shell Latex Particles by Small-Angle X-Ray Scattering." *Macromolecules* 31 (25): 8912–8917.

Ducruix, Arnaud, Jean Pierre Guilloteau, Madeleine Riès-Kautt, and Annette Tardieu. 1996. "Protein Interactions as Seen by Solution X-Ray Scattering prior to Crystallogenesis." *Journal of Crystal Growth* 168 (1): 28–39.

Duffy, David C., J. Cooper McDonald, Olivier JA Schueller, and George M. Whitesides. 1998. "Rapid Prototyping of Microfluidic Systems in Poly (Dimethylsiloxane)." *Analytical Chemistry* 70 (23): 4974–4984.

Duncan, P. Brent, and David Needham. 2004. "Test of the Epstein-Plesset Model for Gas Microparticle Dissolution in Aqueous Media: Effect of Surface Tension and Gas

Undersaturation in Solution." *Langmuir: The ACS Journal of Surfaces and Colloids* 20 (7): 2567–78.

———. 2006. "Microdroplet Dissolution into a Second-Phase Solvent Using a Micropipet Technique: Test of the Epstein−Plesset Model for an Aniline−Water System." *Langmuir* 22 (9): 4190–97. doi:10.1021/la053314e.

Durchschlag, H., P. Zipper, G. Purr, and R. Jaenicke. 1996. "Comparative Studies of Structural Properties and Conformational Changes of Proteins by Analytical Ultracentrifugation and Other Techniques." *Colloid and Polymer Science* 274 (2): 117–37. doi:10.1007/BF00663444.

Eddings, Mark A., Michael A. Johnson, and Bruce K. Gale. 2008. "Determining the Optimal PDMS–PDMS Bonding Technique for Microfluidic Devices." *Journal of Micromechanics and Microengineering* 18 (6): 67001.

Epstein, P. S., and M. S. Plesset. 1950. "On the Stability of Gas Bubbles in Liquid-Gas Solutions." *The Journal of Chemical Physics* 18 (11): 1505. doi:10.1063/1.1747520.

Errando-Herranz, Carlos, Alexander Vastesson, Marina Zelenina, Gaspard Pardon, Gunnar Bergström, Wouter van der Wijngaart, Tommy Haraldsson, Hjalmar Brismar, and Kristinn B. Gylfason. 2013. "Biocompatibility of OSTE Polymers Studied by Cell Growth Experiments." In *The 17th International Conference on Miniaturized Systems for Chemistry and Life Sciences (MicroTAS 2013), Freiburg, 27-31 October 2013*. http://www.diva-portal.org/smash/record.jsf?pid=diva2:652888.

Feigin, L. A., and Dmitriĭ Svergun. 2016. "General Principles of Small-Angle Diffraction." In . Accessed August 7. http://link.springer.com/chapter/10.1007/978-1-4757-6624-0_2.

Finet, S., F. Skouri-Panet, M. Casselyn, F. Bonnete, and A. Tardieu. 2004. "The Hofmeister Effect as Seen by SAXS in Protein Solutions." *Current Opinion in Colloid & Interface Science* 9 (1): 112–116.

Fischer, H., M. de Oliveira Neto, H. B. Napolitano, A. F. Craievich, and I. Polikarpov. 2010. "The Molecular Weight of Proteins in Solution Can Be Determined from a Single SAXS Measurement on a Relative Scale." *J. Appl. Cryst* 43: 101–109.

Fournet, G., and A. Guinier. 1955. "Small Angle Scattering of X-Rays." *Translated by Walker, CB and Yudowitch, KL In: New York: John Wiley & Sons*, 7–78.

Frenz, Lucas, Abdeslam El Harrak, Matthias Pauly, Sylvie Bégin-Colin, Andrew D. Griffiths, and Jean-Christophe Baret. 2008. "Droplet-Based Microreactors for the Synthesis of Magnetic Iron Oxide Nanoparticles." *Angewandte Chemie International Edition* 47 (36): 6817–6820.

Fritz, Jürgen, Emily B. Cooper, Suzanne Gaudet, Peter K. Sorger, and Scott R. Manalis. 2002. "Electronic Detection of DNA by Its Intrinsic Molecular Charge." *Proceedings of the National Academy of Sciences* 99 (22): 14142–14146.

Garland, Shaun P., Terrence M. Murphy Jr, and Tingrui Pan. 2014. "Print-to-Pattern Dry Film Photoresist Lithography." *Journal of Micromechanics and Microengineering* 24 (5): 57002.

Glatter, Otto, and Otto Kratky. 1982. *Small Angle X-Ray Scattering*. Academic Press.

Greaves, Eduardo D., and Andreas Manz. 2005. "Toward on-Chip X-Ray Analysis." *Lab on a Chip* 5 (4): 382–391.

Grobelny, S., M. Erlkamp, J. Möller, M. Tolan, and R. Winter. 2014. "Intermolecular Interactions in Highly Concentrated Protein Solutions upon Compression and the

Role of the Solvent." *The Journal of Chemical Physics* 141 (22): 22D506. doi:10.1063/1.4895542.

Gu, Hao, Michel H. G. Duits, and Frieder Mugele. 2010. "A Hybrid Microfluidic Chip with Electrowetting Functionality Using Ultraviolet (UV)-Curable Polymer." *Lab on a Chip* 10 (12): 1550. doi:10.1039/c001524e.

Guinier, André. 1939. "La Diffraction Des Rayons X Aux Tres Petits Angles: Applications a L'etude de Phenomenes Ultramicroscopiques." http://publikationen.ub.uni-frankfurt.de/frontdoor/index/index/docId/15232.

Halle, Bertil, Thomas Andersson, Sture Forsen, Bjoern Lindman, and Bjoern Lindman. 1981. "Protein Hydration from Water Oxygen-17 Magnetic Relaxation." *Journal of the American Chemical Society* 103 (3): 500–508.

Hansen, J. P., and I. R. McDonald. 1969a. "Theory of Simple Liquids (Academic, New York, 1976)." *And References Therein*, 364–405.

———. 1969b. "Theory of Simple Liquids (Academic, New York, 1976)." *And References Therein*, 364–405.

Haraldsson, Tommy, Carl Fredrik Carlborg, and Wouter van der Wijngaart. 2014. "OSTE: A Novel Polymer System Developed for Lab-on-Chip." In *SPIE MOEMS-MEMS*, 897608–897608. International Society for Optics and Photonics. http://proceedings.spiedigitallibrary.org/proceeding.aspx?articleid=1841812.

Hickl, P., M. Ballauff, and A. Jada. 1996. "Small-Angle X-Ray Contrast-Variation Study of Micelles Formed by Poly (Styrene)-Poly (Ethylene Oxide) Block Copolymers in Aqueous Solution." *Macromolecules* 29 (11): 4006–4014.

Hickl, P., M. Ballauff, Ullrich Scherf, Klaus Müllen, and P. Lindner. 1997. "Characterization of a Ladder Polymer by Small-Angle X-Ray and Neutron Scattering." *Macromolecules* 30 (2): 273–279.

Hoshiya, Naoyuki, Masahiko Shimoda, Hideki Yoshikawa, Yoshiyuki Yamashita, Satoshi Shuto, and Mitsuhiro Arisawa. 2010. "Sulfur Modification of Au via Treatment with Piranha Solution Provides Low-Pd Releasing and Recyclable Pd Material, SAPd." *Journal of the American Chemical Society* 132 (21): 7270–7272.

Hoyle, Charles E., and Christopher N. Bowman. 2010. "Thiol–Ene Click Chemistry." *Angewandte Chemie International Edition* 49 (9): 1540–73. doi:10.1002/anie.200903924.

Hung, Lung-Hsin, Robert Lin, and Abraham Phillip Lee. 2008. "Rapid Microfabrication of Solvent-Resistant Biocompatible Microfluidic Devices." *Lab on a Chip* 8 (6): 983–987.

Hunter, R. J. 1989. "Behaviour of Colloidal Dispersions." *Foundations of Colloid Science* 1: 72–73.

Hwang, Deng-Huei, Yi-Chung Lo, and Kanping Chin. 2001. "Development of a Systematic Recipe Set for Processing SU8-5 Photoresist." In *International Symposium on Microelectronics and MEMS*, 131–139. International Society for Optics and Photonics. http://proceedings.spiedigitallibrary.org/proceeding.aspx?articleid=903476.

Israelachvili, J. N. 1992. *Intermolecular and Surface Forces (; London*. Academic Press.

Jones, Gareth, Chris Lovell, Hywel Morgan, and Klaus-Peter Zauner. 2011. "Organising Chemical Reaction Networks in Space and Time with Microfluidics." *International Journal of Nanotechnology and Molecular Computation (IJNMC)* 3 (1): 35–56.

Jones, Scotten W. 2008. "Photolithography." *IC Knowledge LLC* 1: 1–109.

Kaler, E. W., and H. Brumberger. 1995. “Modern Aspects of Small-Angle Scattering.” *Kluwer Academic, Dordrecht* 140 (142): 329.

Karlsson, J. Mikael, Fredrik Carlborg, Farizah Saharil, Fredrik Forsberg, Frank Niklaus, Wouter van der Wijngaart, and Tommy Haraldsson. 2012. “High-Resolution Micropatterning of off-Stoichiometric Thiol-Enes (OSTE) via a Novel Lithography Mechanism.” In *16th International Conference on Miniaturized Systems for Chemistry and Life Sciences (MicroTAS)*. http://www.mercenelabs.com/wp-content/uploads/2012/11/OSTE-high-aspect-ratio-lithography.pdf.

Kholodenko, A., M. Ballauff, and M. Aguero Granados. 1998. “Conformational Statistics of Semiflexible Polymers: Comparison between Different Models.” *Physica A: Statistical Mechanics and Its Applications* 260 (3): 267–293.

Khvostichenko, Daria S., Elena Kondrashkina, Sarah L. Perry, Ashtamurthy S. Pawate, Keith Brister, and Paul JA Kenis. 2013. “An X-Ray Transparent Microfluidic Platform for Screening of the Phase Behavior of Lipidic Mesophases.” *Analyst* 138 (18): 5384–5395.

Kirby, Nigel M., Stephen T. Mudie, Adrian M. Hawley, David J. Cookson, Haydyn DT Mertens, Nathan Cowieson, and Vesna Samardzic-Boban. 2013. “A Low-Background-Intensity Focusing Small-Angle X-Ray Scattering Undulator Beamline.” *Journal of Applied Crystallography* 46 (6): 1670–1680.

Kirste, R. G., and R. C. Oberthur. 1982. “Synthetic Polymers in Solution.” *Small Angle X-Ray Scattering*, 387–431.

Kratky, O. 1982. “A Survey.” In *Small Angle X-Ray Scattering*. https://inis.iaea.org/search/search.aspx?orig_q=RN:16012431.

Kratky, O., and K. Müller. 1982. “Aggregations and Micellar Structures of Small Molecules in Solution.” *Small Angle X-Ray Scattering. O. Glatter and O. Kratky, Editors. Academic Press, London*, 499–510.

Kubenz, M., U. Ostrzinski, F. Reuther, and G. Gruetzner. 2003. “Effective Baking of Thick and Ultra-Thick Photoresist Layers by Infrared Radiation.” *Microelectronic Engineering* 67: 495–501.

Labit, Hélène, Arach Goldar, Guillaume Guilbaud, Carine Douarche, Olivier Hyrien, and Kathrin Marheineke. 2009. “A Simple and Optimized Method of Producing Silanized Surfaces for FISH and Replication Mapping on Combed DNA Fibers.” *BioTechniques*, no. 45: 649–52.

Lafleur, Josiane P., Detlef Snakenborg, Søren S. Nielsen, Magda Møller, Katrine N. Toft, Andreas Menzel, Jes K. Jacobsen, Bente Vestergaard, Lise Arleth, and Jorg P. Kutter. 2011. “Automated Microfluidic Sample-Preparation Platform for High-Throughput Structural Investigation of Proteins by Small-Angle X-Ray Scattering.” *Journal of Applied Crystallography* 44 (5): 1090–1099.

Laue, Max von. 1960. *Röntgenstrahl-Interferenzen*. Vol. 6. Akad. VerlagGes.

Lee, Bong Soo, Young Shik Chi, Kyung-Bok Lee, Yang-Gyun Kim, and Insung S. Choi. 2007. “Functionalization of Poly (Oligo (Ethylene Glycol) Methacrylate) Films on Gold and Si/SiO2 for Immobilization of Proteins and Cells: SPR and QCM Studies.” *Biomacromolecules* 8 (12): 3922–3929.

Leng, Jacques, and Jean-Baptiste Salmon. 2009. “Microfluidic Crystallization” 9 (1): 24–34. doi:10.1039/B807653G.

Lin, Shi-Yow, Ting-Li Lu, and Woei-Bor Hwang. 1995. “Adsorption Kinetics of Decanol at the Air-Water Interface.” *Langmuir* 11 (2): 555–62. doi:10.1021/la00002a033.

Lindner, Peter, and Th Zemb. 1991. “Neutron, X-Ray and Light Scattering: Introduction to an Investigative Tool for Colloidal and Polymeric Systems.” https://inis.iaea.org/search/search.aspx?orig_q=RN:23077130.

Liu, Yan, Joseph C. Fanguy, Justin M. Bledsoe, and Charles S. Henry. 2000. “Dynamic Coating Using Polyelectrolyte Multilayers for Chemical Control of Electroosmotic Flow in Capillary Electrophoresis Microchips.” *Analytical Chemistry* 72 (24): 5939–5944.

Lorenz, Hubert, M. Despont, N. Fahrni, N. LaBianca, Philippe Renaud, and P. Vettiger. 1997. “SU-8: A Low-Cost Negative Resist for MEMS.” *Journal of Micromechanics and Microengineering* 7 (3): 121.

Lüscher-mattli, Madeleine, and Max Rüegg. 1982. “Thermodynamic Functions of Biopolymer Hydration. I. Their Determination by Vapor Pressure Studies, Discussed in an Analysis of the Primary Hydration Process.” *Biopolymers* 21 (2): 403–18. doi:10.1002/bip.360210212.

Maki, Kara L., and Satish Kumar. 2011. “Fast Evaporation of Spreading Droplets of Colloidal Suspensions.” *Langmuir* 27 (18): 11347–63. doi:10.1021/la202088s.

Manukyan, Selin, Hans M. Sauer, Ilia V. Roisman, Kyle A. Baldwin, David J. Fairhurst, Haida Liang, Joachim Venzmer, and Cameron Tropea. 2013. “Imaging Internal Flows in a Drying Sessile Polymer Dispersion Drop Using Spectral Radar Optical Coherence Tomography (SR-OCT).” *Journal of Colloid and Interface Science* 395: 287–293.

Marmiroli, Benedetta, Gianluca Grenci, Fernando Cacho-Nerin, Barbara Sartori, Enrico Ferrari, Peter Laggner, Luca Businaro, and Heinz Amenitsch. 2009. “Free Jet Micromixer to Study Fast Chemical Reactions by Small Angle X-Ray Scattering.” *Lab on a Chip* 9 (14): 2063–2069.

Martel, Anne, Manfred Burghammer, Richard J. Davies, Emanuela Di Cola, Charlotte Vendrely, and Christian Riekel. 2008. “Silk Fiber Assembly Studied by Synchrotron Radiation SAXS/WAXS and Raman Spectroscopy.” *Journal of the American Chemical Society* 130 (50): 17070–17074.

Martin, Alexandre, Sébastien Teychené, Séverine Camy, and Joëlle Aubin. 2016. “Fast and Inexpensive Method for the Fabrication of Transparent Pressure-Resistant Microfluidic Chips.” *Microfluidics and Nanofluidics* 20 (6): 1–8. doi:10.1007/s10404-016-1757-7.

Martin, Hazel P., Nicholas J. Brooks, John M. Seddon, Nick J. Terrill, Paul F. Luckham, Adam J. Kowalski, and João T. Cabral. 2010. “Complex Fluids under Microflow Probed by SAXS: Rapid Microfabrication and Analysis.” In *Journal of Physics: Conference Series*, 247:12050. IOP Publishing. http://iopscience.iop.org/article/10.1088/1742-6596/247/1/012050/meta.

Mertens, Haydyn DT, and Dmitri I. Svergun. 2010. “Structural Characterization of Proteins and Complexes Using Small-Angle X-Ray Solution Scattering.” *Journal of Structural Biology* 172 (1): 128–141.

MicroChem. n.d. “SU-8 Datasheet.”

Müllenborn, Matthias, H. Dirac, and Jon Wulff Petersen. 1995. “Silicon Nanostructures Produced by Laser Direct Etching.” *Applied Physics Letters* 66 (22): 3001–3003.

“NOA81.” 2016. Accessed September 1. https://www.norlandprod.com/adhesives/noa%2081.html.

Otten, Alexander, Sarah Köster, Bernd Struth, Anatoly Snigirev, and Thomas Pfohl. 2005. "Microfluidics of Soft Matter Investigated by Small-Angle X-Ray Scattering." *Journal of Synchrotron Radiation* 12 (6): 745–750.

Otting, Gottfried, and Kurt Wuethrich. 1989. "Studies of Protein Hydration in Aqueous Solution by Direct NMR Observation of Individual Protein-Bound Water Molecules." *Journal of the American Chemical Society* 111 (5): 1871–1875.

Panine, P., S. Finet, T. M. Weiss, and T. Narayanan. 2006. "Probing Fast Kinetics in Complex Fluids by Combined Rapid Mixing and Small-Angle X-Ray Scattering." *Advances in Colloid and Interface Science* 127 (1): 9–18.

Pardon, Gaspard, Farizah Saharil, J. Mikael Karlsson, and Omkar Supekar. 2014. "Rapid Mold-Free Manufacturing of Microfluidic Devices with Robust and Spatially Directed Surface Modifications." *Microfluidics and Nanofluidics* 17 (4): 773. doi:10.1007/s10404-014-1351-9.

Pasquier, C., Sylvie Beaufils, A. Bouchoux, B. Cabane, S. Rigult, J. Perez, Valérie Lechevalier, et al. 2012. "Equation of State and Structure of Highly Concentrated Globular Protein Solutions." https://hal-agrocampus-ouest.archives-ouvertes.fr/hal-00924769/.

Pasquier, Coralie, Sylvie Beaufils, Antoine Bouchoux, Sophie Rigault, Bernard Cabane, Mikael Lund, Valérie Lechevalier, et al. 2016. "Osmotic Pressures of Lysozyme Solutions from Gas-like to Crystal States" 18 (41): 28458–65. doi:10.1039/C6CP03867K.

Pilz, I. 1982. "Proteins." *Small Angle X-Ray Scattering*, 239–293.

Podsiadlo, Paul, Seok-Youl Choi, Bongsup Shim, Jungwoo Lee, Meghan Cuddihy, and Nicholas A. Kotov. 2005. "Molecularly Engineered Nanocomposites: Layer-by-Layer Assembly of Cellulose Nanocrystals." *Biomacromolecules* 6 (6): 2914–2918.

Pollack, L., M. W. Tate, A. C. Finnefrock, C. Kalidas, S. Trotter, N. C. Darnton, L. Lurio, et al. 2001. "Time Resolved Collapse of a Folding Protein Observed with Small Angle X-Ray Scattering." *Physical Review Letters* 86 (21): 4962.

Pollack, Lois, Mark W. Tate, Nicholas C. Darnton, James B. Knight, Sol M. Gruner, William A. Eaton, and Robert H. Austin. 1999. "Compactness of the Denatured State of a Fast-Folding Protein Measured by Submillisecond Small-Angle X-Ray Scattering." *Proceedings of the National Academy of Sciences* 96 (18): 10115–10117.

Polte, Jorg, Robert Erler, Andreas F. Thunemann, Sergey Sokolov, T. Torsten Ahner, Klaus Rademann, Franziska Emmerling, and Ralph Kraehnert. 2010. "Nucleation and Growth of Gold Nanoparticles Studied via in Situ Small Angle X-Ray Scattering at Millisecond Time Resolution." *ACS Nano* 4 (2): 1076–1082.

Pontoni, D., T. Narayanan, and A. R. Rennie. 2004. "Nucleation and Growth Kinetics of Colloidal Silica." In *Trends in Colloid and Interface Science XVI*, 227–230. Springer. http://link.springer.com/chapter/10.1007/978-3-540-36462-7_49.

Porod, G. 1951. "The X-Ray Small-Angle Scattering of Close-Packed Colloid Systems." *Kolloid Z* 124: 32.

Pötschke, D., and M. Ballauff. 2002. "Structure of Dendrimers in Solution as Probed by Scattering Experiments." In *Structure and Dynamics of Polymer and Colloidal Systems*, 157–187. Springer. http://link.springer.com/chapter/10.1007/978-94-010-0442-8_6.

Rickard, Deborah L., P. Brent Duncan, and David Needham. 2010. “Hydration Potential of Lysozyme: Protein Dehydration Using a Single Microparticle Technique.” *Biophysical Journal* 98 (6): 1075–1084.

Sandison, Mairi E., Michele Zagnoni, Mustafa Abu-Hantash, and Hywel Morgan. 2007. “Micromachined Glass Apertures for Artificial Lipid Bilayer Formation in a Microfluidic System.” *Journal of Micromechanics and Microengineering* 17 (7): S189.

Sandström, N., R. Zandi Shafagh, A. Vastesson, F. Carlborg, W. van der Wijngaart, and others. 2015. “Reaction Injection Molding and Direct Covalent Bonding of OSTE+polymer Microfluidic Devices.” Accessed August 7. http://www.diva-portal.org/smash/get/diva2:808710/FULLTEXT02.

Sandström, Niklas, Reza Zandi Shafagh, C. F. Carlborg, Tommy Haraldsson, Göran Stemme, and Wouter van der Wijngaart. 2011. “One Step Integration of Gold Coated Sensors with OSTE Polymer Cartridges by Low Temperature Dry Bonding.” In *Solid-State Sensors, Actuators and Microsystems Conference (TRANSDUCERS), 2011 16th International*, 2778–2781. IEEE. http://ieeexplore.ieee.org/xpls/abs_all.jsp?arnumber=5969534.

Šegatin, Nataša, and Cveto Klofutar. 2003. “Thermodynamics of the Solubility of Water in 1-Hexanol, 1-Octanol, 1-Decanol, and Cyclohexanol.” *Monatshefte Für Chemie / Chemical Monthly* 135 (3): 241–48. doi:10.1007/s00706-003-0053-x.

———. 2004. “Thermodynamics of the Solubility of Water in 1-Hexanol, 1-Octanol, 1-Decanol, and Cyclohexanol.” *Monatshefte Für Chemie/Chemical Monthly* 135 (3): 241–248.

Sivaji, K. 1989. “Evaporation Rates of Liquid Drops Containing Dissolved Salts.” *The Chemical Engineering Journal* 40 (3): 181–85. doi:10.1016/0300-9467(89)80060-7.

Stehle, Ralf, Guenter Goerigk, Dirk Wallacher, Matthias Ballauff, and Sebastian Seiffert. 2013. “Small-Angle X-Ray Scattering in Droplet-Based Microfluidics.” *Lab on a Chip* 13 (8): 1529–1537.

Stephan, K., P. Pittet, L. Renaud, P. Kleimann, P. Morin, N. Ouaini, and R. Ferrigno. 2007. “Fast Prototyping Using a Dry Film Photoresist: Microfabrication of Soft-Lithography Masters for Microfluidic Structures.” *Journal of Micromechanics and Microengineering* 17 (10): N69.

Su, Jonathan T., P. Brent Duncan, Amit Momaya, Arimatti Jutila, and David Needham. 2010. “The Effect of Hydrogen Bonding on the Diffusion of Water in N-Alkanes and N-Alcohols Measured with a Novel Single Microdroplet Method.” *The Journal of Chemical Physics* 132 (4): 44506. doi:10.1063/1.3298857.

Su, Jonathan T., and David Needham. 2013. “Mass Transfer in the Dissolution of a Multi-Component Liquid Droplet in an Immiscible Liquid Environment.” *Langmuir : The ACS Journal of Surfaces and Colloids* 29 (44). doi:10.1021/la402533j.

Svergun, D., C. Barberato, and M. H. J. Koch. 1995. “CRYSOL–a Program to Evaluate X-Ray Solution Scattering of Biological Macromolecules from Atomic Coordinates.” *Journal of Applied Crystallography* 28 (6): 768–773.

Svergun, D. I., and L. A. Feigin. 1986. “X-Ray and Neutron Small-Angle Scattering.” *Moskva: Nauka*.

Tardieu, A., A. Le Verge, M. Malfois, F. Bonneté, S. Finet, M. Ries-Kautt, and L. Belloni. 1999. “Proteins in Solution: From X-Ray Scattering Intensities to Interaction Potentials.” *Journal of Crystal Growth* 196 (2): 193–203.

Teh, W. H., U. Dürig, U. Drechsler, C. G. Smith, and H.-J. Güntherodt. 2005. "Effect of Low Numerical-Aperture Femtosecond Two-Photon Absorption on (SU-8) Resist for Ultrahigh-Aspect-Ratio Microstereolithography." *Journal of Applied Physics* 97 (5): 54907.

Toft, K. Nørgaard, Bente Vestergaard, Søren S. Nielsen, Detlef Snakenborg, Mads G. Jeppesen, Jes K. Jacobsen, Lise Arleth, and Jörg P. Kutter. 2008. "High-Throughput Small Angle X-Ray Scattering from Proteins in Solution Using a Microfluidic Front-End." *Analytical Chemistry* 80 (10): 3648–3654.

Torre, José García de la, María L. Huertas, and Beatriz Carrasco. 2000. "Calculation of Hydrodynamic Properties of Globular Proteins from Their Atomic-Level Structure." *Biophysical Journal* 78 (2): 719–30. doi:10.1016/S0006-3495(00)76630-6.

Tsai, Yuan-Chien, Hsiu-Ping Jen, Kuan-Wen Lin, and You-Zung Hsieh. 2006. "Fabrication of Microfluidic Devices Using Dry Film Photoresist for Microchip Capillary Electrophoresis." *Journal of Chromatography A* 1111 (2): 267–271.

Uzawa, Takanori, Shuji Akiyama, Tetsunari Kimura, Satoshi Takahashi, Koichiro Ishimori, Isao Morishima, and Tetsuro Fujisawa. 2004. "Collapse and Search Dynamics of Apomyoglobin Folding Revealed by Submillisecond Observations of α-Helical Content and Compactness." *Proceedings of the National Academy of Sciences of the United States of America* 101 (5): 1171–1176.

Uzawa, Takanori, Tetsunari Kimura, Koichiro Ishimori, Isao Morishima, Toshitaka Matsui, Masao Ikeda-Saito, Satoshi Takahashi, Shuji Akiyama, and Tetsuro Fujisawa. 2006. "Time-Resolved Small-Angle X-Ray Scattering Investigation of the Folding Dynamics of Heme Oxygenase: Implication of the Scaling Relationship for the Submillisecond Intermediates of Protein Folding." *Journal of Molecular Biology* 357 (3): 997–1008.

Vastesson, A., X. Zhou, N. Sandstrom, and F. Saharil. 2013. "Robust Microdevice Manufacturing by Direct Lithography and Adhesive-Free Bonding of off-Stoichiometry Thiol-Ene-Epoxy (OSTE) Polymer." In *2013 Transducers & Eurosensors XXVII: The 17th International Conference on Solid-State Sensors, Actuators and Microsystems (TRANSDUCERS & EUROSENSORS XXVII)*, 408–11. IEEE. doi:10.1109/Transducers.2013.6626789.

Verwey, E. J. W., and J. Th G. Overbeek. 1948. *Theory of Lyophobic Colloids*. Elsevier, Amsterdam.

Vivares, D., and F. Bonneté. 2002. "X-Ray Scattering Studies of Aspergillus Flavus Urate Oxidase: Towards a Better Understanding of PEG Effects on the Crystallization of Large Proteins." *Acta Crystallographica Section D: Biological Crystallography* 58 (3): 472–479.

Wägli, Ph, A. Homsy, and N. F. de Rooij. 2011. "Norland Optical Adhesive (NOA81) Microchannels with Adjustable Wetting Behavior and High Chemical Resistance against a Range of Mid-Infrared-Transparent Organic Solvents." *Sensors and Actuators B: Chemical* 156 (2): 994–1001.

Wägli, Philip, B. Y. Guélat, A. Homsy, and N. F. de Rooij. 2010. "Microfluidic Devices Made of UV-Curable Glue (NOA81) for Fluorescence Detection Based Applications." In *Proc. Micro Total Analysis Systems*, 1937–1939. http://www.rsc.org/binaries/LOC/2010/PDFs/Papers/659_0039.pdf.

Weigl, Bernhard H., and Jurgen Sygusch. 2002. *Protein Crystallization in Microfluidic Structures*. Google Patents. https://www.google.com/patents/US6409832.

Williams, John D., and Wanjun Wang. 2004. “Study on the Postbaking Process and the Effects on UV Lithography of High Aspect Ratio SU-8 Microstructures.” *Journal of Micro/Nanolithography, MEMS, and MOEMS* 3 (4): 563–568.

Xia, Younan, and George M. Whitesides. 1998. “Soft Lithography.” *Annual Review of Materials Science* 28 (1): 153–184.

Xu, Qiaobing, Michinao Hashimoto, Tram T. Dang, Todd Hoare, Daniel S. Kohane, George M. Whitesides, Robert Langer, and Daniel G. Anderson. 2009. “Preparation of Monodisperse Biodegradable Polymer Microparticles Using a Microfluidic Flow-Focusing Device for Controlled Drug Delivery.” *Small* 5 (13): 1575–1581.

Yang, Ren, and Wanjun Wang. 2005. “A Numerical and Experimental Study on Gap Compensation and Wavelength Selection in UV-Lithography of Ultra-High Aspect Ratio SU-8 Microstructures.” *Sensors and Actuators B: Chemical* 110 (2): 279–288.

Zheng, Bo, Cory J. Gerdts, and Rustem F. Ismagilov. 2005. “Using Nanoliter Plugs in Microfluidics to Facilitate and Understand Protein Crystallization.” *Current Opinion in Structural Biology* 15 (5): 548–555.

Zheng, Bo, L. Spencer Roach, and Rustem F. Ismagilov. 2003. “Screening of Protein Crystallization Conditions on a Microfluidic Chip Using Nanoliter-Size Droplets.” *Journal of the American Chemical Society* 125 (37): 11170–11171.

Zheng, Bo, Joshua D. Tice, L. Spencer Roach, and Rustem F. Ismagilov. 2004. “A Droplet-Based, Composite PDMS/Glass Capillary Microfluidic System for Evaluating Protein Crystallization Conditions by Microbatch and Vapor-Diffusion Methods with On-Chip X-Ray Diffraction.” *Angewandte Chemie International Edition* 43 (19): 2508–2511.

Zhou, Xiamo, Carl Fredrik Carlborg, Niklas Sandström, Alexander Vastesson, Farizah Saharil, Wouter van der Wijngaart, and Tommy Haraldsson. 2014. “OSTE+ Microfluidic Devices with Lithographically Defined Hydrophobic/Hydrophilic Patterns and Biocompatible Chip Sealing: OSTEmer Allows Easy Fabrication of Microfluidic Chips.” In *DIATECH 2014, Leuven, Belgium*, 26–27. http://www.diva-portal.org/smash/record.jsf?pid=diva2:761357.

Appendix A

I. Discretization of the problem using explicit, implicit and Crank-Nicolson

For this simulation, Fick's second law is used which modified in terms of concentration:

$$\frac{\partial C_w}{\partial t} - \frac{D}{r^2}\frac{\partial}{\partial r}\left(r^2 \frac{\partial C_w}{\partial r}\right) = 0 \qquad \textit{Eq. 1}$$

For this modification, these equations and assumption are needed:

$$\mu_i = {\mu_i}^{std} + KT \ln a_i = {\mu_i}^{std} + KT \ln \gamma C_i \qquad \textit{Eq. 2}$$

From this equation, since γ is constant,

$$\frac{\partial \mu_i}{\partial r} = \frac{\mathrm{KT}}{\mathrm{C_i}}\frac{\partial C_i}{\partial r} \qquad \textit{Eq. 3}$$

With this equation, Fick's first law can be modified,

$$J_i = -D\frac{\partial C_i}{\partial r} \qquad \textit{Eq. 4}$$

Assume that $a_i = \gamma C_i$ (γ is constant) and $\gamma = 1/C_{sat}$

II. Explicit scheme (Euler method)

Explicit scheme is the most basic scheme and this scheme predict future data with recent data. This scheme is stable when $\Delta t \leq \frac{\Delta r^2}{2D}$ and has an error with degree of second term of Taylor's series expansion.

With Fick's first law and definition of activity,

$$\frac{\partial \mu_i}{\partial r} = \frac{\mathrm{KT}}{a_i}\frac{\partial a_i}{\partial r} \qquad \textit{Eq. 5}$$

$$J_i = -D\frac{\partial C_i}{\partial r} = -\frac{DC_i}{a_i}\frac{\partial a_i}{\partial r} \qquad \textit{Eq. 6}$$

Fick's second law can be modified,

$$\frac{\partial C_w}{\partial t} - \frac{D}{r^2}\frac{\partial}{\partial r}\left(r^2 \frac{C_w}{a_w}\frac{\partial a_w}{\partial r}\right) = 0 \qquad \textit{Eq. 7}$$

$$\frac{\partial C_w}{\partial t} - \frac{D}{r^2}\left(2r\frac{C_w}{a_w}\frac{\partial a_w}{\partial r} + r^2\frac{1}{a_w}\frac{\partial C_w}{\partial r}\frac{\partial a_w}{\partial r} - r^2\frac{C_w}{a_w^2}\left(\frac{\partial a_w}{\partial r}\right)^2 + r^2\frac{C_w}{a_w}\frac{\partial^2 a_w}{\partial r^2}\right) = 0 \qquad \textit{Eq. 8}$$

From Eq. 6:

$$\frac{\partial C_w}{\partial t} - \frac{D}{r^2}\left(2r\frac{C_w}{a_w}\frac{\partial a_w}{\partial r} + r^2\frac{C_w}{a_w^2}\left(\frac{\partial a_w}{\partial r}\right)^2 - r^2\frac{C_w}{a_w^2}\left(\frac{\partial a_w}{\partial r}\right)^2 + r^2\frac{C_w}{a_w}\frac{\partial^2 a_w}{\partial r^2}\right) = 0 \qquad \textit{Eq. 9}$$

$$\frac{\partial C_w}{\partial t} - D\frac{C_w}{a_w}\left(\frac{2}{r}\frac{\partial a_w}{\partial r} + \frac{\partial^2 a_w}{\partial r^2}\right) = 0 \qquad \textit{Eq. 10}$$

By discretization,

$$\frac{C_r^{t+1} - C_r^t}{\Delta t} - D\frac{C_r^t}{a_r^t}\left(\frac{2}{r}\frac{a_{r+1}^t - a_{r-1}^t}{\Delta r_r + \Delta r_{r-1}} + \frac{2}{\Delta r_r + \Delta r_{r-1}}\left(\frac{a_{r+1}^t - a_r^t}{\Delta r_r} - \frac{a_r^t - a_{r-1}^t}{\Delta r_{r-1}}\right)\right) = 0 \qquad \textit{Eq. 11}$$

Finally,

$$C_r^{t+1} = C_r^t + D\cdot\Delta t\cdot\frac{C_r^t}{a_r^t}\cdot\left(\frac{2}{r}\frac{a_{r+1}^t - a_{r-1}^t}{\Delta r_r + \Delta r_{r-1}} + \frac{2}{\Delta r_r + \Delta r_{r-1}}\left(\frac{a_{r+1}^t - a_r^t}{\Delta r_r} - \frac{a_r^t - a_{r-1}^t}{\Delta r_{r-1}}\right)\right) \qquad \textit{Eq. 12}$$

And activity in/outside can be calculated:

$$a_r^{t+1} = \frac{C_r^{t+1}}{C_{sat}} \qquad \textit{Eq. 13}$$

After activity calculation, radius at t+1 should be calculated.

$$\mathrm{R}_{t+1} = R_t + DC_{sat}\frac{M}{\rho}\Delta t\frac{a_{R+1}^t - a_R^t}{\Delta r_R} \qquad \textit{Eq. 14}$$

With R_{t+1}, concentration of water at the inside can be calculated.

$$V|_{t+1} = \mathrm{V_p} + V_w = C_p|_{t=0}\cdot V|_{t=0}\cdot M_p\cdot V_{sp,p} + \frac{C_w|_{t+1}\cdot V|_{t+1}\cdot M_w}{\rho_w} \qquad \textit{Eq. 15}$$

$$\mathrm{C}_{w,in}|_{t+1} = \frac{\rho_\mathrm{w}}{M_w} - \frac{\rho_w\cdot V_{sp,p}\cdot M_p\cdot C_p|_{t=0}\cdot V|_{t=0}}{V|_{t+1}\cdot M_w} \qquad \textit{Eq. 16}$$

Finally, activity of water inside the bubble can be calculated

$$\mathrm{h}_{w,in}|_{t+1} = \frac{M_w C_{w,in} V_{drop}|_{t+1}}{M_w C_{w,in} V_{drop}|_{t+1} + M_p C_{p,in} V_{drop}|_{t+1}} \quad \textit{Eq. 17}$$

$$\mathrm{a_w} = -3.0257h^4 + 9.51814h^3 - 10.83145h^2 + 5.34444h \quad \textit{Eq. 18}$$

III. Implicit scheme (Backward Euler method)

Since $C_w = C_{sat}.a_w$ from Eq. 2

$$\frac{\partial C_w}{\partial t} = C_{sat}\frac{\partial a_w}{\partial t} \quad \textit{Eq. 19}$$

Fick's second law in Eq. 10 becomes:

$$\frac{\partial a_w}{\partial t} - D(\frac{2}{r}\frac{\partial a_w}{\partial r} + \frac{\partial^2 a_w}{\partial r^2}) = 0 \quad \textit{Eq. 20}$$

By discretization for implicit scheme,

$$\frac{a_r^{t+1} - a_r^t}{\Delta t} - D(\frac{2}{r^{t+1}} \cdot \frac{a_{r+1}^{t+1} - a_{r-1}^{t+1}}{\Delta r_r + \Delta r_{r-1}} + \frac{2}{\Delta r_r + \Delta r_{r-1}}(\frac{a_{r+1}^{t+1} - a_r^{t+1}}{\Delta r_r} - \frac{a_r^{t+1} - a_{r-1}^{t+1}}{\Delta r_{r-1}}) = 0 \quad \textit{Eq. 21}$$

By organization,

$$a_r^t = -\frac{2D\Delta t}{(\Delta r_r^{t+1} + \Delta r_{r-1}^{t+1})}\left(\frac{1}{\Delta r_r^{t+1}} + \frac{1}{r^{t+1}}\right)a_{r+1}^{t+1} + \left(\frac{2D\Delta t}{\Delta r_r^{t+1}\Delta r_{r-1}^{t+1}} + 1\right)a_r^{t+1} + \frac{2D\Delta t}{(\Delta r_r^{t+1} + \Delta r_{r-1}^{t+1})}\left(\frac{1}{r^{t+1}} - \frac{1}{\Delta r_{r-1}^{t+1}}\right)a_{r-1}^{t+1} \quad \textit{Eq. 22}$$

Let $\frac{2D\Delta t}{(\Delta r_r^{t+1} + \Delta r_{r-1}^{t+1})}\left(\frac{1}{r^{t+1}} - \frac{1}{\Delta r_{r-1}^{t+1}}\right) = m1$, $\left(\frac{2D\Delta t}{\Delta r_r^{t+1}\Delta r_{r-1}^{t+1}} + 1\right) = m2$ and

$-\frac{2D\Delta t}{(\Delta r_r^{t+1} + \Delta r_{r-1}^{t+1})}\left(\frac{1}{\Delta r_r^{t+1}} + \frac{1}{r^{t+1}}\right)a_{r+1}^{t+1} = m3;$

So, Eq. 22 become:

$$a_r^t = m1 \cdot a_{r-1}^{t+1} + m2 \cdot a_r^{t+1} + m3 \cdot a_{r+1}^{t+1} \quad \textit{Eq. 23}$$

This can be expressed in matrix form:

$$\begin{pmatrix} a_1^t \\ a_2^t \\ \vdots \\ a_{r-1}^t \\ a_r^t \end{pmatrix} = \begin{pmatrix} m2 & m3 & 0 & 0 & 0 & 0 \\ m1 & m2 & m3 & 0 & 0 & 0 \\ 0 & m1 & m2 & m3 & 0 & 0 \\ \vdots & \vdots & \vdots & \vdots & \vdots & \vdots \\ 0 & 0 & 0 & m1 & m2 & m3 \\ 0 & 0 & 0 & 0 & m1 & m2 \end{pmatrix} \begin{pmatrix} a_1^{t+1} \\ a_2^{t+1} \\ \vdots \\ a_{r-1}^{t+1} \\ a_r^{t+1} \end{pmatrix} \quad \textit{Eq. 24}$$

$$\mathrm{A^t} = \mathrm{M} \cdot \mathrm{A^{t+1}} \quad \textit{Eq. 25}$$

By using inverse matrix, activity at t+1 can be calculated

$$\mathrm{A^{t+1}} = \mathrm{M^{-1}} \cdot \mathrm{A^t} \quad \textit{Eq. 26}$$

After activity calculation, everything is same with Eq. 14 to Eq. 18

IV. Crank-Nicolson scheme

Crank-Nicolson scheme is combination of explicit and implicit scheme. This scheme is also stable for always but shows oscillating behavior for wave equation when Δt is large. With same Δt and Δr, it has an error with degree of third term of Taylor's series expansion. For this scheme, Fick's second law should be modified in terms of activity like implicit scheme.

From Eq. 20, by discretization for Crank-Nicolson scheme:

$$\frac{a_r^{t+1} - a_r^t}{\Delta t} - \left(D\left(\frac{1}{r^{t+1}} \cdot \frac{a_{r+1}^{t+1} - a_{r-1}^{t+1}}{\Delta r_r + \Delta r_{r-1}} + \frac{1}{\Delta r_r + \Delta r_{r-1}}\left(\frac{a_{r+1}^{t+1} - a_r^{t+1}}{\Delta r_r} - \frac{a_r^{t+1} - a_{r-1}^{t+1}}{\Delta r_{r-1}}\right) + D\left(\frac{1}{r^t} \cdot \frac{a_{r+1}^t - a_{r-1}^t}{\Delta r_r + \Delta r_{r-1}} + \frac{1}{\Delta r_r + \Delta r_{r-1}}\left(\frac{a_{r+1}^t - a_r^t}{\Delta r_r} - \frac{a_r^t - a_{r-1}^t}{\Delta r_{r-1}}\right)\right) = 0 \right. \right. \quad \textit{Eq. 27}$$

By organization

$$\frac{D\Delta t}{(\Delta r_r^t + \Delta r_{r-1}^t)}\left(\frac{1}{\Delta r_r^t} + \frac{1}{r^t}\right) a_{r+1}^t + \left(1 - \frac{D\Delta t}{\Delta r_r^t \Delta r_{r-1}^t}\right) a_r^t + \frac{D\Delta t}{(\Delta r_r^t + \Delta r_{r-1}^t)}\left(\frac{1}{\Delta r_{r-1}^t} - \frac{1}{r^t}\right) a_{r-1}^t$$
$$= -\frac{D\Delta t}{(\Delta r_r^{t+1} + \Delta r_{r-1}^{t+1})}\left(\frac{1}{\Delta r_r^{t+1}} + \frac{1}{r^{t+1}}\right) a_{r+1}^{t+1} + \left(\frac{D\Delta t}{\Delta r_r^{t+1} \Delta r_{r-1}^{t+1}} + 1\right) a_r^{t+1} \quad \textit{Eq. 28}$$
$$+ \frac{D\Delta t}{(\Delta r_r^{t+1} + \Delta r_{r-1}^{t+1})}\left(\frac{1}{r^{t+1}} - \frac{1}{\Delta r_{r-1}^{t+1}}\right) a_{r-1}^{t+1}$$

Set

$$\frac{D\Delta t}{(\Delta r_r^t + \Delta r_{r-1}^t)}\left(\frac{1}{\Delta r_{r-1}^t} - \frac{1}{r^t}\right) a_{r-1}^t = \mathrm{m1} \qquad \left(1 - \frac{D\Delta t}{\Delta r_r^t \Delta r_{r-1}^t}\right) = m2$$

$$\frac{D\Delta t}{(\Delta r_r^t + \Delta r_{r-1}^t)}\left(\frac{1}{\Delta r_r^t} + \frac{1}{r^t}\right) = m3 \qquad \frac{D\Delta t}{(\Delta r_r^{t+1} + \Delta r_{r-1}^{t+1})}\left(\frac{1}{r^{t+1}} - \frac{1}{\Delta r_{r-1}^{t+1}}\right) = m4$$

$$\left(\frac{D\Delta t}{\Delta r_r^{t+1} \Delta r_{r-1}^{t+1}} + 1\right) = m5 \qquad -\frac{D\Delta t}{(\Delta r_r^{t+1} + \Delta r_{r-1}^{t+1})}\left(\frac{1}{\Delta r_r^{t+1}} + \frac{1}{r^{t+1}}\right) a_{r+1}^{t+1} = m6$$

Equation become:

$$m1 \cdot a_{r-1}^t + m2 \cdot a_r^t + m3 \cdot a_{r+1}^t = m4 \cdot a_{r-1}^{t+1} + m5 \cdot a_r^{t+1} + m6 \cdot a_{r+1}^{t+1} \qquad \textit{Eq. 29}$$

This can be expressed in matrix form:

$$\begin{pmatrix} m2 & m3 & 0 & 0 & 0 & 0 \\ m1 & m2 & m3 & 0 & 0 & 0 \\ 0 & m1 & m2 & m3 & 0 & 0 \\ \vdots & \vdots & \vdots & \vdots & \vdots & \vdots \\ 0 & 0 & 0 & m1 & m2 & m3 \\ 0 & 0 & 0 & 0 & m1 & m2 \end{pmatrix} \begin{pmatrix} a_1^t \\ a_2^t \\ \vdots \\ a_{r-1}^t \\ a_r^t \end{pmatrix} = \begin{pmatrix} m5 & m6 & 0 & 0 & 0 & 0 \\ m4 & m5 & m6 & 0 & 0 & 0 \\ 0 & m4 & m5 & m6 & 0 & 0 \\ \vdots & \vdots & \vdots & \vdots & \vdots & \vdots \\ 0 & 0 & 0 & m4 & m5 & m6 \\ 0 & 0 & 0 & 0 & m4 & m5 \end{pmatrix} \begin{pmatrix} a_1^{t+1} \\ a_2^{t+1} \\ \vdots \\ a_{r-1}^{t+1} \\ a_r^{t+1} \end{pmatrix} \qquad \textit{Eq. 30}$$

$$\mathrm{M} \cdot \mathrm{A^t} = \mathrm{M'} \cdot \mathrm{A^{t+1}} \qquad \textit{Eq. 31}$$

By using inverse matrix, activity at t+1 can be calculated

$$\mathrm{A^{t+1}} = \mathrm{M^{-1}} \cdot \mathrm{M} \cdot \mathrm{A^t} \qquad \textit{Eq. 32}$$

After activity calculation, everything is the same with Eq. 14 to Eq. 18.

V. Moving VS Fixed grid

Because of the shrinking of the bubble, two types of grid for distance has been considered.

1. Moving grid

For moving grid, zero point is put at surface of the bubble. Since the surface is moving by time, zero point and every grid point move together by following the surface.

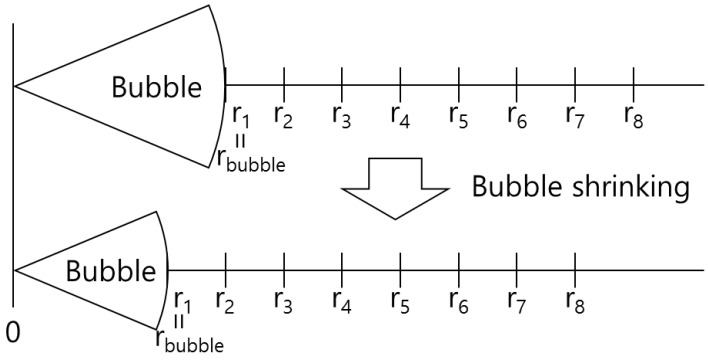

Figure -1: Illustration of moving grid

Since grid follow the surface, every data in grid move also. This moving of data make numerical error in general case. In this case, however, shrinking of bubble can make a flow toward a bubble. After the bubble shrink, a space nearby bubble will be empty, there for fluid will move to pack up the empty space. By using this grid, this phenomenon can be taken into account. However, for accurate simulation, since bubble is sphere shape, compacting of fluid because of shrinking of surface area should be considered.

2. Fixed grid

For fixed grid, zero point is put at center of the bubble. To consider a surface of the bubble, one additional grid should be put at the surface of the bubble, which is moving with surface but has independent value with distance. (Concentration at the surface or activity of inside).

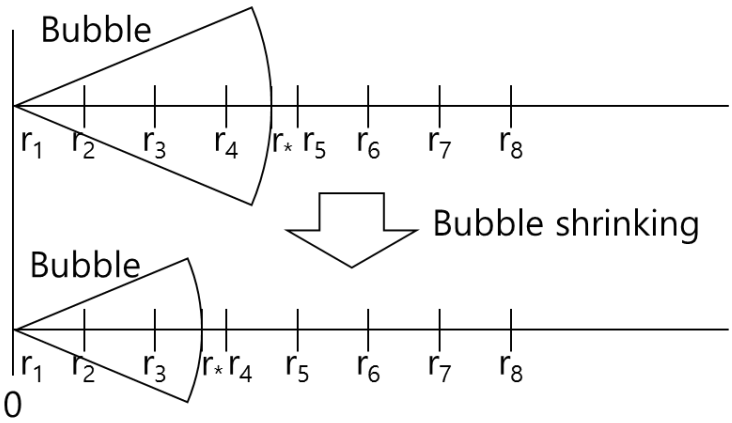

Figure -2: Illustration of fixed grid

VI. The Matlab code for explicit scheme with moving grid

```
%Size of bubble in microfluidic coding

%Explicit scheme

%Including protein

%flash about time


clear all

clc


%Numerical data

dt=0.00001;  %Delta t

dr_ini=0.1;  %Delta r at first grid

dr_rat=1.05;  %Delta r power ratio

dr_exp=94;   %Delta r power step (after 94th grid, size of every grid
remain same)

t_end=50;  %End time

r_step=200;  %Grid number

t_space=0.1;  %Period for recoding


%Input variables

R_sp_0=52.5;  %Initial radius of Bubble

D=595;  %Diffusivity coefficient

C_sat=1.34444/(10^15);  %Saturation concentration (In decanol)

f=0.74;  %Saturation factor

rho=0.9991/(10^12);  %Density of water

M=18;  %Molar weight of water

Vf_p=0.0985;  %Volume fraction of protein

Vsp_p=0.7*(10^12);  %Specific volume of protein
```

```
M_p=14300;  %Molecular weight of protein

C_inf=f*C_sat;  %Concentration of water at outside

C_p=Vf_p/(M_p*Vsp_p);  %Concentration of protein

C_w=(1-Vf_p)*rho/M;  %Concentration of water at inside

C_in=C_w;


%Other variables

t=0;

t_step=round(t_end/dt);

J=zeros(t_end/t_space+1,1);  %Flux

C_temp=zeros(2,r_step);  %Concentration for calculation

C=zeros(t_end/t_space+1,r_step);  %Concentration for record

act_temp=zeros(2,r_step);  %Activity for calculation

act=zeros(t_end/t_space+1,r_step);  %Activity for record

R_sp=zeros(t_end/t_space+1,1);

R_sp_temp=zeros(2,1);

dr=zeros(1,r_step-1);


%initial conditions


%Assignment of grid size

for i=1:r_step-1

    if i<=dr_exp

        dr(i)=dr_ini*dr_rat^(i);

    else

        dr(i)=round(dr(dr_exp));

    end
```

```
end

%Assingnment of previous grid
dr_temp=[dr(2:end),dr(end)];

real_r=cumsum(dr)+R_sp_0;

%Initialization
R_sp_temp(1)=R_sp_0;
C_temp(1,:)=C_inf;
C_temp(:,1)=C_in;
hh=(C_w*M)/((C_p*M_p)+(C_w*M));
a_in=-3.0257*(hh^4)+9.51814*(hh^3)-10.83145*(hh^2)+5.34444*hh;
a_inf=f;
act_temp(1,:)=a_inf;
act_temp(:,1)=a_in;

drr=dr+dr_temp;

for t=1:t_step-1
    C_c=C_temp(1,2:end);
    a_c=act_temp(1,2:end);
    a_pr=act_temp(1,1:end-1);
    a_ne=[act_temp(1,3:end),a_inf];

    %Concentration and activity calculation by discretized fick's second
```

```
law

    C_temp(2,2:end)=C_c+(2*D*dt*C_c./a_c).*((a_ne-
a_pr)./(real_r.*drr)+((a_ne-a_c)./dr_temp-(a_c-a_pr)./dr)./drr);

    act_temp(2,2:end)=C_temp(2,2:end)/C_sat;


    %Radius cacluation


R_sp_temp(2)=R_sp_temp(1)+(M*D*dt*(C_sat)*(reallog(act_temp(1,2)/act_tem
p(1,1))))/(rho*dr(1));


    %Concentration and Activity cacluation at inside

    C_temp(2,1)=(rho/M)-
(rho*C_p*(R_sp_0^3)*M_p*Vsp_p)/((R_sp_temp(2)^3)*M);


hh=(C_temp(2,1)*M*(R_sp_temp(2)^3))/((C_temp(2,1)*M*(R_sp_temp(2)^3))+(C
_p*M_p*(R_sp_0^3)));

    act_temp(2,1)=-3.0257*(hh^4)+9.51814*(hh^3)-
10.83145*(hh^2)+5.34444*hh;%%%%%%%%%%%%%%%


    %Recording

    if mod(dt/t_space*(t-1),1)==0

        R_sp(dt/t_space*(t-1)+1)=R_sp_temp(1);

        J(dt/t_space*(t-1)+1)=-
(D*(C_sat)*(reallog(act_temp(1,2)/act_temp(1,1))))/(dr(1));

        C(dt/t_space*(t-1)+1,:)=C_temp(1,:);

        act(dt/t_space*(t-1)+1,:)=act_temp(1,:);

    end


    real_r=real_r+R_sp_temp(2)-R_sp_temp(1);
```

```
    C_temp(1,:)=C_temp(2,:);
    act_temp(1,:)=act_temp(2,:);
    R_sp_temp(1)=R_sp_temp(2);

    if R_sp_temp(2)<=0.1
        break;
    end

end

realt=0:t_space:t_end;
figure(1)
plot(realt,R_sp*2)
figure(2)
plot(realt,J)
```

VII. The Matlab code for Crank- Nicolson scheme with moving grid

```
%Size of bubble in microfluidic coding
%Crank nicolson scheme
%Including protein
%flash about time

clear all
clc

%Numerical data
```

```
dt=0.001;  %Delta t

dr_ini=0.1;  %Delta r at first grid

dr_rat=1.05;  %Delta r power ratio

dr_exp=94;  %Delta r power step (after 94th grid, size of every grid
remain same)

t_end=50;  %End time

r_step=200;  %Grid number

t_space=0.1;  %Period for recoding


%Input variables

R_sp_0=51.75;  %Initial radius of Bubble

D=595;  %Diffusivity coefficient

C_sat=1.34444/(10^15);  %Saturation concentration (In decanol)

f=0.74;  %Saturation factor

rho=0.9991/(10^12);  %Density of water

M=18;  %Molar weight of water

Vf_p=0.0985;  %Volume fraction of protein

Vsp_p=0.7*(10^12);  %Specific volume of protein

M_p=14300;  %Molecular weight of protein

C_inf=f*C_sat;  %Concentration of water at outside

C_p=Vf_p/(M_p*Vsp_p);  %Concentration of protein

C_w=(1-Vf_p)*rho/M;  %Concentration of water at inside

C_in=C_w;


%Other variables

t=0;

t_step=round(t_end/dt);
```

```
J=zeros(t_end/t_space+1,1);  %Flux
C_temp=zeros(r_step,2);  %Concentration for calculation
C=zeros(r_step,t_end/t_space+1);  %Concentration for record
act_temp=zeros(r_step,2);  %Activity for calculation
act=zeros(r_step,t_end/t_space+1);  %Activity for record
R_sp=zeros(t_end/t_space+1,1);
R_sp_temp=zeros(1,2);
dr=zeros(r_step-1,1);

%initial conditions

%Assignment of grid size
for i=1:r_step
    if i<=dr_exp
        dr(i)=dr_ini*dr_rat^(i);
    else
        dr(i)=round(dr(dr_exp));
    end
end
real_r=cumsum(dr)+R_sp_0;

%Assingnment of next grid
dr_temp=[0;dr(:,1)];
dr_temp(r_step+1,:)=[];

%Initialization
```

```
R_sp_temp(1)=R_sp_0;

C_temp(:,1)=C_inf;

C_temp(1,1)=C_in;

hh=(C_w*M)/((C_p*M_p)+(C_w*M));

a_in=-3.0257*(hh^4)+9.51814*(hh^3)-10.83145*(hh^2)+5.34444*hh;

a_inf=f;

act_temp(:,1)=a_inf;

act_temp(1,1)=a_in;


%Building matrix

mat_b=1+D*dt./(dr.*dr_temp);

mat_b(1)=1;

mat_b(r_step)=1;


mat_e=1-D*dt./(dr.*dr_temp);

mat_e(1)=1;

mat_e(r_step)=1;


R_cri=((rho*C_p*(R_sp_0^3)*M_p*Vsp_p)/(M*((rho/M)-C_sat)))^(1/3);


for t=1:t_step-1

    %Building matrix

    mat_a=(D*dt./(dr+dr_temp)).*((1./real_r)-(1./dr_temp));

    mat_c=-(D*dt./(dr+dr_temp)).*((1./real_r)+(1./dr));

    mat_a(1,:)=[];

    mat_a(r_step-1)=0;
```

```
    mat_c(r_step,:)=[];
    mat_c(1)=0;

    mat_d=-(D*dt./(dr+dr_temp)).*((1./real_r)-(1./dr_temp));
    mat_f=(D*dt./(dr+dr_temp)).*((1./real_r)+(1./dr));
    mat_d(1,:)=[];
    mat_d(r_step-1)=0;
    mat_f(r_step,:)=[];
    mat_f(1)=0;

    M_t=diag(mat_d,-1)+diag(mat_e)+diag(mat_f,1);
    M_t_1=diag(mat_a,-1)+diag(mat_b)+diag(mat_c,1);

    %Activity calculation by using matrix
    act_temp(:,2)=M_t_1\(M_t*act_temp(:,1));
    C_temp(:,2)=C_sat*act_temp(:,2);

    %Radius cacluation
    R_sp_temp(2)=R_sp_temp(1)+(M*(D*C_sat*(act_temp(2,2)-
act_temp(1,2))/dr(1))*dt/rho);

    %Concentration and Activity cacluation at inside
    C_temp(1,2)=(rho/M)-
(rho*C_p*(R_sp_0^3)*M_p*Vsp_p)/((R_sp_temp(2)^3)*M);

hh=(C_temp(1,2)*M*4*pi*(R_sp_temp(2)^3)/3)/((C_temp(1,2)*M*4*pi*(R_sp_te
mp(2)^3)/3)+(C_p*M_p*4*pi*(R_sp_0^3)/3));
    act_temp(1,2)=-3.0257*(hh^4)+9.51814*(hh^3)-
```

```
10.83145*(hh^2)+5.34444*hh;


    %Recording
    if mod(dt/t_space*(t-1),1)==0
        R_sp(dt/t_space*(t-1)+1)=R_sp_temp(1);
        J(dt/t_space*(t-1)+1)=(D*(C_temp(1,2)-C_temp(2,2)))/(dr(1));
        C(:,dt/t_space*(t-1)+1)=C_temp(:,1);
        act(:,dt/t_space*(t-1)+1)=act_temp(:,1);
    end


    real_r=real_r+R_sp_temp(2)-R_sp_temp(1);
    C_temp(:,1)=C_temp(:,2);
    act_temp(:,1)=act_temp(:,2);
    R_sp_temp(1)=R_sp_temp(2);


    if R_sp_temp(2)<=0.1
        break;
    end
  end
 realt=0:t_space:t_end;
figure(1)
plot(realt,R_sp*2)
figure(2)
plot(realt,J)
```

Appendix B

I. Matlab program to detect droplet

```
function []= circle_detect_funct(part,i1,ifin,objective,PathName,fname)

se = strel('disk',5);

switch objective

    case 2.5

        scale=3.831417625;

    case 5

        scale = 1.930501931;

    case 10

        scale=0.957854406;

    case 20

        scale = 0.479386385;

    case 50

        scale = 0.192913639;

end

FPS=40;

xpeakcc_old=0;

scalefactor=4;

n1=1;

% Read in the movie.

mov = VideoReader([PathName fname]);


% Determine how many frames there are.

num_images = mov.NumberOfFrames;
```

```
% Extract the frame from the movie structure.
I =read(mov,i1);
% Create a filename.


%%%%%%%% Calcul du temps
ti=0;
tf=ti+(num_images-1)/FPS;
t=ti:1/FPS:tf;
%%% PREMIERE IMAGE %%%%


if part == 1
Rmin=30;Rmax=80;  % circle radius range
else
   Rmin=20;Rmax=50;  % circle radius range
end


centersDark(1:num_images,1:2)=0;
%radii=0;
%%%%%% TROUVER LA GOUTTEi
[cent, radiiDark] = imfindcircles(I, [Rmin Rmax], ...
    'ObjectPolarity','dark','sensitivity',0.75);
 if isempty(radiiDark)
                [cent, radiiDark] = imfindcircles(I, [Rmin Rmax], ...
                    'ObjectPolarity','dark','sensitivity',0.85);
 end
```

```
center(n1,:)=cent;
radii(n1)=radiiDark;
%%%%% IMAGE ET DETECTION SUPERPOSEE
%%%%%%%%%% GENERATION DU TEMPLATE A PARTIR DE LA POSITION DU CERCLE
template=dropcrop2(I,radiiDark(n1,:),center(n1,:));
time(1)=0;
n=0;
for i=i1+1 :3: ifin
a=zeros(160);
    %%%%%%%% AUTOCORRELATION
I =read(mov,i);
tic
    ncc = normxcorr2(template,I);
    [max_ncc, imaxcc] = max((ncc(:)));%1er pic
    toc
    if(max_ncc>0.8);
      [ypeakcc, xpeakcc] = ind2sub(size(ncc),imaxcc(1));
        max_ncc;
            if(~isempty(xpeakcc_old))
            dx=xpeakcc-xpeakcc_old;
            end
        xpeakcc_old=xpeakcc;

        corr_offsetcc = [(xpeakcc-size(template,2))...
            (ypeakcc-size(template,1))];
        xoffsetcc =  corr_offsetcc(1)+1;
        yoffsetcc =  corr_offsetcc(2)+1;
```

```
        rect1=[max(xoffsetcc-5,1);max(yoffsetcc-
5,1);2*(ceil(max(radiiDark)))+20;2*(ceil(max(radiiDark)))+20];


        %%%%% Definition du nouveau template
        template=imcrop(I,rect1); %%%%%%%%%%%%%%%%%%%%
        %%%%% detection de la goutte dans le template
      if and(rect1(2)+rect1(3)<size(I,1),rect1(1)+rect1(4)<size(I,2))
              n1=n1+1;
        time(n1)=t(i)-t(i1);
        Rmin=max(uint16(radii(n1-1)-5),1);
        Rmax=max(uint16(radii(n1-1)+5),10);  % circle radius range
      im_resized=imresize(I(rect1(2):rect1(2)+rect1(3),rect1(1):rect1(1)
      +rect1(4)),scalefactor);
      [centersDark,                    radiiDark]                    =
imfindcircles(im_resized,scalefactor*[Rmin Rmax], ...
               'ObjectPolarity','dark','sensitivity',0.97);
            if isempty(radiiDark)
                [centersDark,   radiiDark]   =   imfindcircles(im_resized,
scalefactor*[Rmin Rmax], ...

'method','twostage','ObjectPolarity','dark','sensitivity',0.99);
            end


centersDark=round(centersDark/scalefactor);
            radiiDark=radiiDark/scalefactor;
%Recalage des centres par rapport ? la position  du template
      [riri pos]=min(abs(radiiDark - radii(n1-1)));
```

```
        radii(n1)=radiiDark(pos);
        center(n1,2)=centersDark(pos,1) +rect1(2);
        center(n1,1)=centersDark(pos,2) +rect1(1);

        %%%%% IMAGE ET DETECTION SUPERPOSEE
      imagesc(I),hold on
        axis image;
        colormap(gray);
        text(10,  110,  ['t=',  num2str(sprintf('%.2f',time(n1))),'s'],
'FontSize', 14,...
            'BackgroundColor',  [.6,  .6,  .6],  'VerticalAlignment',
'Bottom');
        text(200,                                                  110,
['D=',num2str(sprintf('%.2f',2*radii(n1))),'pixels'], 'FontSize', 14,...
            'BackgroundColor',  [.6,  .6,  .6],  'VerticalAlignment',
'Bottom');%all the text option to try out with
         text(600,                          110,                          [
num2str(sprintf('%d',i)),'/',num2str(sprintf('%d',ifin))],   'FontSize',
14,...
            'BackgroundColor',  [.6,  .6,  .6],  'VerticalAlignment',
'Bottom');%all the text option to try out with
        text(1000, 110, fname, 'FontSize', 14,...
            'BackgroundColor',  [.6,  .6,  .6],  'VerticalAlignment',
'Bottom');%all the text option to try out with
        viscircles(center(n1,:), radii(n1),'LineStyle','--');hold off
%       %%%%% Generation du nouveau template a partir de la nouvelle
taille
        %     %%%%% et nouvelle position de la goutte
        template=dropcrop2(template,radii(n1),centersDark(pos,:));
        end
```

```
    else
        n=n+1;
        if n>400
            break;
        end

    end

end
if part==1
tt=[PathName fname '_data_part1.mat'];
d_p1=2*scale*radii;
i1_p1=i1;
ifin_p1=ifin;
time_p1=time;
save (tt,'d_p1','time_p1','i1_p1','ifin_p1','fname');
else
tt=[PathName fname '_data_part2.mat'];
d_p2=2*scale*radii;
i1_p2=i1;
ifin_p2=ifin;
time_p2=time;
save (tt,'d_p2','time_p2','i1_p2','ifin_p2','fname');
end
```

1. Using a circle Hough function

```
function circles = houghcircles(im, minR, maxR, thresh, delta)
%
```

```
% HOUGHCIRCLES detects multiple disks (coins) in an image using Hough
% Transform. The image contains separating, touching, or overlapping
% disks whose centers may be in or out of the image.

% Check input arguments
if nargin==3
  thresh = 0.33;    % One third of the perimeter
  delta = 12;         % Each element in (x y r) may deviate approx. 4
pixels
elseif nargin==4
  delta = 12;
end
if minR<0 || maxR<0 || minR>maxR || thresh<0 || thresh>1 || delta<0
  disp('Input conditions: 0<minR, 0<maxR, minR<=maxR, 0<thresh<=1,
0<delta');
  return;
end

% Turn a color image into gray
origim = im;
if length(size(im))>2
  im = rgb2gray(im);
end

% Create a 3D Hough array with the first two dimensions specifying the
% coordinates of the circle centers, and the third specifying the radii.
% To accomodate the circles whose centers are out of the image, the
```

```
first
% two dimensions are extended by 2*maxR.
maxR2 = 2*maxR;
hough = zeros(size(im,1)+maxR2, size(im,2)+maxR2, maxR-minR+1);

% For an edge pixel (ex ey), the locations of its corresponding, possible
% circle centers are within the region [ex-maxR:ex+maxR, ey-maxR:ey+maxR].
% Thus the grid [0:maxR2, 0:maxR2] is first created, and then the distances
% between the center and all the grid points are computed to form a radius
% map (Rmap), followed by clearing out-of-range radii.
[X Y] = meshgrid(0:maxR2, 0:maxR2);
Rmap = round(sqrt((X-maxR).^2 + (Y-maxR).^2));
Rmap(Rmap<minR | Rmap>maxR) = 0;

% Detect edge pixels using Canny edge detector. Adjust the lower and/or
% upper thresholds to balance between the performance and detection quality.
% For each edge pixel, increment the corresponding elements in the Hough
% array. (Ex Ey) are the coordinates of edge pixels and (Cy Cx R) are the
% centers and radii of the corresponding circles.
edgeim = edge(im, 'canny', [0.15 0.2]);
[Ey Ex] = find(edgeim);
[Cy Cx R] = find(Rmap);
for i = 1:length(Ex);
```

```
  Index = sub2ind(size(hough), Cy+Ey(i)-1, Cx+Ex(i)-1, R-minR+1);
  hough(Index) = hough(Index)+1;
end

% Collect candidate circles.
% Due to digitization, the number of detectable edge pixels are about 90%
% of the calculated perimeter.
twoPi = 0.9*2*pi;
circles = zeros(0,4);    % Format: (x y r t)
for radius = minR:maxR   % Loop from minimal to maximal radius
  slice = hough(:,:,radius-minR+1);  % Offset by minR
  twoPiR = twoPi*radius;
  slice(slice<twoPiR*thresh) = 0;      % Clear pixel count < 0.9*2*pi*R*thresh
  [y x count] = find(slice);
  circles = [circles; [x-maxR, y-maxR, radius*ones(length(x),1), count/twoPiR]];
end

% Delete similar circles
circles = sortrows(circles,-4);  % Descending sort according to ratio
i = 1;
while i<size(circles,1)
  j = i+1;
  while j<=size(circles,1)
    if sum(abs(circles(i,1:3)-circles(j,1:3))) <= delta
      circles(j,:) = [];
```

```
    else
      j = j+1;
    end
  end
  i = i+1;
end


if nargout==0   % Draw circles
  figure, imshow(origim), hold on;
  for i = 1:size(circles,1)
    x = circles(i,1)-circles(i,3);
    y = circles(i,2)-circles(i,3);
    w = 2*circles(i,3);
    rectangle('Position', [x y w w], 'EdgeColor', 'red', 'Curvature', [1
1]);
  end
  hold off;
end
```

Doctorat de l'Université de Toulouse
Délivré par *Université Toulouse III Paul Sabatier*
Ecole doctorale MEGeP
Spécialité *Génie des Procédés et de l'Environnement*
13 December 2016
Van Nhat PHAM

Development of high throughput microfluidic platforms for the measurement of the protein solution thermodynamic properties

Abstract

This thesis is focused on the development of new protocols and systems, by means of generic microfluidic platforms, for measuring thermodynamic properties of protein solutions. A method for manufacturing pressure-resistant microfluidic structures with high chemical resistance has been developed. The surface properties of the channels can also be adjusted to generate hydrophilic and hydrophobic surfaces. First, the study of protein interactions was successfully performed by coupling a microfluidic platform to small angle X-ray scattering. The obtained experimental data were used to calculate the second virial coefficient, which quantifies protein interactions. A second approach, based on the study of the mass transfer, has also been developed to determine protein Equations Of State (EOS). The resulting EOS was found to be in good agreement with data reported in the literature. To determine the EOS of the protein using a single droplet a first modeling approach was proposed.

keywords: microfluidic, SAXS, Equation of state, protein, interactions

Résumé

Les travaux de cette thèse portent sur le développement de système microfluidiques génériques pour la mesure de propriétés thermodynamiques de solutions de protéines. Un procédé simple de fabrication de puces microfluidiques résistantes à la pression ainsi qu'à la majorité des solvants organiques a été développé. En outre, les propriétés de surface des microcanaux peuvent être ajustées afin de générer des émulsions eau dans huile ou huile dans l'eau.

L'étude des interactions proteines-proteines en solution a été réalisée en couplant ces dispositifs expérimentaux à la diffusion de rayonnement X aux petits angles. Avec seulement quelque milligramme de produit, les données expérimentales obtenues ont permis de calculer le second coefficient du Viriel, grandeur thermodynamique permettant de quantifier les interactions entre protéines.

Une nouvelle approche expérimentale a également été développée afin de déterminer l'équation d'état du lysozyme, équation reliant la pression osmotique à la fraction volumique. Ce système microfluidique est basé sur le transfert de matière entre d'une phase dispersée vers une phase continue. Dans une certaine gamme d'activité de l'eau, l'équation d'état obtenu est en bon accord avec les données de la littérature. Afin de relier la dynamique du transfert aux propriétés thermodynamique du système une première approche de modélisation est proposée. Cette approche a pour but de déterminer l'équation d'état de la protéine avec une seule goutte.

LABORATOIRE DE GENIE CHIMIQUE
4 ALLEE EMILE MONSO 31432 TOULOUSE, FRANCE